Atomic scale characterization of Tc and Pu uptake by magnetite based on atomistic simulations and X-ray absorption spectroscopy

Inaugural dissertation
of the Faculty of Science,
University of Bern

presented by

Anita Sonja Katheras

Supervisor of the doctoral thesis:
Prof. Dr. Sergey V. Churakov
Institute of Geological Sciences, University of Bern

Co-advisor of the doctoral thesis:
Dr. Andreas C. Scheinost
The Rossendorf Beamline (BM20), European Synchrotron Radiation Facility

“Es gibt nichts Besseres im Leben, als gute Lehrer gehabt zu haben.
(There is nothing better in Life than having had good teachers.)”

Gottfried Felix Fischer (1931 - 2023)

Acknowledgements

I would like to express my deepest gratitude to Sergey Churakov, my supervisor, for his unwavering support and guidance throughout this doctoral journey. He introduced me to new concepts, provided clear direction for the thesis, and motivated me during challenging times. His open-door policy and encouragement were invaluable, and I am especially grateful for his meticulous feedback on my writing.

I also extend my sincere thanks to Andreas Scheinost, my co-advisor, for his continuous support, insightful suggestions, and thorough proofreading, which I deeply appreciate. His contributions significantly broadened my understanding of environmental aspects.

Thank you to Matthias Krack and Konstantinos Karalis for their invaluable support in addressing questions about simulations and for their careful revisions of my setups. My gratitude also goes to Thomas Zimmermann, my partner PhD student, for offering an experimental perspective and stimulating discussions. I am grateful to the KRIMI project partners and my colleagues in Berlin, Bremen, Dresden-Rossendorf/Grenoble, Karlsruhe, and Jülich for their friendly collaboration and kind support. Additionally, I deeply appreciate the enriching conversations I had with colleagues I met at conferences.

To my friends and family, thank you for your unwavering support and encouragement. Special thanks go to Georgia for the warm welcome, the joyful moments we shared in the office, and her kindness in all situations. Moreover, I am very grateful to my friends at PSI, the institute, the university, in Bern and Switzerland, who made my time here unforgettable. To my family – especially my parents and siblings – your unconditional love and encouragement across distances have been my anchor throughout this journey.

Lastly, I want to acknowledge my grandfather, whose inspiration and encouragement have been a guiding light. His recitation of the quotation referenced earlier resonates deeply with me, and I agree with it wholeheartedly.

I am profoundly thankful for everyone I encountered during my PhD, each of whom taught me something invaluable. Thank you, all of you!

Abstract

Magnetite is a common iron oxide mineral present in crystalline rocks and subsurface sediments. The mixed valence state of the Fe in magnetite allows for participation in redox reactions and redox buffering. Magnetite plays also an important role for the safe geological disposal of radioactive waste – an ongoing challenge for several countries worldwide. Many countries consider isolation of high level waste in steel casks disposed in deep underground repositories. Over time and in contact with the host-rock pore-water, magnetite will develop as a major corrosion product on the steel surface and, eventually, lead to canisters breaching. The incoming water can then mobilize the radioactive inventory, i.a. technetium and plutonium present in the waste. Experimental observations suggest that magnetite can contribute to their immobilization by participating in surface mediated reductive adsorption and incorporation of hazardous elements into the magnetite structure. This thesis aims at a detailed molecular scale understanding of these phenomena by atomistic simulations and spectroscopic investigations.

The theoretical studies of magnetite as bulk and surface structures as well as nanoparticles were conducted by density functional theory (DFT). The first and fundamental step of this methodology was the development and validation by simulating the appropriate crystal structures. The Hubbard U method (DFT+U) was applied to improve the description of the electrons of octahedrally and tetrahedrally coordinated Fe cations in magnetite. In a similar approach, the Hubbard U correction for Tc and Pu was tuned by simulating oxide structures reflecting relevant oxidation states and coordination environments. A close agreement to experimental crystallographic data could be achieved using $U_{\mathrm{Tc(IV)}} = 0\,\mathrm{eV}$ and $U_{\mathrm{Pu(III)}} = 3.5\,\mathrm{eV}$.

In a second step, the thermodynamic stability of the most common magnetite (111) surface was investigated. Contrasting previous studies focusing on the stability of the magnetite surface under vacuum, environmentally relevant conditions influencing the mineral-water interface could be fully addressed. This includes oxygen-terminated surfaces with various degrees of protonation reflecting varying charges of surface-Fe cations, too. The system energies resulting from the simulations were used to calculate the surface energy as function of E_{h} and pH for different surface terminations. Based on the surface energy thus determined, the most stable surface termination of the magnetite (111) surface was identified. The consideration of the surface-water interaction energy was of great importance and resulted in octahedrally coordinated Fe cations with an oxidation state higher than 2.5 as the energetically most favorable surface termination. Based on this preferential (111) surface termination, 2 nm sized particles

with octahedral shape were simulated. Compared to the infinite magnetite surface, they provide new geometrical features such as edges and vertices resulting in an increased solvent interaction for both water and simple electrolyte systems.

In a third step, the interactions of the magnetite (111) surface with hazardous elements were investigated. The structural incorporation of Tc(IV) studied in the present thesis revealed a preferable substitution mechanism of two octahedrally coordinated Fe by one Tc coupled to the formation of a vacancy. Moreover, the Pu(III) sorption complex as proposed by X-ray absorption spectroscopy (XAS) was confirmed by *ab initio* simulations.

The comparison with XAS – specifically using extended X-ray absorption fine structure (EXAFS) spectroscopy – signifies the main strength of the presented studies. The combination of laboratory experiment, spectroscopic characterization and the here presented atomistic modeling allows for a consistent interpretation of the experimental data and an elucidation of local structural changes as function of parameters such pH, metal loading and magnetite particle size. These findings contribute to a deeper understanding of the radionuclide-mineral interaction and provide a valuable basis for environmental safety analyses.

Contents

List of Figures

List of Tables

Chapter 1: Introduction

1.1 Nuclear waste in geological disposal

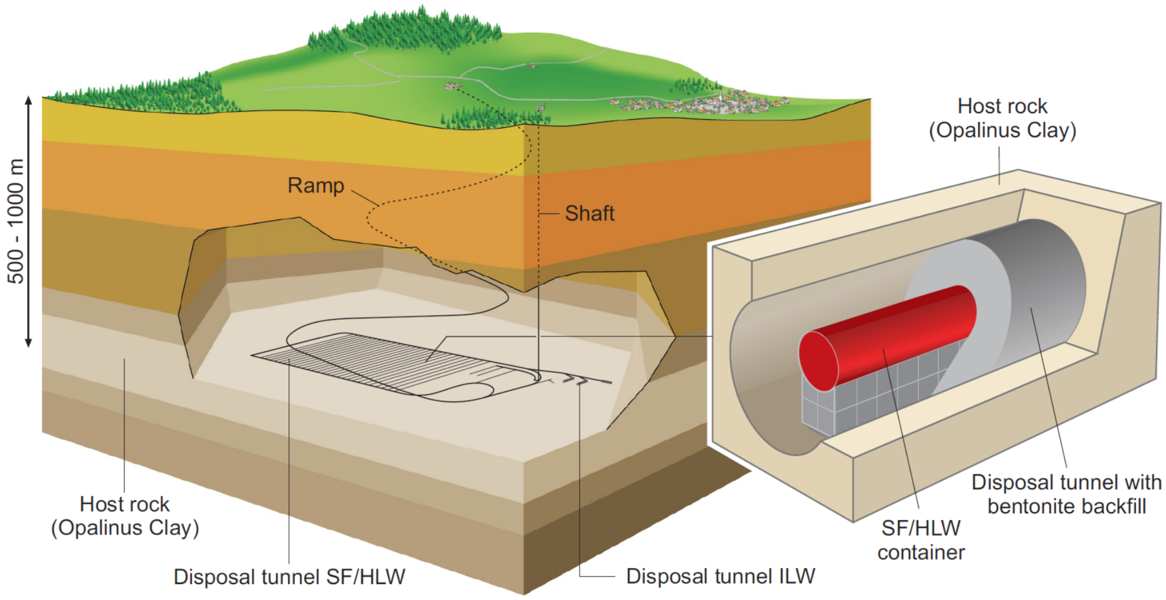

FIGURE 1.1: Diagram of the multi-barrier concept for nuclear waste disposal in canisters placed in the underground repository in Opalinus Clay, with a bentonite clay backfill[1,2].

Radioactive waste is one of the most hazardous substances for the living environment and results in small quantities from medical or research applications. The primary source of radioactive waste is the production of electricity by nuclear power plants[3], from which high-level waste (HLW) and spent nuclear fuel (SNF) remain. Due to their radioactivity exceeding the one of natural uranium ore for several hundred thousand years[1], a stable long-term solution for storage is required. Internationally, the deep geological disposal of radioactive waste is considered as most reliable option, illustrated by the Swiss concept in Figure 1.1. The design of the repository follows a multi-barrier approach, in which several artificial and natural barriers are combined to secure the long-term retention of the radioactive material for up to one million years. HLW is commonly stored in vitrified form[4], while SNF rods prevalently consisting of mixed U/Pu oxides represent the storage matrix themselves. It is foreseen to encapsulate both HLW and SNF in carbon steel canisters (red cylinder in Figure 1.1) with a wall thickness of 0.15 m[2]. The canisters will be placed inside tunnels in the repository facility built in a suitable host-rock formation, e.g., Opalinus Clay in Switzerland. The remaining tunnel cavity will be backfilled with compacted bentonite clay serving as a buffer. In contact with subsurface water, these clay materials not only balance the hydrostatic pressure underground, they also have self-sealing properties. However, the contact of pore-water with the canisters cannot be avoided.

The use of steel as canister material offers the advantage of a relatively inexpensive production as well as well-known physical and chemical properties. Unfortunately, these include a foreseen corrosion of the casks under repository conditions. Zn or Cu can be used as coating materials to slow down this process, but they cannot prevent the corrosion entirely, which occurs in two steps. After sealing the disposal tunnels, there is remaining oxygen from the construction of the disposal facility. This leads to two major oxic processes: First, oxygen is consumed by microbial activity, the oxidation of Fe(II) minerals and sulfides as well as the oxic corrosion of steel. This aerobic corrosion leads to small amounts of hematite (Fe_2O_3) and magnetite (Fe_3O_4)[2]. Second, pore-water is transported through the bentonite buffer and will eventually saturate the bentonite after 50 a to 100 a[5]. This leads to the second anoxic corrosion. Under these conditions at the surface of the canister, an epitaxal, dominantly spinel-type layer will form with an outer porous magnetite layer[5,6]. Moreover, at the interface between canister and surrounding clay, a distinct mix of Fe minerals will be present depending on the given clay inventory. Maghemite (Fe_2O_3), chukanovite ($Fe_2CO_3(OH)_2$) and Fe-phyllosilicates like nontronite at the interface will form as well as siderite ($FeCO_3$) and pyrite (FeS_2) at the clay surface.[7,8]

After around one hundred thousand years, it is expected that the steel canisters encapsulating the waste fail. The incoming water may lead to a dissolution of the still radioactive material. However, the present magnetite can contribute to the retention of the radionuclides, either by sorption at a magnetite surface or by structural incorporation in its inverse spinel structure. This allows for an additional safety layer automatically occurring during the long-term operation of the disposal facility.

1.2 The radionuclides Tc and Pu

Radionuclides are non-stable isotopes of an element, i.e., they spontaneously decay with the emission of electromagnetic radiation or the discharge of high-energy particles. Technetium (Tc) is the lightest element without stable isotopes. The meta-stable isotope ^{99m}Tc with a half-life of 6.01 h is used in various medical applications, e.g., for labeling and tracing medicine in the human body. Other advantages include the facile and low cost production[9]. ^{99m}Tc decays by irradiation of γ-rays[10] to ^{99}Tc with a much longer half-life ($t_{1/2} = 2.1 \times 10^5$ a[10]). Moreover, it is the main fission product of uranium (especially ^{235}U) and plutonium (^{239}Pu), the mass-wise prevalent radioactive elements in nuclear fuel.

Tc with a zero-valent electronic configuration of [Kr] $5s^2 4d^5$ can assume various oxidation states with the environmentally most relevant ones being Tc(IV) and Tc(VII)[11]. Tc(VII) is highly mobile as pertechnetate ion TcO_4^-, while Tc(IV) has been found to precipitate as TcO_2, or to be incorporated, e.g., in magnetite and other spinel-type minerals[11–13]. The oxidation state can be deduced from dedicated experiments such as XANES (X-ray absorption near-edge structure) spectroscopy[14]. Experimentally, transitions from Tc(VII) to Tc(IV) have been observed for various reductive systems[15] leading to an immobilization and assumed safe storage of nuclear waste. The most stable form for Tc waste is a vitrified waste product (glass). However, this form is still sensitive to re-oxidation[16] and, hence, re-mobilization. Therefore, mechanisms of stable incorporation are investigated, e.g., the presence of Fe(II) oxalate as glass melt additive has been shown to increase the retention[17]. As a U decay product in the SNF rods, Tc forms metallic inclusions[18] within the fuel at grain boundaries[19].

Plutonium (Pu) is another radioactive element. It is used in nuclear fuel by up to 30 % in combination with uranium, commonly in a mixed oxide (MOX) form. For the generation of electricity, the main fissile isotopes of Pu are ^{239}Pu ($t_{1/2} = 2.4 \times 10^4$ a[10]), ^{240}Pu ($t_{1/2} = 6.6 \times 10^3$ a[10]), and ^{242}Pu ($t_{1/2} = 3.73 \times 10^5$ a[10]), that can sustain a thermal chain reaction. On the other hand, this chain reaction of especially ^{239}Pu can be used for military applications such as nuclear weapons. The release of Pu by above-ground nuclear weapon tests, nuclear reactor failures as well as incomplete re-processing of SNF[20,21] causes contamination of the environment. Moreover, inside the most common type of nuclear reactor utilizing pressurized water, Pu was also found as a surface contamination in the primary circuit[22]. This further complicates reprocessing and extends the amount of nuclear waste.

Initially, the SNF contains a significant inventory of Pu. E.g., 40 years after the SNF is discharged from the reactor, the Pu nuclides cause approximately 15 % of the total radiation. Yet, PuO_2 accounts for only about 0.01 % of the material.[23] Furthermore, Pu nuclides can develop over time by radioactive decay of other nuclides. E.g., ^{239}Pu is a decay product of ^{238}U and can accumulate over time especially at the rim regions of the SNF rods[19]. As redox-sensitive element with common oxidation states ranging from Pu(III) to Pu(VI), its solubility and mobility depend on the environmental conditions. Pu(IV) has been found to have a lower solubility than the other oxidation states[24]. The reduced mobility is thereby supported by reducing conditions, e.g., due to the anoxic corrosion of Fe and/or the presence of reduction agents such as Fe(II). Accordingly, controlling the redox state controls in turn the amount of dissolved Pu[25].

1.3 Relevance of magnetite

Magnetite is a mixed Fe(II)/Fe(III) oxide and abundant in the subsurface. It participates in many environmentally relevant reactions. In these, it acts as redox buffer in geochemical systems alongside other iron bearing minerals such as wüstite, maghemite and hematite. Moreover, magnetite enables redox controlled interfacial reactions. E.g., the transformation of green rust to magnetite might enable the production of hydroxyl radicals and lead to a strong degradation of organic pollutants[26]. Moreover, magnetite contributes to the redox transformation of metal and semi-metal pollutants that are discussed in more detail in the next section. Other environmentally important reactions include the repeated cycling of Fe(II) oxidation and Fe(III) reduction in microbial environments[27] or the denitrification at the interface between different clayey and crystalline Fe sediments[28].

Apart from naturally occurring magnetite, this iron oxide can be a result of corrosion, too. The corrosion of iron or Fe-steel is a known problem in technology. Depending on the environmental conditions and the type of steel, different iron (hydr)oxides can form. Mild steel, e.g., is one of the most commonly used steel types with applications from the production of vehicle frames to cookware. Corrosion forming thin films has been observed by hydrothermal electrolysis experiments in alkaline solution. These thin films have been found to consist mainly of magnetite and can effectively minimize or even prevent further corrosion of the mild steel.[29] Moreover, the amount[30] and rate[31] of corrosion is increased by increased salinity. Furthermore, the amount of available oxygen is an important factor in the speciation of the corrosion products. E.g., while in oxic water the main corrosion products are ferric hydroxides ($Fe(OH)_3$), under low-oxygen conditions magnetite is the main corrosion product[32].

In the geological disposal of radioactive waste, the anoxic corrosion of carbon steel canisters forms – among other Fe(III) minerals[33] – mostly magnetite (Equation 1.1[1,5]). Over time, the magnetite transforms to the thermodynamically more stable fully oxidized Fe_2O_3 in its α-(hematite) or γ-polymorph (maghemite) (Equation 1.2).

$$3\,Fe_{(s)} + 4\,H_2O_{(l)} \rightarrow Fe_3O_{4(s)} + 4\,H_{2(g)} \tag{1.1}$$

$$4\,Fe_3O_{4(s)} + O_{2(g)} + x\,H_2O_{(l)} \rightarrow 6\,Fe_2O_3 \cdot x\,H_2O_{(s)} \tag{1.2}$$

The magnetite crystal structure belongs to the inverse-spinel type. Normal spinels follow the chemical formula AB_2X_4, where A and B signify cationic and X an anionic species. The anions – oxygen (O^{2-}) for instance – are arranged in a cubic close-packed lattice forming octahedral and tetrahedral coordination sites for the cations. Per formula unit, there are four octahedral and eight tetrahedral sites available. In a normal spinel, one eight of the tetrahedral sites are occupied by the A cations with oxidation state (II), and half of the octahedral sites are occupied by the B cations with an oxidation state (III).

In an inverse spinel such as magnetite (Figure 1.2), the same octahedral sites are half-filled by A(II) cations – in magnetite Fe(II) –, the other half is filled by B(III) cations – in magnetite Fe(III). Furthermore, the tetrahedral sites occupied in a normal spinel are occupied by B(III) cations, in magnetite Fe(III). This altered arrangement of di- and trivalent cations with a specific arrangement of the electronic spin leads to special electronic and magnetic properties. In fact, magnetite is the oldest known magnetic material to mankind.

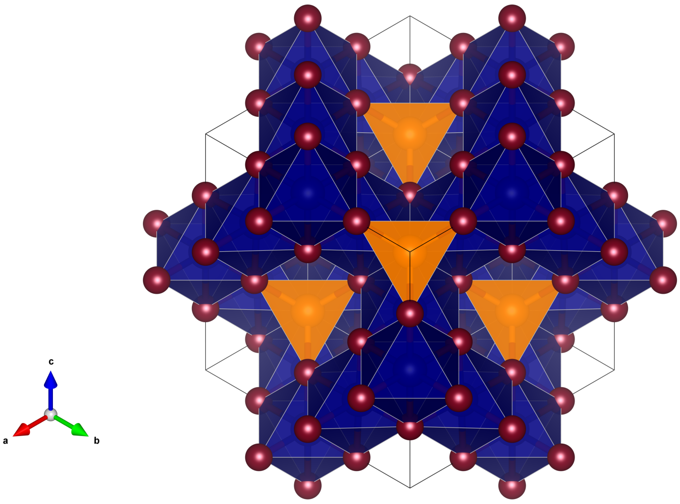

FIGURE 1.2: Unit cell of magnetite[34] depicting the crystal structure, projection along [111]. The red spheres represent oxygen anions forming the basic cubic close-package lattice. With the corresponding polyhedra, octahedrally coordinated Fe are depicted in blue, tetrahedrally coordinated Fe in orange. Atomic sizes are adapted for visualization. The same color scheme is found throughout the thesis.

Due to the variable arrangement of cations in the spinel structure, ion exchange and, hence, immobilization of incorporated ions is possible. Moreover, this is especially true for inverse spinels (magnetite), where the presence of di- and trivalent ions (Fe) in the octahedral sites allows for an adaptation to changing charge due to the insertion of higher valent cations, too. Furthermore, spinels in general have a high stability, at high temperatures, too. Therefore, e.g., they can be used during the vitrification process of radioactive waste as entrapment[35].

1.4 Interaction of magnetite with toxic metal cations

Many hazardous metals have been shown to interact with magnetite allowing for a retention and separation from the environment. This includes toxic metals as well as radioactive elements relevant in the repository context. Thereby, the interaction of magnetite with these heavy metals is dominated by three phenomena.

First, magnetite has been show to cause a reduction of the valence state transforming, e.g., the toxic antimony from Sb(V) to Sb(III)[36] or highly mobile pertechnetate (TcO_4^-) as Tc(VII) to the low-soluble form of Tc(IV)[11,37]. Other examples of these reductive capacities of magnetite include the reduction of uranium (U(VI) to U(IV))[38–45] and plutonium (Pu(V) to Pu(III))[24,46,47]. The corresponding oxidation reaction is provided by the oxidation of Fe(II) to Fe(III)[48] and can be carried out by Fe(II) in equilibrium in solution or in the octahedrally coordinated Fe sites in the magnetite structure. Furthermore, the oxidation of Fe in magnetite can lead to a transformation to maghemite[49].

Second, the (reduced) metal cations can be sorbed at magnetite surfaces as has been shown, e.g., for Cs, Sr, Th, Co, Eu, and Ce with increasing effectivity along this order forming sorption complexes[50–52]. The identification of their structure tends to be difficult, but X-ray absorption spectroscopy (XAS) is a valuable tool in investigating the local atomic structure. E.g., for Se – a pollutant in wastewater as well as daughter radionuclide of U – the sorption mechanism proposed by XAS first follows a monodentate sorption complex to one oxygen anion as part of an FeO_6 octahedron at the magnetite surface. Consecutively, a further reduction with the growth of Se(0) nanowires[49] or the stronger sorption as bidentate sorption complex[53] are possible. Moreover, sorption complexes with three connections to surface-oxygen (tridentate sorption complexes) were proposed for Am and Eu[54], As[55–58], Sb[36], and Pu[24,59]. From XAS analysis, it is proposed that some of these tridentate sorption complexes are located at edge-connected FeO_6 octahedra. This structural composition resembles the octahedral termination of the magnetite (111) surface which is expected to act as sorption basis for TcO_6 dimers[11,60], too. In many cases including Tc and Pu sorption complexes, the confirmation of these local structures at the atomistic scale does not exist yet. Atomistic simulations complimenting the XAS experiments can resolve the geometrical relations also beyond this first coordination by FeO_6 octahedra.

Third, a structural incorporation of toxic metal cations into the magnetite crystal structure is possible. For larger cations such as U[61] or Pu[59], incorporation seems to occur mostly as a result of co-precipitation, i.e., when magnetite is synthesized in presence of dissolved radionuclides. However, this leads to a more distorted coordination environment[59] and a less stable structure. In terms of (simulated) ageing, these large cations tend to be expelled from the magnetite crystal structure and get sorbed to the magnetite surface as in case of Pu[59] or possibly released into the surrounding solution as in case of U[61]. On the other hand, coprecipitation and coupled incorporation have been shown to work effectively for cations similar in size to the Fe cation, such as octahedrally coordinated Tc(IV)[62]. In case of incorporation, it is expected that the radionuclide replaces an octahedrally coordinated Fe cation[11,45,59] leading to solid solutions. The newly incorporated cation can disturb the charge balance of the system. E.g., the incorporation of Tc(IV) into the magnetite structure causes an excess of positive charge compared to the initial Fe(II) or Fe(III) cations. It is not understood, yet, how the charge compensation is achieved alongside the substitution. Overall, the stable structural incorporation via formation of solid solutions is expected to be the most effective retention mechanism in the long run. Beyond that, the magnetite crystal structure may be partly transformed to new mineral phases such as FeSe in nanoparticulate form[63].

As was shown above, these three phenomena dominating the interaction of magnetite with radionuclides can also occur in several steps within the same system. E.g., Se has been shown to first get reduced from Se(VI) to Se(IV) in presence of magnetite[49] or its precursor phases such as green rust[63] and gets sorbed subsequently. Another example is, first, the reduction of U(VI) to U(V) in close proximity to the magnetite surface and, second, sorption to it. Further reduction leads to the formation of insoluble U(IV)O_2[44,64]. The ratio of Fe(II)/Fe(III) may lead to a dominance of one or the other structure[40]. Similarly, as was identified by Yalçıntaş et al.[11], two reduced Tc species – one sorbed, one incorporated – can occur simultaneously and the predominance of one or the other product may depend on environmental conditions such as E_h and pH. Hence, as in an experimental setup several signals may overlap, a clear identification of the respective structures can be supported by atomistic simulations of the various crystal structures and the comparison with their corresponding (theoretical) XAS spectra.

1.5 Research objectives and scientific questions

The understanding of the magnetite surface, its termination and speciation such as protonation state, is of fundamental importance to investigate possible interaction and retention mechanisms of radionuclides. In the majority of studies conducted previously around the world[65–68], magnetite surfaces used to be investigated under well-defined vacuum and at low temperature. Based on these, the interaction with single molecules were studied[69,70]. However, such specific laboratory conditions are very different from a natural environment including the presence of solvents and dissolved ions. Moreover, environmental parameters such as temperature, hydrogen potential (pH), and redox potential (E_h) most likely influence the surface speciation. This results in an alteration of the surface and leads to a different starting point for chemical reactions. Hence, for this PhD thesis, the most commonly observed (111) surface of magnetite was investigated and a special focus was given to the stability of different surface terminations over a wide range of environmental conditions.

Another gap in the present understanding is the stability and formation of magnetite nanoparticles (MNPs) as smallest self-contained unit. Previous studies investigating MNPs found precipitated, i.e., experimentally produced, nanoparticles commonly in a size range of mean diameters from 6 nm to 10 nm or larger[71,72]. However, by even smaller particles that are conceivable as corrosion products, a different behavior can be expected due to the increased ratio of surface to volume of the bulk portion of the particles[73]. Moreover, the nanoparticles could be a better representation of non-idealized surfaces due to additional structural features. The availability of edges and vertices of the MNPs provides different sites and enables different sorption mechanisms. Moreover, the interaction with solvents may be different due to these geometrical features. The investigation of all of these factors requires a detailed knowledge about the shape and size of the particles and can be used as basis for thermodynamic calculations.

The detailed investigation of the magnetite-radionuclide interaction remains a challenging task. On the one hand, experimental approaches face the question of safety while working with radioactive substances as well as a commonly limited spacial resolution and identification of structural geometry. On the other hand, computational approaches require a solid basis in terms of reliable computational parameters to perform meaningful atomistic simulations. In this PhD thesis, sensible setups for the open-source CP2K code were developed to both investigate Tc(IV) and Pu(III) under the expected repository conditions.

Following up for Tc, the precipitation on magnetite and the following incorporation have been shown experimentally[11]. Recent computational studies investigated possible $TcO_2 \cdot xH_2O$ precipitation products at the surface[60] or studied the Tc incorporation at the magnetite (001) surface[74]. However, the investigation of the incorporation at the dominant (111) magnetite surface has not been studied, yet. Furthermore, the incorporation of Tc(IV) in magnetite replacing an octahedrally coordinated Fe cation leaves an important question: Although the ionic radii match perfectly between Fe(III) and Tc(IV) in octahedral coordination[75], the substitution provokes a charge imbalance. Based on thermodynamic considerations, the formation of a vacancy alongside the substitution is proposed as charge compensation. In the proposed scenario[76], one Tc(IV) replaces two Fe(II) in edge-connected FeO_6 octahedra. However, the confirmation of this specific crystal structure considering the effect on the surrounding magnetite crystal structure remains unknown.

For the interaction of Pu with magnetite resulting in a retaining complex, a tridentate sorption complex is proposed. From the analysis of experimental EXAFS data[24,59], the sorption complex is expected to be positioned at three edge-sharing FeO_6 octahedra. As these are part of the magnetite (111) surface with octahedral coordination, this is the expected location and, in turn, another confirmation of this magnetite surface speciation. However, so far only few coordination shells were taken into account to resolve the atomic structure. Following the aforementioned development of a reasonable computational setup, the proposed sorption complex was investigated in the present thesis, shedding light on the resulting local geometry.

1.6 Methods and approach

1.6.1 Atomistic simulations

To understand the structure, stability and interaction of materials, an investigation at an atomistic level can be very helpful. Fundamentally[77], the time-independent Schrödinger equation (Equation 1.3) needs to be solved, where $\hat{H}$ is the Hamilton operator of the system. $\hat{H}$ accounts for all interactions between N electrons and M nuclei in the system, ψ is the corresponding wave function. The Hamilton operator accounts for the interactions based on the kinetic and potential energies of the present particles and, if only the initial state is considered, the term *ab initio* – based on first-principles – is commonly used.

$$\hat{H}\psi = E\psi \tag{1.3}$$

The solution of this eigenvalue equation yields the total energies of the system, E, the lowest among them is referred to as ground-state of the system. However, the analytical solution can be achieved only for simple systems such as the hydrogen atom, definitely not for complex systems including many electrons.

Several approximations have been made, one of the most famous is the Born-Oppenheimer approximation. It conceptually relies on the very different masses of the particles, i.e., in the lightest element hydrogen, the nucleus – one proton – is about 1836 times heavier than the electron and it will move much slower than the electron. Hence, in the Born-Oppenheimer approximation, the equations of motion of electrons and nuclei are separated and are assumed to result in the ground state for atomic cores and electrons at each moment of time.

In the Hartree-Fock approach, the wave functions of many-body systems are approximated as antisymmetric product (Slater determinant) of one-electron wave functions. Moreover, the electrons are not considered to interact explicitly with one another, rather they interact with the mean electrostatic field caused by the sum of all electrons (mean-field approach). The number of possibly considered electrons, i.e., the investigated system size, can be increased by this approximation of the wave-function. Hence, the Hartree-Fock method is a powerful tool to simulate small molecules. However, the computational costs scale as N^4 with the number of electrons, making calculations for large system prohibitively expensive.

Density functional theory (DFT) is in this way a popular *ab initio* method from a quantum-chemical point-of-view. It is used commonly for condensed matter simulations due to its computational efficiency. The electrons of the system are approximated by their density as system-specific quantity. DFT also incorporates the exchange-correlation, including electron-electron interactions beyond the classical Coulombic repulsion (exchange) as well as the energy difference between exact kinetic energy and kinetic energy of the electronic density (correlation). However, the exact description of the exchange-correlation as functional is not available and cannot be applied in simulations. Hence, various approximations have been used. Among them is the generalized gradient approach (GGA) which is used as basis for this thesis. Specifically the PBE functional developed by Perdew, Burke and Ernzerhof[78,79] is applied.

However, conventional DFT tends to fail in the approximation for systems containing *d*- and *f*-electrons, as these electrons are strongly correlated and more localized. A common related problem is the identification of materials to be conductors, although they show semi-conducting or insulating behavior in reality. These materials are called Mott-insulators[80]. This phenomenon can concern materials containing transition metal elements such as Fe and Tc as well as actinides such as Pu. To overcome this issue, a standard method is the introduction of an additional Hubbard parameter U[81] to correct the electronic state of the localized electronic states. As shown in Equation 1.4, the conventional DFT energy, E_{DFT}, is corrected by another term including on-site Coulomb repulsion, U, and the screened exchange energy, J. ρ^{σ} refers to the spin-dependent *d*- or *f*-orbital occupation matrix, respectively. The main DFT computer code used for this thesis is the CP2K code[82], which has the DFT+U method implemented.

$$E_{DFT+U} = E_{DFT} + \frac{U-J}{2}\sum_{\sigma}\mathrm{Tr}[\rho^{\sigma} - \rho^{\sigma}\rho^{\sigma}] \tag{1.4}$$

The DFT+U method has been recently proven as an effective *ab initio* method in the prediction of radioactive waste materials[83]. The high influence of the U parameter has been shown in both studies on lanthanide monazites[84] as well as pyrochlores and monazite-like ceramics including actinides[85].

The value of the U parameter has only limited transferability between codes and systems, as several points can possibly influence its value:

- the implementation in the code in relation to existing algorithms
- the element type
- the oxidation state
- the coordination environment with type and number of ligand.

Consequently, there needs to be vigorous benchmarking in determining the parameter value with regard to the system of interest.

In a previous study in our research group using CP2K[86], a suitable U value had been found and validated for octahedrally coordinated Fe(II) and Fe(III) occurring in the iron oxides wüstite and hematite, respectively. With regard to magnetite, the transferability for the similar, octahedrally coordinated mixed Fe(II/III) can be assumed. However, for the tetrahedrally coordinated Fe(III) a confirmation was required[87] and is now present in the thesis at hand. Accordingly, for the Tc and Pu species relevant in the context of this thesis, the determination of a useful U value was necessary. Moreover, recently new basis sets and corresponding pseudopotentials were published for actinides[88] and were tested in this way.

With Equation 1.3, the lowest energy state of a system can be approximated signifying the stable electronic and, in turn, structural configuration. However, to study an interaction of materials over time, i.e., several possible and potentially consecutive positions of atoms, other methods must be employed. The most common method is molecular dynamics (MD) simulations capturing the subsequent movement of atoms (trajectory). Following an iterative algorithm, the next position of each atom is calculated based on the previous step. The corresponding change of position is calculated based on forces applied to this atom at the previous step following Newton's mechanics. The approximation of these forces can be conducted based on empirical forces, i.a. Coulombic attraction or repulsion and Lennard-Jones potentials, as combined in force-fields. The corresponding MD approach is referred to as classical MD and is especially useful to study surface-solvent interactions with low computational costs. However, to improve the accuracy and allow for a detailed investigation of the chemical bond structure, the electronic exchange-correlation interactions can be taken into account in a combination of MD simulations and DFT simulations. In these so-called *ab initio* MD (AIMD) simulations, the forces affecting each atomic position are obtained by a DFT optimization at each step.

1.6.2 X-ray absorption spectroscopy

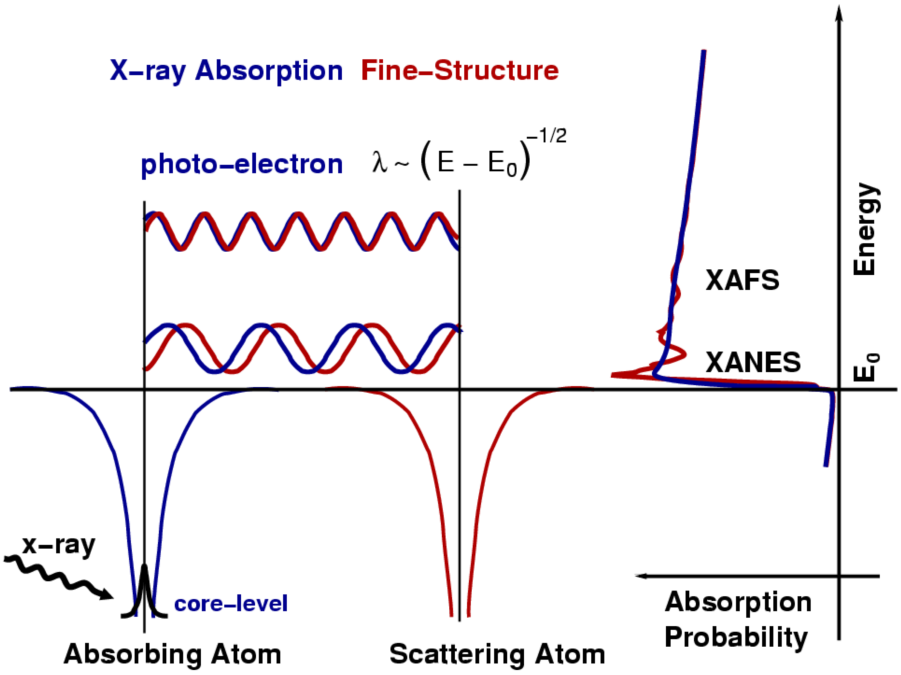

FIGURE 1.3: Signals of X-ray absorption spectroscopy (XAS). The incoming X-ray photons can excite core-level electrons; these photo-electrons can be scattered at the electron shells of surrounding atoms producing an element- and coordination-specific absorption spectrum with distinct interference oscillations (XANES/(E)XAFS)[89].

The identification of the atomic configuration at hand is of utmost importance to make predictions about the long-term stability of the complexes and possible further chemical reactions. The local crystal structure can be investigated by the powerful method of X-ray absorption spectroscopy (XAS) usually conducted at synchrotron radiation facilities.

XAS relies on the principle (Figure 1.3), that photons in the X-ray range can be absorbed by atoms and, thereby, excite core-level electrons to an unoccupied state (XANES) or continuum (EXAFS), depending on the exciting photon energy. The emitted photo-electrons can interact with electrons at atoms in the vicinity of the absorber atom, e.g., by getting scattered. XAS can be divided into two methods: XANES (X-ray absorption near-edge structure) spectroscopy is focused on the absorption process itself. From XANES measurements, information about the absorber atom can be obtained as the absorption energy is connected to the individual electron shells reflected in absorption edges. Hence, the energy where the XANES edge rises is highly element-specific, but is modulated by the oxidation state of the element. However, the XANES signal is further modulated by multiple scattering of the photo-electron by neighboring atoms. Therefore, the interpretation of the oxidation state of an unknown sample requires the availability of well-defined reference samples. These reference samples represent ideal oxidation states of the element of interest as well as a similar coordination geometry. Another challenge lies in the preservation of ionic species with reduced oxidation states instable under atmospheric conditions. Especially for samples prepared under anoxic conditions in a glovebox, the storage and transport to the synchrotron can be challenging. A contact with air and the inherent oxygen may alter the oxidation state of the absorber element and falsify the experimental results.

The investigation of scattering events and interference of the electron waves is conducted by the method of EXAFS (extended X-ray absorption fine structure) spectroscopy. In the subsequent analysis, information about the atomic environment around the absorber atom can be obtained up to a few angstrom (Å) from the photo-absorbing atom. This includes the elemental species of the neighbors, their number (coordination number, CN) as well as the distance to the absorber (r). Furthermore, the degree of (dis-)order of each coordination shell can be identified (Debye-Waller factor, σ^2). It is to be noted, though, that although the distance can be determined reliably up to 0.01 Å, the estimation of the CN may vary by up to 25 %. However, for rigid systems such as crystalline iron minerals, it provides a meaningful estimation of the crystal structure. This thesis focuses on EXAFS, as the coordination environment and possible local geometries can be revealed.

To obtain high-quality EXAFS data, synchrotron radiation as high-energy, high-flux, high-coherence photon source is required. Depending on the scientific question and investigated materials, dedicated instruments are needed to perform experiments successfully[90]. Complementary to experiments, computer software such as FEFF[91–93] can be used to model EXAFS spectra. The simulation of these spectra is based on a possibly relevant crystal structure. Moreover, parameters such as the expected radius of back-scattering around the absorber and the Debye-Waller factor need to be provided. In a following step, the comparison between theoretical spectra with experimental ones can be used to identify the prevalent atomic order and crystal structure.

1.7 Relevance and impact

This thesis provides reliable parameters for the atomistic simulation of magnetite, plutonium and technetium. In this way, it contributes to the in-depth understanding of selected molecular-level aspects of the disposal of radioactive waste and relevant crystal structures. Beyond the deep geological disposal of radioactive waste, the methodologies developed in this thesis can be transferred to a wide range of topics of environmental and economic impact like geochemistry and materials science.

These include magnetite as common mineral in the subsurface together with other Fe minerals such as hematite, goethite and siderite. The ensemble of iron minerals of various oxidation states can react and adapt to changing environmental conditions and contributes to maintain a geochemical equilibrium. Moreover, studying the properties of magnetite can be of high economical importance including the formation as steel corrosion product as significant topic. Furthermore from a mining perspective, magnetite deposits commonly from high-Fe melts[94] are globally not only the second largest resource of Fe. They may include critical resources such as rare-earth elements needed for modern technology, too.

The crystal structure of magnetite can serve as host-matrix for various metals, be them scarce and commercially important and/or toxic and harmful to the living environment. The basis for possible substitution is the availability of different coordination sites. The inherent presence of Fe(II) and Fe(III) allows for an adaptation to changing environmental conditions and resilience in close-contact to higher valence state ions. This allows for stable incorporation structures of, e.g., Ti(IV) in magnetite contributing to a range of stable solid solutions, so-called titanomagnetites[95]. Moreover, magnetite nanoparticles have been shown to act as effective reduction and retention agents for heavy metals (e.g., As, Cr, Sb, Se) and organic pollutants from wastewaters. Furthermore, the purification of drinking water using magnetite (nano-) particles is easy and does not require complicated technical setups. The inherent magnetic properties allow for an simple separation of the contaminants, too, and this drinking water purification method allows for a cost-effective way to improve the health and life quality of living beings.

1.8 Structure of the thesis

The introduction to the subject of the thesis is given in chapter 1. The background of the studied system, relevant chemical compounds and the modeling approach are highlighted.

The magnetite crystal structure, magnetite (111) surface terminations relevant under environmental conditions and the development of a corresponding reasonable simulation setup are focused on in chapter 2. These findings were published in *Environmental Science & Technology* (DOI: 10.1021/acs.est.3c07202).

In chapter 3, octahedral magnetite nanoparticles are investigated in a logical consequence of the previous results. These findings were published in *Environmental Science & Technology* (DOI: 10.1021/acs.est.4c06531).

The development of a computational description (DFT+U) for octahedrally coordinated Tc(IV) is focused on in chapter 4. Further, mechanisms of structural incorporation are investigated. The corresponding manuscript has been submitted to *Environmental Science & Technology*.

The development of a computational description in the DFT+U scheme for Pu(III) and an investigation regarding the sorption at the magnetite (111) surface are presented in chapter 5. A corresponding manuscript is currently in preparation.

In chapter 6, the findings of the thesis are concluded. Moreover, an outlook regarding further scientific questions is presented.

1.9 References

[1] Johnson, L.; Schneider, J.; Zuidema, P.; Gribi, P.; Mayer, G.; Smith, P.; Kunz, B.; Frei, C. *Project Opalinus Clay - Demonstration of Disposal for Spent Fuel, Vitrified High-level Wast and Long-lived Intermediate-level Waste*; NAGRA tech. report 02-05, 2002.

[2] Landolt, D.; Davenport, A.; Prayer, J.; Shoesmith, D. *A Review of Materials and Corrosion Issues Regarding Canisters for Disposal of Spent Fuel and High-level Waste in Opalinus Clay*; NAGRA tech. report 09-02, 2009.

[3] Churakov, S. V.; Hummel, W.; Fernandes, M. M. Fundamental Research on Radiochemistry of Geological Nuclear Waste Disposal. *Chimia* **2020**, *74*, 1000–1009.

[4] Hummel, W.; Schneider, J. W. Safety of Nuclear Waste Repositories. *Chimia* **2005**, *59*, 909–915.

[5] King, F. *Corrosion of Carbon Steel under Anaerobic Conditions in a Repository for SF and HLW in Opalinus Clay*; NAGRA tech. report 08-12, 2008.

[6] Grambow, B.; Smailos, E.; Geckeis, H.; Müller, R.; Hentschel, H. Sorption and Reduction of Uranium(VI) on Iron Corrosion Products under Reducing Saline Conditions. *Radiochim. Acta* **1996**, *74*, 149–154.

[7] Schlegel, M. L.; Bataillon, C.; Benhamida, K.; Blanc, C.; Menut, D.; Lacour, J.-L. Metal Corrosion and Argillite Transformation at the Water-saturated, High-Temperature Iron–Clay Interface: A Microscopic-scale Study. *Appl. Geochem.* **2008**, *23*, 2619–2633.

[8] Schlegel, M. L.; Bataillon, C.; Blanc, C.; Prêt, D.; Foy, E. Anodic Activation of Iron Corrosion in Clay Media under Water-saturated Conditions at 90 °C: Characterization of the Corrosion Interface. *Environ. Sci. Technol.* **2010**, *44*, 1503–1508.

[9] Papagiannopoulou, D. Technetium-99m Radiochemistry for Pharmaceutical Applications. *J. Labelled Compd. Radiopharm.* **2017**, *60*, 502–520.

[10] Live Chart of Nuclides. `https://www-nds.iaea.org/relnsd/vcharthtml/VChartHTML.html`, International Atomic Energy Agency (IAEA).

[11] Yalçıntaş, E.; Scheinost, A. C.; Gaona, X.; Altmaier, M. Systematic XAS Study on the Reduction and Uptake of Tc by Magnetite and Mackinawite. *Dalton Trans.* **2016**, *45*, 17874–17885.

[12] Lukens, W. W.; Magnani, N.; Tyliszczak, T.; Pearce, C. I.; Shuh, D. K. Incorporation of Technetium into Spinel Ferrites. *Environ. Sci. Technol.* **2016**, *50*, 13160–13168.

[13] Wang, G.; Um, W.; Kim, D.-S.; Kruger, A. A. ^{99}Tc Immobilization from Off-gas Waste Streams Using Nickel-doped Iron Spinel. *J. Hazard. Mater.* **2019**, *364*, 69–77.

[14] Bauters, S.; Scheinost, A. C.; Schmeide, K.; Weiss, S.; Dardenne, K.; Rothe, J.; Mayordomo, N.; Steudtner, R.; Stumpf, T.; Abram, U.; Butorin, S. M.; Kvashnina, K. O. Signatures of Technetium Oxidation States: A New Approach. *Chem. Commun.* **2020**, *56*, 9608–9611.

[15] Kobayashi, T.; Scheinost, A. C.; Fellhauer, D.; Gaona, X.; Altmaier, M. Redox Behavior of Tc(VII)/Tc(IV) under Various Reducing Conditions in 0.1 M NaCl Solutions. *Radiochim. Acta* **2013**, *101*, 323–332.

[16] Soderquist, C. Z.; Schweiger, M. J.; Kim, D.-S.; Lukens, W. W.; McCloy, J. S. Redox-dependent Solubility of Technetium in Low Activity Waste Glass. *J. Nucl. Mater.* **2014**, *449*, 173–180.

[17] Pegg, I. L. Behavior of Technetium in Nuclear Waste Vitrification Processes. *J. Radioanal. Nucl. Chem.* **2015**, *305*, 287–292.

[18] Giménez, J.; De Pablo, J.; García-Gómez, S.; Serrano-Purroy, D.; Iglesias, L.; Clarens, F.; Martínez-Torrents, A. Modelling the Release of Mo, Tc, Ru and Rh from High Burnup Spent Nuclear Fuel at Alkaline and Hyperalkaline pH. *MRS Adv.* **2023**,

[19] Johnson, L.; McGinnes, D. *Partitioning of Radionuclides in Swiss Power Reactor Fuels*; NAGRA tech. report 02-07, 2003.

[20] Batuk, O. N. et al. Multiscale Speciation of U and Pu at Chernobyl, Hanford, Los Alamos, Mcguire Afb, Mayak, and Rocky Flats. *Environ. Sci. Technol.* **2015**, *49*, 6474–6484.

[21] Skipperud, L.; Salbu, B.; Oughton, D. H.; Drozcho, E.; Mokrov, Y.; Strand, P. Plutonium Contamination in Soils and Sediments at Mayak PA, Russia. *Health Phys.* **2005**, *89*, 255–266.

[22] Kádár, P.; Varga, K.; Németh, Z.; Vajda, N.; Pintér, T.; Schunk, J. Accumulation of Uranium, Transuranium and Fission Products on Stainless Steel Surfaces. *J. Radioanal. Nucl. Chem.* **2010**, *284*, 303–308.

[23] Johnson, L.; Niemeyer, M.; Klubertanz, G.; Siegel, P.; Gribi, P. *Model Radioactive Waste Inventory for Reprocessing Waste and Spent Fuel*; NAGRA tech. report 01-01, 2002.

[24] Kirsch, R.; Fellhauer, D.; Altmaier, M.; Neck, V.; Rossberg, A.; Fanghänel, T.; Charlet, L.; Scheinost, A. C. Oxidation State and Local Structure of Plutonium Reacted with Magnetite, Mackinawite, and Chukanovite. *Environ. Sci. Technol.* **2011**, *45*, 7267–7274.

[25] Schramke, J.; Santillan, E.; Peake, R. Plutonium Oxidation States in the Waste Isolation Pilot Plant Repository. *Appl. Geochem.* **2020**, *116*, 104561.

[26] Zhang, X.; Jia, Q.; Deng, J.; Wu, F.; Huang, L.-Z. Interaction between Green Rust and Tribromophenol under Anoxic, Oxic and Anoxic-to-oxic Conditions: Adsorption, Desorption and Oxidative Degradation. *Water Res.* **2022**, *217*, 118398.

[27] Mejia, J.; Roden, E. E.; Ginder-Vogel, M. Influence of Oxygen and Nitrate on Fe (Hydr)oxide Mineral Transformation and Soil Microbial Communities during Redox Cycling. *Environ. Sci. Technol.* **2016**, *50*, 3580–3588.

[28] Robinson, T. C.; Latta, D. E.; Notini, L.; Schilling, K. E.; Scherer, M. M. Abiotic Reduction of Nitrite by Fe(II): A Comparison of Rates and N_2O Production. *Environ. Sci.: Processes Impacts* **2021**, *23*, 1531–1541.

[29] Machmudah, S.; Zulhijah, R.; Wahyudiono; Setyawan, H.; Kanda, H.; Goto, M. Magnetite Thin Film on Mild Steel Formed by Hydrothermal Electrolysis for Corrosion Prevention. *Chem. Eng. J.* **2015**, *268*, 76–85.

[30] Smith, F.; Brownlie, F.; Hodgkiess, T.; Toumpis, A.; Pearson, A.; Galloway, A. Effect of Salinity on the Corrosive Wear Behaviour of Engineering Steels in Aqueous Solutions. *Wear* **2020**, *462–463*, 203515.

[31] Zhang, G.; Tian, Y.; Fu, C.; Wan-Wendner, L.; Li, Y.; Yan, D. The Impact of Oxygen Availability on Steel Corrosion Considering the Self-balance between Anodic and Cathodic Corrosion Cells. *Corros. Sci.* **2024**, *236*, 112252.

[32] Cox, G. L.; Roetheli, B. E. Effect of Oxygen Concentration on Corrosion Rates of Steel and Composition of Corrosion Products Formed in Oxygenated Water. *Ind. Eng. Chem.* **1931**, *23*, 1012–1016.

[33] Johnson, L. H.; Smith, P. A. *The Interaction of Radiolysis Products and Canister Corrosion Products and the Implications for Spent Fuel Dissolution and Radionuclide Transport in a Repository for Spent Fuel*; NAGRA tech. report 00-04, 2000.

[34] Sasaki, S. Radial Distribution of Electron Density in Magnetite, Fe_3O_4. *Acta Cryst. B* **1997**, *53*, 762–766.

[35] Lee, M.-S.; Um, W.; Wang, G.; Kruger, A. A.; Lukens, W. W.; Rousseau, R.; Glezakou, V.-A. Impeding ^{99}Tc(IV) Mobility in Novel Waste Forms. *Nat. Commun.* **2016**, *7*.

[36] Kirsch, R.; Scheinost, A. C.; Rossberg, A.; Banerjee, D.; Charlet, L. Reduction of Antimony by Nano-particulate Magnetite and Mackinawite. *Mineral. Mag.* **2008**, *72*, 185–189.

[37] Heald, S. M.; Krupka, K. M.; Brown, C. F. Incorporation of Pertechnetate and Perrhenate into Corroded Steel Surfaces Studied by X-ray Absorption Fine Structure Spectroscopy. *Radiochim. Acta* **2011**, *100*, 243–253.

[38] Missana, T.; Maffiotte, C.; García-Gutiérrez, M. Surface Reactions Kinetics between Nanocrystalline Magnetite and Uranyl. *J. Colloid Interface Sci.* **2003**, *261*, 154–160.

[39] Aamrani, S. E.; Giménez, J.; Rovira, M.; Seco, F.; Grivé, M.; Bruno, J.; Duro, L.; de Pablo, J. A Spectroscopic Study of Uranium(VI) Interaction with Magnetite. *Appl. Surf. Sci.* **2007**, *253*, 8794–8797.

[40] Latta, D. E.; Gorski, C. A.; Boyanov, M. I.; O'Loughlin, E. J.; Kemner, K. M.; Scherer, M. M. Influence of Magnetite Stoichiometry on U(VI) Reduction. *Environ. Sci. Technol.* **2011**, *46*, 778–786.

[41] Singer, D. M.; Chatman, S. M.; Ilton, E. S.; Rosso, K. M.; Banfield, J. F.; Waychunas, G. A. U(VI) Sorption and Reduction Kinetics on the Magnetite (111) Surface. *Environ. Sci. Technol.* **2012**, *46*, 3821–3830.

[42] Singer, D. M.; Chatman, S. M.; Ilton, E. S.; Rosso, K. M.; Banfield, J. F.; Waychunas, G. A. Identification of Simultaneous U(VI) Sorption Complexes and U(IV) Nanoprecipitates on the Magnetite (111) Surface. *Environ. Sci. Technol.* **2012**, *46*, 3811–3820.

[43] Ma, Y.; Cheng, X.; Kang, M.; Yang, G.; Yin, M.; Wang, J.; Gang, S. Factors Influencing the Reduction of U(VI) by Magnetite. *Chemosphere* **2020**, *254*, 126855.

[44] Pan, Z.; Bártová, B.; LaGrange, T.; Butorin, S. M.; Hyatt, N. C.; Stennett, M. C.; Kvashnina, K. O.; Bernier-Latmani, R. Nanoscale Mechanism of UO_2 Formation through Uranium Reduction by Magnetite. *Nat. Commun.* **2020**, *11*, 4001.

[45] Fu, D.-m.; Li, M.; Hua, Y.-l.; Gao, F.-y.; Wu, X.-y.; Zhang, X.-w.; Fang, Q.; Bi, L.; Cai, T. Evidence for In-situ Electric-Induced Uranium Incorporation into Magnetite Crystal in Acidic Wastewater. *Sep. Purif. Technol.* **2022**, *291*, 120957.

[46] Powell, B. A.; Fjeld, R. A.; Kaplan, D. I.; Coates, J. T.; Serkiz, S. M. Pu(V)O_2^+ Adsorption and Reduction by Synthetic Magnetite (Fe_3O_4). *Environ. Sci. Technol.* **2004**, *38*, 6016–6024.

[47] Felmy, A. R.; Moore, D. A.; Pearce, C. I.; Conradson, S. D.; Qafoku, O.; Buck, E. C.; Rosso, K. M.; Ilton, E. S. Controls on Soluble Pu Concentrations in PuO_2/Magnetite Suspensions. *Environ. Sci. Technol.* **2012**, *46*, 11610–11617.

[48] Scott, T. B. Sorption of Uranium onto Iron Bearing Minerals. Ph.D. thesis, University of Bristol, 2005.

[49] Poulain, A.; Fernandez-Martinez, A.; Greneche, J.-M.; Prieur, D.; Scheinost, A. C.; Menguy, N.; Bureau, S.; Magnin, V.; Findling, N.; Drnec, J.; Martens, I.; Mirolo, M.; Charlet, L. Selenium Nanowire Formation by Reacting Selenate with Magnetite. *Environ. Sci. Technol.* **2022**, *56*, 14817–14827.

[50] Rojo, I.; Seco, F.; Rovira, M.; Giménez, J.; Cervantes, G.; Martí, V.; de Pablo, J. Thorium Sorption onto Magnetite and Ferrihydrite in Acidic Conditions. *J. Nucl. Mater.* **2009**, *385*, 474–478.

[51] Singh, B.; Jain, A.; Kumar, S.; Tomar, B.; Tomar, R.; Manchanda, V.; Ramanathan, S. Role of Magnetite and Humic Acid in Radionuclide Migration in the Environment. *J. Contam. Hydrol.* **2009**, *106*, 144–149.

[52] Efimova, N. V.; Krasnopyorova, A. P.; Yuhno, G. D.; Sofronov, D. S.; Rucki, M. Uptake of Radionuclides ^{60}Co, ^{137}Cs, and ^{90}Sr with α-Fe_2O_3 and Fe_3O_4 Particles from Aqueous Environment. *Materials* **2021**, *14*, 2899.

[53] Börsig, N.; Scheinost, A. C.; Schild, D.; Neumann, T. Mechanisms of Selenium Removal by Partially Oxidized Magnetite Nanoparticles for Wastewater Remediation. *Appl. Geochem.* **2021**, *132*, 105062.

[54] Morelová, N.; Finck, N.; Lützenkirchen, J.; Schild, D.; Dardenne, K.; Geckeis, H. Sorption of Americium / Europium onto Magnetite under Saline Conditions: Batch Experiments, Surface Complexation Modelling and X-ray Absorption Spectroscopy Study. *J. Colloid Interface Sci.* **2020**, *561*, 708–718.

[55] Wang, Y.; Morin, G.; Ona-Nguema, G.; Menguy, N.; Juillot, F.; Aubry, E.; Guyot, F.; Calas, G.; Brown, G. E. Arsenite Sorption at the Magnetite–Water Interface during Aqueous Precipitation of Magnetite: EXAFS Evidence for a New Arsenite Surface Complex. *Geochim. Cosmochim. Acta* **2008**, *72*, 2573–2586.

[56] Roy, P. K.; Choudhury, M. R.; Ali, M. A. As(III) and As(V) Adsorption on Magnetite Nanoparticles: Adsorption Isotherms, Effect of pH and Phosphate, and Adsorption Kinetics. *Int. J. Chem. Environ. Eng.* **2013**, *4*, 55–63.

[57] Liu, C.-H.; Chuang, Y.-H.; Chen, T.-Y.; Tian, Y.; Li, H.; Wang, M.-K.; Zhang, W. Mechanism of Arsenic Adsorption on Magnetite Nanoparticles from Water: Thermodynamic and Spectroscopic Studies. *Environ. Sci. Technol.* **2015**, *49*, 7726–7734.

[58] Mejia-Santillan, M.; Pariona, N.; Bravo-C., J.; Herrera-Trejo, M.; Montejo-Alvaro, F.; Zarate, A.; Perry, D.; Mtz-Enriquez, A. Physical and Arsenic Adsorption Properties of Maghemite and Magnetite Sub-microparticles. *J. Magn. Magn. Mater.* **2018**, *451*, 594–601.

[59] Dumas, T.; Fellhauer, D.; Schild, D.; Gaona, X.; Altmaier, M.; Scheinost, A. C. Plutonium Retention Mechanisms by Magnetite under Anoxic Conditions: Entrapment Versus Sorption. *ACS Earth Space Chem.* **2019**, *3*, 2197–2206.

[60] Oliveira, A. F.; Kuc, A.; Heine, T.; Abram, U.; Scheinost, A. C. Shedding Light on the Enigmatic $TcO_2 \cdot x$ H_2O Structure with Density Functional Theory and EXAFS Spectroscopy. *Chem. Eur. J.* **2022**, *28*.

[61] Townsend, L. T.; Morris, K.; Harrison, R.; Schacherl, B.; Vitova, T.; Kovarik, L.; Pearce, C. I.; Mosselmans, J. F. W.; Shaw, S. Sulfidation of Magnetite with Incorporated Uranium. *Chemosphere* **2021**, *276*, 130117.

[62] Lukens, W. W.; Saslow, S. A. Facile Incorporation of Technetium into Magnetite, Magnesioferrite, and Hematite by Formation of Ferrous Nitrate in Situ: Precursors to Iron Oxide Nuclear Waste Forms. *Dalton Trans.* **2018**, *47*, 10229–10239.

[63] Börsig, N.; Scheinost, A. C.; Shaw, S.; Schild, D.; Neumann, T. Retention and Multiphase Transformation of Selenium Oxyanions during the Formation of Magnetite Via Iron(II) Hydroxide and Green Rust. *Dalton Trans.* **2018**, *47*, 11002–11015.

[64] Pan, Z.; Loreggian, L.; Roebbert, Y.; Bartova, B.; Hunault, M. O. J. Y.; Weyer, S.; Bernier-Latmani, R. Pentavalent U Reactivity Impacts U Isotopic Fractionation during Reduction by Magnetite. *Environ. Sci. Technol.* **2024**,

[65] Dedkov, Y. S.; Fonin, M.; Vyalikh, D. V.; Hauch, J. O.; Molodtsov, S. L.; Rüdiger, U.; Güntherodt, G. Electronic Structure of the Fe_3O_4 (111) Surface. *Phys. Rev. B* **2004**, *70*, 073405.

[66] Paul, M.; Sing, M.; Claessen, R.; Schrupp, D.; Brabers, V. A. M. Thermodynamic Stability and Atomic and Electronic Structure of Reduced Fe_3O_4(111) Single-crystal Surfaces. *Phys. Rev. B* **2007**, *76*, 075412.

[67] Shimizu, T. K.; Jung, J.; Kato, H. S.; Kim, Y.; Kawai, M. Termination and Verwey Transition of the (111) Surface of Magnetite Studied by Scanning Tunneling Microscopy and First-Principles Calculations. *Phys. Rev. B* **2010**, *81*, 235429.

[68] Noh, J.; Osman, O. I.; Aziz, S. G.; Winget, P.; Brédas, J.-L. Magnetite Fe_3O_4 (111) Surfaces: Impact of Defects on Structure, Stability, and Electronic Properties. *Chem. Mater.* **2015**, *27*, 5856–5867.

[69] Joseph, Y.; Kuhrs, C.; Ranke, W.; Ritter, M.; Weiss, W. Adsorption of Water on FeO(111) and Fe_3O_4(111): Identification of Active Sites for Dissociation. *Chem. Phys. Lett.* **1999**, *314*, 195–202.

[70] Asakawa, K.; Miura, Y.; Nagatsuka, N.; Takeyasu, K.; Matsumoto, M.; Fukutani, K. Electronic and Spin Structure of O- and H-Adsorbed Fe_3O_4 (111) Surfaces. *Phys. Rev. B* **2019**, *99*, 085442.

[71] Scheinost, A. C.; Charlet, L. Selenite Reduction by Mackinawite, Magnetite and Siderite: XAS Characterization of Nanosized Redox Products. *Environ. Sci. Technol.* **2008**, *42*, 1984–1989.

[72] Scheinost, A. C.; Kirsch, R.; Banerjee, D.; Fernandez-Martinez, A.; Zaenker, H.; Funke, H.; Charlet, L. X-ray Absorption and Photoelectron Spectroscopy Investigation of Selenite Reduction by Fe^{II}-bearing Minerals. *J. Contam. Hydrol.* **2008**, *102*, 228–245.

[73] Hochella, M. F.; Lower, S. K.; Maurice, P. A.; Penn, R. L.; Sahai, N.; Sparks, D. L.; Twining, B. S. Nanominerals, Mineral Nanoparticles, and Earth Systems. *Science* **2008**, *319*, 1631–1635.

[74] Bianchetti, E.; Oliveira, A. F.; Scheinost, A. C.; Valentin, C. D.; Seifert, G. Chemistry of the Interaction and Retention of Tc(VII) and Tc(IV) Species at the Fe_3O_4 (001) Surface. *J. Phys. Chem. C* **2023**, *127*, 7674–7682.

[75] Shannon, R. D. Revised Effective Ionic Radii and Systematic Studies of Interatomic Distances in Halides and Chalcogenides. *Acta Cryst. A* **1976**, *32*, 751–767.

[76] Smith, F. N.; Um, W.; Taylor, C. D.; Kim, D.-S.; Schweiger, M. J.; Kruger, A. A. Computational Investigation of Technetium(IV) Incorporation into Inverse Spinels: Magnetite (Fe_3O_4) and Trevorite ($NiFe_2O_4$). *Environ. Sci. Technol.* **2016**, *50*, 5216–5224.

[77] Koch, W. *A Chemist's Guide to Density Functional Theory*; Wiley-VCH: Weinheim New York, 2001.

[78] Perdew, J. P.; Burke, K.; Ernzerhof, M. Generalized Gradient Approximation Made Simple. *Phys. Rev. Lett.* **1996**, *77*, 3865–3868.

[79] Perdew, J. P.; Burke, K.; Ernzerhof, M. Generalized Gradient Approximation Made Simple [Phys. Rev. Lett. 77, 3865 (1996)]. *Phys. Rev. Lett.* **1997**, *78*, 1396–1396.

[80] Mott, N. F. Metal-Insulator Transition. *Rev. Mod. Phys.* **1968**, *40*, 677–683.

[81] Hubbard, J. Electron Correlations in Narrow Energy Bands. *Proc. Roy. Soc. Lond. Math. Phys. Sci.* **1963**, *276*, 238–257.

[82] Kühne, T. D. et al. CP2K: An Electronic Structure and Molecular Dynamics Software Package - Quickstep: Efficient and Accurate Electronic Structure Calculations. *J. Chem. Phys.* **2020**, *152*, 194103.

[83] Ji, Y.; Beridze, G.; Li, Y.; Kowalski, P. M. Large Scale Simulation of Nuclear Waste Materials. *Energy Procedia* **2017**, *127*, 416–424.

[84] Romero, A. B.; Kowalski, P. M.; Beridze, G.; Schlenz, H.; Bosbach, D. Performance of DFT+U Method for Prediction of Structural and Thermodynamic Parameters of Monazite-type Ceramics. *J. Comput. Chem.* **2014**, *35*, 1339–1346.

[85] Kowalski, P. M.; Beridze, G.; Li, Y.; Ji, Y.; Friedrich, C.; Şaşioğlu, E.; Blügel, S. Feasible and Reliable *AB initio* Approach to Computation of Materials Relevant for Nuclear Waste

Management. *Additive Manufacturing and Strategic Technologies in Advanced Ceramics* **2016**, 205–217.

[86] Kéri, A.; Dähn, R.; Krack, M.; Churakov, S. V. Combined XAFS Spectroscopy and *Ab Initio* Study on the Characterization of Iron Incorporation by Montmorillonite. *Environ. Sci. Technol.* **2017**, *51*, 10585–10594.

[87] Naveas, N.; Pulido, R.; Marini, C.; Gargiani, P.; Hernandez-Montelongo, J.; Brito, I.; Manso-Silván, M. First-Principles Calculations of Magnetite (Fe_3O_4) above the Verwey Temperature by Using Self-consistent DFT $+U+V$. *J. Chem. Theory Comput.* **2023**, *19*, 8610–8623.

[88] Lu, J.-B.; Cantu, D. C.; Xu, C.-Q.; Nguyen, M.-T.; Hu, H.-S.; Glezakou, V.-A.; Rousseau, R.; Li, J. Norm-conserving Pseudopotentials and Basis Sets to Explore Actinide Chemistry in Complex Environments. *J. Chem. Theory Comput.* **2021**, *17*, 3360–3371.

[89] Newville, M. Fundamentals of XAFS. *Rev. Mineral. Geochem.* **2014**, *78*, 33–74.

[90] Scheinost, A. C. et al. ROBL-II at ESRF: A Synchrotron Toolbox for Actinide Research. *J. Synchrotron Rad.* **2021**, *28*, 333–349.

[91] Rehr, J. J.; Albers, R. C. Theoretical Approaches to X-ray Absorption Fine Structure. *Rev. Mod. Phys.* **2000**, *72*, 621–654.

[92] Ankudinov, A. L.; Ravel, B.; Rehr, J. J.; Conradson, S. D. Real-Space Multiple-Scattering Calculation and Interpretation of X-ray-Absorption Near-Edge Structure. *Phys. Rev. B* **1998**, *58*, 7565–7576.

[93] Rehr, J. J.; Kas, J. J.; Prange, M. P.; Sorini, A. P.; Takimoto, Y.; Vila, F. *Ab Initio* Theory and Calculations of X-ray Spectra. *Comptes Rendus. Physique* **2008**, *10*, 548–559, Theoretical spectroscopy.

[94] Tornos, F.; Hanchar, J. M.; Steele-MacInnis, M.; Crespo, E.; Kamenetsky, V. S.; Casquet, C. Formation of Magnetite-(Apatite) Systems by Crystallizing Ultrabasic Iron-rich Melts and Slag Separation. *Miner. Deposita* **2023**, *59*, 189–225.

[95] Pearce, C.; Qafoku, O.; Liu, J.; Arenholz, E.; Heald, S.; Kukkadapu, R.; Gorski, C.; Henderson, C.; Rosso, K. Synthesis and Properties of Titanomagnetite ($Fe_{3-x}Ti_xO_4$) Nanoparticles: A Tunable Solid-state Fe(II/III) Redox System. *J. Colloid Interface Sci.* **2012**, *387*, 24–38.

Chapter 2: Investigation of the magnetite bulk crystal structure and (111) surface

Stability and speciation of hydrated magnetite {111} surfaces from *ab initio* simulations with relevance for geochemical redox processes

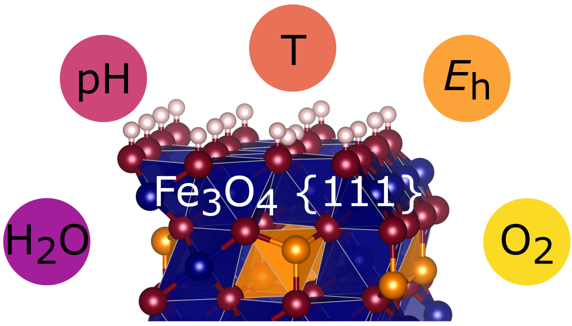

This chapter was published as article in *Environmental Science and Technology*, 2024, 58, 1, 935–946 (DOI: 10.1021/acs.est.3c07202), reprinted with permission, copyright 2024 American Chemical Society. The manuscript was written in cooperation with Konstantinos Karalis, Matthias Krack, Andreas C. Scheinost, and Sergey V. Churakov.

Abstract

Magnetite is a common mixed Fe(II,III) iron oxide in mineral deposits and the product of (anaerobic) iron corrosion. In various Earth systems, magnetite surfaces participate in surface mediated redox reactions. The reactivity and redox properties of the magnetite surface depend on the surface speciation, which varies with the environmental conditions. In this study, Kohn-Sham density functional theory (DFT+U method) was used to examine the stability and speciation of the prevalent magnetite crystal face {111} in a wide range of pH and E_h conditions. The simulations reveal that oxidation state and speciation of the surface depend strongly on imposed redox conditions and, in general, may differ from those of the bulk state. Corresponding predominance phase diagrams for the surface speciation and structure were calculated from first principles. Further, classical molecular dynamics (MD) simulations were conducted investigating the mobility of water near the magnetite surface. The obtained knowledge of surface structure and oxidation state of iron is essential for modeling retention of redox-sensitive nuclides.

2.1 Introduction

Magnetite as mixed Fe(II)/Fe(III) oxide participates alongside other iron minerals in many redox reactions. These include the possible CO_2 storage in glauconite with conversion to siderite and magnetite[1] or the chemo-denitrification by Fe(II) bearing minerals[2,3]. Further, the complete redox cycling of different Fe minerals under the presence of Fe redox bacteria could be shown[4,5] suggesting a similar behavior in the seasonal redox cycling in soils and sediments. Another example from the biogeochemical cycle is the combination of Fe minerals and humic substances with the inherent electron transfer[6], e.g., allowing for enhanced or suppressed methanogenesis depending on the mineral[7]. Moreover, Fe compounds play an important role in the retention of contaminants. In the subsurface under anoxic conditions, halogenated organic compounds were reductively degraded especially by Fe(II) bearing minerals such as green rust, siderite, pyrite, and magnetite[8–12]. Moreover, in sewage sulfide decrease was found to be more effective by Fe minerals compared to Fe salts[13]. The immobilization of heavy metals such as Se is another important application of subsurface Fe minerals and was successfully shown, e.g., for green rust, siderite, mackinawite, and magnetite[14–17]. Further, As in aqueous solutions was shown to be removed by mixed iron oxides in recycled Ni smelter slag[18] combining two waste materials.

While many of these examples focus on the interaction of naturally occurring iron minerals, magnetite also forms by iron or steel corrosion. In several countries, including Switzerland, thick wall steel casks are foreseen for the geological storage of nuclear waste in underground clay formations[19]. In contact with pore water, the steel casks are expected to corrode forming mixed iron oxides, mainly magnetite (Fe_3O_4)[20]. Eventually after several hundreds to thousands of years, the canisters may breach potentially enabling access of groundwater to the radionuclides of the waste matrix. However, the corrosion products are expected to provide a significant contribution to the retention of the radionuclides. The extent of this interaction depends on the speciation and the surface structure of the corrosion products and, to the best of our knowledge, the identification of structure and stability of the magnetite surface remains challenging.

Magnetite belongs to the inverse spinel structural type (space group $Fd\bar{3}m$) with the tetrahedral sites occupied by ferric iron (Fe^{3+}) and octahedral sites occupied by equal amounts of ferric and ferrous iron (Fe^{2+}). In order to investigate the interaction of magnetite with possible radionuclides, a suitable description of the surface is crucial. As face-centered cubic structure, the {111} facets yield a lower surface energy than {100} and {110} facets[21,22] and are, hence, more stable in long-term experiments. The {111} facet has six structurally different surface terminations (Figure 2.1). Two of these terminations show complete monolayers (ML) of oxygen (O_1 and O_2), i.e., in a hexagonal unit cell[23] there are four O^{2-} per layer, that enclose a $\frac{3}{4}$ ML of octahedrally coordinated iron (Fe_{oct1}). Further, a sandwich-like structure of two tetrahedrally coordinated iron layers (Fe_{tet1} and Fe_{tet2}) around an octahedrally coordinated iron layer (Fe_{oct2}) is found; each of these three layers covers $\frac{1}{4}$ ML.

The pristine {111} surface has been investigated extensively using both experimental as well as theoretical approaches such as the generalized gradient approach of density functional theory (DFT) with Hubbard U correction[24] (GGA+U) as we applied it in our study. Generally, the Fe_{tet1} termination was found to be the most stable over a wide range of redox conditions[24–29], while at very low oxygen potentials the Fe_{oct2} termination and under strongly oxidizing conditions the O_1 terminated surface prevail[23,30–33]. In theoretical studies on the {111} magnetite surface, usually a slab of a limited number of layers is used keeping the computational expenses to a reasonable amount. One of the first studies in this regard was conducted by Ahdjoudj et al.[25] who applied Hartree-Fock simulations of few-layer slabs in vacuum favoring symmetric slabs. Considering the electronic properties, Berdunov et al.[32] suggest a hybridization between the O_1 and Fe_{oct1} orbitals resulting in conductivity at the surface. Contrasting under vacuum, Jordan et al.[34] report a band gap of ≈ 0.2 eV and a half-metallic character due to the t_{2g} band being located near the Fermi energy and occupied by spin-down electrons in octahedrally coordinated iron cations.

Based on the preferential stability of Fe_{tet1} and Fe_{oct2} terminations, most studies focus on the sorption of individual and small molecules such as CO_2[35] or formic acid[36–38]. Further, the interaction with water molecules has been studied such as the coverage dependent water dissociation[39,40] and the following chemi- and physisorption of OH groups on the pristine Fe_{tet1} termination[41–49]. Contrasting the preference for the Fe_{tet1} termination under vacuum, some computational studies proclaim the Fe_{oct2} termination to be more active chemically[50] leading to more dissociation[51]. Closer to environmental systems, Petitto et al.[52] conducted X-ray crystal truncation rod (CTR) diffraction under ambient conditions (hydrated and circum-neutral pH) of the {111} surface of a commercial magnetite crystal after wet chemical mechanical polishing (CMP). They observed the occurrence of hydro-oxo terminated surfaces corresponding to 75 % O_1 and 25 % O_2-Fe_{oct2} termination. The latter are expected to be less stable due to the missing Fe_{tet2} layer.

The surface speciation controls the mechanism of surface processes, which are important in safety and environmental considerations, e.g., regarding pH or the (non-) availability of oxygen. In this regard, several studies investigated the interaction of heavy metal ions with magnetite surfaces. Magnetite was shown to act successfully as reduction agent for heavy or even radioactive metals (e.g., Sb[53], Tc[54], U[55–60], Pu[61–63]) often resulting in less soluble products. Hence, magnetite efficiently contributes to the immobilization of these hazardous elements. The reduction of the heavy metal cations is thereby accompanied by the oxidation of Fe(II) to Fe(III)[64] either as octahedrally coordinated Fe cations in the magnetite crystal structure or in equilibrium in solution. (Reduced) metal species can be sorbed strongly and even further reduced, e.g. as proposed by Pan et al.[60] for U. Furthermore, most experimental studies favor an octahedrally terminated surface for sorption, resulting in pH stable bidentate (Se[17], Cr and Pb[65]) or tridentate complexes (As[66–69], Sb[53], Pu[62,70]) expected at the (H)-O_1 termination. Similar to the latter are Tc-Tc-dimers as suggested by Yalçıntaş et al.[71]. Sorption was shown to be more effective with higher surface/volume ratio[72] and newly-formed magnetite by steel corrosion even more effective than commercially available synthetic crystals[73]. Further, even the incorporation of radionuclides was suggested for Tc[54,71,74] and Pu[70], resulting in a very stable structure especially for octahedrally coordinated Tc[74] as Tc(IV) and Fe(III) are very close in ionic radius[75].

The previous studies clearly reveal that the {111} surface plays a central role in the sorption properties of magnetite. It is also evident that the structural details of the surface termination are influenced by the chemical conditions. Further, the details of the radionuclide magnetite interactions can not be fully resolved without understanding the magnetite surface stability at different conditions. The central aim of this study is to reveal the structure and speciation of the {111} magnetite surface as function of T, O_2, H_2O, E_h, and pH, based on the state-of-the-art methods of computational chemistry. These result should provide the basis to interpretation of radionuclides uptake on the magnetite {111} surface.

2.2 Materials and Methods

2.2.1 Modeling setup

A cubic magnetite unit cell contains 8 Fe_3O_4 units. The simulations of the bulk magnetite structure as model validation were performed using a (3×3×3) supercell. The structure and cell parameters were optimized using a fully flexible simulation supercell starting with the experimentally measured lattice constant of $3 \times 8.3958(5)$ Å[76].

The low index {111} surface, investigated in this work, is one of the most common faces observed in the octahedral shape of magnetite nanocrystals[69,77,78] and nanoparticles synthesized under anoxic conditions[62,63,66,71]. The magnetite {111} face is a type 3 surface according to the Tasker classification scheme[79] leading to a slab with a dipole moment perpendicular to the surface. The simulation slabs were made symmetrical to cancel the surface dipole moment, meaning that the slab has mirror symmetric sequence structural layers on either surface. The simulated structure consists of three distinctive domains, i.e., two surface regions separated by a bulk domain (Figure 2.1). Although the {111} lattice plane has intrinsic hexagonal symmetry[23], an orthorhombic supercell was applied for the sake of computational performance. The surface was, thus, modeled using a 23.69 Å by 20.52 Å orthorhombic lattice. The third cell dimension was set to 54.04 Å allowing for a 40 Å domain filled with vacuum between periodic images of the simulation slab.

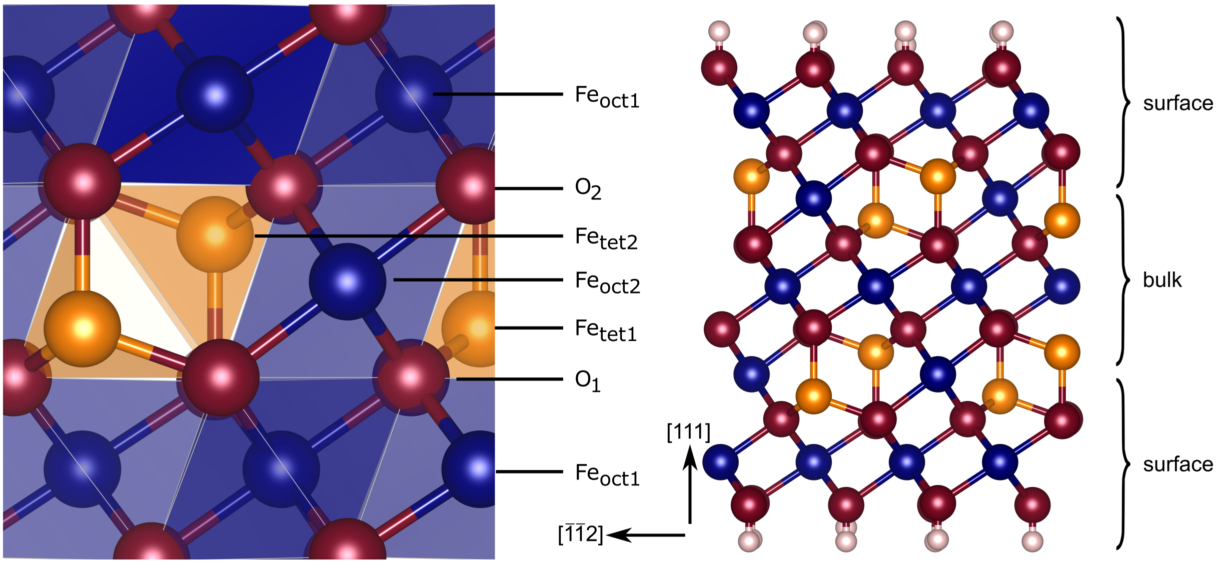

FIGURE 2.1: Left: Side view of different layers of magnetite in {111} direction. Fe in octahedral (oct, blue) or tetrahedral (tet, orange) coordination are surrounded by O (red). Right: oct1_out2.5 as example of simulation slab with distinctive bulk and surface sections.

Considering layer-like arrangement of iron and oxygen atoms parallel to the {111} lattice plane, six structurally different surface terminations can be envisaged (Figure 2.1). The current study is focused on magnetite surface stability in natural environment, in which the bare Fe-terminations of the surface are not expected to be stable. Therefore, only surface terminations saturated with oxygen atoms, OH and H_2O surface groups were considered. The four terminations investigated in this work are referred to as oct1, oct2, tet1, tet2 corresponding to the out-most lying octahedral and tetrahedral coordinated iron sites, respectively.

In natural systems, surface Fe^{2+} and Fe^{3+} sites can be involved in oxidation and reduction reactions, respectively. It is assumed that in presence of water the oxidation/reduction reactions are accompanied by protonation/deprotonation of the surfaces sites. Since magnetite is a conducting material, it is, hence, expected that magnetite surfaces should not build up permanent surface charge in the course of redox reactions or surface hydrolysis. Accordingly, all the simulations were performed for charge neutral periodic slabs representing different terminations of the magnetite surface in which protons were added to surface oxygen sites to maintain the desired oxidation state and the stoichiometry of the surface sites.

The system setup for oct1, oct2, tet1, and tet2 termination is illustrated in Supporting Information (SI, Figure S2.3 and Figure S2.4). Therein, we investigated relative energies of possible surface reconstructions depending on external redox conditions. The naming convention follows "(termination)_out(formal charge)", where "termination" is the outer surface layer type, and the "formal charge" is the average oxidation state of the outermost surface layer. For the tet2 surface, also some of the further oxidations occurring in the underlying Fe_{oct2} layer were investigated following a respective naming convention ("tet2_out3_oct2_out(formal charge)"). The charge change is verified by the Mulliken charge analysis (Table S2.4 and Table S2.5 in SI).

2.2.2 *Ab initio* calculations

Simulations conducted in this study comprise the lattice constant optimization, electronic properties of bulk magnetite, speciation and thermodynamic stability of the {111} magnetite surface in a wide range of pH and E_h conditions. Spin-polarized crystal structure calculations applying 3D periodic boundary conditions were performed based on Density Functional Theory (DFT) using the Gaussian Plane Wave (GPW) method as it is implemented in the QUICKSTEP module of the open source CP2K code[80,81]. To avoid the explicit consideration of the core electrons (electronic configuration for iron: [Ne] $3s^2$ $3p^6$ $4s^2$ $3d^6$, for oxygen: [He] $2s^2$ $2p^4$), the norm-conserving scalar-relativistic pseudo-potentials of Goedecker, Teter and Hutter (GTH)[82,83] were applied. The wave functions of the valence electrons were described by a linear combination of contracted Gaussian-type orbitals using MOLOPT basis sets.[84] An auxiliary basis set of plane waves was employed to expand the electronic density using an electronic density cutoff of 600 Ry for the electronic density of states calculation. Prior to the production runs, the performance of PBE exchange-correlation (XC) functional in the original parametrization[85,86] and the one tailored for solids and liquids (PBEsol)[87] were tested against structural properties for magnetite (Table S2.1 in SI).

Conventional DFT is known to underestimate the Coulomb repulsion between the localized 3d-electrons in oxide materials[88–90], also for Fe in iron oxides, e.g., hematite[91]. The so called DFT+U method was applied[92,93] to improve the description of 3d-electronic states in magnetite. The value of the Hubbard parameter implemented in CP2K as $U_{\mathrm{eff}} = U - J$ ranging from 0.0 eV to 3.8 eV was selected for cross-benchmarking the simulation against known structural and electronic properties of iron oxides. The best agreement with experimental data was obtained for $U_{\mathrm{eff}} = 1.9\,\mathrm{eV}$, which was also used in the previous investigation of Fe bearing minerals[94] with iron in octahedral coordination and was used in this study, accordingly. The initialization of wave functions was performed applying the spin multiplicity of $(2S + 1)_{Fe^{2+}} = 5$ for ferrous iron and $(2S + 1)_{Fe^{3+}} = 6$ for ferric iron, respectively. Ferric and ferrous irons are assumed to alternate in the octahedral layer resulting in $(2S + 1)_{Fe_{oct}} = 5.5$ with all spins aligned up. The tetrahedral sites were considered as spin down.

2.2.3 Surface energy

Depending on the redox conditions, surface iron atoms are expected to participate in oxidation and reduction reactions. Therefore, the stable oxidation state of surface iron may differ from the formal oxidation state expected in the magnetite crystal. The energy of {111} magnetite surfaces for different termination, speciation and oxidation state of the surface iron was calculated from *ab initio* geometry optimization with Equation 2.1. A is the surface area and G_f is the Gibbs free energy of formation of the slab. Further details for the calculation of the formation energy G_f are provided in SI. The formation energies of water and magnetite were taken from standard thermodynamic tables[95]. Moreover, the building components of the volume material (magnetite (Mag)) and possible components i regarding their number N and chemical potential μ were considered and the surface energy was expressed as function of oxygen fugacity and water potential (Equation 2.2). The stability of different surfaces as function of redox condition, proton activity and water potential was calculated and represented using Pourbaix diagrams (Equation 2.3). A more detailed description for both methods is provided in SI. Due to the inherent equivalence of both approaches, the E_h-pH-dependent results are discussed in this manuscript while the fugacity analysis is shown in SI.

Although many more configurations of the possible four surface setups regarding the outmost Fe layer (oct1, oct2, tet1, tet2) were investigated (Table S2.6 in SI), it was found that only few of oct1 and tet2 surfaces are dominant based on thermodynamic considerations and, hence, these are discussed in further detail.

$$\gamma = \frac{1}{2A}\left(G_f - N\,E_{\text{bulk}} - \sum_i N_i\,\mu_i\right) \tag{2.1}$$

$$\gamma = \frac{1}{2A}\left(G_f - N_{\text{Mag}}\mu_{\text{Mag}} - N_{O_2}\mu_{O_2} - N_{H_2O}\mu_{H_2O}\right) \tag{2.2}$$

$$\begin{aligned}\gamma = \frac{1}{2A}\Big(G_f - N_{\text{Mag}}\,E_{\text{Mag}} - N_O\,\mu_{H_2O} - E_h\big(Q - N_H + 2\,N_O\big)&\\ + RT\big(N_H - 2\,N_O\big)\,\ln(10)\,\text{pH}\Big)&\end{aligned} \tag{2.3}$$

2.2.4 Classical molecular dynamics (MD) simulations

Molecular dynamics (MD) simulations of the heterogeneous magnetite/water interface on the previously determined most stable magnetite configurations were performed using LAMMPS v. 2020 code[96]. The supercell was composed of 4000 H_2O molecules and magnetite slabs of 3040 atoms. The water molecules were modeled using the non-polarizable SPC/E water model[97] and the magnetite ions were modeled using the potential parameters developed by Konuk et al.[36]. The SPC/E model provides a middle ground between achieving a high degree of precision and maintaining computational speed for extensive simulations. More specifically, the SPC/E water model adequately anticipates various physical properties such as density, compressibility, self-diffusion coefficients and dielectric constant[98]. The Lorentz Berthelot combining rule was used to determine the unlike Lennard-Jones parameters[99,100]. The diffusion coefficient of pure water was determined accordingly for 1536 atoms and is in good agreement with literature[101].

Periodic boundary conditions in all dimensions were applied. The system was equilibrated for 2 ns in the NP_zT ensemble with final box dimensions approximately 45.9 Å × 39.8 Å × 78.5 Å. The geometry of the SPC/E water molecules were held fixed using the rigid body approach[102]. The magnetite atoms (iron and bridging oxygen) were held frozen, utilizing the pre-optimized coordinates from the previously described *ab initio* simulations, while the surface hydroxyl group atoms were allowed to move. An integration time step of 1 fs was used to ensure energy conservation. In the equilibration, the temperature was controlled using a Nosé-Hoover thermostat with a relaxation time of 0.1 ps, while the pressure was controlled using an anisotropic Parrinello-Rahman barostat with a relaxation time of 1 ps. Finally, the production run was performed in the NVT ensemble using a Nosé-Hoover thermostat with a relaxation time of 0.1 ps, spanning a total duration of 2 ns. The results of the classical MD simulation were used to evaluate the contribution of water-surface interaction to the surface energy and the water diffusivity as function of distance to the surface. The obtained interaction energy E_{int} can be used to further refine the surface energy according to Equation 2.4.

$$\gamma' = \gamma + E_{int} \tag{2.4}$$

2.3 Results and Discussion

2.3.1 Model validation for magnetite

TABLE 2.1: Band gaps of volume crystal magnetite obtained with the PBE XC functional with original (PBE) and PBEsol parametrization applying different U_{eff} values. α and β refer to spin up and spin down, respectively. In the literature, band gaps of ≈1.4 eV for the majority (alpha) spin[103] and 0.1 eV for the minority (beta) spin[104] have been reported.

	$E_g(\alpha)$ [eV]	$E_g(\beta)$ [eV]
PBE (0.0 eV)	0.844	0.045
PBE (1.9 eV)	1.558	0.274
PBE (3.8 eV)	2.048	1.010
PBEsol (0.0 eV)	0.719	0.016
PBEsol (1.9 eV)	1.549	0.172
PBEsol (3.8 eV)	2.057	0.802

The spin dependent projected electronic density of states (PDOS) for bulk magnetite calculated with PBE and PBEsol parametrization in combination with the different U_{eff} values are reported in SI (Figure S2.1). The extracted band gap values are reported in Table 2.1, where α and β refer to spin up and spin down, respectively. The overall trend of increased band gap with increased U_{eff} value is consistent with previous studies[90,94]. Compared to the values of band gaps reported in literature of around 0.1 eV at room temperature[104], the combination of PBEsol as parametrization method and $U_{eff} = 1.9$ eV appears to be closest considering that band gaps decrease slightly with temperature. PDOS for the PBEsol and $U_{eff} = 1.9$ eV (Figure 2.2(a)) is also similar to the magnetite GGA+U study by Kiejna et al.[105].

Figure 2.2(b) shows the obtained lattice parameters for each U_{eff} value and PBE parametrization including thermal expansion effects[106] (Table S2.1 in SI). A minimum deviation of the lattice parameters was obtained using the combination of PBEsol parametrization and U_{eff} =

1.9 eV and are below 0.5 % compared to experimental data[107]. Combining these results with the PDOS and band gap analysis, this combination of parametrization and U_{eff} was, hence, used throughout further computations on magnetite. Further, it is to be noted that the mixed charge and spin state of the octahedrally coordinated Fe(II,III) were preserved in the simulation corroborating the validity of our modeling setup (Figure S2.2 in SI).

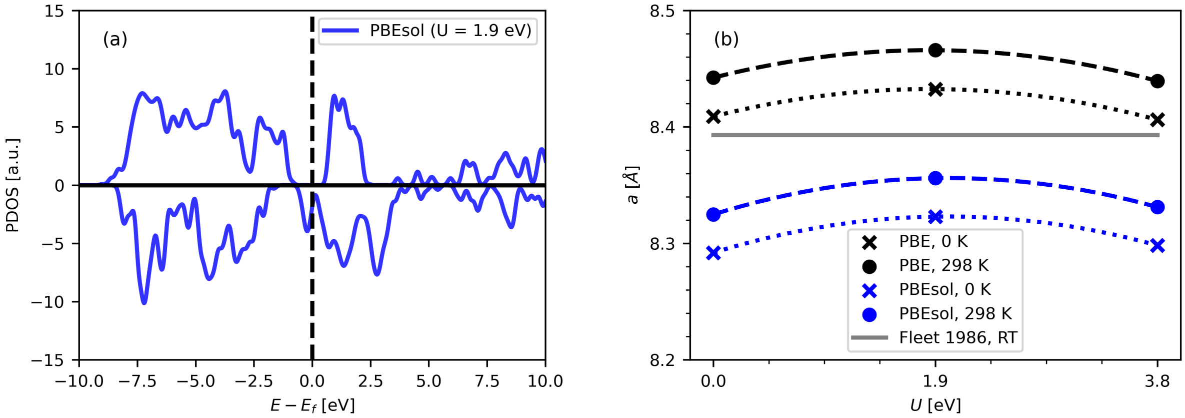

FIGURE 2.2: (a) Projected density of states (PDOS) of magnetite crystal with Hubbard U correction for iron of 1.9 eV using the PBEsol parametrization of the PBE functional. (b) Averaged lattice parameter obtained at 0 K from geometry optimization of bulk magnetite (crosses). Thermal expansion correction[106] was applied to convert to 298 K (spheres). The dotted/dashed lines were inserted to guide the eye.

2.3.2 Oxidation state and geometry of stable surfaces

The geometry optimization of the slabs (Figure S2.4 in SI) preserved the general positions of Fe and O ions of the magnetite structure. However, the adsorbed hydrogen ions tend to rearrange forming hydrogen bonds (HB) to the neighboring oxygen and OH groups. Further, as can be seen for the oct2_out2.5 termination, the HB are formed even to the next underlying O layer which is facilitated by the (intended) vacancy of Fe_{tet2} underneath the completely filled O_2 layer.

The distances between the Fe and O layers are reported in Table S2.2 and Table S2.3 in SI. Most notably, the strong decrease in the O-H layer distance is a result of the formation of HB bringing some of the H cations in the same plane as the underlying O layer. Comparing differently charged terminations of the same kind, a stronger relaxation can be observed for surfaces with higher Fe cation charge compensating for the higher deviation from the bulk-like interactions. In other GGA+U studies reported for pristine O-termination[22,23,33,105], the same trend of increase and decrease between the layers have been observed, albeit the relative change between the atomic layers is much larger. These differences can be explained by important contribution of hydrogen chemisorption stabilizing the surface structure analyzed in our study.

With the number of adsorbed H and the charge neutrality condition imposed on the entire system, the effective charge of Fe cations changes (Table S2.4 and Table S2.5 in SI). This change can be mainly observed in the minority spin of Fe ions where 0 signifies Fe(III) and 1 represents Fe(II). It is notable, that oxidation and reduction occurs mostly in the octahedral layers closest to the surface confirming the labeling, too. A change to higher outmost oxidation of octahedrally coordinated Fe was also observed in computational studies by Konuk et al.[36], whereas Petitto et al.[52] argue for mixed Fe(II)/Fe(III) in the octahedral layer. This difference could be caused by the incomplete filling of expected Fe positions in the experimental study, while our results are based on the perfect magnetite bulk structure in line with other computational studies.

2.3.3 Surface energy and stability of the magnetite {111} surface

The formation energies of the reaction components and the specific energy of the magnetite {111} surfaces with different oxidation state of Fe at zero E_h and pH are provided in Table S2.6, Table S2.7 and Table S2.8 in SI. With this data, the surface energy γ can be expressed as function of E_h and pH (Equation 2.3) with exemplary results depicted in Figure 2.3. The results of the alternative yet equivalent description as depending on water and oxygen fugacity (Equation 2.2) can be found in SI.

An increase in temperature leads to a slight decrease of the absolute value of the surface energies ($\approx -0.14\,\%$ for 25 K). A shift of the phase stability diagram towards lower E_h (higher oxygen fugacities) with higher temperature can be observed, this would result only in a slight change in a surface stability plot. However, the general relationships of the surface energies relatively to each other remain unchanged.

According to the surface energy calculations within our *ab initio* setup (without correction of surface-fluid interaction), oct1_out2.5, several tet2 surfaces and oct1_out3.0 appear energetically favorable depending on redox conditions. The other investigated surface terminations (Table S2.6 in SI) result in much higher surface energies and are, hence, not considered for further discussion here. The corresponding stability diagram for $T = 298\,\mathrm{K}$ revealing the order of tet2 surfaces is shown in Figure 2.4 (a). The calculated Pourbaix diagram suggests that under oxidizing conditions the oxidation state of the Fe in the outermost surface layer would change from bulk-like mixed oxidation of 2.5 to a fully oxidized ferric state in the oct1 surface. A similar behavior is observed for the tet2 termination. The calculations suggest that at the repository relevant redox and pH conditions[108] the further oxidized tet2 terminations have lowest energy.

In contrast to these theoretical calculations, experimental studies of the magnetite surface by CTR[52] or XAS[53,70,71] under aqueous conditions conclude the prevalence of the oct1 termination. To explain these apparent differences, several aspects have to be taken into consideration. First of all, the surface energies for oct1 and tet2 terminations predicted by the *ab initio* model are very close and are even within the accuracy of the *ab initio* simulations. The predicted small energy difference is in line with the plausible and anticipated co-existence of different terminations[22,52].

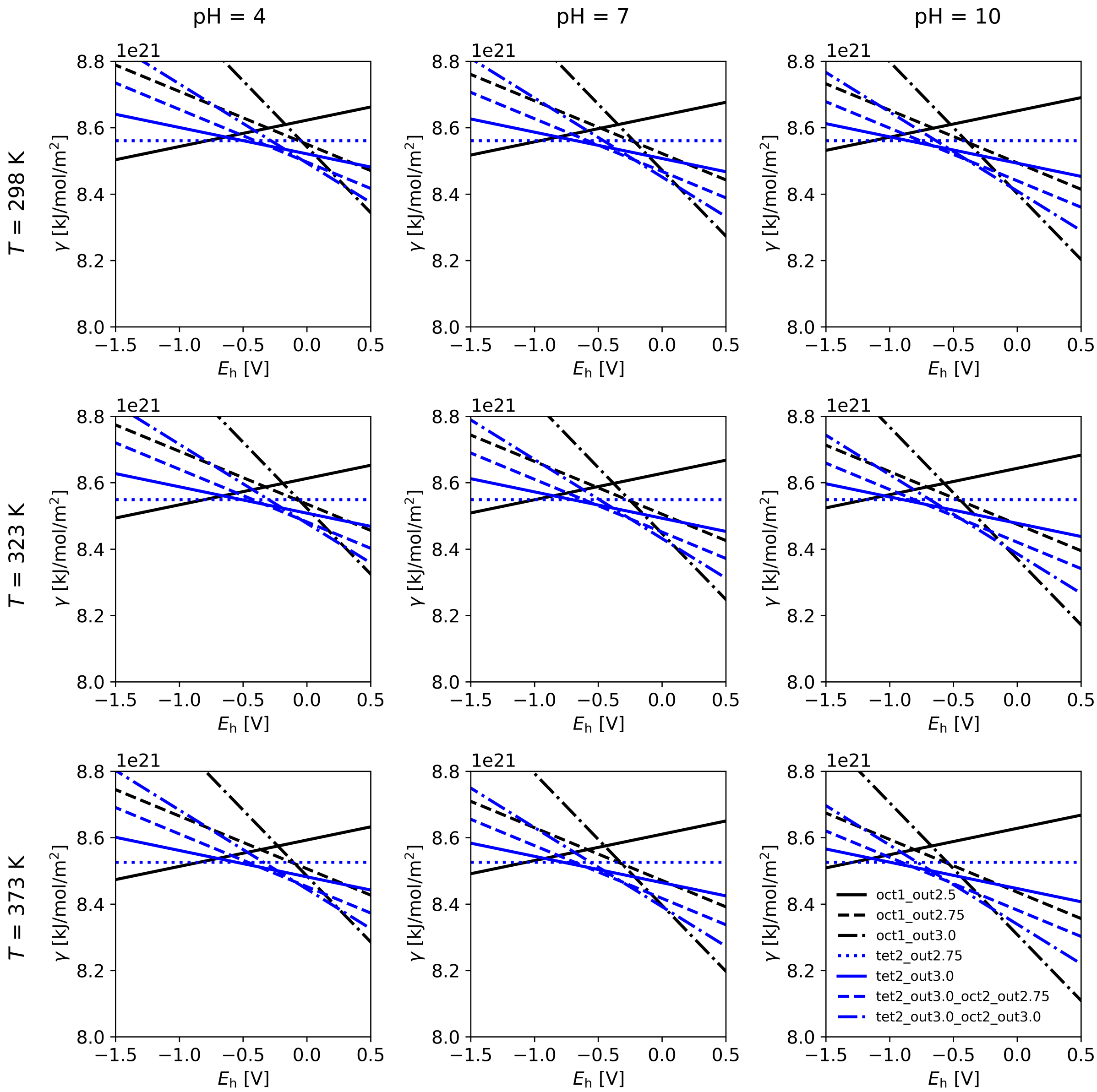

FIGURE 2.3: Specific surface energy γ as function of E_h for constant pH (4, 7, 10) and different temperatures (298 K, 323 K and 373 K).

We estimate the accuracy of the calculated surface energies to be within $0.1 \times 10^{21}\,\mathrm{kJ\,mol^{-1}\,m^{-2}}$ based upon the deviation of the magnetite lattice parameters (Table S2.1 in SI), and the hydrogen atom position, although the PBEsol(+U) approach is already expected to yield closer results closer to experiments compared to other XC functionals[109,110]. Such an energy difference is sufficient to favor the stability of the oct1 termination over the tet2 termination. A corresponding stability diagram is shown in Figure 2.4(b). Interestingly, adding the correction term for the surface -fluid interaction to the surface energy of tet2 would favor the stability of the oct1 over the tet2 termination, too, as shown in Figure 2.4(c).

For the energetically similar surfaces, the surface stability will strongly depend on the presence and composition of a solvent and possible ion interaction. Further, the presence and stability of sorption complexes or another kinetic aspect of the surface site nucleation can favor the dominance of one or another termination during the growth.

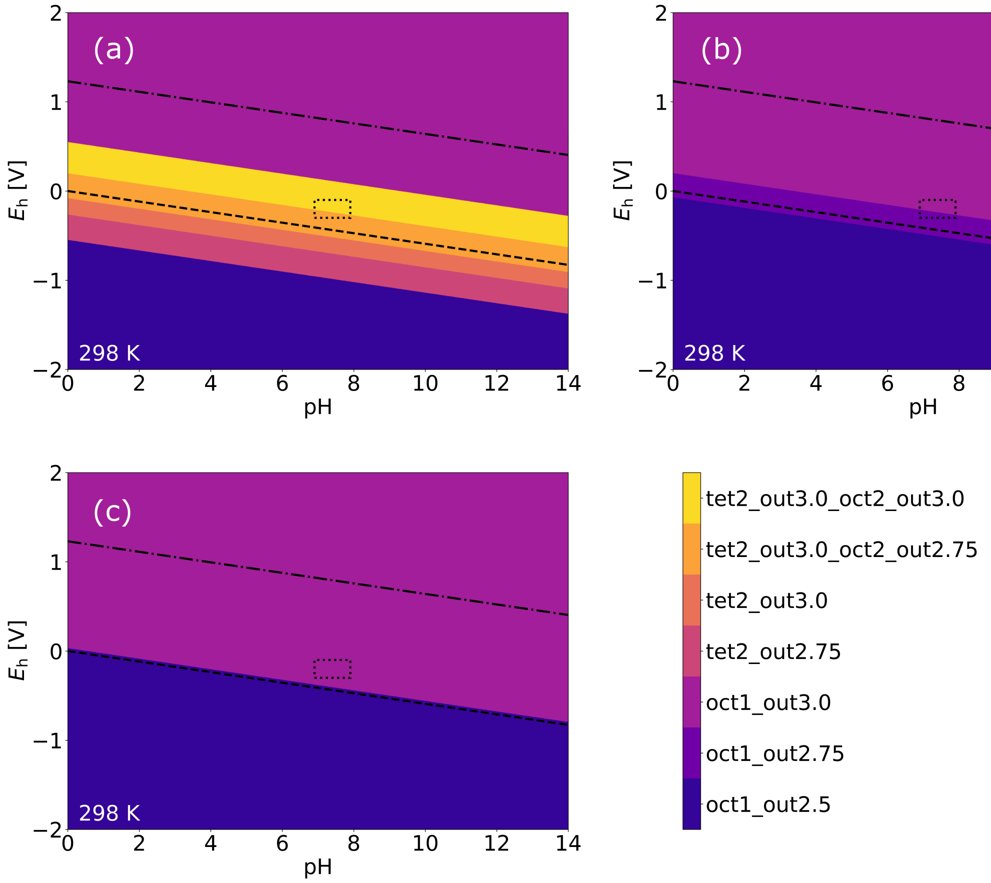

FIGURE 2.4: Surface stability plots of magnetite surfaces at 298 K as function of E_h and pH. (a) Stability plot based on *ab initio* data reported in fig. 3, (b) with penalized energy of tet2 terminations, and (c) with the consideration of the correction term for surface-water interactions obtained by classical MD simulations (see text for detailed description). In each Pourbaix diagram, the dotted black box indicates the expected long-term repository conditions in the range of $E_h = -0.1\,\mathrm{V}$ to $-0.3\,\mathrm{V}$ and pH = 6.9 to 7.9[108], the dashed line the lower water stability (production of H_2), the dash-dotted line the upper water stability (decomposition to O_2).

2.3.4 Magnetite water interface

Figure 2.5 depicts the mass density profiles of the water molecules above the chosen surfaces as obtained with classical MD. Based on these density distributions and their respective local minima, three water layers were determined, their height (Δz) ranging for the oct1-surface terminations 1.75 Å to 2.0 Å for layer 1, 3.5 Å to 4.0 Å for layer 2 and 2.5 Å to 4.0 Å for layer 3. Accordingly, for the tet2-terminations the layers ranged from 1.475 Å to 2.75 Å, 3.25 Å to 4.25 Å and 3.25 Å to 3.75 Å for layers 1, 2 and 3, respectively. For each layer, the diffusion coefficient parallel to the surface (x- and y-direction) as well as the residence times of a water molecule are given in Table 2.2. Further, the radial pair distribution function $g(r)$ (RDF, Figure S2.8) as well as the coordination numbers (Table S2.9) are reported in SI.

For each surface type, oct1 or tet2, there are only small differences in the MD obtained properties. The large variance of water mass density layer height could result from the weaker (higher value of Δz) to stronger (lower value of Δz) interaction of the water molecules with the surface especially observable for the first water layer. The diffusion coefficients within one layer vary only slightly signifying almost an isotropy parallel to the surface. With increasing height and layer number, the diffusion coefficient increases indicating weaker specific interaction with the surface and approaches the diffusion coefficient of bulk water. The strong hydrophilic properties of the surface is further indicated by a strong decrease of water residence time from layer 1 to layer 3. The lower distance of surface-H and water-O as well as the increased absolute value in the RDF for oct1_out2.5 and oct1_out3.0 terminations (Figure S2.6 in SI) indicate an increased acidity and stronger interaction of these surfaces with water compared to the tet2 terminations.

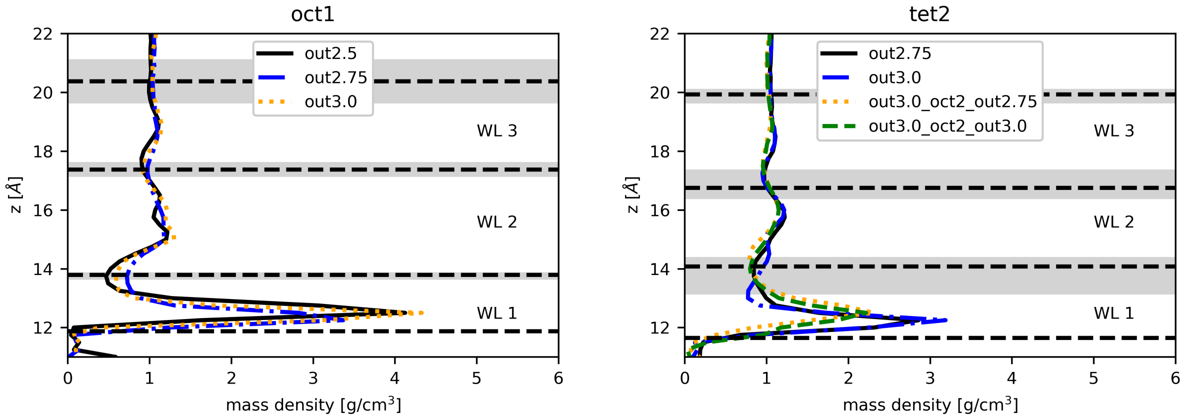

FIGURE 2.5: Mass density profiles of water above chosen oct1 (left) and tet2 (right) surface terminations. The average extent of the water layers (WL 1, WL 2, WL 3) is depicted as dashed horizontal lines, their deviation as grey bar.

TABLE 2.2: Diffusion coefficient D^* in x- and y-direction normalized to bulk water ($D_{bulk} = 2.6 \times 10^{-9}\,\mathrm{m^2\,s^{-1}}$) and residence time (rt, in 10^2 fs) of water molecules above the chosen oct1 and tet2 terminations in different water layers (WL 1, WL 2, WL 3).

		oct1			tet2			
WL	out	2.5	2.75	3.0	2.75	3.0	3.0_oct2_2.75	3.0_oct2_3.0
1	D_x^*	0.16	0.09	0.07	0.13	0.09	0.13	0.11
	D_y^*	0.14	0.10	0.07	0.12	0.08	0.11	0.11
	rt	3.03	3.18	3.23	3.17	2.34	3.41	3.31
2	D_x^*	0.48	0.29	0.30	0.46	0.47	0.46	0.46
	D_y^*	0.45	0.30	0.31	0.46	0.47	0.40	0.40
	rt	2.50	2.33	2.81	1.86	2.41	2.01	2.03
3	D_x^*	0.68	0.33	0.38	0.60	0.62	0.47	0.53
	D_y^*	0.65	0.40	0.40	0.61	0.60	0.54	0.55
	rt	0.26	1.66	2.25	1.43	0.77	1.28	1.73

2.3.5 Discussion of experimental findings from the literature

The theoretical prediction of the surface stability is a challenging task as it requires the consideration of different energy contributions related to the cohesive energy, the electronic state of the ions, and the surface-solvent interaction. These latter factors are often comparable in their amplitude and the obtained results are highly sensitive to their relative accuracy. Thus, in absence of explicit solvent contribution the tetrahedrally terminated surface is favored over the octahedral configuration. The consideration of surface-solvent interaction with pure water solvent favors the stability of the octahedral configuration. The consideration of the method/model dependent differences in the surface stability predictions clearly indicates that both stoichiometries and terminations have very close energies, and their relative stability can be affected by slight variation of boundary conditions (fluid composition, temperature, E_h, pH, etc.). Eventually, several configurations and terminations could and should co-exist to enable crystal growth. It is likely that cation selective adsorption processes may result in stabilization of specific surface stoichiometry. This aspect, however, goes beyond the scope of this study.

Contrasting with many studies relying on ultra-high vacuum conditions or the low partial pressure/low surface coverage conditions, our computational study deals with hydrated magnetite {111} surfaces, which remain poorly understood from the experimental and theoretical point of view. In particular, the interplay between the redox state of the surface Fe cations, the structure and surface stability is addressed in detail. Petitto et al.[52] conducted an experimental study in which they applied CMP on a bought magnetite crystal showing {111} facets under wet conditions and observed a terrace structure with AFM hinting at different terminations. Further, they measured CTR XRD in a humid helium stream facilitating the full hydration of the surface and concluded to have obtained a ratio of 75% of purely octahedrally terminated and 25% of a mixed octahedrally terminated surface. The difference in occurrence was further attributed to the different stability of the terminations and is in good agreement with our results. Each termination would include a densely packed oxygen layer on top as expected under these conditions resembling the oct1 and oct2 termination, respectively. However, they refer the missing Fe_{tet2} cations – for a complete tet2 termination as we report it – to the common occurrence of the Fe_{oct2} terminated {111} surface under vacuum conditions as they started with a commercial crystal. Moreover, they observed a contradicting pattern of layer relaxation possibly due to the real hydrated conditions while we used vacuum over our slabs. This is even more evident for the less perceived mixed iron terminated surface in their study, where the layers have to compensate for the missing Fe_{tet2}, too. Additionally, a higher stability of the oct1 compared to the oct2 termination was proposed.

Moreover, the preference of the oct1 termination coincides with adsorption geometries of heavy metal and radioactive ions on the magnetite {111} surface proposed by XAS studies[53,57,62,70,71] further validating our results. The obtained structural and thermodynamic data provide a solid basis for future atomistic modeling of the ion adsorption on the magnetite {111} surface including surface redox reactions.

2.3.6 Implications for the repository

Although magnetite is the expected main corrosion product in the repository, further mixed Fe(II,III) minerals including green rust and nontronite, the Fe(II) (hydroxo-) carbonates siderite and chukanovite, as well as the Fe(III) (hydr-) oxides lepidocrocite and hematite may be present in the bentonite liner after interaction with host-rock pore water, possibly partly as passivation layer on top of magnetite[20]. The pH range was estimated from bentonite porewater modeling by Curti and Wersin[111] taking into account p_{CO_2} of permeating groundwater. The E_h range is controlled by the Fe(II)/Fe(III) redox couple, which in turn depends on the mineral phase inventory such as siderite, magnetite, and goethite[108].

Our results suggest that for the mixed Fe(II)/Fe(III) oxide magnetite, the oct1 and tet2 terminations yield the lowest surface energies. Moreover, the top-most iron surface layers are expected to be (almost) completely oxidized to Fe(III) (Figure 2.4). However, the close surface energies of the different terminations allow for respective plausible charge layer configurations with more Fe(II), too. In a large and continuous system of oxidized canister material, a change in the iron charge even to lower layers might be possible, given the small band gap of magnetite and, hence, inherent conductivity. Further, the availability of redox active iron results from the magnetite/solution equilibrium, i.e., dissolved Fe(II) to allow for enhanced reduction and possible immobilization of heavy metals and radionuclides. Missana et al.[55] found a different E_h range (50 mV to 100 mV) in their experimental setup, but pointed out this strongly depends on the actual presence of oxidizing species. Moreover, it was reported that Fe(II) also results from the transition of magnetite to maghemite only containing Fe(III), although the growing passivation layer may hinder the ongoing dissolution of Fe(II)[112].

2.3.7 Transferability to other geochemical reactions and systems

Magnetite is a common mixed Fe(II)/Fe(III) oxide and acts as redox buffer in geochemical systems together with other iron bearing minerals such as wüstite, maghemite, and hematite. It also enables redox controlled interfacial reactions. The transformation of green rust to magnetite, e.g., might enable the production of hydroxyl radicals and lead to a strong degradation of organic pollutants.[12] Other environmentally important reactions include the repeated cycling of Fe(III) reduction and Fe(II) oxidation in microbial environments[5] and the denitrification at the interface between different clayey and crystalline Fe sediments[3].

Due to the variability of the surface stoichiometry imposed by the crystal structure of magnetite allowing for different terminations and the possibility of surface induced redox reactions involving near-surface Fe(II)/Fe(III) redox couples, magnetite is known to be part of the most important redox active systems in geochemical environments[14,15]. The reactivity can be increased when magnetite is present as nanoparticles or as nanoparticle coating[9,11]. The prevalent facets of these nanoparticles were confirmed to be {111}[21,22,66] in environmentally relevant aqueous conditions. The redox activity of these facets contributes to the immobilization of environmental pollutants such as As[66,68,69], Sb[53], or Se[16,17] from ground or drinking water and over a wide pH range. The characteristics of sorption and reactive sites are strongly dependent on the surface speciation. This might also influence how easily reduction/oxidation might occur. Furthermore, although we discussed only charge neutral systems in this work, charged surfaces could also be described.

2.4 Supporting Information

2.4.1 Benchmarking results for magnetite volume crystal

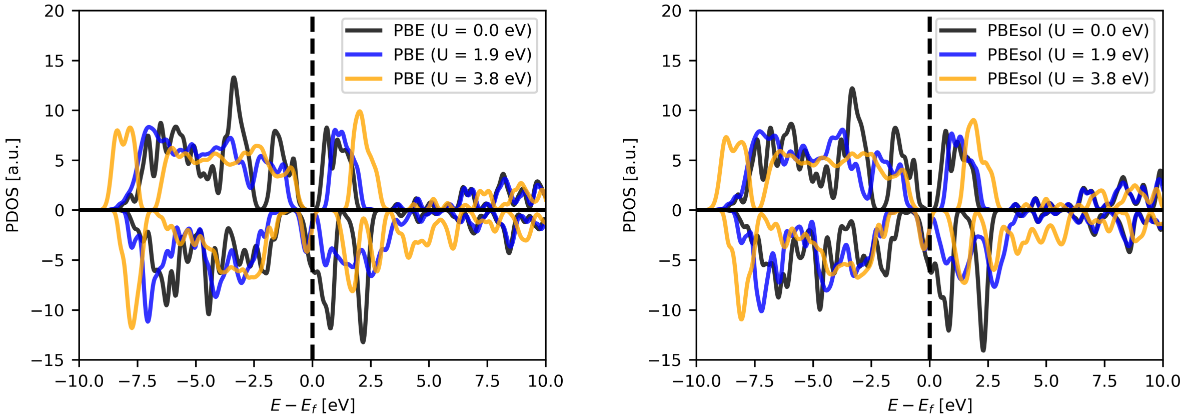

FIGURE S2.1: Projected density of states (PDOS) of bulk magnetite with Hubbard U correction for iron of 0.0 eV, 1.9 eV or 3.8 eV using the original (PBE) parametrization (left) or PBEsol parametrization (right) of the PBE functional. The PDOS script by Tiziano Müller was used, deconvolution with Gaussian functions, standard deviation $\sigma = 0.004$ eV.

TABLE S2.1: Lattice parameters of bulk magnetite using PBE XC functional with PBE and PBEsol parametrization and different U_{eff} values including thermal expansion[106] for 298 K.

	a [Å]	b [Å]	c [Å]	avg. deviation to lit.[107] [%]
PBE (0.0 eV)	8.4423	8.4418	8.4428	0.59
PBE (1.9 eV)	8.4629	8.4689	8.4659	0.87
PBE (3.8 eV)	8.4353	8.4408	8.4423	0.55
PBEsol (0.0 eV)	8.3239	8.3224	8.3284	−0.81
PBEsol (1.9 eV)	8.3565	8.3560	8.3555	−0.44
PBEsol (3.8 eV)	8.3299	8.3304	8.3334	−0.74

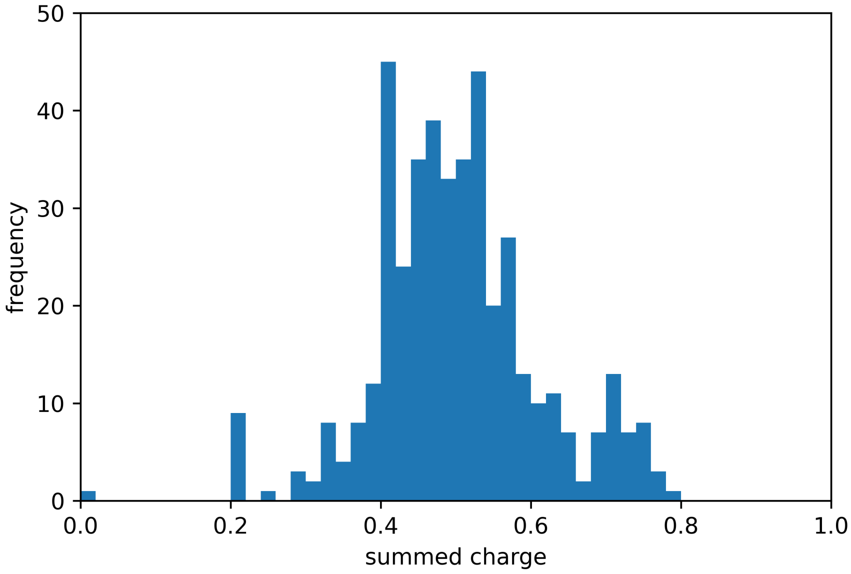

FIGURE S2.2: Histogram of the frequency of partial atomic charges, i.e., minority spin, obtained from the Mulliken population analysis of octahedrally coordinated Fe (spin down only, bin width = 0.02) in magnetite (supercell with 3x3x3 unit cells). The charges of all *d*-orbitals of each Fe (d-2, d-1, d0, d+1, d+2) were summed (threshold per orbital: 0.2). As the distribution is unimodal and almost continuous, a clear distinction between Fe^{2+} and Fe^{3+} appears to be difficult. However, the mean (0.5011) and the median (0.4935) are close, confirming an almost symmetric distribution. Hence, equal amounts of Fe^{2+} and Fe^{3+} in the octahedral positions in the simulated magnetite volume crystal can be assumed, although the deciding value of 0.5 can only be estimated and for the single ions percentages of each extreme could be attributed.

2.4.2 Magnetite {111} surface

Surface geometry, relaxation and charge distribution

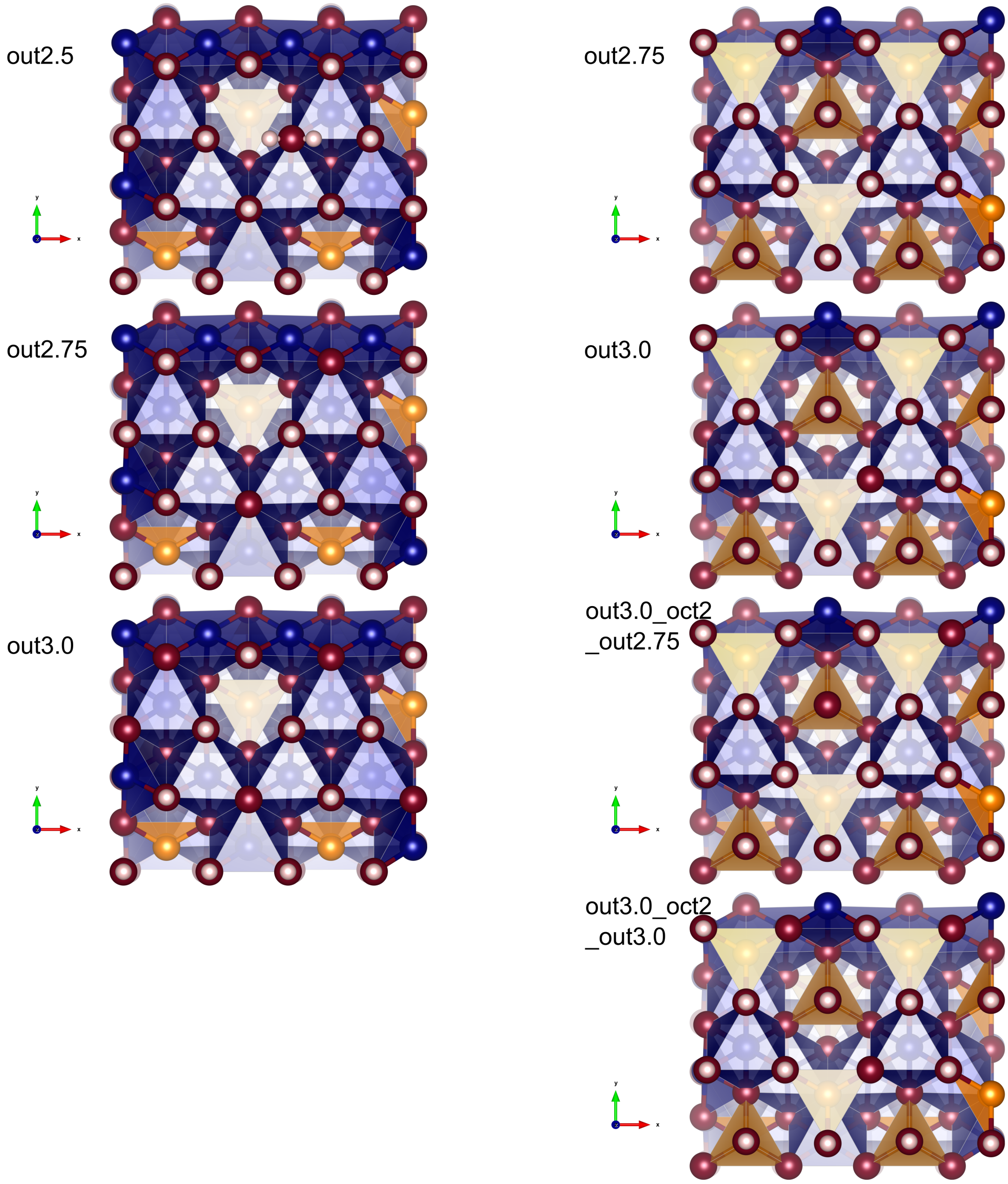

FIGURE S2.3: Top view of initial distribution of hydrogen ions on the chosen 3 oct1- (left) and four tet2- (right) surface terminations resulting in lowest system energy. Shown are reduced cells with one quarter of the actual surface area. Tetrahedrally coordinated iron is depicted in orange, octahedrally coordinated Fe in blue, oxygen in red and hydrogen in white.

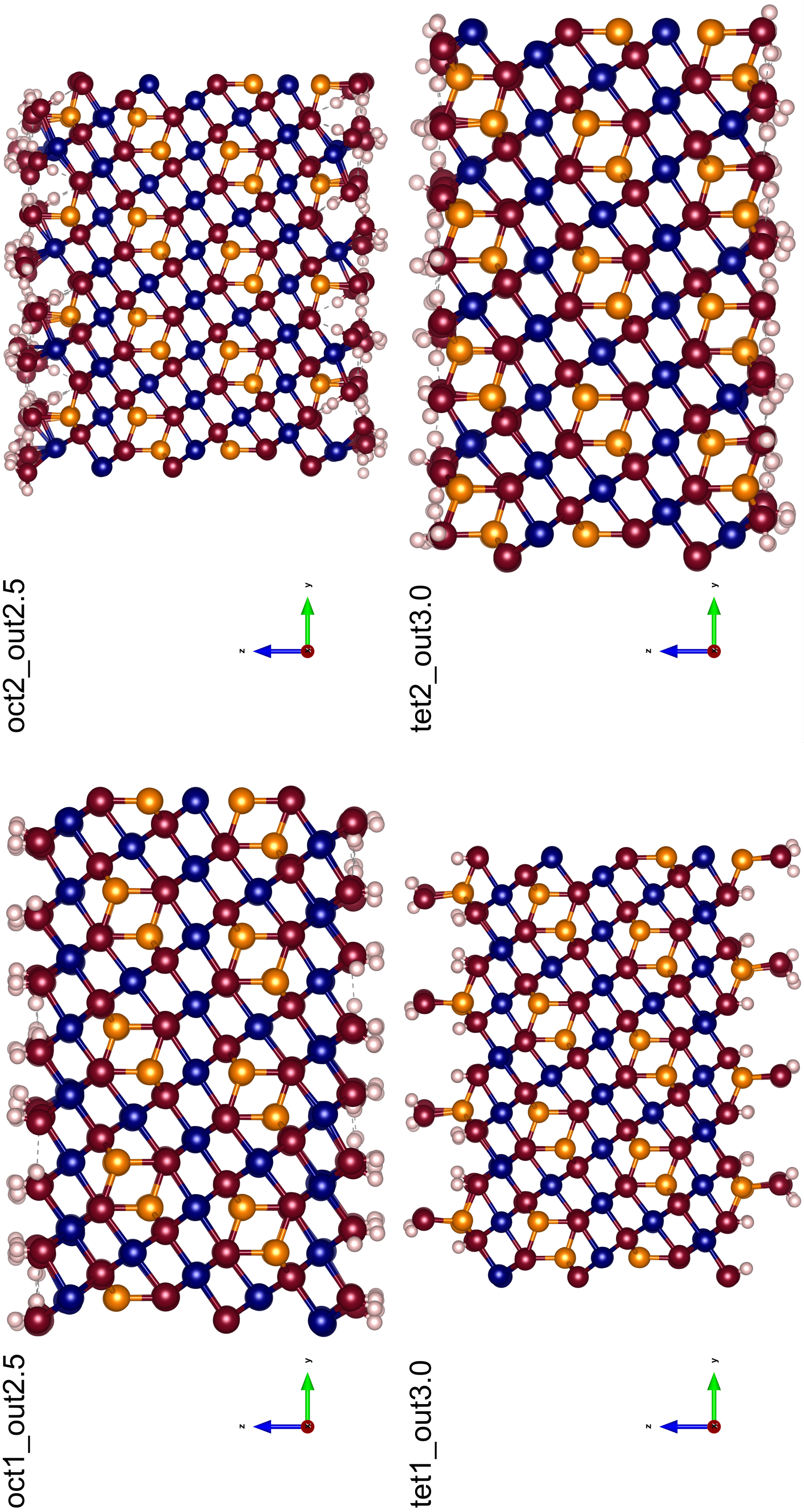

FIGURE S2.4: Side view of optimized surface geometry of the four main surface termination types oct1, oct2, tet1 and tet2 with their respective bulk-like surface charges. The formation of H bridges is suggested by dashed lines. Octahedrally coordinated Fe is depicted in blue, tetrahedrally Fe in orange, O in red and H in white. Sizes are adapted for visualization.

TABLE S2.2: Average layer distance of the six Fe and O layers closest to the surface in the chosen oct1 surfaces. The absolute distance in Å is given as distance to the layer below. In brackets, the deviation of the layer distance compared to the distance of the optimized bulk distance is given in percent.

layer	out2.5		out2.75		out3.0	
O1	1.1507	(0.22)	1.0657	(-7.18)	0.9711	(-15.42)
Fe_{oct1}	1.1529	(-0.08)	1.1891	(3.07)	1.2502	(8.36)
O2	0.6059	(-4.27)	0.5945	(-6.07)	0.5793	(-8.47)
Fe_{tet2}	0.6125	(1.28)	0.6376	(5.44)	0.6412	(6.03)
Fe_{oct2}	0.6469	(7.12)	0.5962	(-1.27)	0.5637	(-6.65)
Fe_{tet1}	0.5941	(-5.95)	0.6215	(-1.62)	0.6517	(3.17)
(O1)						

TABLE S2.3: Average layer distance of the six Fe and O layers closest to the surface in the chosen tet2 surfaces. The absolute distance in Å is given as distance to the layer below. In brackets, the deviation of the layer distance compared to the distance of the optimized bulk distance is given in percent.

layer	out2.75		out3.0		out3.0_oct2_out2.75		out3.0_oct2_out3.0	
O2	0.6524	(3.08)	0.6322	(-0.12)	0.5924	(-6.40)	0.5950	(-5.99)
Fe_{tet2}	0.4943	(-18.26)	0.4799	(-20.64)	0.4582	(-24.23)	0.4147	(-31.43)
Fe_{oct2}	0.7819	(29.48)	0.7835	(29.74)	0.8402	(39.13)	0.8497	(40.71)
Fe_{tet1}	0.5328	(-15.65)	0.5437	(-13.94)	0.5225	(-17.28)	0.5515	(-12.70)
O1	1.1573	(0.79)	1.1565	(0.73)	1.1570	(0.77)	1.1503	(0.18)
Fe_{oct1}	1.1471	(-0.57)	1.1457	(-0.70)	1.1442	(-0.83)	1.1497	(-0.35)
(O2)								

TABLE S2.4: Mean minority spin of oct1 surfaces obtained from Mulliken charge analysis. For high spin configuration minority spin of ≈0 signifies Fe^{3+} and ≈1 Fe^{2+}, values in-between a mixture of these two. A drastic change in the oct1-layer closest to the surface can be perceived, while the tet-layers keep their charge. However, also a slight change for the oct2-layer is shown.

	surface				bulk
Fe-layer	oct1	tet2	oct2	tet1	oct1
oct1_out2.5	0.4920	0.0000	0.4210	0.0000	0.4133
oct1_out2.75	0.2306	0.0000	0.3648	0.0000	0.4471
oct1_out3.0	0.0022	0.0000	0.2880	0.0000	0.4054

TABLE S2.5: Mean minority spin of tet2 surfaces obtained from Mulliken charge analysis. Minority spin of ≈0 signifies Fe^{3+} and ≈1 Fe^{2+}, values in-between a mixture of these two. While the Fe layers close to the center of the slab (bulk) show stable minority spin, the outmost layers, especially tet2 and oct2 change their minority spin drastically.

	surface					bulk
Fe-layer	tet2	oct2	tet1	oct1	tet2	oct2
tet2_out2.75	0.1846	0.5002	0.0607	0.4360	0.0000	0.5751
tet2_out3.0	0.0000	0.5450	0.0000	0.4394	0.0000	0.5838
tet2_out3.0_oct2_out2.75	0.0126	0.2313	0.0068	0.4217	0.0000	0.6671
tet2_out3.0_oct2_out3.0	0.0126	0.0663	0.0063	0.4111	0.0000	0.5553

Surface energy

The Gibbs free energy of formation of a slab G_f can be approximated by its formation enthalpy H_f. To convert the energy obtained by the self-consistent field (SCF) computer simulation $E_\mathrm{SCF,\ slab}$, a correction is conducted considering the individual components hydrogen, oxygen and iron regarding their number N and energies (Equation S2.1). As the first two exist as molecular gases, simulations of H_2 and O_2 were conducted as reference. $E_\mathrm{SCF,\ Fe}$ was obtained from a single sphere simulation, although not comparable to real-life circumstances, it is in line with the previous computer simulations for volume crystal magnetite (DFT+U).

To account for the entropy of the slab system mainly caused by the attached H and OH groups, a computational expensive vibrational analysis was conducted for the seven considered surfaces. In principle, $3N-6$ vibrational normal modes can be obtained from such an analysis for N slab atoms. As the slabs possess a different number of individual layers to account for symmetry, dipole moment, etc., the magnetite bulk-like portion of these vibrational modes should be removed, too. The number M of these atoms can be calculated from the number of Fe atoms approximating from them the number of magnetite formula units. The vibrational modes from these almost fixed atoms are then $3M-6$, accordingly. The number of the remaining vibrational modes from O-H oscillations can then be obtained with $3N-6-(3M-6)=3(N-M)$ and they can be expected to have the highest vibrational frequency $\tilde{\nu}$ (in cm^{-1}) as obtained from the analysis. These frequencies are then converted to their respective angular frequencies $\omega = 2\pi\nu = 2\pi\tilde{\nu}c$ and the vibrational free energy of the surface part of the slab is obtained following Equation S2.3[113] (Table S2.8).

$$H_\mathrm{f} = E_\mathrm{SCF,\ slab} - \frac{1}{2}N_\mathrm{H}\,E_{\mathrm{H}_2} - \frac{1}{2}N_\mathrm{O}\,E_{\mathrm{O}_2} - N_\mathrm{Fe}\,E_\mathrm{SCF,\ Fe} \tag{S2.1}$$

$$E_{\mathrm{H}_2,\ \mathrm{O}_2} = E_\mathrm{SCF} + E_\mathrm{ZPE} + \Delta G(0\,\mathrm{K} \rightarrow 298\,\mathrm{K}) \tag{S2.2}$$

$$\begin{aligned} G_\mathrm{f} &= H_\mathrm{f} + F_\mathrm{vib} = H_\mathrm{f} + E_\mathrm{ZPE} + F_\mathrm{th} \\ &= H_\mathrm{f} + \frac{\hbar}{2}\sum_{i=1}^{3(N-M)} \omega_i + k_\mathrm{B}T \sum_{i=1}^{3(N-M)} \ln\left(1 - \exp\frac{-\hbar\omega_i}{k_\mathrm{B}T}\right) \end{aligned} \tag{S2.3}$$

TABLE S2.6: Energy and number of elemental species in each of the modeled surface terminations. Given is the lowest self-consistent field (SCF) surface energy of (several) possible setups, the number of tetrahedrally and octahedrally coordinated iron (Fe_{tet}, Fe_{oct}), the number of oxygen (O) and hydrogen (H). The number following the first notation of the surface termination denotes the expected charge in the outmost laying Fe-ions, these were found plausible by the Mulliken charge analysis (Table S2.4, Table S2.5).

surface termination	SCF Energy [kJ/mol]	Fe_{tet}	Fe_{oct}	O	H
oct1_out2.0	−94 152 203.0318	64	176	384	184
oct1_out2.5	−94 082 259.3451	64	176	384	136
oct1_out2.75	−94 045 133.0799	64	176	384	112
oct1_out3.0	−94 007 377.2273	64	176	384	88
oct2_out2.0	−120 339 400.7806	96	208	512	232
oct2_out2.5	−120 314 883.1225	96	208	512	216
oct2_out3.0	−120 290 287.5247	96	208	512	200
tet1_out2.0	−105 789 627.6375	96	176	416	136
tet1_out2.5	−105 766 135.0180	96	176	416	120
tet1_out3.0	−105 742 496.6687	96	176	416	104
tet2_out2.0	−94 106 572.9019	96	144	384	152
tet2_out2.5	−94 082 286.6137	96	144	384	136
tet2_out2.75	−94 070 297.2586	96	144	384	128
tet2_out3.0	−94 058 059.1000	96	144	384	120
tet2_out3.0_oct2_out2.75	−94 045 682.9103	96	144	384	112
tet2_out3.0_oct2_out3.0	−94 033 107.3453	96	144	384	104

TABLE S2.7: Energies for component species H_2, O_2, H_2O, Fe, magnetite (Mag), wüstite (Wüs), and hematite (Hem) per formula unit. The energy values were obtained by self-consistent field method (SCF) in CP2K, the zero-point energy (ZPE) in Gaussian and the temperature correction for the fluid phases ($\Delta G(0\,\mathrm{K} \rightarrow 298\,\mathrm{K})$) based on standard tabulated thermodynamic data[114].

species	SCF Energy [kJ/mol]	E_{ZPE} [kJ/mol]	$\Delta G(0\,\mathrm{K} \rightarrow 298\,\mathrm{K})$ [kJ/mol]
H_2	−3050.6345	27.7788	−24.2393
O_2	−83 827.9392	11.9539	−52.3337
H_2O	−45 210.1230	60.3471	−35.4496
Fe	−323 935.7098		
Wüs	−365 908.2925		
Mag	−1 139 861.4090		
Hem	−773 924.0187		

TABLE S2.8: Vibrational free energy (F_{vib}) and interaction energies E_{int} of water with the chosen surfaces as obtained from classical MD simulations.

surface termination	F_{vib} [kJ/mol]	E_{int} [kJ/mol/m^2]
oct1_out2.5	4760.1382	-3.6922×10^{20}
oct1_out2.75	4045.3271	-3.1557×10^{20}
oct1_out3.0	3327.8653	-3.8472×10^{20}
tet2_out2.75	4566.8465	-2.2062×10^{20}
tet2_out3.0	4316.8542	-2.0720×10^{20}
tet2_out3.0_oct2_out2.75	4070.3932	-2.3003×10^{20}
tet2_out3.0_oct2_out3.0	3840.0902	-2.2115×10^{20}

Surface energy as function of fugacities

In geological sciences, expressing the surface energy as function of (gas) fugacities is common[115] (ch. 6). Accordingly, in this paper oxygen fugacity and water potential are used to calculate the surface energy according to Equation S2.4. A correction for the mobile species oxygen and water based on standard thermodynamic data[95] is applied as depicted in Equation S2.5, including also the dependency on the fugacity f.

Here, p^0 depicts the standard pressure, being 1 bar for oxygen and the saturation pressure at T for water ($p^0_{\mathrm{H_2O,\ sat}}(T = 298\,\mathrm{K}) = 0.031\,417\,\mathrm{bar}$)[114].

$$\gamma = \frac{1}{2A}\left(G_\mathrm{f} - N_\mathrm{Mag}\mu_\mathrm{Mag} - N_{\mathrm{O_2}}\mu_{\mathrm{O_2}} - N_{\mathrm{H_2O}}\mu_{\mathrm{H_2O}}\right) \tag{S2.4}$$

$$\mu_{mobile} = \Delta H^0_\mathrm{f} - T\,S^0 + k_\mathrm{B}\,T\,\ln\left(\frac{f}{p^0}\right) \tag{S2.5}$$

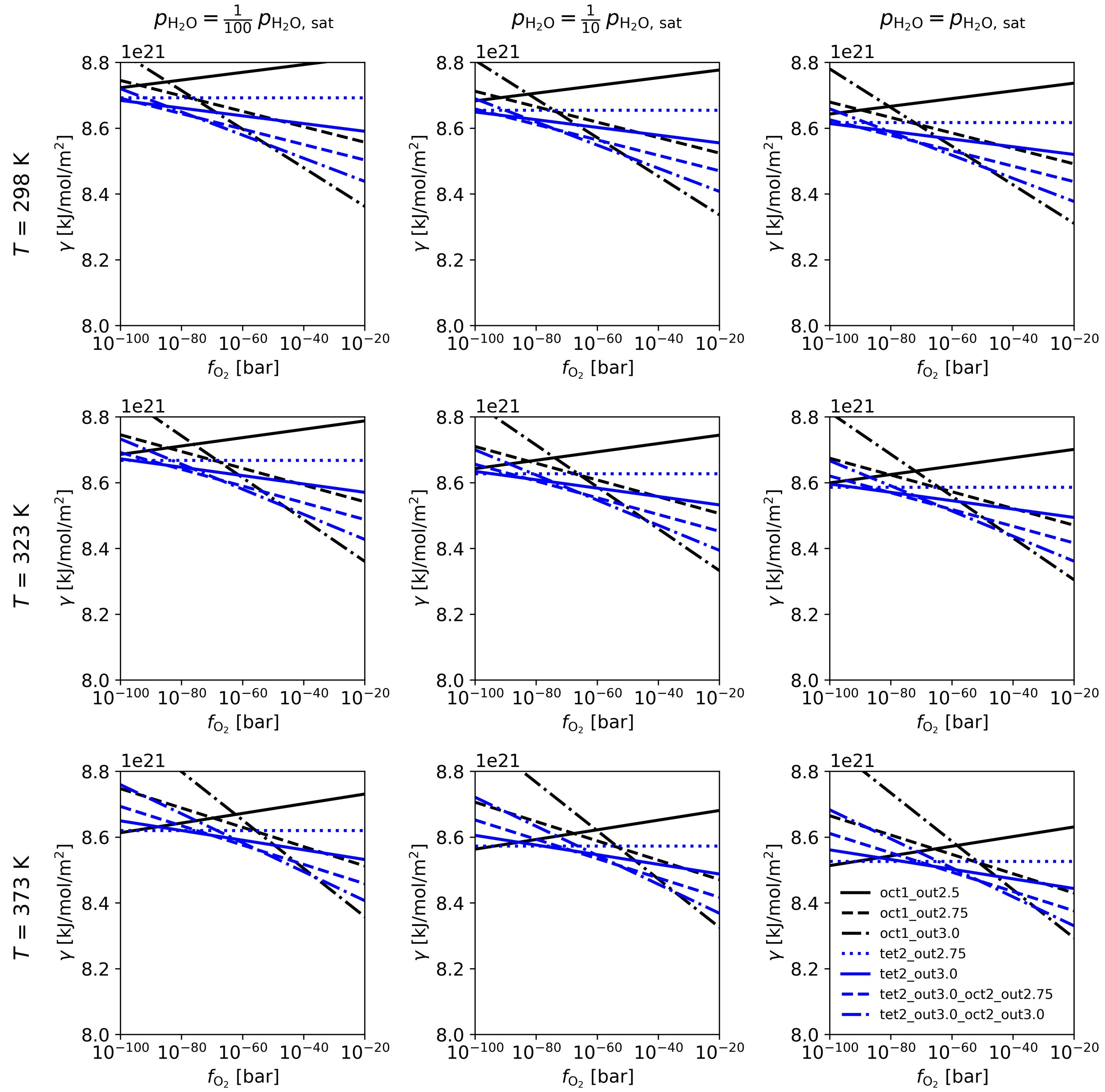

FIGURE S2.5: Specific surface energy γ as function of oxygen fugacity $f_{\mathrm{O_2}}$ at different temperatures (298 K, 323 K and 373 K) for fractions of the temperature dependent saturation water pressure, i.e., 0.031 42 bar, 0.122 60 bar and 1.008 80 bar, respectively[114].

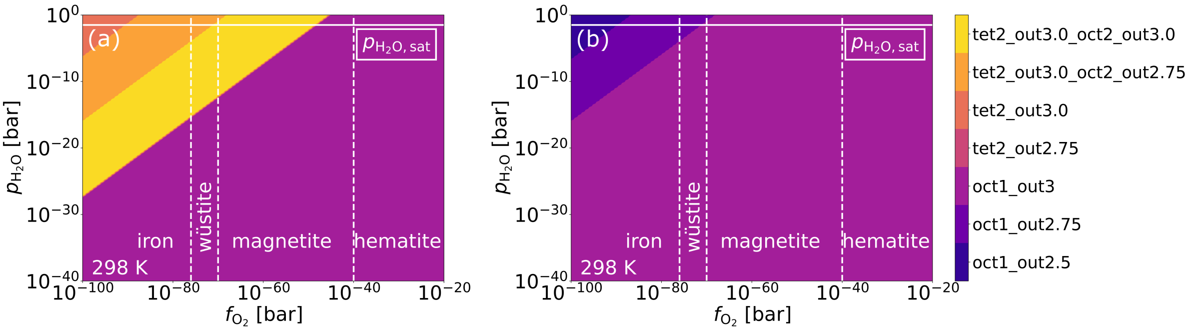

FIGURE S2.6: Surface stability plots of the chosen magnetite surfaces at 298 K as function of water and oxygen fugacity. (a) Surface stability plot according to Figure S2.5, (b) with suppression of tet2-terminations (see main text).

Figure S2.5 and Figure S2.6 depict the results of the fugacity analysis. The range of oxygen fugacity was chosen from the range of petrological mineral redox buffers[116] of pure iron and the common iron oxides ranging from ferrous wüstite (FeO) over mixed ferrous/ferric magnetite (Fe_3O_4) to ferric hematite (Fe_2O_3). The temperature-dependent equilibrium between two phases depicting the mineral redox buffer can be expressed according to Equation S2.6 and Equation S2.7 and is shown in Figure S2.7. G of the minerals were obtained by SCF simulations and noted in Table S2.7. The zero-point energy E_{ZPE} was obtained with thermodynamic modeling in *Gaussian*[117]. The temperature correction from 0 K to the chosen temperature T, was calculated as shown in equation S2.8 with a linear approximation for $\Delta H(0\,\text{K})$ and neglection of entropy at 0 K. For the considerations in this paper, T was chosen to be 298 K, 323 K or 373 K. The pressure-volume work for the solids is neglected.

$$a\, G_{\text{higher oxidation}} = b\, G_{\text{lower oxidation}} + c\, G_{O_2} \tag{S2.6}$$

$$G_{O_2} = E_{\text{SCF}} + E_{\text{ZPE}} + \Delta G(0 \to T) + RT \ln\left(\frac{f}{p^0}\right) \tag{S2.7}$$

$$\Delta G(0\,\text{K} \to T) = \Delta G(T) - \Delta G(0\,\text{K}) = \Delta G(T) - \Delta H(0\,\text{K}) \tag{S2.8}$$

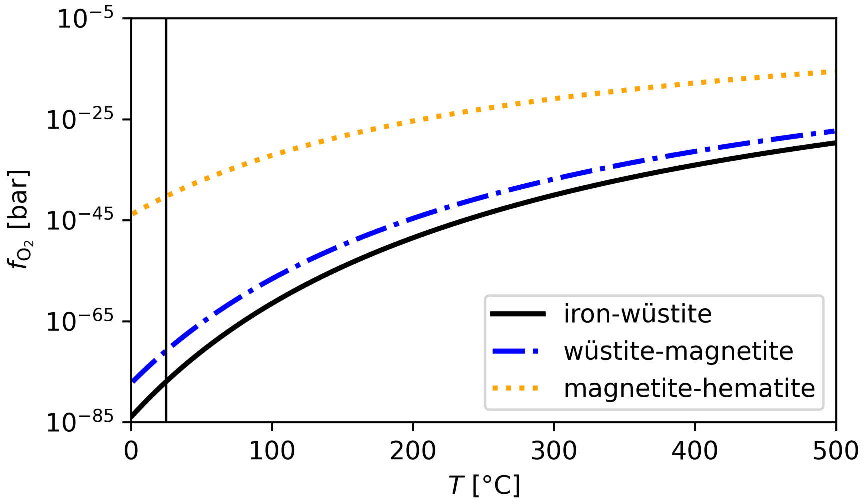

FIGURE S2.7: Mineral redox buffers of iron and iron oxides (wüstite, magnetite, hematite). The vertical line marks $T = 298\,\mathrm{K}$, exemplarily.

Pourbaix approach of surface energy

The applied Pourbaix approach[118] where the surface energy is expressed as function of E_h and pH is based on hydrogen H and oxygen O also allowing for possible charge Q (eq. (S2.9)). However, all system investigated in this study were charge neutral. With substitutions for the chemical potentials (eqs. (S2.10) and (S2.11)), the surface energy can be expressed as function of E_h and pH (eq. (S2.12)).

$$\gamma = \frac{1}{2A}\left(G_\mathrm{f} - N_\mathrm{Mag}\,E_\mathrm{Mag} - N_\mathrm{H}\,\left(\mu_{\mathrm{H}^+} - E_\mathrm{h}\right) - E_\mathrm{h}\,Q - N_\mathrm{O}\,\mu_\mathrm{O}\right) \tag{S2.9}$$

$$\mu_\mathrm{O} = \mu_{\mathrm{H_2O}} - 2\,\mu_{\mathrm{H}^+} + 2\,E_\mathrm{h} \tag{S2.10}$$

$$\mu_{\mathrm{H}^+} = -RT\ln(10)\,\mathrm{pH} \tag{S2.11}$$

$$\begin{aligned}\gamma = \frac{1}{2A}\big(&G_\mathrm{f} - N_\mathrm{Mag}\,E_\mathrm{Mag} - N_\mathrm{O}\,\mu_{\mathrm{H_2O}} - E_\mathrm{h}\left(Q - N_\mathrm{H} + 2\,N_\mathrm{O}\right)\\ &+ RT\left(N_\mathrm{H} - 2\,N_\mathrm{O}\right)\,\ln(10)\,\mathrm{pH}\big)\end{aligned} \tag{S2.12}$$

While the pressure-volume work for the solids is neglected, $\mu_{\mathrm{H_2O}}$ in Equation 3 of the paper can be expressed as depicted in Equation S2.13. ΔH_f^0 and S^0 were taken from standard thermodynamic tables[95]. For the considerations in this paper, temperature T was chosen to be 298 K, 323 K or 373 K.

$$\mu_{\mathrm{H_2O}} = \Delta H_\mathrm{f}^0 - T\,S^0 \tag{S2.13}$$

Coordination of surface-H by water-O

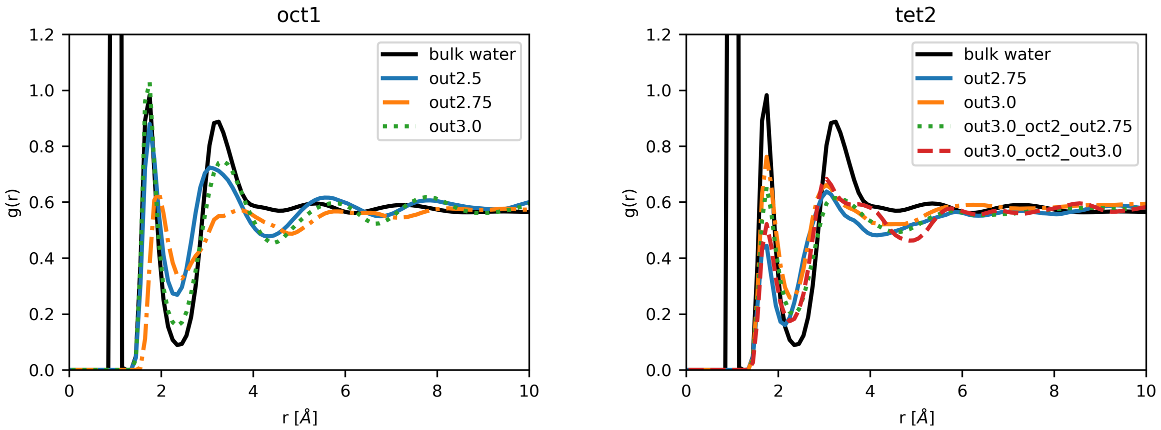

FIGURE S2.8: Radial pair distribution function (RDF) g(r) of surface-adsorbed hydrogen surrounded by water-oxygen of chosen oct1 (left) and tet2 (right) surface terminations obtained from application of the corresponding tool in VMD[119] to the last 10001 frames of the classcial MD. As comparison, the interaction of hydrogens of pure water surrounded by water-O is (scaled) depicted for comparison. The slightly higher radius (peak position) of the first coordination shell of surface-H compared to the second of water-H can be interpreted as a slightly decreased acidity of the surface OH groups compared to water.

TABLE S2.9: Coordination numbers of surface-adsorbed hydrogen surrounded by water-oxygen of the chosen surfaces as obtained in the RDF analysis of the water layers (WL) from classical MD simulations.

surface termination	WL 1	WL 2	WL 3
oct1_out2.5	0.5709	5.3362	20.6993
oct1_out2.75	0.5827	6.8798	23.7364
oct1_out3.0	0.5405	5.6210	20.4487
tet2_out2.75	0.2380	4.0925	16.0914
tet2_out3.0	0.4675	5.5228	25.6788
tet2_out3.0_oct2_out2.75	0.4197	5.3897	17.2465
tet2_out3.0_oct2_out3.0	0.3049	6.7287	15.7793

2.5 References

[1] Tutolo, B. M.; Kiesel, T.; Luhmann, A. J.; Solheid, P.; Seyfried, W. E. Experimental Evaluation of the Role of Redox during Glauconite-CO_2-Brine Interactions. *Appl. Geochem.* **2020**, *115*, 104558.

[2] Gorski, C. A.; Nurmi, J. T.; Tratnyek, P. G.; Hofstetter, T. B.; Scherer, M. M. Redox Behavior of Magnetite: Implications for Contaminant Reduction. *Environ. Sci. Technol.* **2009**, *44*, 55–60.

[3] Robinson, T. C.; Latta, D. E.; Notini, L.; Schilling, K. E.; Scherer, M. M. Abiotic Reduction of Nitrite by Fe(II): A Comparison of Rates and N_2O Production. *Environ. Sci.: Processes Impacts* **2021**, *23*, 1531–1541.

[4] O'Loughlin, E. J.; Boyanov, M. I.; Flynn, T. M.; Gorski, C. A.; Hofmann, S. M.; McCormick, M. L.; Scherer, M. M.; Kemner, K. M. Effects of Bound Phosphate on the Bioreduction of Lepidocrocite (γ-FeOOH) and Maghemite (γ-Fe_2O_3) and Formation of Secondary Minerals. *Environ. Sci. Technol.* **2013**, *47*, 9157–9166.

[5] Mejia, J.; Roden, E. E.; Ginder-Vogel, M. Influence of Oxygen and Nitrate on Fe (Hydr)oxide Mineral Transformation and Soil Microbial Communities during Redox Cycling. *Environ. Sci. Technol.* **2016**, *50*, 3580–3588.

[6] Xiao, Z.; Yang, L.; Chen, C.; Chen, D.; Zhou, X. Redox Reaction between Solid-phase Humins and Fe(III) Compounds: Toward a Further Understanding of the Redox Properties of Humin and Its Possible Environmental Effects. *J. Environ. Manage.* **2022**, *310*, 114793.

[7] Zhou, S.; Xu, J.; Yang, G.; Zhuang, L. Methanogenesis Affected by the Co-occurrence of Iron(III) Oxides and Humic Substances. *FEMS Microbiol. Ecol.* **2014**, *88*, 107–120.

[8] Elsner, M.; Schwarzenbach, R. P.; Haderlein, S. B. Reactivity of Fe(II)-bearing Minerals toward Reductive Transformation of Organic Contaminants. *Environ. Sci. Technol.* **2003**, *38*, 799–807.

[9] Jentzsch, T. L.; Chun, C. L.; Gabor, R. S.; Penn, R. L. Influence of Aluminum Substitution on the Reactivity of Magnetite Nanoparticles. *J. Phys. Chem. C* **2007**, *111*, 10247–10253.

[10] Mohamad, N. D.; Zaki, Z. M.; Amir, A. Mechanisms of Enhanced Oxidative Degradation of Tetrachloroethene by Nano-magnetite Catalysed with Glutathione. *Chem. Eng. J.* **2020**, *393*, 124760.

[11] Yin, X.; Hua, H.; Dyer, J.; Landis, R.; Fennell, D.; Axe, L. Degradation of Chlorinated Solvents with Reactive Iron Minerals in Subsurface Sediments from Redox Transition Zones. *J. Hazard. Mater.* **2023**, *445*, 130470.

[12] Zhang, X.; Jia, Q.; Deng, J.; Wu, F.; Huang, L.-Z. Interaction between Green Rust and Tribromophenol under Anoxic, Oxic and Anoxic-to-oxic Conditions: Adsorption, Desorption and Oxidative Degradation. *Water Res.* **2022**, *217*, 118398.

[13] Zhang, L.; Verstraete, W.; de Lourdes Mendoza, M.; Lu, Z.; Liu, Y.; Huang, G.; Cai, L. Decrease of Dissolved Sulfide in Sewage by Powdered Natural Magnetite and Hematite. *Sci. Total Environ.* **2016**, *573*, 1070–1078.

[14] Scheinost, A. C.; Charlet, L. Selenite Reduction by Mackinawite, Magnetite and Siderite: XAS Characterization of Nanosized Redox Products. *Environ. Sci. Technol.* **2008**, *42*, 1984–1989.

[15] Scheinost, A. C.; Kirsch, R.; Banerjee, D.; Fernandez-Martinez, A.; Zaenker, H.; Funke, H.; Charlet, L. X-ray Absorption and Photoelectron Spectroscopy Investigation of Selenite Reduction by Fe^{II}-bearing Minerals. *J. Contam. Hydrol.* **2008**, *102*, 228–245.

[16] Börsig, N.; Scheinost, A. C.; Shaw, S.; Schild, D.; Neumann, T. Retention and Multiphase Transformation of Selenium Oxyanions during the Formation of Magnetite Via Iron(II) Hydroxide and Green Rust. *Dalton Trans.* **2018**, *47*, 11002–11015.

[17] Börsig, N.; Scheinost, A. C.; Schild, D.; Neumann, T. Mechanisms of Selenium Removal by Partially Oxidized Magnetite Nanoparticles for Wastewater Remediation. *Appl. Geochem.* **2021**, *132*, 105062.

[18] Chowdhury, S. R.; Yanful, E. K.; Pratt, A. R. Recycling of Nickel Smelter Slag for Arsenic Remediation - An Experimental Study. *Environ. Sci. Pollut. Res.* **2014**, *21*, 10096–10107.

[19] Johnson, L.; Schneider, J.; Zuidema, P.; Gribi, P.; Mayer, G.; Smith, P.; Kunz, B.; Frei, C. *Project Opalinus Clay - Demonstration of Disposal for Spent Fuel, Vitrified High-level Wast and Long-lived Intermediate-level Waste*; NAGRA tech. report 02-05, 2002.

[20] King, F. *Corrosion of Carbon Steel under Anaerobic Conditions in a Repository for SF and HLW in Opalinus Clay*; NAGRA tech. report 08-12, 2008.

[21] Zhao, L.; Zhang, H.; Xing, Y.; Song, S.; Yu, S.; Shi, W.; Guo, X.; Yang, J.; Lei, Y.; Cao, F. Morphology-Controlled Synthesis of Magnetites with Nanoporous Structures and Excellent Magnetic Properties. *Chem. Mater.* **2007**, *20*, 198–204.

[22] Yu, X.; Huo, C.-F.; Li, Y.-W.; Wang, J.; Jiao, H. Fe_3O_4 Surface Electronic Structures and Stability from GGA+U. *Surf. Sci.* **2012**, *606*, 872–879.

[23] Noh, J.; Osman, O. I.; Aziz, S. G.; Winget, P.; Brédas, J.-L. Magnetite Fe_3O_4 (111) Surfaces: Impact of Defects on Structure, Stability, and Electronic Properties. *Chem. Mater.* **2015**, *27*, 5856–5867.

[24] Shimizu, T. K.; Jung, J.; Kato, H. S.; Kim, Y.; Kawai, M. Termination and Verwey Transition of the (111) Surface of Magnetite Studied by Scanning Tunneling Microscopy and First-Principles Calculations. *Phys. Rev. B* **2010**, *81*, 235429.

[25] Ahdjoudj, J.; Martinsky, C.; Minot, C.; Hove, M. A. V.; Somorjai, G. A. Theoretical Study of the Termination of the Fe_3O_4 (111) Surface. *Surf. Sci.* **1999**, *443*, 133–153.

[26] Ritter, M.; Weiss, W. Fe_3O_4(111) Surface Structure Determined by LEED Crystallography. *Surf. Sci.* **1999**, *432*, 81–94.

[27] Dedkov, Y. S.; Fonin, M.; Vyalikh, D. V.; Hauch, J. O.; Molodtsov, S. L.; Rüdiger, U.; Güntherodt, G. Electronic Structure of the Fe_3O_4 (111) Surface. *Phys. Rev. B* **2004**, *70*, 073405.

[28] Paul, M.; Sing, M.; Claessen, R.; Schrupp, D.; Brabers, V. A. M. Thermodynamic Stability and Atomic and Electronic Structure of Reduced Fe_3O_4(111) Single-crystal Surfaces. *Phys. Rev. B* **2007**, *76*, 075412.

[29] Yang, T.; Wen, X.-d.; Ren, J.; Li, Y.-w.; Wang, J.-g.; Huo, C.-f. Surface Structures of Fe_3O_4 (111), (110), and (001): A Density Functional Theory Study. *J. Fuel Chem. Technol.* **2010**, *38*, 121–128.

[30] Berdunov, N.; Murphy, S.; Mariotto, G.; Shvets, I. V. Room Temperature Study of a Strain-induced Electronic Superstructure on a Magnetite (111) Surface. *Phys. Rev. B* **2004**, *70*, 085404.

[31] Berdunov, N.; Murphy, S.; Mariotto, G.; Shvets, I. V.; Mykovskiy, Y. M. Spin-polarized Tunneling Effects Observed on the Oxygen-terminated Fe_3O_4 (111) Surface. *J. Appl. Phys.* **2004**, *95*, 6891–6893.

[32] Berdunov, N.; Murphy, S.; Mariotto, G.; Shvets, I. V. Atomically Resolved Spin-Dependent Tunneling on the Oxygen-Terminated Fe_3O_4 (111). *Phys. Rev. Lett.* **2004**, *93*, 057201.

[33] Zhu, L.; Yao, K. L.; Liu, Z. L. First-principles Study of the Polar (111) Surface of Fe_3O_4. *Phys. Rev. B* **2006**, *74*, 035409.

[34] Jordan, K.; Cazacu, A.; Manai, G.; Ceballos, S. F.; Murphy, S.; Shvets, I. V. Scanning Tunneling Spectroscopy Study of the Electronic Structure of Fe_3O_4 Surfaces. *Phys. Rev. B* **2006**, *74*, 085416.

[35] Mirabella, F.; Zaki, E.; Ivars-Barcelo, F.; Schauermann, S.; Shaikhutdinov, S.; Freund, H.-J. CO_2 Adsorption on Magnetite Fe_3O_4(111). *J. Phys. Chem. C* **2018**, *122*, 27433–27441.

[36] Konuk, M.; Sellschopp, K.; Vonbun-Feldbauer, G. B.; Meißner, R. H. Modeling Charge Redistribution at Magnetite Interfaces in Empirical Force Fields. *J. Phys. Chem. C* **2021**, *125*, 4794–4805.

[37] Creutzburg, M.; Sellschopp, K.; Tober, S.; Grånäs, E.; Vonk, V.; Mayr-Schmölzer, W.; Müller, S.; Noei, H.; Vonbun-Feldbauer, G. B.; Stierle, A. Heterogeneous Adsorption and Local Ordering of Formate on a Magnetite Surface. *J. Phys. Chem. Lett.* **2021**, *12*, 3847–3852.

[38] Creutzburg, M.; Sellschopp, K.; Gleißner, R.; Arndt, B.; Vonbun-Feldbauer, G. B.; Vonk, V.; Noei, H.; Stierle, A. Surface Structure of Magnetite (111) under Oxidizing and Reducing Conditions. *J. Phys.: Condens. Matter* **2022**, *34*, 164003.

[39] Cutting, R.; Muryn, C.; Vaughan, D.; Thornton, G. Substrate-Termination and H_2O-Coverage Dependent Dissociation of H_2O on Fe_3O_4(111). *Surf. Sci.* **2008**, *602*, 1155–1165.

[40] Grillo, M. E.; Finnis, M. W.; Ranke, W. Surface Structure and Water Adsorption on Fe_3O_4(111): Spin-density Functional Theory and On-site Coulomb Interactions. *Phys. Rev. B* **2008**, *77*, 075407.

[41] Joseph, Y.; Kuhrs, C.; Ranke, W.; Ritter, M.; Weiss, W. Adsorption of Water on FeO(111) and Fe_3O_4(111): Identification of Active Sites for Dissociation. *Chem. Phys. Lett.* **1999**, *314*, 195–202.

[42] Joseph, Y.; Ranke, W.; Weiss, W. Water on FeO(111) and Fe_3O_4(111): Adsorption Behavior on Different Surface Terminations. *J. Phys. Chem. B* **2000**, *104*, 3224–3236.

[43] Kendelewicz, T.; Liu, P.; Doyle, C.; Brown, G.; Nelson, E.; Chambers, S. Reaction of Water with the (100) and (111) Surfaces of Fe_3O_4. *Surf. Sci.* **2000**, *453*, 32–46.

[44] Yang, T.; Wen, X.-D.; Huo, C.-F.; Li, Y.-W.; Wang, J.; Jiao, H. Structure and Energetics of Hydrogen Adsorption on Fe_3O_4(111). *J. Mol. Catal. A: Chem.* **2009**, *302*, 129–136.

[45] Yang, T.; dong Wen, X.; bo Cao, D.; wang Li, Y.; guo Wang, J.; fang Huo, C. Structures and Energetics of H_2O Adsorption on the Fe_3O_4 (111) Surface. *J. Fuel Chem. Technol.* **2009**, *37*, 506–512.

[46] Mirabella, F.; Zaki, E.; Ivars-Barceló, F.; Li, X.; Paier, J.; Sauer, J.; Shaikhutdinov, S.; Freund, H.-J. Cooperative Formation of Long-Range Ordering in Water Ad-layers on Fe_3O_4 (111) Surfaces. *Angew. Chem. - Int. Ed.* **2018**, *57*, 1409–1413.

[47] Zaki, E.; Mirabella, F.; Ivars-Barceló, F.; Seifert, J.; Carey, S.; Shaikhutdinov, S.; Freund, H.-J.; Li, X.; Paier, J.; Sauer, J. Water Adsorption on the Fe_3O_4(111) Surface: Dissociation and Network Formation. *Phys. Chem. Chem. Phys.* **2018**, *20*, 15764–15774.

[48] Zaki, E.; Jakub, Z.; Mirabella, F.; Parkinson, G. S.; Shaikhutdinov, S.; Freund, H.-J. Water Ordering on the Magnetite Fe_3O_4 Surfaces. *J. Phys. Chem. Lett.* **2019**, *10*, 2487–2492.

[49] Asakawa, K.; Miura, Y.; Nagatsuka, N.; Takeyasu, K.; Matsumoto, M.; Fukutani, K. Electronic and Spin Structure of O- and H-Adsorbed Fe_3O_4 (111) Surfaces. *Phys. Rev. B* **2019**, *99*, 085442.

[50] Zhou, C.; Zhang, Q.; Chen, L.; Han, B.; Ni, G.; Wu, J.; Garg, D.; Cheng, H. Density Functional Theory Study of Water Dissociative Chemisorption on the Fe_3O_4(111) Surface. *J. Phys. Chem. C* **2010**, *114*, 21405–21410.

[51] Li, X.; Paier, J. Adsorption of Water on the Fe_3O_4(111) Surface: Structures, Stabilities, and Vibrational Properties Studied by Density Functional Theory. *J. Phys. Chem. C* **2016**, *120*, 1056–1065.

[52] Petitto, S. C.; Tanwar, K. S.; Ghose, S. K.; Eng, P. J.; Trainor, T. P. Surface Structure of Magnetite (111) under Hydrated Conditions by Crystal Truncation Rod Diffraction. *Surf. Sci.* **2010**, *604*, 1082–1093.

[53] Kirsch, R.; Scheinost, A. C.; Rossberg, A.; Banerjee, D.; Charlet, L. Reduction of Antimony by Nano-particulate Magnetite and Mackinawite. *Mineral. Mag.* **2008**, *72*, 185–189.

[54] Heald, S. M.; Krupka, K. M.; Brown, C. F. Incorporation of Pertechnetate and Perrhenate into Corroded Steel Surfaces Studied by X-ray Absorption Fine Structure Spectroscopy. *Radiochim. Acta* **2011**, *100*, 243–253.

[55] Missana, T.; Maffiotte, C.; García-Gutiérrez, M. Surface Reactions Kinetics between Nanocrystalline Magnetite and Uranyl. *J. Colloid Interface Sci.* **2003**, *261*, 154–160.

[56] Aamrani, S. E.; Giménez, J.; Rovira, M.; Seco, F.; Grivé, M.; Bruno, J.; Duro, L.; de Pablo, J. A Spectroscopic Study of Uranium(VI) Interaction with Magnetite. *Appl. Surf. Sci.* **2007**, *253*, 8794–8797.

[57] Singer, D. M.; Chatman, S. M.; Ilton, E. S.; Rosso, K. M.; Banfield, J. F.; Waychunas, G. A. U(VI) Sorption and Reduction Kinetics on the Magnetite (111) Surface. *Environ. Sci. Technol.* **2012**, *46*, 3821–3830.

[58] Singer, D. M.; Chatman, S. M.; Ilton, E. S.; Rosso, K. M.; Banfield, J. F.; Waychunas, G. A. Identification of Simultaneous U(VI) Sorption Complexes and U(IV) Nanoprecipitates on the Magnetite (111) Surface. *Environ. Sci. Technol.* **2012**, *46*, 3811–3820.

[59] Ma, Y.; Cheng, X.; Kang, M.; Yang, G.; Yin, M.; Wang, J.; Gang, S. Factors Influencing the Reduction of U(VI) by Magnetite. *Chemosphere* **2020**, *254*, 126855.

[60] Pan, Z.; Bártová, B.; LaGrange, T.; Butorin, S. M.; Hyatt, N. C.; Stennett, M. C.; Kvashnina, K. O.; Bernier-Latmani, R. Nanoscale Mechanism of UO_2 Formation through Uranium Reduction by Magnetite. *Nat. Commun.* **2020**, *11*, 4001.

[61] Powell, B. A.; Fjeld, R. A.; Kaplan, D. I.; Coates, J. T.; Serkiz, S. M. $Pu(V)O_2^+$ Adsorption and Reduction by Synthetic Magnetite (Fe_3O_4). *Environ. Sci. Technol.* **2004**, *38*, 6016–6024.

[62] Kirsch, R.; Fellhauer, D.; Altmaier, M.; Neck, V.; Rossberg, A.; Fanghänel, T.; Charlet, L.; Scheinost, A. C. Oxidation State and Local Structure of Plutonium Reacted with Magnetite, Mackinawite, and Chukanovite. *Environ. Sci. Technol.* **2011**, *45*, 7267–7274.

[63] Felmy, A. R.; Moore, D. A.; Pearce, C. I.; Conradson, S. D.; Qafoku, O.; Buck, E. C.; Rosso, K. M.; Ilton, E. S. Controls on Soluble Pu Concentrations in PuO_2/Magnetite Suspensions. *Environ. Sci. Technol.* **2012**, *46*, 11610–11617.

[64] Scott, T.; Allen, G.; Heard, P.; Randell, M. Reduction of U(VI) to U(IV) on the Surface of Magnetite. *Geochim. Cosmochim. Acta* **2005**, *69*, 5639–5646.

[65] Rajput, S.; Pittman, C. U.; Mohan, D. Magnetic Magnetite (Fe_3O_4) Nanoparticle Synthesis and Applications for Lead (Pb^{2+}) and Chromium (Cr^{6+}) Removal from Water. *J. Colloid Interface Sci.* **2016**, *468*, 334–346.

[66] Wang, Y.; Morin, G.; Ona-Nguema, G.; Menguy, N.; Juillot, F.; Aubry, E.; Guyot, F.; Calas, G.; Brown, G. E. Arsenite Sorption at the Magnetite–Water Interface during Aqueous Precipitation of Magnetite: EXAFS Evidence for a New Arsenite Surface Complex. *Geochim. Cosmochim. Acta* **2008**, *72*, 2573–2586.

[67] Roy, P. K.; Choudhury, M. R.; Ali, M. A. As(III) and As(V) Adsorption on Magnetite Nanoparticles: Adsorption Isotherms, Effect of pH and Phosphate, and Adsorption Kinetics. *Int. J. Chem. Environ. Eng.* **2013**, *4*, 55–63.

[68] Liu, C.-H.; Chuang, Y.-H.; Chen, T.-Y.; Tian, Y.; Li, H.; Wang, M.-K.; Zhang, W. Mechanism of Arsenic Adsorption on Magnetite Nanoparticles from Water: Thermodynamic and Spectroscopic Studies. *Environ. Sci. Technol.* **2015**, *49*, 7726–7734.

[69] Mejia-Santillan, M.; Pariona, N.; Bravo-C., J.; Herrera-Trejo, M.; Montejo-Alvaro, F.; Zarate, A.; Perry, D.; Mtz-Enriquez, A. Physical and Arsenic Adsorption Properties of Maghemite and Magnetite Sub-microparticles. *J. Magn. Magn. Mater.* **2018**, *451*, 594–601.

[70] Dumas, T.; Fellhauer, D.; Schild, D.; Gaona, X.; Altmaier, M.; Scheinost, A. C. Plutonium Retention Mechanisms by Magnetite under Anoxic Conditions: Entrapment Versus Sorption. *ACS Earth Space Chem.* **2019**, *3*, 2197–2206.

[71] Yalçıntaş, E.; Scheinost, A. C.; Gaona, X.; Altmaier, M. Systematic XAS Study on the Reduction and Uptake of Tc by Magnetite and Mackinawite. *Dalton Trans.* **2016**, *45*, 17874–17885.

[72] Duro, L.; Aamrani, S. E.; Rovira, M.; de Pablo, J.; Bruno, J. Study of the Interaction between U(VI) and the Anoxic Corrosion Products of Carbon Steel. *Appl. Geochem.* **2008**, *23*, 1094–1100.

[73] Rovira, M.; Aamrani, S. E.; Duro, L.; Giménez, J.; de Pablo, J.; Bruno, J. Interaction of Uranium with in Situ Anoxically Generated Magnetite on Steel. *J. Hazard. Mater.* **2007**, *147*, 726–731.

[74] Marshall, T. A.; Morris, K.; Law, G. T. W.; Mosselmans, J. F. W.; Bots, P.; Parry, S. A.; Shaw, S. Incorporation and Retention of 99-Tc(IV) in Magnetite under High pH Conditions. *Environ. Sci. Technol.* **2014**, *48*, 11853–11862.

[75] Lukens, W. W.; Saslow, S. A. Facile Incorporation of Technetium into Magnetite, Magnesioferrite, and Hematite by Formation of Ferrous Nitrate in Situ: Precursors to Iron Oxide Nuclear Waste Forms. *Dalton Trans.* **2018**, *47*, 10229–10239.

[76] Fleet, M. E. The Structure of Magnetite: Symmetry of Cubic Spinels. *J. Solid State Chem.* **1986**, *62*, 75–82.

[77] Hu, C.; Gao, Z.; Yang, X. Fabrication and Magnetic Properties of Fe_3O_4 Octahedra. *Chem. Phys. Lett.* **2006**, *429*, 513–517.

[78] Lovely, G. R.; Brown, A. P.; Brydson, R.; Kirkland, A. I.; Meyer, R. R.; Chang, L.; Jefferson, D. A.; Falke, M.; Bleloch, A. Observation of Octahedral Cation Coordination on the (111) Surfaces of Iron Oxide Nanoparticles. *Appl. Phys. Lett.* **2006**, *88*, 093124.

[79] Tasker, P. W. The Stability of Ionic Crystal Surfaces. *J. Phys. C: Solid State Phys.* **1979**, *12*, 4977–4984.

[80] CP2K. `http://www.cp2k.org`.

[81] Kühne, T. D. et al. CP2K: An Electronic Structure and Molecular Dynamics Software Package - Quickstep: Efficient and Accurate Electronic Structure Calculations. *J. Chem. Phys.* **2020**, *152*, 194103.

[82] Goedecker, S.; Teter, M.; Hutter, J. Separable Dual-Space Gaussian Pseudopotentials. *Phys. Rev. B* **1996**, *54*, 1703–1710.

[83] Krack, M. Pseudopotentials for H to Kr Optimized for Gradient-corrected Exchange-Correlation Functionals. *Theor. Chem. Acc.* **2005**, *114*, 145–152.

[84] VandeVondele, J.; Hutter, J. Gaussian Basis Sets for Accurate Calculations on Molecular Systems in Gas and Condensed Phases. *J. Chem. Phys.* **2007**, *127*, 114105.

[85] Perdew, J. P.; Burke, K.; Ernzerhof, M. Generalized Gradient Approximation Made Simple. *Phys. Rev. Lett.* **1996**, *77*, 3865–3868.

[86] Perdew, J. P.; Burke, K.; Ernzerhof, M. Generalized Gradient Approximation Made Simple [Phys. Rev. Lett. 77, 3865 (1996)]. *Phys. Rev. Lett.* **1997**, *78*, 1396–1396.

[87] Perdew, J. P.; Ruzsinszky, A.; Csonka, G. I.; Vydrov, O. A.; Scuseria, G. E.; Constantin, L. A.; Zhou, X.; Burke, K. Restoring the Density-Gradient Expansion for Exchange in Solids and Surfaces. *Phys. Rev. Lett.* **2008**, *100*, 136406.

[88] Dudarev, S. L.; Botton, G. A.; Savrasov, S. Y.; Humphreys, C. J.; Sutton, A. P. Electron-Energy-Loss Spectra and the Structural Stability of Nickel Oxide: An LSDA+U Study. *Phys. Rev. B* **1998**, *57*, 1505–1509.

[89] Dorado, B.; Amadon, B.; Freyss, M.; Bertolus, M. DFT+U Calculations of the Ground State and Metastable States of Uranium Dioxide. *Phys. Rev. B* **2009**, *79*, 235125.

[90] Barcaro, G.; Thomas, I. O.; Fortunelli, A. Validation of Density-Functional Versus Density-Functional+U Approaches for Oxide Ultrathin Films. *J. Chem. Phys.* **2010**, *132*, 124703.

[91] Rollmann, G.; Rohrbach, A.; Entel, P.; Hafner, J. First-Principles Calculation of the Structure and Magnetic Phases of Hematite. *Phys. Rev. B* **2004**, *69*, 165107.

[92] Hubbard, J. Electron Correlations in Narrow Energy Bands. *Proc. Roy. Soc. Lond. Math. Phys. Sci.* **1963**, *276*, 238–257.

[93] Liechtenstein, A. I.; Anisimov, V. I.; Zaanen, J. Density-Functional Theory and Strong Interactions: Orbital Ordering in Mott-Hubbard Insulators. *Phys. Rev. B* **1995**, *52*, R5467–R5470.

[94] Kéri, A.; Dähn, R.; Krack, M.; Churakov, S. V. Combined XAFS Spectroscopy and *Ab Initio* Study on the Characterization of Iron Incorporation by Montmorillonite. *Environ. Sci. Technol.* **2017**, *51*, 10585–10594.

[95] Chase, J. M. W. *Nist-Janaf Thermochemical Tables Set*; SPRINGER NATURE, 1998.

[96] Plimpton, S. Fast Parallel Algorithms for Short-range Molecular Dynamics. *J. Comput. Phys.* **1995**, *117*, 1–19.

[97] Berendsen, H. J. C.; Grigera, J. R.; Straatsma, T. P. The Missing Term in Effective Pair Potentials. *J. Phys. Chem.* **1987**, *91*, 6269–6271.

[98] Karalis, K.; Zahn, D.; Prasianakis, N. I.; Niceno, B.; Churakov, S. V. Deciphering the Molecular Mechanism of Water Boiling at Heterogeneous Interfaces. *Sci. Rep.* **2021**, *11*, 19858.

[99] Karalis, K. T.; Dellis, D.; Antipas, G. S. E.; Xenidis, A. Bona-fide Method for the Determination of Short Range Order and Transport Properties in a Ferro-aluminosilicate Slag. *Sci. Rep.* **2016**, *6*, 30216.

[100] Karalis, K.; Ludwig, C.; Niceno, B. Supercritical Water Anomalies in the Vicinity of the Widom Line. *Sci. Rep.* **2019**, *9*, 15731.

[101] Mark, P.; Nilsson, L. Structure and Dynamics of the TIP3P, SPC, and SPC/E Water Models at 298 K. *J. Phys. Chem. A* **2001**, *105*, 9954–9960.

[102] Martyna, G. J.; Klein, M. L.; Tuckerman, M. Nosé–Hoover Chains: The Canonical Ensemble Via Continuous Dynamics. *J. Chem. Phys.* **1992**, *97*, 2635–2643.

[103] Zhang, Z.; Satpathy, S. Electron States, Magnetism, and the Verwey Transition in Magnetite. *Phys. Rev. B* **1991**, *44*, 13319–13331.

[104] Wang, W. et al. Fe t2g Band Dispersion and Spin Polarization in Thin Films of Fe_3O_4(001)/MgO(001): Half-Metallicity of Magnetite Revisited. *Phys. Rev. B* **2013**, *87*, 085118.

[105] Kiejna, A.; Ossowski, T.; Pabisiak, T. Surface Properties of the Clean and Au/Pd Covered Fe_3O_4(111): DFT and DFT+U. *Phys. Rev. B* **2012**, *85*, 125414.

[106] Sharma, S. S. Thermal Expansion of Crystals. *Proc. Indian Acad. Sci. Sect. A* **1950**, *31*, 83–94.

[107] Cornell, R. M.; Schwertmann, U. *The Iron Oxides: Structure, Properties, Reactions, Occurrences, and Uses*; Wiley-VCH: Weinheim, 2003.

[108] Wersin, P.; Johnson, L.; Schwyn, B.; Berner, U.; Curti, E. *Redox Conditions in the Near Field of a Repository for SF/HLW and ILW in Opalinus Clay*; NAGRA tech. report 02-13, 2003.

[109] Fishman, M.; Zhuang, H. L.; Mathew, K.; Dirschka, W.; Hennig, R. G. Accuracy of Exchange-Correlation Functionals and Effect of Solvation on the Surface Energy of Copper. *Phys. Rev. B* **2013**, *87*, 245402.

[110] Tavadze, P.; Boucher, R.; Avendaño-Franco, G.; Kocan, K. X.; Singh, S.; Dovale-Farelo, V.; Ibarra-Hernández, W.; Johnson, M. B.; Mebane, D. S.; Romero, A. H. Exploring DFT+U Parameter Space with a Bayesian Calibration Assisted by Markov Chain Monte Carlo Sampling. *npj Comput. Mater.* **2021**, *7*, 182.

[111] Curti, E.; Wersin, P. *Assessment of Porewater Chemistry in the Bentonite Backfill for the Swiss SF/HLW Repository*; NAGRA tech. report 02-09, 2002.

[112] Johnson, L. H.; Smith, P. A. *The Interaction of Radiolysis Products and Canister Corrosion Products and the Implications for Spent Fuel Dissolution and Radionuclide Transport in a Repository for Spent Fuel*; NAGRA tech. report 00-04, 2000.

[113] Churakov, S. V. Thermoelastic Properties of Solid Phases: C++ Object Oriented Library SolidEOS. *Comput. Geosci.* **2005**, *31*, 786–791.

[114] Lemmon, E. W.; Bell, I. H.; Huber, M. L.; McLinden, M. O. In *Thermophysical Properties of Fluid Systems*; Linstrom, P. J., Mallard, W., Eds.; NIST Chemistry WebBook, NIST Standard Reference Database 69.

[115] Garrels, R. M.; Christ, C. L. *Solutions, Minerals, and Equilibria*, 2nd ed.; Jones and Bartlett Publishers, Inc.: Boston, 1990.

[116] Frost, B. R. *Oxide Minerals*; De Gruyter, 1991; pp 1–10.

[117] Frisch, M. J. et al. Gaussian~16 Revision C.01. 2016; Gaussian Inc. Wallingford CT.

[118] Sun, W.; Kitchaev, D. A.; Kramer, D.; Ceder, G. Non-equilibrium Crystallization Pathways of Manganese Oxides in Aqueous Solution. *Nat. Commun.* **2019**, *10*.

[119] Visual Molecular Dynamics. `https://www.ks.uiuc.edu/Research/vmd/`.

Chapter 3: Investigation of octahedrally shaped magnetite nanoparticles

Computational study on the octahedral surfaces of magnetite nanoparticles and their solvent interaction

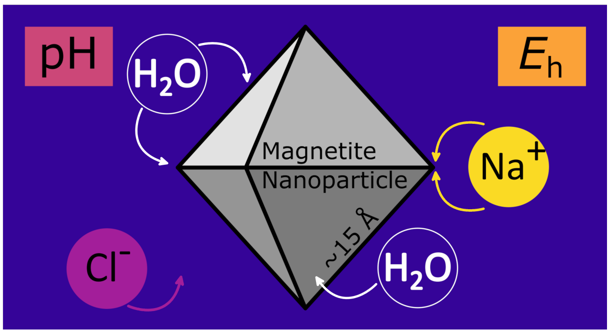

This chapter was published as article in *Environmental Science and Technology*, 2024, 58, 47, 21068–21076 (DOI: 10.1021/acs.est.4c06531), reprinted with permission, copyright 2024 American Chemical Society. The manuscript was written in cooperation with Konstantinos Karalis, Matthias Krack, Andreas C. Scheinost, and Sergey V. Churakov.

Abstract

Magnetite nanoparticles (MNPs) play an important role in geological and environmental systems because of their redox reactivity and their ability to sequester a wide range of metals and metalloids. X-ray absorption spectroscopy conducted at metal and metalloid edges has suggested that the magnetite {111} faces of octahedrally-shaped nanoparticles play a dominant role in the redox and sorption processes of these elements. However, studies directly probing the magnetite surfaces – especially in their fully solvated state – are scarce. Therefore, we investigated the speciation and stability over a wide E_h/pH range of octahedrally shaped MNPs of 2 nm size by means of Kohn-Sham Density Functional Theory with Hubbard correction (DFT+U). By altering the protonation state of the crystals, a redox-sensitive response of the octahedrally coordinated Fe could be achieved. Further, the preferential H distribution could be identified highlighting the difference between edges, vertices and facets of the nanocrystals. Subsequently, the interactions of the MNPs with a solvent of pure water or 0.5 M NaCl solution were studied by classical molecular dynamics (MD) simulations. Finally, a comparison of the corresponding macroscopic magnetite (111) surface with the investigated MNPs was conducted.

3.1 Introduction

Magnetite (Mag) is a common Fe oxide mineral with an inverse spinel structure. Tetrahedral sites are occupied by Fe(III) whereas octahedral sites host an equal amount of Fe(II) and Fe(III) ions. Thanks to the high abundance in natural rocks and the inherent mixed valence state of Fe, magnetite is one of the most important redox active partners in environmentally and geochemically relevant reactions. Depending on the redox conditions, presence of anionic and bacterial species, a delicate equilibrium between several iron containing minerals, e.g., lepidocrocite, hematite, and magnetite is maintained[1,2]. Further, magnetite is known to play an important role in sorption and immobilization of toxic organic compounds[3–5], and heavy metals such as As[6,7] and Se[8,9].

The kinetics of redox reactions or sorption processes are primarily controlled by the reactivity and speciation of the magnetite mineral surface. Several studies investigated different crystallographic facets and their prevalent surface speciation. The (111) facet is of special focus for these, as both natural as well as synthetic magnetite crystals often exhibit an octahedral shape[10]. Although many studies focus on the equilibrium surface reconstruction in vacuum and the subsequent interaction mechanism with sorbate species[11,12], there are only few studies addressing the surface speciation under environmentally relevant conditions such as hydration[13] or the interaction with radionuclides[14–16]. In our previous study[17] on hydrated magnetite (111) surfaces, we investigated different surface terminations with regard to Fe coordination and protonation state. Under various geochemical relevant acidity and redox conditions, we identified the preferential termination to be a structurally complete layer of FeO_6 octahedra over a mixed layer of Fe tetrahedra/Fe octahedra/Fe tetrahedra to represent the macroscopic surface.

However, magnetite is often present as nanoparticles (NPs), e.g., as a product of steel corrosion[18,19]. The effective size and shape of the magnetite nanoparticles (MNPs) depend highly on the reaction or synthesis conditions such as temperature[10,20]. Moreover, crystals of octahedral shape can be preferably achieved by more hydrophilic conditions in coprecipitation[21], higher concentration of oxidizing agent[22,23] or a higher heating rate in hydrothermal experiments[24]. Although an octahedral shape of the crystal is usually based on the (111) surface, the prevalent characteristics of the MNP may differ from the macroscopic crystal. An example is the observed maghemitization of MNPs at their surface under controlled acidic[25,26] and oxidizing conditions[27–29]. However, also some recharging in contact with Fe(II) in solution could be observed[29].

In the present study we specifically focus on the stability and speciation of octahedral MNPs formed by the magnetite (111) surface. While MNPs forming under aqueous conditions seem to have mean diameters of 6 nm to 10 nm or larger as observed by means of TEM, PDF and others[30,31], we investigated here particles of 2 nm in diameter. This size was chosen firstly as a compromise to maintain the computational costs at a reasonable level while keeping magnetite {111} faces still prevalent. Second, MNPs of this size have been observed by Cryo-TEM as the first nucleation products, which then grow into secondary particles by coalescence[32,33]. By comparing these nanoparticle surfaces with the macroscopic surface, we intend to contribute to the understanding of the environmental behavior of both species.

3.2 Materials and Methods

3.2.1 First principles calculations

The atomistic simulations were performed following the methodology developed and validated in our previous study[17]. In brief, the spin-polarized crystal structure calculations were performed based on Density Functional Theory (DFT) applying the PBE exchange-correlation functional[34,35] using the parametrization tailored for solids and liquids (PBEsol)[36]. The Gaussian and Plane Wave (GPW) method implemented in the QUICKSTEP[37] module of CP2K[38] (version 2023.1) applying 3D periodic boundary conditions was used. Norm-conserving scalar-relativistic pseudo-potentials (GTH[39,40]) were applied to avoid an explicit consideration of the core electrons. MOLOPT basis sets (DZVP)[41] were used to describe the wave functions of the valence electrons. To expand the electronic charge density, an auxiliary basis set of plane waves with a density cutoff of 600 Ry was employed. The target accuracy (EPS_SCF) of the self-consistent field (SCF) cycles was 3.0E-7 using the orbital transformation method[42] as minimizer for the wave function optimization. Additional parameters regarding the accuracy of the structure optimization can be found in Supporting Information (SI). To improve the description of the 3d-electronic states of iron, the DFT+U method[43,44] was employed with an effective Hubbard U parameter of 1.9 eV as validated in our previous study[17].

3.2.2 Modeling setup

Magnetite has an inverse spinel structure with Fe(III) in tetrahedral coordination (Fe_{tet}) and Fe(II)/Fe(III) with a ratio of 1:1 in octahedral coordination (Fe_{oct}). Our previous study on the common magnetite (111) surface over wide environmentally relevant conditions resulted in the preferred termination with O(H)-coordinated Fe_{oct} at the surface[17], which is well in line with the spectroscopically identified tridentate sorption complexes on magnetite and maghemite nanoparticles of, e.g., Pu, and As[14,45–48]. In agreement with experimental observations by TEM[10,22,47,48], the MNPs were assumed to have octahedral shape (Figure 3.1c)). Our system setup results in a distance of opposite vertices of approximately 2 nm and includes 52 octahedrally and 10 tetrahedrally coordinated Fe with 140 O coordinating the Fe, respectively. Each simulated MNP crystal was placed in a non-cubic box of 47 Å × 47 Å × 44 Å allowing for at least 30 Å of vacuum between periodic images[17] with an orientation of the crystal in a way that two opposite facets are perpendicular to the z-direction. Hence, possible interactions between these images become negligible and the computational effort can be minimized.

We tested different system compositions regarding the protonation state of the MNP surface. In combination with the imposed charge neutrality, a change in number of surface-H resulted in a different Fe(II)/Fe(III) ratio in the octahedrally coordinated Fe. In our previous study[17], an averaged Fe_{oct} oxidation state between +2.5 as in bulk magnetite and +3.0 was predicted. Hence, we simulated five systems in a similar range of oxidation states. In this way, the charge of Fe_{oct} at the surface ('out') as well as the four Fe_{oct} in the center of the MNPs ('in') was influenced. Subsequently, a Mulliken charge analysis was performed to track where oxidation would occur first.

3.2.3 Surface stoichiometry and protonation schema

The octahedrally shaped MNPs investigated in this study exhibit two types of facets that are referred to as A and B (Figure 3.1). Facet A has 9 FeO_6 octahedra at the surface and one central cavity (with a tetrahedrally coordinated Fe(III) underneath), facet B consists of 15 FeO_6 octahedra with three cavities. Each triangular cavity is formed by six FeO_6 octahedra with three O at its corners and 3 bridging O. The three cavities on the B side are connected by a central O atom.

Each vertex of the octahedral NP is built by two FeO_6 octahedra resulting in two corners being one O atom each. These edge-connected octahedra represent the (001) termination as predicted for octahedral nanoparticles by Meng et al.[49]. Excluding the corner atoms, the edges of the octahedral NP are built by three O atoms (Figure 3.1c).

In the following analysis, surface oxygen sites available for protonation are denoted as C (corner), E (edge), A (bridging on A side), B (bridging on B side) and T (triple, connection between the three cavities on side B). Additional H at the corners of the cavities are not considered as separate type as these are either equivalent to T or E. For each H distribution, the H were initially assigned at 1 Å distance from the respective O. If two H atoms are assigned to the same O, their orientation resembled the geometry of a water molecule.

Several combinations of protonation were tested and the protonation energy for each system was obtained in two steps. First, the setup yielding lowest self-consistent field (SCF) energy (E_{SCF}) was identified allowing the H to fully relax while the rest of the crystal was held frozen (Table S3.1 in SI) keeping the computational expenses to a reasonable amount. In the second step, all atomic position were allowed to fully relax and their respective energies are reported in Table S3.4 in SI. The optimized structures were further used as input structures for the molecular dynamics (MD) simulations.

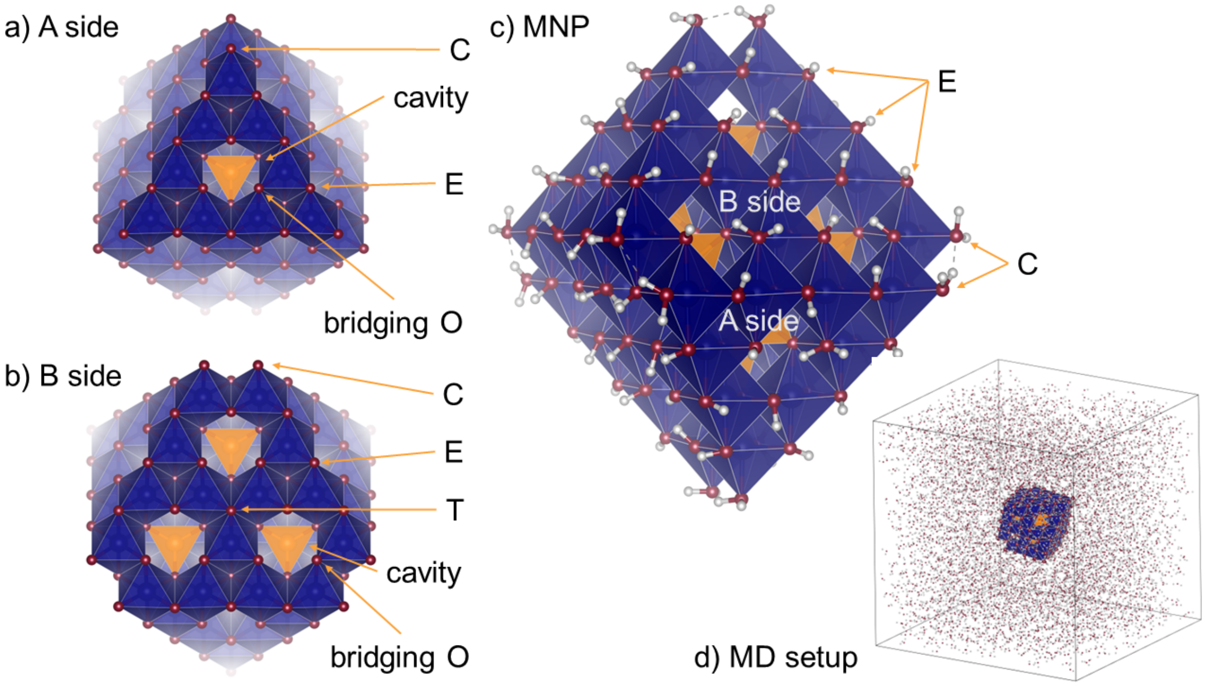

FIGURE 3.1: Schematic depiction of the MNP as obtained from bulk-like magnetite showing the possible protonation positions. a) perpendicular view on the A side without H, b) on the B side without H. c) out2.5_in2.5 as example for hydrogenated MNP, d) impression of the simulation box for the classical MD setup including 4000 water molecules. Octahedrally coordinated Fe is depicted in blue, tetrahedrally coordinated Fe in orange, O in red, H in gray. Atomic sizes are adapted for visualization.

3.2.4 Molecular dynamics (MD) simulations

Classical MD simulations were performed using a similar set of parameters validated in our previous study[17]. The LAMMPS code (version 2020)[50] was used to investigate the interaction of the previously determined preferential nanoparticles with a solvent. The initial setup was obtained using the Packmol software[51] by randomly surrounding the MNP with 4000 water molecules (pure water setup) or also additional 18 Na^+ and 18 Cl^- ions (electrolyte setup) corresponding to 0.5 M. The MD simulations were performed in a cubic supercell with a lattice constant of 49.27 Å (Figure 3.1d) applying 3D periodic boundary conditions. The non-polarizable SPC/E water model[52] was used to model the water molecules. The potential parameters developed by Smith and Dang[53] and Konuk et al.[54] were used to model the NaCl and magnetite ions, respectively. Increased oxidation states of the octahedrally coordinated Fe starting from the surface of the MNPs required a corresponding adaptation of the parameters.

First, each system was equilibrated for 2 ns in the NPT ensemble. The rigid body approach[55] was used to fix the geometry of the SPC/E water molecules. All Fe atoms and O sites of magnetite in the center of the MNP were kept frozen at the relative position obtained with *ab initio* geometry optimization. In contrast, the hydroxyl groups at the nanoparticle surface were allowed to move. An integration time step of 1 fs was used to ensure energy conservation. Second, in the equilibration, the temperature was controlled using a Nosé-Hoover thermostat with a relaxation time of 0.1 ps, while the pressure was controlled using an anisotropic Parrinello-Rahman barostat with a relaxation time of 1 ps. Finally, the production run was performed in the NVT ensemble using a Nosé-Hoover thermostat with a relaxation time of 0.1 ps, spanning a total duration of 2 ns. The results of the classical MD simulations were used to evaluate the solvent-surface interaction to the surface energy.

3.2.5 Stability under various conditions

Following the strategy developed in our previous study on magnetite {111} surfaces[17], we conducted a stability and speciation analysis of MNPs with respect to E_h and pH. For each system, the specific surface energy γ was calculated according to Equation 3.1 for the H configuration resulting in the lowest total energy of the system. In accordance with our previous study[17], the DFT calculations reflect the state of each system at $E_\mathrm{h} = 0\,\mathrm{eV}$ and $\mathrm{pH} = 0$. The surface area A was determined to be $712.0882\,\mathrm{Å}^2$ for each NP, its determination can be found in SI. The number and energy of the magnetite volume material, N_Mag and E_Mag, the number of O, N_O, exceeding the Fe:O = 3:4 ratio, as well as the water potential, $\mu_{\mathrm{H_2O}}$, are the same for each nanoparticle system. Contrary, the Gibbs free energy of formation G_f as well as the number of H, N_H, influencing the redox state of the octahedrally coordinated Fe are system specific. Moreover, the interaction energy of the NP with solvent (water or 0.5 M NaCl), E_int, can be taken into account as shown in Equation 3.2. The respective values can be found in SI.

$$\begin{aligned}\gamma = \frac{1}{A}\big(&G_\mathrm{f} - N_\mathrm{Mag}\,E_\mathrm{Mag} - N_\mathrm{O}\,\mu_{\mathrm{H_2O}} - E_\mathrm{h}\big(2\,N_\mathrm{O} - N_\mathrm{H}\big)\\ &- RT\big(2\,N_\mathrm{O} - N_\mathrm{H}\big)\,\ln(10)\,\mathrm{pH}\big)\end{aligned} \tag{3.1}$$

$$\gamma' = \gamma + E_\mathrm{int} \tag{3.2}$$

3.3 Results and Discussion

3.3.1 Oxidation state of octahedrally coordinated Fe

The stable protonation state of the surface and the variable oxidation state of the surface cations are sensitive to the E_h/pH condition. The MNP systems investigated in this study are subject to charge neutrality conditions, thus, deprotonation of the surface leads to the oxidation of Fe from magnetite-like mixed oxidation state +2.5 to fully oxidized octahedral layers with Fe in +3.0 oxidation state. This change of oxidation state can be deduced from the Mulliken charge analysis (Table 3.1) and can be distinguished for the inner/core and outer/close-to-surface octahedrally coordinated Fe. Based on the atomic configuration of $4s^2\,3d^6$ for Fe(0), the electronic states $4s^0\ 3d^6$ and $4s^0\ 3d^5$ are assumed for Fe(II) and Fe(III), respectively. The distribution of the electrons in the individual d-orbitals is considered in a high-spin configuration, i.e., for Fe(III) all 3d orbitals are half-occupied with all electron spins aligned in the same direction. For the minority spin, this implies a spin orbital occupation zero. Similarly, for idealized Fe(II), the additional electron would be paired to one of the half-filled orbitals and the minority spin would count 1. However, as can be seen from Table 3.1, the minority spin ranges from 0 to 1 and often represents a mix between Fe(III) and Fe(II). Hence, we attributed the labels for charge with the values of 2.5, 2.75 and 3.0 for clarity.

TABLE 3.1: Number of H (N_H), lowest total energy (E_{SCF}) and mean minority spin obtained from Mulliken charge analysis of octahedrally coordinated Fe cations in the NP systems. The latter are given for those located at the core of the NP (in) or at the surface. These in turn can be further distinguished by their location, being close to the T-point of the B sides (triple), at the edges or the corners of the whole MNP, respectively.

system	N_H	E_{SCF} [Ha]	Fe_{in}	Fe_{triple}	Fe_{edge}	Fe_{corner}
out2.5_in2.5	120	−9958.4426	0.5918	0.3897	0.4191	0.5363
out2.75_in2.5	108	−9951.4990	0.3160	0.0976	0.2547	0.2819
out2.75_in2.75	107	−9950.8881	0.2910	0.0208	0.1939	0.3728
out3.0_in2.75	96	−9943.4755	0.1945	0.0000	0.0000	0.0000
out3.0_in3.0	95	−9942.8121	0.0000	0.0000	0.0000	0.0000

Our results show that oxidation occurs from the surface towards the center of the crystal as surface-near FeO_6 octahedra can be oxidized more easily adapting to changing surrounding conditions. Both characteristics, the strong coupling of the oxidation state of octahedrally coordinated Fe to the protonation state of the system as well as the local order of successive oxidation, are consistent with our previous study on the magnetite (111) surface[17]. Hence, the systems will be referred to as, e.g., out3.0_in2.75 for an averaged system with charge of 3.0 of the outer FeO_6 octahedra and 2.75 for the inner, etc.

Moreover, there is a difference of assumed oxidation state between various octahedrally coordinated Fe ions located close to the surface of the NP. As can be observed in Table 3.1, and in line with previous considerations, the minority spin value mostly decreases with lower number of hydrogen atoms. Among the systems with an assumed outer octahedral Fe charge below 3, the most oxidized Fe are located close to the center of the B facets (T), while the edge sites are slightly less oxidized, and the corner Fe are least oxidized. This can be attributed to the H distribution, as the protonation number increases from the center of the facets towards the vertices of the MNP (Table S3.1 in SI).

Furthermore, the electronic band gaps of the MNP systems can be obtained (Table S3.2 in SI). In the analysis, we focus on the commonly smaller band gap reflecting the spin down electronic states. Comparing the NP with the expected intermediate oxidation state of +2.5 to bulk magnetite investigated with the same methods[17], a reduction of the band gap can be observed. This can be attributed to a perturbation of the continuous system due to the existence of surfaces and, by extension, edges and vertices. Moreover, with an increase of the oxidation state of octahedrally coordinated Fe in the NP systems, a widening of the electronic band gap can be observed. This signifies a marked change in the conductive properties, transitioning towards a rather semi-conductive material.

3.3.2 Surface speciation and protonation state of MNPs

For a given protonation state, several geometrical distributions of hydrogen atoms were tested using the bond valence sum as the guiding principle for initial assignment of protons to oxygen sites. The exact H distributions for each system specifying A, B, C, E, and T, are listed in Table S3.1 in SI. The following paragraphs focus on the overall trends regarding total energy (SCF energy).

The initial analysis of an energetically favorable proton distribution in the system was performed for MNPs with a bulk-like oxidation state of the iron ions (out2.5_in2.5). In total, thirteen systems of symmetric and symmetry-broken H distributions were analyzed and resulted in significant energy differences (Table S3.1 in SI). From the comparison of the energies, we narrowed down the range of relevant options for higher oxidation, accordingly. These tested systems appear reasonable and preferable among possible options, as the resulting SCF energies became closer. This is especially evident for the system kinds of higher oxidation, i.e., in systems of out2.75_in2.75 and above. Hence, we are confident to have found a reasonable H distribution for each kind, the according total energies are given in Table 3.1.

The general trend for each system of oxidation state is a lower affinity of protons to the edges (E) of the MNP, compared to a higher proton affinity to the corners (C). This is plausible, as the edge-O are bridging two FeO_6 octahedra each and are, hence, twice coordinated. On the other hand, each corner O is coordinated with only one Fe atom, resulting in a state of high underbonding. A similar explanation applies to the connecting oxygen atoms of the three cavities on the B sides, where there is a preference of little to no protonation at these already threefold coordinated connecting O.

Moreover, the number of H attached to the edge- and corner-O has the highest influence on the energy of the system reflecting the large influence of these specific sites for interactions with the surroundings. In fact, an over-coordination of the edges and corners results in an incomplete convergence of the simulation and/or a complete detachment of the initially sorbed H. This is further enhanced by the surrounding medium (vacuum), whereby the free-to-move H have to compensate for the missing solvent. This is especially true for OH_3 groups at the corners and OH_2 groups (water) at the edges.

By comparing the A and B sides, there is a tendency to have almost equal affinity for sorption on the bridging O at the cavities reflecting the similarity between the sides. The slight preference of protonation on the B side could be a result of the number of cavities. I.e., it is preferred to have the bridging O at the sole cavity on the A side not covered by at least one H compared to missing H at the three equal cavities at the B sides.

3.3.3 Dependence on redox and hydrogen potential

Figure 3.2 shows the specific surface energy of the NP according to Equation 3.1 as function of pH (upper figure) and E_h (lower figure). As can be derived from the equation, there is a linear dependency of the specific surface energy on both E_h and pH; both depend on the difference between twice the number of oxygen and the number of hydrogen. This difference increases towards higher Fe oxidation state as there are fewer H in the system resulting in a shift from a positive slope for the bulk-like oxidation towards increasingly negative slope of the linear function (Figure 3.2). Further, a decrease of surface energy with higher temperature can be assumed based on Equation 3.1. All of these trends are in accordance to our previous study on bulk magnetite (111) surfaces[17] where a similar approach was applied.

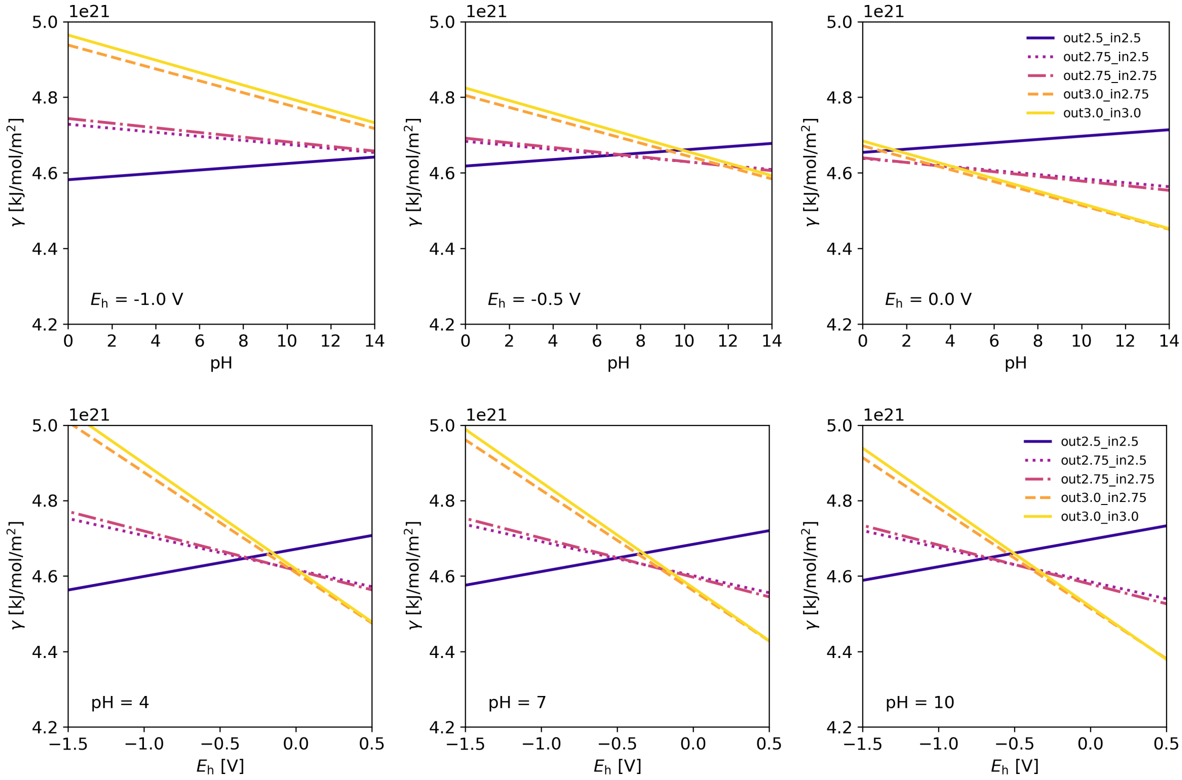

FIGURE 3.2: Exemplary results for the specific surface energy γ according to Equation 3.1 as function of pH (constant E_h, upper row) and as function of E_h (constant pH, lower row) at $T = 298\,\mathrm{K}$. 'out' and 'in' refer to the approximated oxidation state of the octahedrally coordinated Fe at the surface or at the core of the MNP, respectively.

A comparison of the obtained absolute value of specific surface energy between the MNP and bulk (111) magnetite systems is difficult or even not possible. First, both systems are not in equilibrium with a solvent, as the SCF simulations for both systems were conducted in vacuum. Second, the stoichiometry in terms of both the absolute number of atoms as well as the ratio of magnetite to water is different in both systems. Compared to the (111) magnetite slabs[17], the MNP contains more water. In contrast, if a MNP was to be designed with the same stoichiometry as the (111) surface slabs, there would be Fe exposed at the surface, which is unlikely under environmentally relevant/non-vacuum conditions. Third, the vibrational free energy as parameter for G_f in Equation 3.1 reflecting the entropy of each system is different and does not seem interchangeable for surface and MNP (SI for detailed analysis). This further corroborates the limited comparability of absolute specific surface energies.

The stability diagram revealing the MNP system with lowest surface energy according to Equation 3.1 is shown in Figure 3.3. As can be observed, the pattern is similar to those of our previous study[17], as towards higher E_h and pH, systems with higher Fe oxidation state are favored. The dotted box in Figure 3.3 refers to the expected long-term environmental conditions in a deep geological repository for high-level radioactive waste[56]. This result suggests a preference for an oxidation state of the octahedrally coordinated Fe higher than in ideal bulk magnetite. This observation based on atomistic modeling is in line with the surface maghemitization observed experimentally[26,57–60].

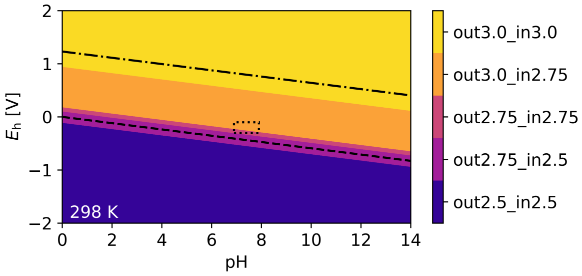

FIGURE 3.3: Surface stability plot of magnetite nanoparticle systems at 298 K as function of E_h and pH according to Equation 3.1. In the Pourbaix diagram, the dotted black box indicates the expected long-term repository conditions in the range of E_h −0.3 V to −0.1 V and pH 6.9 to 7.9[56], the dashed line the lower water stability (production of H_2), the dash-dotted line the upper water stability (decomposition to O_2). 'out' and 'in' refer to the approximated oxidation state of the octahedrally coordinated Fe at the surface or at the center of the MNP, respectively.

3.3.4 Interaction of the MNP with a solvent

To study the effect of a solvent, classical MD was used to obtain the interaction energy E_{int} that is reported in Table S3.4 in SI. As can be observed, the interaction energy decreases – absolute negative value increases – with increased Fe_{oct} oxidation state. This behavior can be explained by the increased electrostatic attraction if the Fe charge in the MNP is higher. Further, as the MNP surface is less protonated for higher oxidation states, there is less steric hindrance facilitating interaction. Within the same oxidation state, E_{int} decreases by 5 % to 10 % if electrolytes are present. In this case, the water molecules screen the additional charge which reduces their screening capabilities for magnetite. Hence, the water molecules interact less with the MNP itself.

If the interaction energy is considered in Equation 3.2, plots similar to Figure 3.2 could be obtained in which the specific surface energy is reduced. Although this is similar to the behavior of the (111) magnetite surface, the interaction energy of the MNP is almost one order of magnitude larger compared to the surface slabs[17]. This effect can be attributed to the existence of edges and corners in the MNP systems allowing the water molecules to completely surround the magnetite center. Moreover, the interaction energy leads to a very clear stability diagram (Figure S3.2 in SI) revealing a broad stability field of the system with highest oxidation over the considered range of pH 0 to 14 and E_h $-2\,\mathrm{V}$ to $2\,\mathrm{V}$. Although a similar behavior was observed for the magnetite surface slabs, it is not to be excluded, however, that the actual value of E_int in both cases might be slightly different as in the classical MD applied in both studies the magnetite crystal portion of the system was held frozen. Nonetheless, it can be assumed that significant structural changes in terms of a reconstruction would have been noticed in the vacuum setup already.

During the 2 ns long classical MD simulations, no exchange of surface-OH_2 groups with solvent water was observed suggesting strong affinity of surface water towards the MNP. However, another interesting phenomenon can be observed: The cavities at the MNP-surface entrap and stabilize water molecules inside the cavities (Figure S3.3 in SI). This corroborates the strong interaction of magnetite with water.

Furthermore, the radial pair distribution function (RDF, $g(r)$, Figure S3.4 in SI) shows the water distribution as a function of distance, suggesting a similar interaction of surface-O with water-H as within pure water in terms of radius r of the prevalent water coordination shells. However, the peaks of the second shell and beyond appear broader and less pronounced than those of pure water. Still, this may be resulting from the difficulty that with surface-O, especially those at the corners of the MNP, there is an overlap of the coordination shells of surface-O in close proximity, e.g., one neighbor's first coordination shell is the second of another neighbor's, and this effect intensifies for higher shells.

When comparing the MNP systems with different Fe oxidation states, an increase of the RDF can be observed with higher oxidation being a similar effect as discussed for E_int (Figure S3.5 in SI). Equally, a decrease of the RDF in the electrolyte setting can be observed. This effect can also be observed by displaying the RDF of Na and Cl around the surface-O. As shown in Figure S3.6 in SI, Na is much closer to the surface than Cl indicative of a net negative charge of the MNP surface. Furthermore, Na tends to localize close to the corners of the MNP (Figure S3.7 in SI), and its strong electrostatic interaction with the surface-O lead to a distortion of the FeO_6 octahedra located at the corners of the MNP. In the long-term, these FeO_6 octahedra may be weakened and the dissolution of the crystal starting from these positions might be facilitated.

In contrast, Cl is much further away from the surface and – if at all – tends to assume a position above the second water coordination shell in the position above the center of the B sides (T). As this is, however, at a much higher distance from the surface, there is more fluctuation and a higher sensitivity to changes leading to a more diffuse pattern in the RDF (Figure S3.6 in SI). Furthermore, the initial guess as random distribution of particles for the MD simulation has a higher impact. In fact, only if in the NPT equilibration a Cl ion has reached this position, it tends to localize for the 2 ns of simulation in the NVT ensemble.

3.3.5 Implications of this study

Strengths and limitations of the analysis method

The applied analysis method used in the previous[17] as well as in this current study is straightforward. Environmentally expected subsystems of magnetite – as surface slab or NP – are tested and possible options narrowed down based on DFT+U simulations. In order to keep computational costs to a minimum, the solvent interaction is investigated based on classical MD only for the selected systems.

The equations used to determine the preferable system are based on thermodynamic considerations. There are certain challenges that can influence the result: First, the analyzed systems are assumed to represent the actual options, i.e., an idealized octahedral MNP. Second, there has to be a separation of the system characteristics regarding volume crystal and surface. This raises the question whether also NP specific characteristics need to be considered and, if yes, which ones and how. Third, the surface area may be difficult to determine and, hence, absolute values of the specific surface energy may have a limited comparability.

Finally, we use the vibrational free energy as a proxy for the entropy of the system (details in SI). As we observed, this is specific whether it is a MNP or the magnetite (111) surface, so there is only limited transferability. However, it can be assumed that within one system there is a linear dependence of the vibrational free energy on a certain parameter, in the presented cases on the number of hydrogen present in the system (Figure S3.1 in SI). Hence, significant computational resources can be saved with this approach.

In natural aqueous environments or given laboratory conditions, the protonation of the surface depends on solution chemistry and pH influencing the surface charge. The latter would be screened by a diffuse double layer, whose structural properties and thermodynamics depend on the solution chemistry. The calculation of the surface energies based on an *ab initio* approach can be performed most accurately for the charge neutral surface. Therefore, the system setup, for which the surface energies are calculated in the *ab initio* geometry optimizations, corresponds to the surface state at point of zero charge. It should be further noted that simulations are also performed for pure water and the effect of solution chemistry is not explicitly addressed in the simulation setup. Accordingly, the relative stability of the surface energies as function of pH are evaluated using the thermodynamic approach described in Equation 3.1 for the charge neutral surface speciation. It must be emphasized that corresponding calculations do not consider the potential changes in the thermodynamic activity of the surface sites due to the protonation/deprotonation of the surface groups and/or interaction with ions. These processes could be described either by thermodynamic sorption modeling[61] or grand canonical simulations of electrolytes[62], but go beyond the scope of this study.

Comparison of investigated magnetite systems

Based on our previous study on the macroscopic magnetite (111) surface[17], we built octahedral MNPs with the expected termination of FeO_6 octahedra at the particle surface. The inherent structural difference are the edges and corners of the MNP presenting more and newly available protonation sites. The protonation schemes applied as initial guess in both systems followed the bond valence sum. Consequently, the edges and corners have the highest affinity for protonation as they have the highest influence on the system energy.

Furthermore, the corners are important for the interaction with ions in close proximity. It can be assumed that there is a high relevance especially for sorption of cations, as they seem to interact primarily with the vertices of the MNP. Moreover, the edges and vertices offer different sorption sites.

The overall affinity of OH-groups on the most stable oxidized magnetite (111) surface (out3.0) and the oxidized MNP (out3.0_in3.0) to donate to and accept hydrogen bonds is similar to the one of pure water and can be differentiated to surface-O to water-H and surface-H to water-O interaction. It can be deduced from similar position and the shape of the peaks of the radial probability density function (RPDF) in the range of 1.5 Å to 2.4 Å (Figure S3.8 and Figure S3.9 in SI). By contrast to the conventional radial distribution function (RDF), the RDPF used for the analysis is omitting a normalization factor describing a homogeneous radial density. In the surface analysis, RPDF is preferred over RDF as the radial symmetry is broken near the mineral-fluid interface.

The detailed analysis of the surface OH-groups reveals a conformation dependent affinity of the surface group donating or accepting hydrogen bonds which is largely controlled by the structure and speciation of the system's surface. For the infinite (111) surface, the interaction of surface-H surrounded by water-O shows almost the same first water coordination shell as bulk water (Figure S3.8 in SI). In contrast to the same magnetite system, the surface-O do not appear to accept hydrogen bonds from water (Figure S3.9 in SI). This can be attributed to the dominant alignment of the surface-OH-groups being normal to the surface, where surface-H are shielding the surface-O. Contrasting, the structural diversity of the MNP is richer due to additional interaction and symmetry at the edges and corners of the nanoparticle. As the protonation pattern of the out3.0_in3.0 differs from the out3.0-surface, the newly present structural features – the edges and corners of the MNP — are focused on. As can be seen from the RPDF, the MNP-O interact slightly more strongly with the water-H resulting in a shorter distance (Figure S3.9 in SI). This also influences the MNP-H in their interaction with the water-O leading to a larger distance and lower coordination number in the first water coordination shell (Figure S3.8 in SI).

Geochemical implications

This study compares magnetite nanoparticles of octahedral shape and with different Fe oxidation states. The presence of octahedrally coordinated Fe in mixed oxidation state allows for an effective reduction of contaminants, often leading to an immobilization[8,9,14–16]. The Fe(II) to Fe(III) ratio highly influences the kinetics of the reduction, and more Fe(II) was shown to both increase the amount of reduced sorbed species[63] as well as to increase the speed of the reaction[3,64]. The ratio of ferrous to ferric iron was also shown to be adjustable, e.g. by substituting with Ti(IV) for Fe(III) in octahedral coordination leading to an increased ratio[65].

Moreover, the ratio can also influence the preference if rather sorption (higher ratio) or incorporation (lower ratio) of contaminants occur[66]. The important characteristics of the Fe(II) to Fe(III) ratio was shown to be not only relevant in magnetite, but also in other systems bearing mixed Fe such as smectites[64]. Although the results of our study suggest a higher oxidation state of the octahedrally coordinated Fe – especially of those close to the surface – which would lead to a confinement of reductive capabilities, we showed that these Fe react sensitively to environmental conditions.

The reductive capabilities of MNPs were experimentally proven to depend on the salinity and ionic strength of the aqueous medium. Urbánová et al.[67] showed that with increasing amount of NaCl the reduction of Se by MNPs decreased. In agreement with our results this behavior can be attributed to the attraction of Na ions to the MNP surface and, hence, a competitive behavior towards other metal ions.

In natural systems such as the sub-surface, the process of maghemitization leads to a degradation and decomposition of magnetite thereby changing the structural, chemical and electronic properties. Concerning the modeling applied in the present study, it would require detailed knowledge about the location of vacancies near the NP surface; this goes beyond the scope of our study. Although we did not simulate maghemitization, it can be imagined that it can occur as next step after the complete oxidation of the octahedrally coordinated Fe as predicted in our study. Accordingly, the dissolution of the distorted FeO_6 octahedra located at the corner of the NP may lead to a reshaping of the NP and might enable a possible creation of vacancies in the structure, too.

Another interesting aspect is the size of the NPs and – based on the surface energy – the respective stability. For many metallic NPs, a decrease of the surface energy with increased size was observed[68,69]. Subsequently, larger NPs would be favored over smaller ones. In fact, Li et al.[70] predicted the stability of MNPs with a size larger than 2 nm in the region of pH 7 to 9 and E_h -0.5 V to -0.3 V and a prevalence of MNPs over NPs of other Fe minerals in this range. On the other hand, Yin et al.[71] experimentally showed an increase in reactivity with an increased surface area of Fe minerals including magnetite in order to degrade chlorinated solvents. This corresponds to smaller particles, hence, for the application of contaminant degradation or sorption, e.g., of heavy metal ions[8,30,45] or radionuclide ions[14–16], MNPs of smaller particle size could be preferred.

3.4 Acknowledgments

The authors acknowledge the funding from the German Federal Ministry of Education and Research (BMBF, KRIMI project - 02NUK056C), access to Swiss National Supercomputing Centre (CSCS, project number s1179) and access to the HPC cluster (UBELIX) at the University of Bern. Further, the authors thank the editor and four anonymous reviewers for their valuable comments in careful consideration of the manuscript.

3.5 Supporting Information

3.5.1 Magnetite nanoparticles (MNPs) in vacuum

H distribution

Table S3.1 lists all tested systems with different H distributions sorted from highest to lowest self-consistent field energy (E_{SCF}) as obtained from the *ab initio* simulations in CP2K. Denoted are the numbers of H attached to the O bridging the cavities at sides A or B of the NP, the connection point of three cavities on side B (T), as well as the H attached to the corners (C), or the edges (E), respectively. For example, "A 1" means that on each of the A sides, one of the three bridging O has one H attached. It is to be noted, that the value of "B" denotes the number of H at the bridging O on each of the three cavities. I.e., "B 2" means that on each of the three cavities on the B sides, two of the bridging O form an OH group.

Further, in some cases H had to be distributed to additional positions leading to slightly asymmetric systems. These structures are denoted in the simplest way if possible: If the number is followed by a letter in the second position, it reflects that some H had to be added (p - plus) or removed (m - minus) to/from all of equivalent sides. E.g., "A 3p1" means that to the three H at each cavity on side A another H has been added; this results in one OH_2 group at each A side. Further, "B 1m1" means that two of the cavities on each B side have 1 H, the third cavity has no H.

If there is also a respective letter in the fourth position, this reflects changes that had to be made to achieve the exact number of H for the intended Fe oxidation. This leads to completely symmetry-broken systems, e.g., "A 2p0p1" means that to the 2 H at the A cavity there was another H added but only to one A side of the NP. In this case, on this specific A side, all bridging O have one H attached whereas on the other three A sides, only two O form OH groups. A respective approach is used for the B sides, too.

TABLE S3.1: Total system energy as obtained from self-consistent field approach (E_{SCF}) for the different H distributions of each NP oxidation state system. † denotes systems that did not converge, ⋆ denotes the system with lowest energy. For ease of comparison of the system out2.5_in2.5 regarding the best positioning of H, fully symmetric systems regarding the three-fold axis perpendicular to each facet are labeled with ∼; all other setups as well as the systems with higher assumed Fe charges can be considered as symmetry-broken.

system	A	B	C	E	T	E_{SCF} [Ha]
out2.5_in2.5 ∼	3	3	3	1	0	†
	1	1m1	3	2	0	†
	0	1	3	2	0	†
	1	1p2	2	2	0	-9956.5885
∼	0	3	1	2	0	-9956.5925
	2	2p1	1	2	0	-9956.7284
	3	2	1	2	0	-9956.8428
	2	1p1	2	2	0	-9957.1861

Continuation of Table S3.1

system	A	B	C	E	T	E_{SCF} [Ha]
∼	3	3	0	2	0	-9957.9016
	3p2	3p3	1	1	1	-9958.0641
	3p1	3p4	1	1	1	-9958.1363
	3	3p2	2	1	1	-9958.3944
⋆	3p1	3p1	2	1	1	-9958.4426
out2.75_in2.5	0	1	2	2	0	†
	1	1p2	1	2	0	-9949.1744
	3p2	3	1	1	2	-9951.1884
	3	3p2	1	1	1	-9951.2483
	3p1	3p1	1	1	1	-9951.2809
⋆	3	3	2	1	0	-9951.4990
out2.75_in2.75	3p1p2	3	1	1	1	-9950.6437
	3	3p1p3	1	1	1	-9950.6719
	3p1m1	3p1	1	1	1	-9950.6889
⋆	3p0m1	3	2	1	0	-9950.8881
out3.0_in2.75	3p0m1	2	2	1	0	-9943.1943
	2	2p0p3	2	1	0	-9943.2290
	3	3p0m1	1	1	0	-9943.4746
⋆	3p0m1	3	1	1	0	-9943.4755
out3.0_in3.0	2p0p1	2p0p1	2	1	0	-9942.5301
	2	2p0p2	2	1	0	-9942.5503
	3	3p0m2	1	1	0	-9942.7920
⋆	2p0p2	3	1	1	0	-9942.8121

Electronic band gap

TABLE S3.2: Electronic band gaps E_g of the different NP systems and, for comparison, of bulk magnetite as determined in the previous study[17]. α and β refer to spin up and spin down, respectively.

system	$E_g(\alpha)$ [eV]	$E_g(\beta)$ [eV]
Mag[17]	1.5490	0.1720
out2.5_in2.5	1.6901	0.0871
out2.75_in2.5	1.7102	0.0766
out2.75_in2.75	1.3707	0.0654
out3.0_in2.75	1.1704	0.2046
out3.0_in3.0	1.1935	1.2336

Surface area of MNPs

The surface area is used in Equation 3.1 as system specific normalization parameter. However, the estimation of its value of the MNPs used in this study is challenging due to several reasons. The following discusses several solutions to this question. Note, that assumption taken is that the surface is located at the level of the O the furthest away from the center of the MNP. If Fe were used as reference points, the estimated values would be smaller. Contrary, if the surface would be approximated by H, its area would be larger.

Therefore, the presented options are dependent on the number of included FeO_6 octahedra. As these smaller octahedral units have equal amount of edges of length $a' = 2.8307\,\text{Å}$ and $a'' = 2.9624\,\text{Å}$, we use the averaged $a = 2.8966\,\text{Å}$ as reasonable proxy. Moreover, a plane surface is approximated and the cavities are neglected.

As the MNPs have octahedral shape, a common approach is to estimate the surface area based on an ideal octahedron. A valid estimation would be to base the edge length of the ideal octahedron on the averaged number of FeO_6 octahedra present on the A and B sides. On the respective edges, the A sides have four FeO_6 octahedra, while the B sides would have six if the two corners are completed to one, Figure 3.1. Hence, the average number of FeO_6 octahedra is five resulting in an approximated length of the idealized NP edge of $a''' = 14.4826\,\text{Å}$.

In general, the range of acceptable values for octahedral particles can be achieved then by approximation of spheres. Possible options in this regard may include the midsphere, spanning the edges of the octahedron, and the circumscribed sphere, where the whole octahedral MNP is enclosed in a sphere. The radii can be calculated as $r' = a'''/2$ and $r'' = a'''/\sqrt(2)$, respectively, resulting in the corresponding surface areas of $A' = 658.9720\,\text{Å}^2$ and $A'' = 1317.9439\,\text{Å}^2$.

More specific would be to estimate directly on the shape of an idealized octahedron. As the surface area of each of the eight facets can be calculated by $\sqrt(3)/4 \times a'''^2$, the corresponding surface area of $A''' = 726.6206\,\text{Å}^2$ would result.

The last refinement presented here is to take into account the individual shapes and sizes of the A and B sides based on the number of FeO_6 octahedra. The area of each A side can be estimated as $A_A = \sqrt(3)/4 \times (a''' \times 4)^2 = 58.1296\,\text{Å}^2$. For the B side, the octahedron missing to complete an equilateral triangle can be considered in $A_B = \sqrt(3)/4 \times (a''' \times 6)^2 - 3 \times \sqrt(3)/4 \times a'''^2 = 119.8924\,\text{Å}^2$. The resulting surface area of this octahedral crystal can be calculated as $A = 4 \times A_A + 4 \times A_B = 712.0882\,\text{Å}^2$. Finally, this value is used in the present study.

Specific surface energy including vibrational free energy

The Gibbs free energy of formation of a slab G_f can be approximated by its formation enthalpy H_f. To convert the energy obtained by the self-consistent field (SCF) computer simulation E_SCF, a correction is conducted considering the individual components hydrogen, oxygen and iron regarding their number N and energies (Equation S3.2). As the first two exist as molecular gases, simulations of H_2 and O_2 were conducted as reference and the respective corrections applied (Equation S3.1). $E_\text{SCF, Fe}$ was obtained from a single sphere simulation, although not comparable to real-life circumstances, it is in line with the previous computer simulations for volume crystal magnetite and the magnetite (111) surface. The respective values are given in Table S3.3.

TABLE S3.3: Energies for component species H_2, O_2, H_2O, Fe, and magnetite (Mag) per formula unit. The energy values were obtained by self-consistent field method (SCF) in CP2K, the zero-point energy (ZPE) in Gaussian and the temperature correction for the fluid phases ($\Delta G(0\,\mathrm{K} \rightarrow 298\,\mathrm{K})$) based on standard tabulated thermodynamic data[72].

system	SCF Energy [kJ/mol]	E_{ZPE} [kJ/mol]	$\Delta G(0\,\mathrm{K} \rightarrow 298\,\mathrm{K})$ [kJ/mol]
H_2	−3050.6345	27.7788	−24.2393
O_2	−83 827.9392	11.9539	−52.3337
H_2O	−45 210.1230	60.3471	−35.4496
Fe	−323 935.7098		
Mag	−1 139 861.4090		

To account for the entropy of each NP system, a computationally expensive vibrational analysis was conducted for the five NPs following the methodology tested in our previous study[17]. In principle, $3N-6$ vibrational normal modes can be obtained from such an analysis for N NP atoms. The magnetite bulk-like vibrational modes are excluded from the consideration, as it is assumed that the major contribution to the thermal vibration energy is provided by OH groups. The number M of these atoms can be calculated from the number of Fe atoms approximating from them the number of magnetite formula units. The vibrational modes from these almost fixed atoms are then $3M-6$, accordingly. The number of the remaining vibrational modes from O-H oscillations can then be obtained with $3N-6-(3M-6) = 3(N-M)$ and they can be expected to have the highest vibrational frequency $\tilde{\nu}$ (in cm^{-1}) as obtained from the analysis. These frequencies are then converted to their respective angular frequencies $\omega = 2\pi\nu = 2\pi\tilde{\nu}c$ and the vibrational free energy of the part reflecting the NP surface is obtained following Equation S3.3[73] (Table S3.4).

$$E_{\mathrm{H_2,\,O_2}} = E_{\mathrm{SCF}} + E_{\mathrm{ZPE}} + \Delta G(0\,\mathrm{K} \rightarrow 298\,\mathrm{K}) \tag{S3.1}$$

$$H_{\mathrm{f}} = E_{\mathrm{SCF,\,slab}} - \frac{1}{2} N_{\mathrm{H}}\, E_{\mathrm{H_2}} - \frac{1}{2} N_{\mathrm{O}}\, E_{\mathrm{O_2}} - N_{\mathrm{Fe}}\, E_{\mathrm{SCF,\,Fe}} \tag{S3.2}$$

$$\begin{aligned} G_{\mathrm{f}} &= H_{\mathrm{f}} + F_{\mathrm{vib}} = H_{\mathrm{f}} + E_{\mathrm{ZPE}} + F_{\mathrm{th}} \\ &= H_{\mathrm{f}} + \frac{\hbar}{2} \sum_{i=1}^{3(N-M)} \omega_i + k_{\mathrm{B}}T \sum_{i=1}^{3(N-M)} \ln\left(1 - \exp\frac{-\hbar\omega_i}{k_{\mathrm{B}}T}\right) \end{aligned} \tag{S3.3}$$

As stated above, each of these vibrational analysis simulations is computationally expensive. Analyzing the results of the vibrational energy study on the magnetite (111) surface, a linear correlation between the vibrational free energy and the H number was revealed (Figure S3.1).

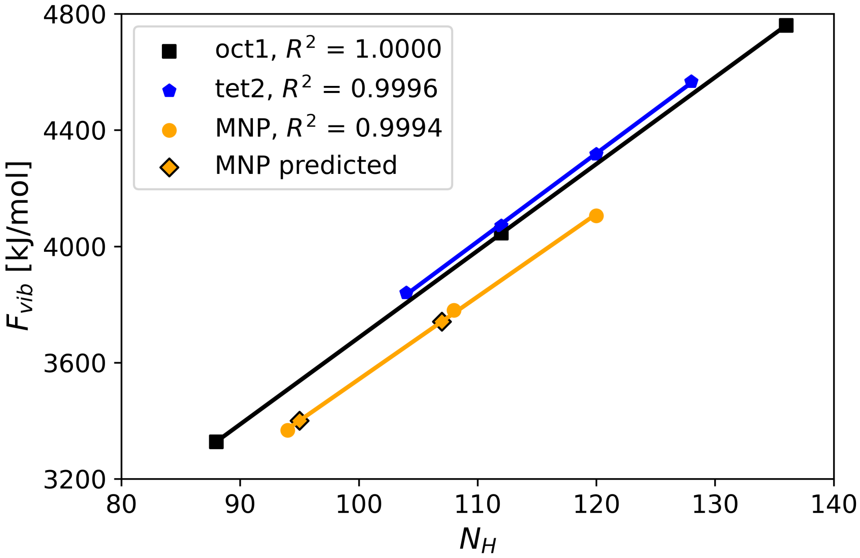

FIGURE S3.1: Linear fit of vibrational free energy F_{vib} as function of number of H in each system. oct1 and tet2 refer to preferred terminations of the magnetite (111) surface systems[17], MNP to the nanoparticle systems investigated in the study at hand. For the NPs, the two additional markers represent the approximated values of F_{vib} based on the respective linear equation.

Another argument for this dependence is that the vibrational free energy depends on the number of OH-groups, i.e., in turn on the number of hydrogen atoms. This linear behavior is also confirmed for the NP systems (see result for out2.75_in2.5 Figure S3.1) and, as this almost perfectly fits the linear regression (see fit parameters), an equivalent behavior of the other two NP systems can be assumed. The remaining values can be calculated, accordingly (Table S3.4).

TABLE S3.4: Formation enthalpy H_f and vibrational free energy F_{vib} (in kJ/mol) of the systems in vacuum, as well as interaction energies E_{int} (in kJ/mol/m^2) with solvent, H_2O or 0.5 M NaCl. In the F_{vib} column, * denotes values that were obtained from linear regression (Figure S3.1).

system	H_f	F_{vib}	$E_{int,\,\text{H}_2\text{O}}$	$E_{int,\,\text{NaCl}}$
out2.5_in2.5	-9320.4807	4105.7222	-1.6995E+21	-1.5635E+21
out2.75_in2.5	-9109.0060	3780.5758	-1.8465E+21	-1.6462E+21
out2.75_in2.75	-9058.9739	3741.7440*	-1.8007E+21	-1.7062E+21
out3.0_in2.75	-8492.3840	3400.5600*	-2.2724E+21	-2.0017E+21
out3.0_in3.0	-8366.9042	3367.2979	-2.4228E+21	-2.2330E+21

3.5.2 Solvent interaction

Stability analysis

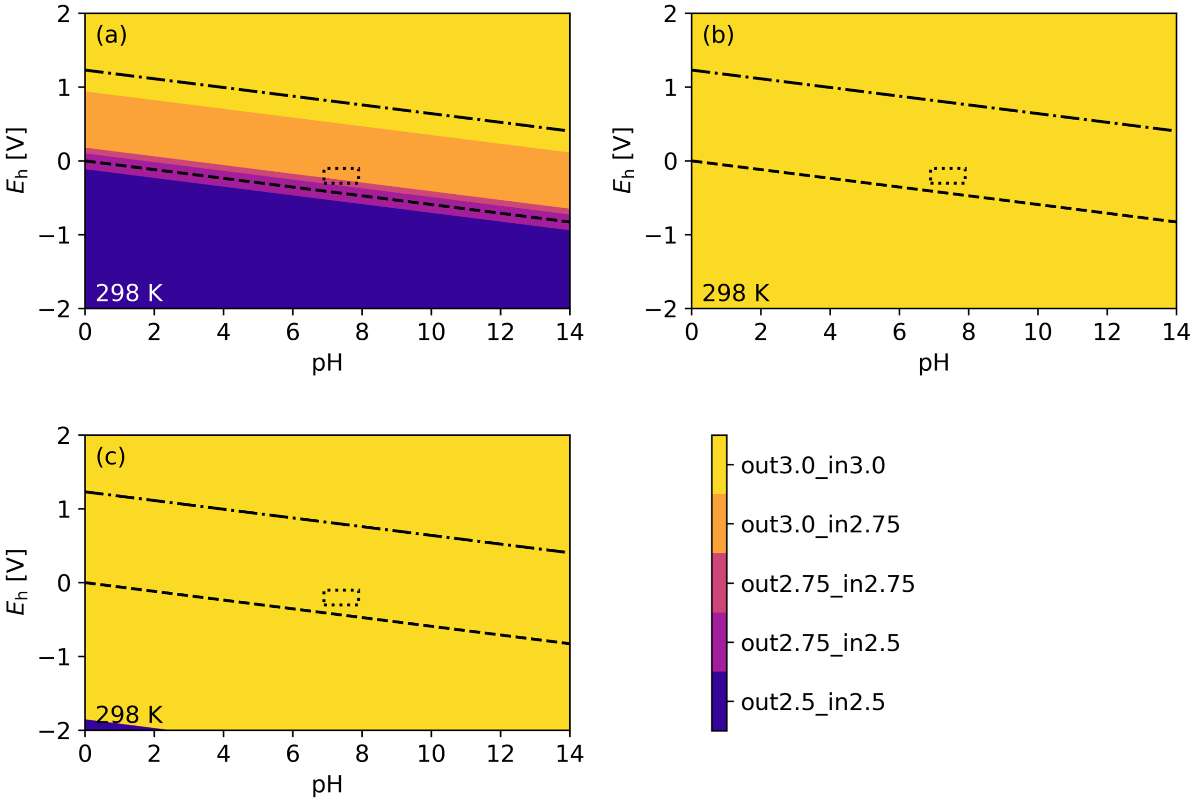

FIGURE S3.2: Surface stability plots of magnetite nanoparticle systems at 298 K as function of E_h and pH. (a) Stability plot based on *ab initio* data according to Equation 3.1 as given in the manuscript, (b) based on Equation 3.2 including the interaction energy of pure water obtained from classical MD, and (c) based on Equation 3.2 including the interaction energy of 0.5 M NaCl solvent obtained from classical MD. In each Pourbaix diagram, the dotted black box indicates the expected long-term repository conditions in the range of $E_h = -0.1\,\mathrm{V}$ to $-0.3\,\mathrm{V}$ and pH = 6.9 to 7.9[56], the dashed line the lower water stability (production of H_2), the dash-dotted line the upper water stability (decomposition to O_2).

Entrapment of water molecules

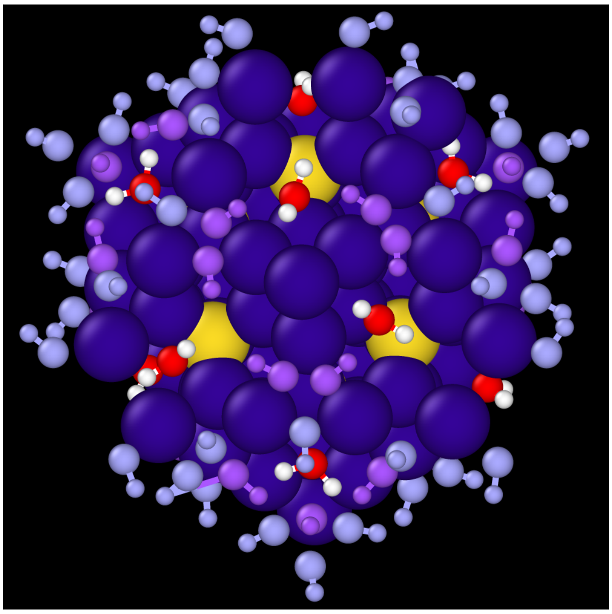

FIGURE S3.3: Exemplary snapshot of the MNP out3.0_in3.0 interacting with the water solvent, the view is perpendicular to one of the B facets. Depicted is the entrapment of water molecules in the cavities stable over the duration of the classical MD simulation. The most part of the frozen MNP is shown in dark blue spheres, except the tetrahedrally coordinated Fe in yellow directly below the cavity. The surface-OH-groups are depicted in purple (facet-OH) and light blue (edges including corners). The entrapped water molecules are shown in red (O) and white (H); atomic sizes are adapted for visualization. The entrapment can be envisaged for the three cavities at the B facet as well as for the single cavities at the adjacent A facets.

Radial pair distribution function (RDF)

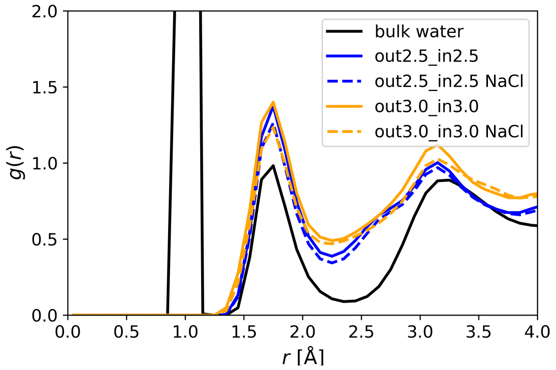

FIGURE S3.4: Radial pair distribution function (RDF, $g(r)$) of all MNP-O surrounded by water-H; as comparison with pure water (black).

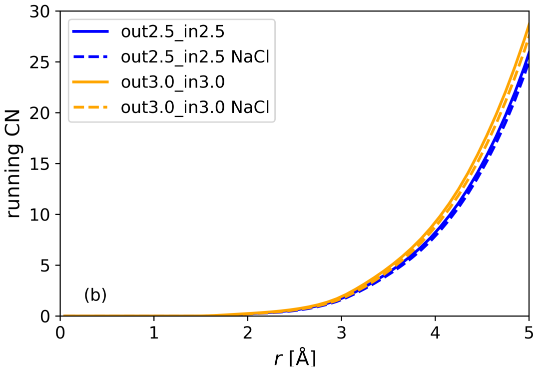

FIGURE S3.5: Running coordination number of MNP-O with respect to water-H.

Interaction with electrolyte ions

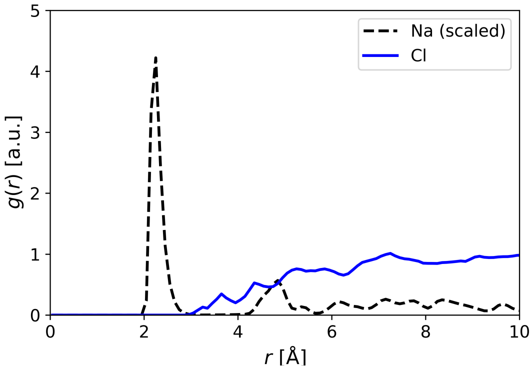

FIGURE S3.6: Exemplary RDF of surface-O surrounded by Na and Cl, respectively, of the system out2.75_in2.75.

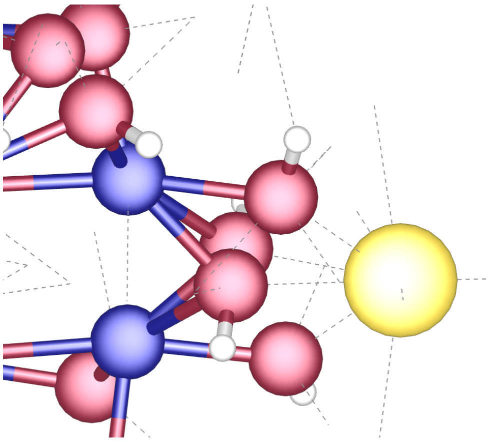

FIGURE S3.7: Visualization of Na ion close to a vertex of the MNP. Fe in blue (previously octahedrally coordinated), O in red, H in white and Na in yellow. The spheres representing water are not shown for visual clarity, yet the corresponding hydrogen-bonds as well as electrostatic interactions of O-Na are depicted by dashed lines.

Radial probability density function (RPDF)

The radial probability density function (RPDF) used in this manuscript is calculated from the radial pair distribution function (RDF) obtained from VMD of one species A being surround by species B. N represents the number of B atoms, V the volume of the cell. r is the distance from A to B, Δr represents incremental changes (binwidth).

$$\text{RPDF} = \frac{4}{3}\pi\,\frac{N}{V}\,\left((r+\Delta r)^3 - r^3\right)\,\text{RDF} \tag{S3.4}$$

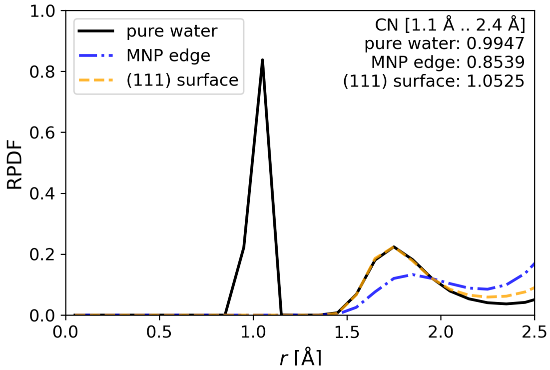

FIGURE S3.8: Radial probability density function (RPDF) and corresponding coordination number (CN) of surface-H of the infinite magnetite (111) surface[17] and MNP-edge-H surrounded by water-O, respectively. For simplicity, the edges include the vertices of the MNP. For comparison, the RPDF of pure water is given in black.

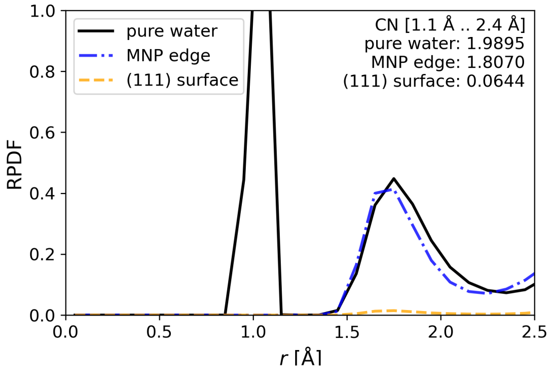

FIGURE S3.9: Radial probability density function (RPDF) and corresponding coordination number (CN) of surface-O of the infinite magnetite (111) surface[17] and MNP-edge-O surrounded by water-H, respectively. For simplicity, the edges include the vertices of the MNP. For comparison, the RPDF of pure water is given in black.

3.5.3 Accuracy of geometry optimizations

The structure optimization was conducted according to the following CP2K convergence criteria for geometry optimization in comparison of the current to the previous configuration, a_0 is the Bohr radius.

- Convergence criterion for the maximum atomic displacement: 1.0E-3 a_0
- Convergence criterion for the root mean square (RMS) of all atomic displacements: 1.0E-4 a_0
- Convergence criterion for the maximum atomic force: 3.0E-4 Ha/a_0
- Convergence criterion for the RMS of all atomic forces: 3.0E-5 Ha/a_0

3.6 References

[1] Mejia, J.; Roden, E. E.; Ginder-Vogel, M. Influence of Oxygen and Nitrate on Fe (Hydr)oxide Mineral Transformation and Soil Microbial Communities during Redox Cycling. *Environ. Sci. Technol.* **2016**, *50*, 3580–3588.

[2] Xiao, Z.; Yang, L.; Chen, C.; Chen, D.; Zhou, X. Redox Reaction between Solid-phase Humins and Fe(III) Compounds: Toward a Further Understanding of the Redox Properties of Humin and Its Possible Environmental Effects. *J. Environ. Manage.* **2022**, *310*, 114793.

[3] Gorski, C. A.; Nurmi, J. T.; Tratnyek, P. G.; Hofstetter, T. B.; Scherer, M. M. Redox Behavior of Magnetite: Implications for Contaminant Reduction. *Environ. Sci. Technol.* **2009**, *44*, 55–60.

[4] Park, H.; May, A.; Portilla, L.; Dietrich, H.; Münch, F.; Rejek, T.; Sarcletti, M.; Banspach, L.; Zahn, D.; Halik, M. Magnetite Nanoparticles As Efficient Materials for Removal of Glyphosate from Water. *Nat. Sustain.* **2019**, *3*, 129–135.

[5] Mohamad, N. D.; Zaki, Z. M.; Amir, A. Mechanisms of Enhanced Oxidative Degradation of Tetrachloroethene by Nano-magnetite Catalysed with Glutathione. *Chem. Eng. J.* **2020**, *393*, 124760.

[6] Mejia-Santillan, M.; Pariona, N.; Bravo-C., J.; Herrera-Trejo, M.; Montejo-Alvaro, F.; Zarate, A.; Perry, D.; Mtz-Enriquez, A. Physical and Arsenic Adsorption Properties of Maghemite and Magnetite Sub-microparticles. *J. Magn. Magn. Mater.* **2018**, *451*, 594–601.

[7] Narouei, F. H.; Andreescu, D.; Andreescu, S. Rapid Characterization of Arsenic Adsorption on Single Magnetite Nanoparticles by Collisions at Microelectrodes. *Environ. Sci.: Nano* **2020**, *7*, 1999–2009.

[8] Börsig, N.; Scheinost, A. C.; Shaw, S.; Schild, D.; Neumann, T. Retention and Multiphase Transformation of Selenium Oxyanions during the Formation of Magnetite Via Iron(II) Hydroxide and Green Rust. *Dalton Trans.* **2018**, *47*, 11002–11015.

[9] Börsig, N.; Scheinost, A. C.; Schild, D.; Neumann, T. Mechanisms of Selenium Removal by Partially Oxidized Magnetite Nanoparticles for Wastewater Remediation. *Appl. Geochem.* **2021**, *132*, 105062.

[10] Hu, C.; Gao, Z.; Yang, X. Fabrication and Magnetic Properties of Fe_3O_4 Octahedra. *Chem. Phys. Lett.* **2006**, *429*, 513–517.

[11] Yang, T.; Wen, X.-d.; Ren, J.; Li, Y.-w.; Wang, J.-g.; Huo, C.-f. Surface Structures of Fe_3O_4 (111), (110), and (001): A Density Functional Theory Study. *J. Fuel Chem. Technol.* **2010**, *38*, 121–128.

[12] Asakawa, K.; Miura, Y.; Nagatsuka, N.; Takeyasu, K.; Matsumoto, M.; Fukutani, K. Electronic and Spin Structure of O- and H-Adsorbed Fe_3O_4 (111) Surfaces. *Phys. Rev. B* **2019**, *99*, 085442.

[13] Petitto, S. C.; Tanwar, K. S.; Ghose, S. K.; Eng, P. J.; Trainor, T. P. Surface Structure of Magnetite (111) under Hydrated Conditions by Crystal Truncation Rod Diffraction. *Surf. Sci.* **2010**, *604*, 1082–1093.

[14] Kirsch, R.; Fellhauer, D.; Altmaier, M.; Neck, V.; Rossberg, A.; Fanghänel, T.; Charlet, L.; Scheinost, A. C. Oxidation State and Local Structure of Plutonium Reacted with Magnetite, Mackinawite, and Chukanovite. *Environ. Sci. Technol.* **2011**, *45*, 7267–7274.

[15] Yalçıntaş, E.; Scheinost, A. C.; Gaona, X.; Altmaier, M. Systematic XAS Study on the Reduction and Uptake of Tc by Magnetite and Mackinawite. *Dalton Trans.* **2016**, *45*, 17874–17885.

[16] Dumas, T.; Fellhauer, D.; Schild, D.; Gaona, X.; Altmaier, M.; Scheinost, A. C. Plutonium Retention Mechanisms by Magnetite under Anoxic Conditions: Entrapment Versus Sorption. *ACS Earth Space Chem.* **2019**, *3*, 2197–2206.

[17] Katheras, A. S.; Karalis, K.; Krack, M.; Scheinost, A. C.; Churakov, S. V. Stability and Speciation of Hydrated Magnetite {111} Surfaces from *Ab Initio* Simulations with Relevance for Geochemical Redox Processes. *Environ. Sci. Technol.* **2024**, *58*, 935–946.

[18] Jin, P.; Robbins, W.; Bota, G. Mechanism of Magnetite Formation in High Temperature Corrosion by Model Naphthenic Acids. *Corros. Sci.* **2016**, *111*, 822–834.

[19] Deng, J.; Chen, T.; Arbid, Y.; Pasturel, M.; Bae, S.; Hanna, K. Aging and Reactivity Assessment of Nanoscale Zerovalent Iron in Groundwater Systems. *Water Res.* **2023**, *229*, 119472.

[20] Torres-Gómez, N.; Nava, O.; Argueta-Figueroa, L.; García-Contreras, R.; Baeza-Barrera, A.; Vilchis-Nestor, A. R. Shape Tuning of Magnetite Nanoparticles Obtained by Hydrothermal Synthesis: Effect of Temperature. *J. Nanomater.* **2019**, *2019*, 1–15.

[21] Aphesteguy, J.; Kurlyandskaya, G.; de Celis, J.; Safronov, A.; Schegoleva, N. Magnetite Nanoparticles Prepared by Co-Precipitation Method in Different Conditions. *Mater. Chem. Phys.* **2015**, *161*, 243–249.

[22] Zhao, L.; Zhang, H.; Xing, Y.; Song, S.; Yu, S.; Shi, W.; Guo, X.; Yang, J.; Lei, Y.; Cao, F. Morphology-Controlled Synthesis of Magnetites with Nanoporous Structures and Excellent Magnetic Properties. *Chem. Mater.* **2007**, *20*, 198–204.

[23] Navarro, E.; Luengo, Y.; Veintemillas, S.; Morales, P.; Palomares, F. J.; Urdiroz, U.; Cebollada, F.; González, J. M. Slow Magnetic Relaxation in Well Crystallized, Monodispersed, Octahedral and Spherical Magnetite Nanoparticles. *AIP Adv.* **2019**, *9*, 125143.

[24] Mitra, A.; Mohapatra, J.; Meena, S. S.; Tomy, C. V.; Aslam, M. Verwey Transition in Ultrasmall-sized Octahedral Fe_3O_4 Nanoparticles. *J. Phys. Chem. C* **2014**, *118*, 19356–19362.

[25] Sun, Y.-k.; Ma, M.; Zhang, Y.; Gu, N. Synthesis of Nanometer-size Maghemite Particles from Magnetite. *Colloids Surf., A* **2004**, *245*, 15–19.

[26] Jungcharoen, P.; Pédrot, M.; Heberling, F.; Hanna, K.; Choueikani, F.; Catrouillet, C.; Dia, A.; Marsac, R. Prediction of Nanomagnetite Stoichiometry (Fe(II)/Fe(III)) under Contrasting pH and Redox Conditions. *Environ. Sci.: Nano* **2022**, *9*, 2363–2371.

[27] Schwaminger, S. P.; Bauer, D.; Fraga-García, P.; Wagner, F. E.; Berensmeier, S. Oxidation of Magnetite Nanoparticles: Impact on Surface and Crystal Properties. *Cryst. Eng. Comm.* **2017**, *19*, 246–255.

[28] Winsett, J.; Moilanen, A.; Paudel, K.; Kamali, S.; Ding, K.; Cribb, W.; Seifu, D.; Neupane, S. Quantitative Determination of Magnetite and Maghemite in Iron Oxide Nanoparticles Using Mössbauer Spectroscopy. *SN Appl. Sci.* **2019**, *1*, 1636.

[29] Jungcharoen, P.; Pédrot, M.; Choueikani, F.; Pasturel, M.; Hanna, K.; Heberling, F.; Tesfa, M.; Marsac, R. Probing the Effects of Redox Conditions and Dissolved Fe^{2+} on Nanomagnetite Stoichiometry by Wet Chemistry, XRD, XAS and XMCD. *Environ. Sci.: Nano* **2021**, *8*, 2098–2107.

[30] Scheinost, A. C.; Charlet, L. Selenite Reduction by Mackinawite, Magnetite and Siderite: XAS Characterization of Nanosized Redox Products. *Environ. Sci. Technol.* **2008**, *42*, 1984–1989.

[31] Scheinost, A. C.; Kirsch, R.; Banerjee, D.; Fernandez-Martinez, A.; Zaenker, H.; Funke, H.; Charlet, L. X-ray Absorption and Photoelectron Spectroscopy Investigation of Selenite Reduction by Fe^{II}-bearing Minerals. *J. Contam. Hydrol.* **2008**, *102*, 228–245.

[32] Baumgartner, J.; Dey, A.; Bomans, P. H. H.; Le Coadou, C.; Fratzl, P.; Sommerdijk, N. A. J. M.; Faivre, D. Nucleation and Growth of Magnetite from Solution. *Nat. Mater.* **2013**, *12*, 310–314.

[33] Mirabello, G.; Ianiro, A.; Bomans, P. H. H.; Yoda, T.; Arakaki, A.; Friedrich, H.; de With, G.; Sommerdijk, N. A. J. M. Crystallization by Particle Attachment Is a Colloidal Assembly Process. *Nat. Mater.* **2019**, *19*, 391–396.

[34] Perdew, J. P.; Burke, K.; Ernzerhof, M. Generalized Gradient Approximation Made Simple. *Phys. Rev. Lett.* **1996**, *77*, 3865–3868.

[35] Perdew, J. P.; Burke, K.; Ernzerhof, M. Generalized Gradient Approximation Made Simple [Phys. Rev. Lett. 77, 3865 (1996)]. *Phys. Rev. Lett.* **1997**, *78*, 1396–1396.

[36] Perdew, J. P.; Ruzsinszky, A.; Csonka, G. I.; Vydrov, O. A.; Scuseria, G. E.; Constantin, L. A.; Zhou, X.; Burke, K. Restoring the Density-Gradient Expansion for Exchange in Solids and Surfaces. *Phys. Rev. Lett.* **2008**, *100*, 136406.

[37] VandeVondele, J.; Krack, M.; Mohamed, F.; Parrinello, M.; Chassaing, T.; Hutter, J. QUICKSTEP: Fast and Accurate Density Functional Calculations Using a Mixed Gaussian and Plane Waves Approach. *Comput. Phys. Commun.* **2005**, *167*, 103–128.

[38] Kühne, T. D. et al. CP2K: An Electronic Structure and Molecular Dynamics Software Package - Quickstep: Efficient and Accurate Electronic Structure Calculations. *J. Chem. Phys.* **2020**, *152*, 194103.

[39] Goedecker, S.; Teter, M.; Hutter, J. Separable Dual-Space Gaussian Pseudopotentials. *Phys. Rev. B* **1996**, *54*, 1703–1710.

[40] Krack, M. Pseudopotentials for H to Kr Optimized for Gradient-corrected Exchange-Correlation Functionals. *Theor. Chem. Acc.* **2005**, *114*, 145–152.

[41] VandeVondele, J.; Hutter, J. Gaussian Basis Sets for Accurate Calculations on Molecular Systems in Gas and Condensed Phases. *J. Chem. Phys.* **2007**, *127*, 114105.

[42] VandeVondele, J.; Hutter, J. An Efficient Orbital Transformation Method for Electronic Structure Calculations. *J. Chem. Phys.* **2003**, *118*, 4365–4369.

[43] Hubbard, J. Electron Correlations in Narrow Energy Bands. *Proc. Roy. Soc. Lond. Math. Phys. Sci.* **1963**, *276*, 238–257.

[44] Dudarev, S. L.; Botton, G. A.; Savrasov, S. Y.; Humphreys, C. J.; Sutton, A. P. Electron-Energy-Loss Spectra and the Structural Stability of Nickel Oxide: An LSDA+U Study. *Phys. Rev. B* **1998**, *57*, 1505–1509.

[45] Kirsch, R.; Scheinost, A. C.; Rossberg, A.; Banerjee, D.; Charlet, L. Reduction of Antimony by Nano-particulate Magnetite and Mackinawite. *Mineral. Mag.* **2008**, *72*, 185–189.

[46] Auffan, M.; Rose, J.; Proux, O.; Borschneck, D.; Masion, A.; Chaurand, P.; Hazemann, J.-L.; Chaneac, C.; Jolivet, J.-P.; Wiesner, M. R.; Van Geen, A.; Bottero, J.-Y. Enhanced Adsorption of Arsenic onto Maghemites Nanoparticles: As(III) as a Probe of the Surface Structure and Heterogeneity. *Langmuir* **2008**, *24*, 3215–3222.

[47] Wang, Y.; Morin, G.; Ona-Nguema, G.; Menguy, N.; Juillot, F.; Aubry, E.; Guyot, F.; Calas, G.; Brown, G. E. Arsenite Sorption at the Magnetite–Water Interface during Aqueous Precipitation of Magnetite: EXAFS Evidence for a New Arsenite Surface Complex. *Geochim. Cosmochim. Acta* **2008**, *72*, 2573–2586.

[48] Morin, G.; Wang, Y.; Ona-Nguema, G.; Juillot, F.; Calas, G.; Menguy, N.; Aubry, E.; Bargar, J. R.; Brown, G. E. EXAFS and HRTEM Evidence for As(III)-containing Surface Precipitates on Nanocrystalline Magnetite: Implications for As Sequestration. *Langmuir* **2009**, *25*, 9119–9128.

[49] Meng, Y.; Liu, X.-W.; Bai, M.; Guo, W.-P.; Cao, D.-B.; Yang, Y.; Li, Y.-W.; Wen, X.-D. Prediction on Morphologies and Phase Equilibrium Diagram of Iron Oxides Nanoparticles. *Appl. Surf. Sci.* **2019**, *480*, 478–486.

[50] Thompson, A. P.; Aktulga, H. M.; Berger, R.; Bolintineanu, D. S.; Brown, W. M.; Crozier, P. S.; in 't Veld, P. J.; Kohlmeyer, A.; Moore, S. G.; Nguyen, T. D.; Shan, R.; Stevens, M. J.; Tranchida, J.; Trott, C.; Plimpton, S. J. LAMMPS - a Flexible Simulation Tool for Particle-based Materials Modeling at the Atomic, Meso, and Continuum Scales. *Comput. Phys. Commun.* **2022**, *271*, 108171.

[51] Martínez, L.; Andrade, R.; Birgin, E. G.; Martínez, J. M. Packmol: A Package for Building Initial Configurations for Molecular Dynamics Simulations. *J. Comput. Chem.* **2009**, *30*, 2157–2164.

[52] Berendsen, H. J. C.; Grigera, J. R.; Straatsma, T. P. The Missing Term in Effective Pair Potentials. *J. Phys. Chem.* **1987**, *91*, 6269–6271.

[53] Smith, D. E.; Dang, L. X. Computer Simulations of Nacl Association in Polarizable Water. *J. Chem. Phys.* **1994**, *100*, 3757–3766.

[54] Konuk, M.; Sellschopp, K.; Vonbun-Feldbauer, G. B.; Meißner, R. H. Modeling Charge Redistribution at Magnetite Interfaces in Empirical Force Fields. *J. Phys. Chem. C* **2021**, *125*, 4794–4805.

[55] Martyna, G. J.; Klein, M. L.; Tuckerman, M. Nosé–Hoover Chains: The Canonical Ensemble Via Continuous Dynamics. *J. Chem. Phys.* **1992**, *97*, 2635–2643.

[56] Wersin, P.; Johnson, L.; Schwyn, B.; Berner, U.; Curti, E. *Redox Conditions in the Near Field of a Repository for SF/HLW and ILW in Opalinus Clay*; NAGRA tech. report 02-13, 2003.

[57] Jolivet, J.-P.; Tronc, E. Interfacial Electron Transfer in Colloidal Spinel Iron Oxide. Conversion of Fe_3O_4-γFe_2O_3 in Aqueous Medium. *J. Colloid Interface Sci.* **1988**, *125*, 688–701.

[58] White, A. F.; Peterson, M. L.; Hochella, M. F. Electrochemistry and Dissolution Kinetics of Magnetite and Ilmenite. *Geochim. Cosmochim. Acta* **1994**, *58*, 1859–1875.

[59] Yuan, K.; Lee, S. S.; Cha, W.; Ulvestad, A.; Kim, H.; Abdilla, B.; Sturchio, N. C.; Fenter, P. Oxidation Induced Strain and Defects in Magnetite Crystals. *Nat. Commun.* **2019**, *10*.

[60] Li, Z.; Chanéac, C.; Berger, G.; Delaunay, S.; Graff, A.; Lefèvre, G. Mechanism and Kinetics of Magnetite Oxidation under Hydrothermal Conditions. *RSC Adv.* **2019**, *9*, 33633–33642.

[61] van Riemsdijk, W.; Hiemstra, T. *Surface Complexation Modelling*; Interface Science and Technology; Elsevier, 2006; pp 251–268.

[62] Churakov, S. V.; Labbez, C.; Pegado, L.; Sulpizi, M. Intrinsic Acidity of Surface Sites in Calcium Silicate Hydrates and Its Implication to Their Electrokinetic Properties. *J. Phys. Chem. C* **2014**, *118*, 11752–11762.

[63] Cheng, W.; Marsac, R.; Hanna, K. Influence of Magnetite Stoichiometry on the Binding of Emerging Organic Contaminants. *Environ. Sci. Technol.* **2017**, *52*, 467–473.

[64] Qian, Y.; Scheinost, A. C.; Grangeon, S.; Hoving, A.; Churakov, S. V.; Marques Fernandes, M. Influence of Structural Fe Content in Clay Minerals on Selenite Redox Reactions: Kinetics and Structural Transformations. *Geochim. Cosmochim. Acta* **2024**, *377*, 19–33.

[65] Pearce, C.; Qafoku, O.; Liu, J.; Arenholz, E.; Heald, S.; Kukkadapu, R.; Gorski, C.; Henderson, C.; Rosso, K. Synthesis and Properties of Titanomagnetite ($Fe_{3-x}Ti_xO_4$) Nanoparticles: A Tunable Solid-state Fe(II/III) Redox System. *J. Colloid Interface Sci.* **2012**, *387*, 24–38.

[66] Latta, D. E.; Gorski, C. A.; Boyanov, M. I.; O'Loughlin, E. J.; Kemner, K. M.; Scherer, M. M. Influence of Magnetite Stoichiometry on U(VI) Reduction. *Environ. Sci. Technol.* **2011**, *46*, 778–786.

[67] Urbánová, L.; Bujdoš, M.; Matulová, M.; Miglierini, M. B.; Vyhnáleková, S.; Orovčík, L'.; Machata, P.; Mičušík, M.; Dobročka, E.; Kollár, J.; Matúš, P.; Urík, M. Investigating the Sorption Behavior of Selenite on Commercial Partially Oxidized Magnetite Nanopowder under Aerobic Conditions: Characterization and Mechanisms. *Sep. Purif. Technol.* **2024**, *348*, 127688.

[68] Molleman, B.; Hiemstra, T. Size and Shape Dependency of the Surface Energy of Metallic Nanoparticles: Unifying the Atomic and Thermodynamic Approaches. *Phys. Chem. Chem. Phys.* **2018**, *20*, 20575–20587.

[69] Vollath, D.; Fischer, F. D.; Holec, D. Surface Energy of Nanoparticles – Influence of Particle Size and Structure. *Beilstein J. Nanotechnol.* **2018**, *9*, 2265–2276.

[70] Li, X.; Sheng, A.; Ding, Y.; Liu, J. A Model Towards Understanding Stabilities and Crystallization Pathways of Iron (Oxyhydr)oxides in Redox-Dynamic Environments. *Geochim. Cosmochim. Acta* **2022**, *336*, 92–103.

[71] Yin, X.; Hua, H.; Dyer, J.; Landis, R.; Fennell, D.; Axe, L. Degradation of Chlorinated Solvents with Reactive Iron Minerals in Subsurface Sediments from Redox Transition Zones. *J. Hazard. Mater.* **2023**, *445*, 130470.

[72] Lemmon, E. W.; Bell, I. H.; Huber, M. L.; McLinden, M. O. In *Thermophysical Properties of Fluid Systems*; Linstrom, P. J., Mallard, W., Eds.; NIST Chemistry WebBook, NIST Standard Reference Database 69.

[73] Churakov, S. V. Thermoelastic Properties of Solid Phases: C++ Object Oriented Library SolidEOS. *Comput. Geosci.* **2005**, *31*, 786–791.

Chapter 4: Incorporation of Tc(IV) in the magnetite crystal structure

Incorporation mechanism of Tc(IV) in magnetite revealed by EXAFS measurements and *ab initio* simulations

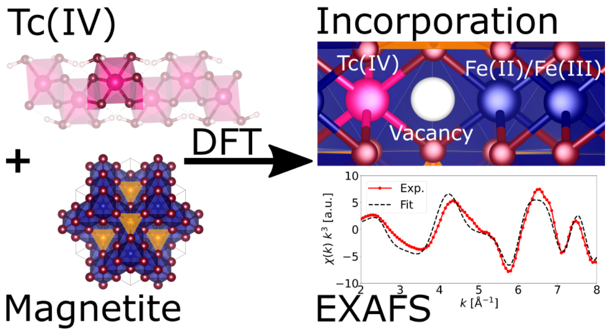

This chapter was submitted as article in *Environmental Science and Technology* on December 27, 2024. The manuscript was written in cooperation with Matthias Krack, Thomas Zimmermann, Andreas C. Scheinost, and Sergey V. Churakov.

After acceptance of the dissertation, the manuscript has been slightly adapted and has been resubmitted to *The Journal of Physical Chemistry C*. It was published as article in *The Journal of Physical Chemistry C*, 2025, 129, 12, 5921-5930 (DOI: 10.1021/acs.jpcc.5c00357), copyright 2025 the Authors, licensed under CC-BY 4.0.

Abstract

Tc is a long-lived U and Th fission product present in nuclear waste. It can be highly mobile in the oxidized pertechnetate form but becomes almost insoluble under reducing conditions. Magnetite is a common iron mineral capable of the reductive immobilization of Tc by structural incorporation. Based on ionic radius and similarity in charge, Tc(IV) is expected to substitute for Fe(II,III) in octahedral positions. Several mechanisms have been proposed in the past on how the necessary charge compensation for the aliovalent cation substitution is obtained. In this study, we developed a reliable computational approach based on density functional theory to investigate the Tc-magnetite interaction. By comparing our simulation results to spectroscopic data, we can confirm a preference for the incorporation mechanisms including the formation of a vacancy. For both the magnetite bulk structure as well its commonly observed (111) surface, these findings are based on structural information and thermodynamic considerations. Our results are in line with the experimentally observed topotactical transition of the magnetite crystal structure towards the higher oxidized iron mineral maghemite and reflect a component in long-term geochemical mineral transformations.

4.1 Introduction

Technetium is the lightest element in the Periodic Table without stable isotopes. Among its nuclides, the short-lived gamma-emitting isotope ^{99m}Tc is routinely used for medical imaging of tissues and organs in the human body[1]. Apart from natural processes like spontaneous fission of natural uranium and neutron capture by molybdenum, where only trace quantities of Tc form, the major inventory of technetium is contained in spent nuclear fuel as the nuclide ^{99}Tc with a long half-life of 200 ka. The mobility of Tc in the environment is strongly controlled by its oxidation state. Tc(VII) is very soluble and mobile as pertechnetate anion (TcO_4^-), whereas Tc(IV)O_2 was found to stay immobilized over a wide pH range[2].

In many countries, the disposal of radioactive waste is foreseen in deep geological repositories aiming for a long-term separation of hazardous elements and the living environment. To ensure the separation, the repository safety relies on a system of natural and engineered barriers[3]. The retention mechanisms and mobility are influenced by the surrounding chemical conditions, including salinity[4,5] and the presence of ligands. In contact with oxygen-containing pore-water, technetium from spent nuclear fuel can be oxidized and mobilized to the form of Tc(VII). Considering the long-term reducing conditions expected in the near-field of geological repositories[6], it can be reduced to Tc(IV) in presence of Fe(II), e.g., in clay minerals such as nontronite[7], preferably by Fe(II) associated with the solid phase of clay minerals[8,9], or on Fe precipitates by a surface-mediated mechanism[10]. Furthermore, the reduction has been shown to occur at Fe(II) bearing minerals such as mackinawite, siderite, chukanovite and magnetite[4,11,12]. The latter mineral might also contain Ti (titanomagnetite), in which the presence of Ti stabilizes Fe(II) leading to increased Tc reduction capabilities[13]. The reduction may lead to the formation of insoluble colloids[14].

Moreover, Tc(IV) can be immobilized by sorption or structural incorporation, e.g., on humic substances[14] or in other environmentally relevant Fe compounds such as hematite[15], goethite[16], pyrite[17], zero-valent iron[18] or chukanovite[12]. It has been observed that the interaction of Tc with Fe containing minerals often leads to the formation of magnetite[17,18]. Significant quantities of iron oxide minerals and magnetite in particular are expected to form as main corrosion product of the disposal casks containing high level nuclear waste[19–24]. Thus, magnetite is likely among the first mineral phases the mobile Tc(VII) might come in contact with after breaching of the disposal casks and ingress of formation water.

The interaction of Tc with magnetite and other corrosion products[25] has been studied both experimentally, e.g., using X-ray absorption spectroscopy (XAS)[4,11,26] as well as by computational methods[27–29]. It was found that at high Tc concentrations, a stabilization of a TcO_2 precipitate in solution occurs first[4,26] resembling β-TcO_2[30], before it may get sorbed onto the magnetite surface[11,29]. On the other hand, at low concentrations of Tc and under low alkaline pH[11], the structural incorporation of Tc(IV) occurs at octahedral sites of the magnetite structure[26,27,31–34]. Moreover, the resulting Tc-magnetite structure was found to be quite stable under alkaline or acidic leaching conditions[35] and even under oxidation[36], although leading to a partial transformation to maghemite/goethite[37].

The incorporation of Tc in octahedral Fe position in magnetite can be explained by the concordance of the ionic radius of Fe(III) and Tc(IV)[38]. However, the details of the charge substitution mechanism and potential formation of structural vacancies remain a subject of debate[29,32]. This study reveals the molecular mechanism of Tc uptake by magnetite combining spectroscopic investigations and theoretical modeling at the level of density functional theory (DFT). For this purpose, we rely on the previous characterization of the magnetite surface regarding stability and speciation as function of environmental E_h and pH conditions[39]. This study discusses the thermochemical conditions for redox processes coupled to Tc incorporation and reveal the important role of vacancy formations leading to a maghemitization of the magnetite surface.

4.2 Materials and Methods

4.2.1 Modeling setup

Ab initio simulations

Atomistic simulations were performed following the methodology developed and validated in our previous studies[39,40]. In brief, Density Functional Theory (DFT) based spin-polarized structural optimizations were performed using the PBE functional (PBEsol parametrization). The Gaussian Plane Wave (GPW) method implemented in the QUICKSTEP module[41] of CP2K (version 2023.1)[42] was used applying 3D periodic boundary conditions. GTH[43–45]-like norm-conserving scalar-relativistic pseudo-potentials were applied to avoid an explicit consideration of the core electrons. MOLOPT basis sets (DZVP)[46] were used to describe the wave functions of the valence electrons. To expand the electronic density, an auxiliary basis set of plane waves with an electronic density cutoff of 600 Ry was employed. The target accuracy (EPS_SCF) of the self-consistent field (SCF) cycles, 3.0×10^{-7} Ha, was achieved using the orbital transformation method[47] for the wave function optimization. To improve the description of the 3d-electronic states of iron, the DFT+U method[48,49] was employed with an effective Hubbard U parameter of 1.9 eV as validated in a previous study[39]. In all simulations, if not stated otherwise, the valence electron count in the system fulfilled the electro-neutrality condition.

Furthermore, spin polarization was applied to the initialization of wave functions in the magnetite systems. For ferrous iron, it measured $(2S + 1)_{Fe^{2+}} = 5$ and $(2S + 1)_{Fe^{3+}} = 6$ for ferric iron, respectively. Ferric and ferrous irons are assumed to alternate in the octahedral positions of the magnetite structure resulting in $(2S + 1)_{Fe_{oct}} = 5.5$ with all spins aligned up. The ferric tetrahedral sites in magnetite were considered as spin down. Tc(IV) was initialized as $5s^0 4d^3$ with initial up-spin multiplicity of $(2S + 1)_{Tc^{4+}} = 4$.

Benchmarking of Hubbard *U* parameter for Tc

In line with our previous studies[39,40] on the magnetite structure, surface stability and nanoparticle speciation, the DFT+U approach[48,49] was applied to improve the description of the Tc 4d-orbitals[50–52]. The necessary preparatory step in this study was, hence, the determination of the U parameter for tetravalent Tc octahedrally coordinated by oxygen. Based on the commonly used chemical analog Re[53,54] as presented in the comparative study by Oliveira et al.[30], the three polymorphs of Tc(IV) oxide exhibiting octahedrally coordinated Tc were simulated. The crystal structure of α-TcO_2 is monoclinic (space group $P2_1/c$)[55] and it is the only experimentally proven polymorph. In analogy to Re, β- and γ-TcO_2 are assumed as orthorhombic (space group $Pbcn$) and tetragonal (space group $P4_2/mnm$), respectively[30].

For the 4d-electronic states of Tc, several values ranging from 0 eV to 4 eV were tested as Hubbard U parameter in different Tc(IV) oxides. For comparison of the obtained benchmarking results and further method validation, spin-polarized PBE+U simulations on α-, β- and γ-TcO_2 were performed in VASP[56–59] (version 5.4.4) with an electronic cutoff of 600 eV and $8 \times 8 \times 8$ k-points for α-, β-TcO_2 and $8 \times 8 \times 16$ k-points for γ-TcO_2, respectively.

To identify an optimal value of the Hubbard U parameter for Tc, the lattice constants and angles of simulated structures were compared to literature data. As they are predicted as the most stable phases[30], the α- and β-structures were tested as $3 \times 3 \times 3$ superstructures in CP2K as main simulation program for this study. Complementary, VASP simulations as $1 \times 1 \times 1$ supercells of each of the three polymorphs were tested. The best structural agreement was obtained with $U_{\mathrm{eff,\,Tc(IV)}} = 0$ eV which was then applied in the simulations investigating the interactions with magnetite. Moreover, β-TcO_2 chains were identified as the expected sorbed Tc-species by Oliveira et al.[30] and for additional validation of the intended modeling setup, these *zigzag* chains of six TcO_6 octahedra were simulated. Further details can be found in the Supporting Information (SI).

Potential mechanisms of Tc incorporation and system setup

Magnetite has a cubic inverse spinel structure (space group $Fd\bar{3}m$) with octahedrally (Fe_{oct}) and tetrahedrally (Fe_{tet}) coordinated Fe. The tetrahedral positions are occupied by ferric iron (Fe^{3+}), while the octahedral positions are occupied by equal amounts of ferric and ferrous iron (Fe^{2+}). As Tc(IV) and Fe(III) in octahedral coordination by oxygen have the same ionic radius of 78.5 pm[38], an incorporation based on substituting Fe with Tc is possible[32]. Two distinct mechanism can be envisaged to maintain local charge balance for the Tc-Fe aliovalent substitution: First, an isostructural substitution of Tc for Fe_{oct} (mechanism "Iso"). Second, the substitution of two Fe in edge-shared octahedra for one Tc(IV) and one vacancy as proposed by Smith et al.[32] (mechanism "Vac"). Compared to the previous study[32], the possible mechanism of substituting four Fe(III) by three Tc(IV) and a vacancy was not considered, as it represents a striking alteration of the magnetite crystal structure and was found to require stabilization by external factors[32]. Hence, as for the current study, in both investigated cases (Iso and Vac) the total system charge is assigned to zero implying a redox reaction between Tc and Fe present in the system.

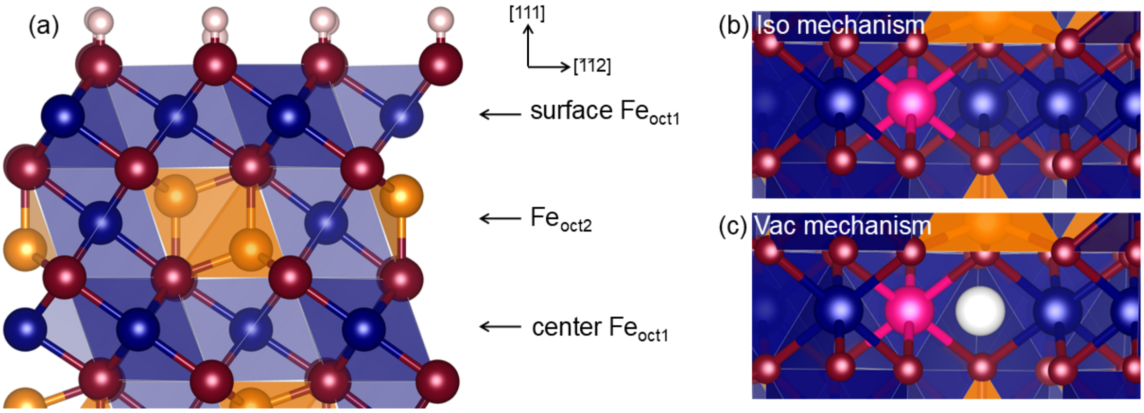

FIGURE 4.1: (a) Side view of half of the symmetric magnetite (111) surface slab[39]. Tetrahedrally coordinated Fe are shown in orange, octahedrally coordinated Fe (Fe_{oct}) in blue, O in red, H in pale pink. (b) Substitution of octahedrally coordinated Fe by Tc (pink) representing the isostructural substitution (Iso mechanism) and (c) with an additional vacancy (white) in place of an edge-connected octahedrally coordinated Fe (Vac mechanism). Atomic sizes are adapted for visualization.

The molecular geometry and substitution energy for both mechanisms were investigated in the bulk crystal structure of magnetite with lattice parameter of 8.375 Å[60] using a 2 × 2 × 2 supercell. Moreover, systems resembling the saturated magnetite (111) surface[39] were tested as incorporation matrix. Theses systems followed the slab geometry with slab dimensions 23.69 Å × 20.52 Å × 14.04 Å as tested in our previous study[39]. Under repository conditions[6], the prevailing surface termination has been identified as protonated FeO_6 octahedra (Figure 4.1 (a)). The protonation state of the surfaces for the present was chosen according to the setup with an idealized Fe_{oct} charge of 2.5+[39] for comparison with bulk magnetite. In the bulk magnetite structure, the octahedrally coordinated Fe occupy equivalent crystallographic sites, hence, for the Iso mechanism one Fe_{oct} was replaced with one Tc (Figure 4.1 (b)).

The alternative Vac mechanism with a vacancy was realized by additionally removing a Fe_{oct} from an edge-sharing FeO_6 octahedron (Figure 4.1 (c)). In this way, Tc makes up around 0.6 wt % similar to the Tc incorporation in hematite[15]. For the magnetite surface slab, several options were possible due to the layered structure of the magnetite (111) surface slab. The symmetric slab has three distinctive Fe_{oct}-layers: one in the center, one intermediate Fe_{oct}-layer between two Fe_{tet} and another Fe_{oct}-layer close to the surface (Figure 4.1 (a)). Each of these Fe_{oct}-layers was tested for the Iso mechanism, they will be referred to based on the respective position of the substituted Fe_{oct} with an abbreviated subscript: Iso_{cent}, Iso_{oct2}, and Iso_{surf}.

Similarly for the Vac mechanism, all six possible options of positioning Tc and vacancy were tested. The options can be differentiated by the position of the initial Fe_{oct} that are replaced by a Tc ion and a vacancy (Figure S4.3 in SI). The naming convention is similar to the Iso mechanisms, but with two subscripts parted by a hyphen to depict the position of Tc-Vac: Both octahedral positions in the same layer of center Fe_{oct1} ($Vac_{cent\text{-}cent}$) or surface Fe_{oct1} ($Vac_{surf\text{-}surf}$), Tc in the center with vacancy in Fe_{oct2} ($Vac_{cent\text{-}oct2}$) or vice-versa ($Vac_{oct2\text{-}cent}$), or Tc in Fe_{oct2} position and the vacancy in surface-Fe_{oct1} position ($Vac_{oct2\text{-}surf}$) or vice-versa ($Vac_{surf\text{-}oct2}$). A substitution only within the Fe_{oct2}-layer is not possible due to the magnetite crystal structure.

4.2.2 EXAFS spectra

In this study, experimental and theoretical EXAFS spectra were compared to investigate the Tc incorporation mechanism. Experimentally, a Tc magnetite coprecipitation sample with 600 ppm Tc was prepared in a glovebox under anoxic conditions ($c(O_2) < 1$ ppm). First, 110 mg $Fe(II)Cl_2 \cdot 4\ H_2O$ and 280 mg $Fe(III)Cl_3 \cdot 4\ H_2O$ (resulting in 200 mg magnetite) were dissolved in 20 mL of 0.01 M HCl. Subsequently, an aliquot of a 10 mM $KTcO_4$ stock solution was added to the Fe(II) and Fe(III) solution, followed by the addition of 2.5 mL of 6 M NH_4OH under vivid shaking. The resulting black solid, was washed three times with milli-Q water and then stored in the final washing solution for seven days.

After centrifugation, the wet paste was mounted with Kapton tape in a doubly sealed HDPE plastic sample holder inside the glovebox. To prevent an alteration of the sample during further storage and transport to the synchrotron facility, the sample was flash-frozen with liquid nitrogen immediately after removal from the glovebox, and stored in a liquid nitrogen container for transportation. Experimental spectra were acquired at the Rossendorf Beamline (BM20 at ESRF)[61] in fluorescence mode at the Tc K-edge (21 044 eV). The energy of the Si(111) double crystal monochromator was calibrated using a Mo foil (edge energy 20 000 eV). Two Rh-coated mirrors in 2.5 mrad grazing angle were used to suppress higher harmonics and to collimate the beam onto the monochromator crystal. Fluorescence spectra were collected with a 18-element, high-purity, solid-state Ge detector (Ultra-LEGe, GUL0055, Mirion Technologies) with digital spectrometer (XIA Falcon-X). During the measurement, the samples were kept at 15 K within a closed cycle He cryostat to avoid photon-induced changes of oxidation state and to reduce thermal disorder.

Theoretical EXAFS spectra were obtained with the FEFF code[62–64] (version 8.4) for each structural configuration considered in the *ab initio* calculations. A cluster with a radius of a 9.0 Å around each Tc cation was used as input. The synthetic spectra were used for linear combination fitting of experimental data in the range of $2\,\text{Å}^{-1} \leq k \leq 10\,\text{Å}^{-1}$. Different approaches and parameter combinations were tested, the best agreement with the experimental data could be obtained with the synthetic dataset obtained with a non-SCF muffin-tin potential model, Debye-Waller factor (σ^2) of 0.005 and amplitude reduction factor (S_0^2) of 0.99.

4.3 Results and Discussion

4.3.1 Determination of Hubbard *U* parameter for Tc(IV)

TABLE 4.1: Structural parameters of different TcO_2-polymorphs obtained by DFT calculations with the Hubbard *U*-correction set to 0 eV.

	Method	init. spin	a[Å]	b[Å]	c[Å]	β[°]
α-TcO_2	Rodriguez et al.[55]	(experiment, RT)	5.689	4.755	5.520	121.5
	Oliveira et al.[30]	*	5.733	4.825	5.588	121.5
	CP2K	AFM	5.631	4.771	5.512	121.4
		FM	6.241	4.680	5.571	124.1
	VASP	AFM	5.663	4.792	5.558	121.3
		FM	5.663	4.792	5.558	121.3
β-TcO_2	Oliveira et al.[30]	*	4.760	5.708	4.706	90.0
	CP2K	AFM	4.717	5.600	4.625	90.0
		FM	4.536	5.653	5.166	90.0
	VASP	AFM	4.763	5.636	4.649	90.0
		FM	4.763	5.636	4.649	90.0

* Oliveira et al.[30] did not specify how the spin polarization of the setup was initialized, antiferromagnetic (AFM) or ferromagnetic (FM).

A possible Hubbard *U* correction for the transition metal element of Tc was investigated. The testing results for a wide range of *U*-values with two different computational codes (Table S4.1 in SI) suggest that for Tc(IV) octahedrally coordinated by oxygen, no Hubbard correction is required to obtain sufficiently accurate electronic and structural properties. Especially the latter is in line with findings by Taylor et al.[65]. The analysis of the density of states (DOS) resolves TcO_2 to be metallic, both from Oliveira et al.[30] as well as from the simulations conducted in the present study (Figure S4.1 in SI). Contrasting, the use of a *U* parameter would in turn shift the unoccupied d-states to higher energies and open a band gap.

Moreover, as in general 4d-orbitals occupy more space than the 3d-orbitals, the electrons can be considered as less correlated[51] and less localized[50]. This further corroborates our modeling setup using $U = 0\,\text{eV}$ for Tc(IV) six-fold coordinated by oxygen. The corresponding occupation numbers are shown in Table S4.2 in SI.

Table 4.1 lists the lattice parameters and angles of the two polymorphs with lowest total energy, α- and β-TcO_2. A reasonable fit to available literature data using the aforementioned basis sets and pseudo-potentials in CP2K and VASP could be obtained. Our simulations energetically favor the β-TcO_2-polymorph (Table S4.3 in SI) and achieve a good agreement with literature data, also for ReO_2 as TcO_2 analog. Hence, for the subsequent simulations of Tc(IV) octahedrally coordinated by oxygen, the parameter of $U_{\text{eff}} = 0\,\text{eV}$ was used. Furthermore, focusing on β-TcO_2 as the polymorph with lowest energy, both the initial anti- and ferromagnetic setup converge into the same anti-ferromagnetic state in agreement with previous studies[52,65,66]. Thus, this setting was used for the following simulations if at least two neighboring TcO_6 octahedra are present in the system.

In this way, a system of a β-TcO_2 chain was tested as suggested by Oliveira et al.[30] as dominant sorption product developing on the magnetite surface over a long time. Each of the Tc(IV) is expected to be octahedrally coordinated by two OH_2-groups and four oxygen connecting to the next TcO_6-octahedra in the *zigzag* chain (Figure S4.2 in SI). However, as can be observed from Table S4.4 in SI, neither the use of dispersion correction nor larger basis sets for O and H lead to improvements of all structural parameters relative to the previous study[30]. Hence, for the main subject of this study, the simulations were continued with the DZVP basis sets.

4.3.2 Substitution of octahedrally coordinated Fe ions by Tc in the magnetite crystal structure

Analysis of structural and electronic properties

TABLE 4.2: Coordination numbers (CN) and distances (r) of the coordinating shells around Tc substituting an octahedrally coordinated Fe ion in a $2 \times 2 \times 2$ supercell of magnetite, without (Iso) or with vacancy (Vac). For comparison, equivalent results for the pristine magnetite structure (Mag) around octahedrally coordinated Fe as well as the fit results of experimental EXAFS assuming incorporated Tc are given.

	Mag		Iso		Vac		EXAFS[11]	
shell	CN	r [Å]	CN	r [Å]	CN	r [Å]	CN	r [Å]
O	6	2.038	6	2.027	6	2.025	6	2.01
Fe_{oct}	6	2.951	6	2.973	5	2.962	6	3.08
Fe_{tet}	6	3.450	6	3.476	6	3.482	6	3.49

The substitution of Tc for Fe in the magnetite structure is feasible due to the concordance of ionic radius of Fe^{3+} and Tc^{4+} in octahedral coordination[38]. Structural parameters of the Fe_{oct}

and Tc_{oct} coordination shells in bulk magnetite are compared in Table 4.2, analogous results for the substitution in the magnetite (111) surface slab can be found in Table S4.5 in SI. The Tc-O distance in the first coordination shell is slightly shortened compared to the original magnetite structure, whereas the Tc-Fe distances in the second and third coordination shells to edge-sharing Fe_{oct} and corner-sharing Fe_{tet} are increased.

The predicted changes in the Tc-magnetite coordination environment for both substitution mechanisms agree well with the structural results obtained by the analysis of experimental EXAFS data[11]. The distances match experimental observations with a maximum deviation of radius below 3 % in the O shell, below 7 % deviation in the Fe_{oct} shell, and below 0.4 % deviation in the Fe_{tet} shell. The coordination numbers agree within the known uncertainties, too. Hence, the local structural environment of Tc in magnetite can be confirmed by two independent methods.

Compared to the pristine magnetite system, both systems with Tc substitution reveal only few changes in the total density of states (TDOS, Figure S4.4 (a) in SI). These merely small changes can be expected from the substitution of one to two (with vacancy) out of 128 Fe_{oct} in the system. However, the Tc d-states (Figure S4.4 (b) in SI) contribute to the electronic density around the Fermi level leading to a slight overall decrease in the electronic band gap (Table S4.6 in SI). This is especially true for the Vac mechanism, where the decrease of both α and β band gap may reflect an increased conductivity of the system. Moreover, as the valence states of Tc have slightly lower energy, a preferred occupation of these compared to the Fe valence states can be assumed. This behavior is reflected in the increased Mulliken occupation (Table S4.7 in SI).

Interpretation of EXAFS spectra

In Figure 4.2, the experimental and simulated EXAFS spectra for the substitution mechanisms in bulk magnetite are depicted. As can be seen, the spectra of the individual mechanisms are very different among each other and in comparison to the experimental data. However, the best fit to qualitatively reproduce the experimental spectrum can be achieved by combining the two substitution mechanisms. With this fit, the mechanism including a vacancy appears to be dominant and can be assumed to prevail with approximately 69.3 %.

For the substitution in the magnetite (111) surface slab, a similar result is achieved. The corresponding plot is shown in Figure 4.3, displaying the best fit with approximately 60.3 % $Vac_{cent\text{-}cent}$, 16.7 % $Vac_{surf\text{-}surf}$ and 23.0 % $Vac_{oct2\text{-}surf}$. The other mechanisms - including all Iso mechanisms - account each for below 1×10^{-6} % in the superposition of the fit and can, hence, be considered as of less importance.

Concluding, the prevalence of the substitution mechanism including the formation of a vacancy can be deduced. Moreover, with a preference for Tc in the central and almost central position (center Fe_{oct1} and Fe_{oct2}), Tc seems to be surrounded by octahedrally coordinated Fe dominantly in a three-dimensional arrangement.

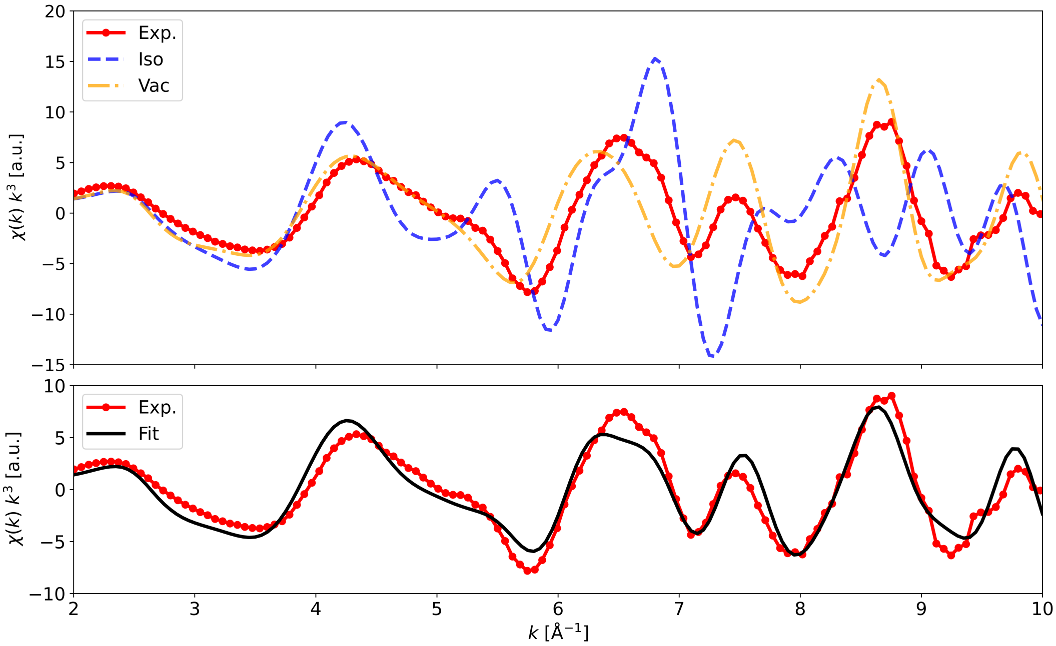

FIGURE 4.2: Theoretical k^3-weighted EXAFS spectra of systems based on $2 \times 2 \times 2$ magnetite supercell with substitution of one Tc (Iso, blue) and one Tc and one vacancy (Vac, orange) to experimentally obtained EXAFS data (red). The black line represents a fit as combination of both mechanisms with approximately 30.7 % Iso and 69.3 % Vac.

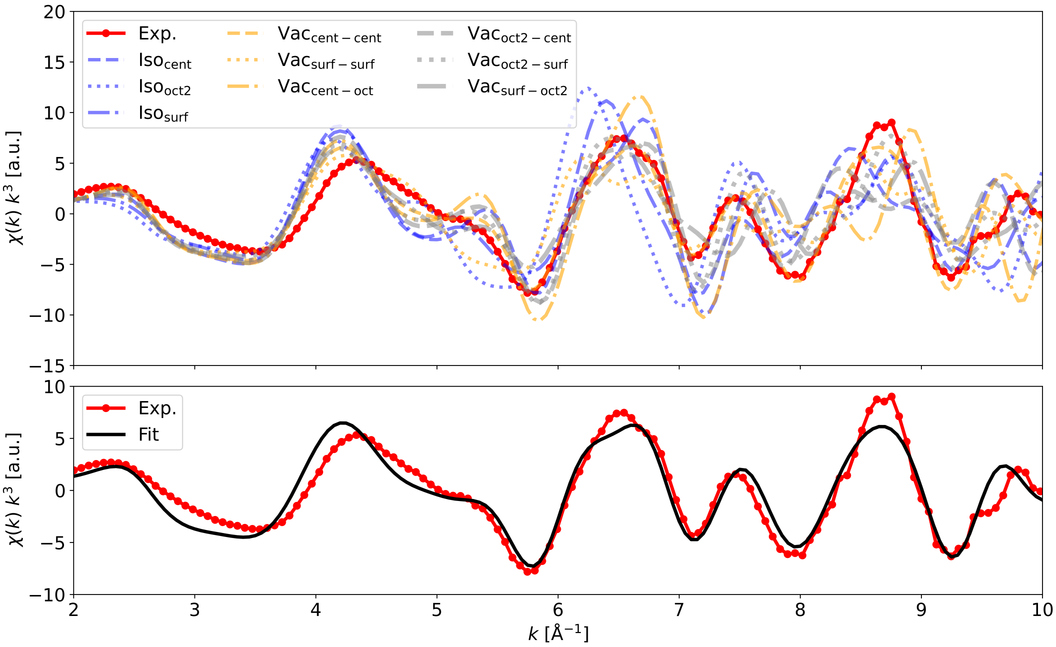

FIGURE 4.3: Theoretical k^3-weighted EXAFS spectra of systems based on the magnetite (111) surface slab with substitution of one Tc (mechanisms Iso, blue) and one Tc and one vacancy (mechanisms Vac, orange and gray) to experimentally obtained EXAFS data (red). The black line represents a fit as combination of all surface mechanisms with approximately 60.3 % $\mathrm{Vac_{cent\text{-}cent}}$, 16.7 % $\mathrm{Vac_{surf\text{-}surf}}$ and 23.0 % $\mathrm{Vac_{oct2\text{-}surf}}$.

Relative stability of Tc substitutions in magnetite

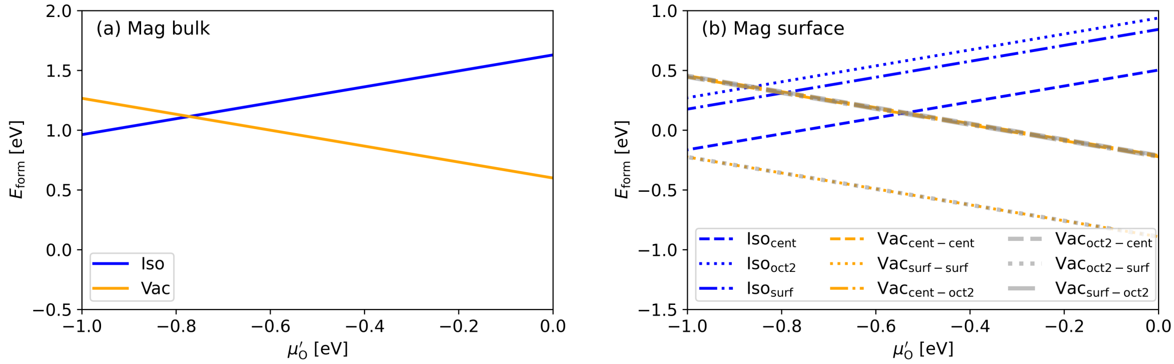

FIGURE 4.4: Formation energy, E_{form}, as function of the chemical potential of oxygen, μ'_O,[29] for the different Tc incorporation mechanisms for (a) magnetite bulk substitution, and (b) substitution in the magnetite surface slab.

To reveal the favorable thermodynamic conditions for the different mechanisms of Tc incorporation in magnetite, the formation energy of the $Fe^{2.5+}$-Tc^{4+} exchange as function of oxygen potential was calculated (Figure 4.4) following the same approach as proposed by Bianchetti et al.[29] (further details see SI). The predicted stability fields for different Tc incorporation mechanisms agree with the data reported in literature for similar systems[29]. For mechanisms with a substitution in the bulk magnetite structure (Figure 4.4 (a)), at lower oxygen potentials ($\mu'_O = -1\,\text{eV}$), the Iso mechanism results in a lower formation energy. Hence, it can be assumed the mechanism without the formation of a vacancy is favored at low oxygen pressures. Contrasting, at high oxygen potentials ($\mu'_O = 0\,\text{eV}$), the Vac mechanism is favored energetically. For the incorporation in bulk magnetite, the generally positive formation energy signifies a less favorable setting as the ideal magnetite structure is disturbed.

To better understand the dynamics of the Tc incorporation during the crystal growth and the role of the surface structure in the Tc entrapment, the corresponding stability calculations were conducted and displayed in Figure 4.4 (b) denoting the Tc-Vac-distance to the surface. Over the whole range of relevant oxygen potentials, the Vac mechanisms with the vacancy located close to the surface ($Vac_{oct2\text{-}surf}$ and $Vac_{surf\text{-}surf}$) yield the lowest energy. The Iso mechanisms are energetically less favorable.

It can be assumed, that in a dynamic process of dissolution and recrystallization at the dominant (111) surface of magnetite, layers of only octahedrally coordinated Fe ions (oct1, here center Fe and surface Fe) are more likely to incorporate Tc. This might be because of their higher number of octahedrally coordinated Fe which is three times as high as those in the oct2-layer with oxygen coordinated Fe_{oct2}. Moreover, the oct1-layers have been found to have a higher stability under geochemically relevant conditions[39] and may experience a longer exposure allowing for extended fluid-surface interaction and, hence, serve as the substitution matrix. In the process of crystal growth of the magnetite nanoparticles, these oct1-layers may be overgrown. A position of Tc not-directly at the surface in line with the EXAFS results might as well be more stabilized by the surrounding magnetite structure. The resulting structure of a (potential) nanoparticle with a magnetite core, a subsequent shell enriched in Tc and an outer Tc-depleted shell has been observed experimentally for octahedrally shaped magnetite nanocrystals[67] corroborating this assumed growth mechanism.

Compared to the previous study on the Tc(IV) incorporation in the magnetite (001) surface[29], we report higher formation energies for the incorporation in the idealized magnetite (111) surface. These difference are to be attributed to the principally different facet type and their surface reconstruction. Moreover, the system studied by Bianchetti et al.[29] includes undercoordinated Fe at the surface contrasting the hydrogen-saturated surface-oxygen present in our models to reflect environmental conditions. However, the identified preferred incorporation mechanisms for both surface types include the formation of a vacancy. This may alter the magnetite crystal structure and, in the long-term and with several incorporated Tc-Vac pairs, lead to a transition towards maghemite, also observed experimentally by the oxidation of magnetite[68].

4.3.3 Octahedrally coordinated Tc ions surrounded by oxygen – Interpretation of Tc(IV)

Tc is initialized in this study as Tc(IV) as expected from experiments[11]. Based on the idealized chemical conception of perfect ionic behavior of the species involved, this requires a change in the electron configuration of [Kr] $5s^2 4d^5$ for Tc(0) to [Kr] $5s^0 4d^3$ for Tc(IV). However, the idealized viewpoint does not necessarily uphold perfectly in the simulations.

First, by analogy for Tc, the octahedrally coordinated Fe as mix of Fe(II) and Fe(III) can be investigated as was done before[39,40]. From an idealized perspective, a shift from [Ar] $4s^2$ $3d^6$ for Fe(0) to [Ar] $4s^0$ $3d^6$ for Fe(II) and [Ar] $4s^0$ $3d^5$ for Fe(III) would be expected. Due to the high-spin configuration in magnetite, for both oxidation states the five d-orbitals would be half-filled with same spin alignment (spin up, majority spin), whereas for Fe(II) the sixth 3d-electron would be paired with an anti-parallel orientation (spin down, minority spin) in one of the d-orbitals[69]. The occupation can be analyzed by different methods, this study is based on the Mulliken population analysis[70]. As can be observed by the actual values of occupation (Figure S4.5 and Table S4.6 in SI) for the pristine magnetite system, the minority spin is approximately 0.5 signifying an intermediate oxidation state of all Fe_{oct} equivalent to an assumed average charge of +2.5.

Second, by analogy to Fe, the occupation of Tc states in TcO_2 (Table S4.2 in SI) were analyzed. Surprisingly, the sum of both spin up and spin down lies between 3.7 and 4.7 contrasting the idealized chemical conception. Yet, these investigated Tc systems have only octahedrally coordinated Tc surrounded by O and, hence, can be assumed to yield a reasonable interpretation of Tc(IV) in the simulations. In comparison, if Tc substituted magnetite is considered (Table S4.7), the occupation resembles that of the Tc dioxides indicating a stable configuration, especially for the ferromagnetic (FM) phases. This is in line with the design of the present study, where single Fe_{oct} are substituted by Tc ions representing a ferromagnetic setup, of course. Deriving the present oxidation state of Tc by comparing with Tc oxide is also commonly done in XAS experiments, e.g., deducing Tc(IV) in presence of magnetite by comparing XANES spectra to those of $TcO_2 \cdot x\, H_2O$ (s)[11].

The exchange of cations by substituting Fe by Tc results in a re-partitioning of electron density according to the electrochemical potential difference for these two redox-sensitive elements. In has to be considered, however, that magnetite is a conductive material and the Tc:Fe_{oct} ratio is smaller than 1:100. In such a system, a change of electron density of Fe_{oct} in range of 0.8 % would be sufficient to explain the observed electronic state of Tc, and is indeed the same order of magnitude of Fe_{oct} occupation change perceived (Table S4.6 in SI). Moreover, a test simulation was performed on the isostructural substitution setup with total system charge imposed to be +1 mimicking a change of Fe^{3+} with Tc^{4+}. It resulted in the nearly identical electronic occupation state of Tc (Table S4.7 in SI), whereas the charge compensation is almost entirely provided and reflected in a decreased minority spin of the Fe_{oct} ions signifying a slight overall tendency towards Fe(III). Contrasting in a system with total charge zero, the substitution of one Fe_{oct} by one Tc leads to a slight increase of minority spin.

This indicates that Fe_{oct} buffers the redox equilibrium in the system. I.e., a substitution of one $Fe^{2.5+}$ to Tc^{4+} results in an excess of positive charge (+1.5), which is in turn compensated by a reduction of the other octahedrally coordinated Fe. Similarly, the substitution of two $Fe^{2.5+}$ by one Tc^{4+} and a vacancy results in a deficit of positive charge (-1) being compensated by oxidizing the other Fe_{oct}, hence, a decrease in Fe minority spin. These shifts are observed only among the group of octahedrally coordinated Fe, as these have from the beginning an intermediate oxidation state in the (semi-)conductive material magnetite.

4.3.4 Interpretation in the context of nuclear waste and geochemical implications

The structural incorporation of Tc(IV) in iron minerals promises a stable separation of the radiotoxic element and the environment. With the Fe(II)-bearing minerals goethite and magnetite, a stable incorporation product can be achieved and these minerals can be used in the treatment of waste streams[31] such as the vitrification of nuclear waste, e.g., emerging from the Hanford site[71]. During the subsequent long-term disposal of radioactive waste, especially magnetite can play a major role in retention. Under expected repository conditions, the incorporation of Tc(IV) replacing octahedrally coordinated Fe ions has been experimentally proven[11]. In the present study, the dominating incorporation mechanism could be identified based on structural and spectroscopical analysis in comparison with these experiments. The incorporation favors the associated formation of a vacancy, while the octahedrally coordinated Fe cations can adapt to the changing charge conditions.

The formation of a vacancy in the magnetite leads to a topotactical formation of a crystal structure resembling maghemite. The associated trivalent state of all Fe cations as were observed in our previous computational studies on the magnetite surface[39] and magnetite nanoparticles[40]. Moreover, maghemite has been observed as oxidation product at the magnetite surface, commonly leading to particles with a magnetite core and maghemite shell[68,72]. These were observed in big-scale geological systems such as marine sediments[73], too. In the oxidation process, the formation of vacancies has been found to stabilize magnetite towards further oxidation[68,74] and leading to less strain in the crystal structure compared to a mere oxidation of the Fe cations[75]. Furthermore, the presence of vacancies might facilitate the uptake of ions that would otherwise not enter the magnetite structure[76]. Moreover, maghemite has been shown to act as better sorption matrix compared to magnetite for other environmentally toxic elements such as Se[77] and As[78].

The substitution of Fe(III) by a tetravalent cation provides the possibility of the formation of an adapted mineral phase. Octahedrally coordinated Ti(IV) has been observed in titanomagnetites[79] ($Ti_xFe_{3-x}O_4$) and titanomaghemites[80]. Especially the mixed-valence Fe cations in magnetite allow for a system with perfectly tunable Fe oxidation state depending on the amount of incorporated Ti[81]. In this case, an elevated amount of Fe(II) supports the reduction of mobile Tc(VII) and the incorporation of Tc(IV) into titanomagnetite may follow up[13]. Hence, magnetite/maghemite and adapted systems have the ability to ensure a long-term retention of Tc reducing risks for the living environment.

4.4 Acknowledgment

The authors acknowledge the funding from the German Federal Ministry of Education and Research (BMBF, KRIMI project - 02NUK056C), access to Swiss National Supercomputing Centre (CSCS, project number s1179) and access to UBELIX, the high-performance computing cluster at the University of Bern.

4.5 Supporting Information

4.5.1 Determination of Hubbard *U* parameter for Tc(IV)

TcO_2

TABLE S4.1: Results of spin-polarized VASP PBE simulations for α-TcO_2 with para- (PM), ferro- (FM) and anti-ferromagnetic (AFM) initialization. a and b in FM/AFM refer to the initialized spin up and down, respectively, of the four neighboring Tc present in a unit cell and that were preserved after convergence. Reported are the applied method, applied effective Hubbard U parameter, magnetization m, lattice parameters a, b, c and angle β of the monoclinic system. The last two columns comprise the electronic band gap E_g as well as the total energy E_{tot} of each unit cell.

Method	U_{eff} [eV]	m [μ_B]	a [Å]	b [Å]	c [Å]	β [°]	E_g [eV]	E_{tot} [eV]
(exp.)[55]			5.689	4.755	5.520	121.453		
PM								
	0.000	0.000	5.663	4.792	5.558	121.282	0.006	-99.073
	2.000	0.000	5.680	4.795	5.566	121.274	0.006	-89.942
	4.000	0.000	5.699	4.803	5.581	121.156	0.017	-81.139
FM								
(aaaa)	0.000	0.000	5.663	4.792	5.558	121.283	0.006	-99.073
(aaaa)	2.000	2.709	5.632	4.822	5.589	120.893	0.001	-89.991
(aaaa)	4.000	10.838	6.307	4.700	5.658	123.874	1.157	-84.351
AFM								
(aabb)	0.000	0.000	5.663	4.792	5.558	121.282	0.006	-99.073
(abba)	0.000	0.000	5.663	4.792	5.558	121.282	0.006	-99.073
(aabb)	2.000	1.239	5.707	4.819	5.604	121.013	0.002	-90.496
(abba)	2.000	2.153	6.199	4.705	5.602	123.306	0.402	-90.910
(aabb)	4.000	1.471	5.739	4.839	5.625	121.016	0.450	-83.019
(abba)	4.000	2.353	6.266	4.700	5.629	123.617	1.473	-84.806

TABLE S4.2: Averaged occupation for 4d-orbitals of Tc in TcO_2 based on Mulliken charge analysis (threshold per orbital: 0.2) in CP2K.

	AFM		FM	
Polymorph	spin up	spin down	spin up	spin down
α-TcO_2	2.355	2.355	3.885	0.648
β-TcO_2	2.332	2.332	3.717	0.000

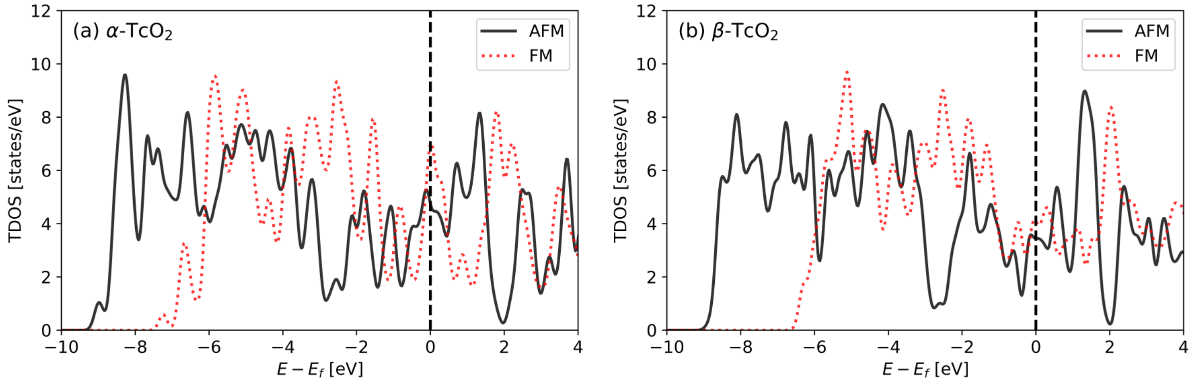

FIGURE S4.1: Total density of states (TDOS) of (a) α- and (b) β-TcO$_2$ obtained from CP2K ($U = 0\,\text{eV}$). Shown are the results of both the anti-ferromagnetic (AFM) as well as the ferromagnetic (FM) setup.

TABLE S4.3: Results of VASP PBE simulations for ReO$_2$- and corresponding TcO$_2$-polymorphs (Hubbard $U = 0$) in comparison to experiment and a previous computational study by Oliveira et al.[30]. Reported are the structural properties of lattice parameters (a, b, c) and the monoclinic angle (β), the electronic band gaps E_g as well as the relative energies ΔE.

Polymorph	Method	a [Å]	b [Å]	c [Å]	β [°]	E_g [eV]	ΔE [eV]
α-ReO$_2$	Experiment[82]	5.611	4.805	5.548	120.300		
	Oliveira et al.[30]	5.693	4.850	5.626	121.100		
	Materials Cloud[83]	5.552	4.877	5.623	119.861		
	PBE	5.548	4.872	5.619	119.839	0.004	22.423
β-ReO$_2$	Experiment[84]	4.809	5.643	4.601	90.000		
	Oliveira et al.[30]	4.799	5.746	4.650	90.000		
	Materials Cloud[83]	4.877	5.671	4.606	90.000		
	PBE	4.875	5.666	4.603	90.000	0.006	0.000
γ-ReO$_2$	Experiment[85]	4.798	4.798	2.808	90.000		
	Oliveira et al.[30]	4.900	4.900	2.755	90.000		
	Materials Cloud[83]	4.925	4.925	2.706	90.000		
	PBE	4.922	4.922	2.704	90.000	0.005	35.683
α-TcO$_2$	Experiment[55]	5.692	4.762	5.523	121.500		
	Oliveira et al.[30]	5.733	4.825	5.588	121.500		
	PBE	5.502	4.792	5.558	118.462	0.004	5.084
β-TcO$_2$	Oliveira et al.[30]	4.760	5.708	4.706	90.000		
	PBE	4.763	5.636	4.649	90.000	0.018	0.000
γ-TcO$_2$	Oliveira et al.[30]	4.813	4.813	2.842	90.000		
	PBE	4.824	4.824	2.763	90.000	0.006	19.046

β-TcO_2-chain

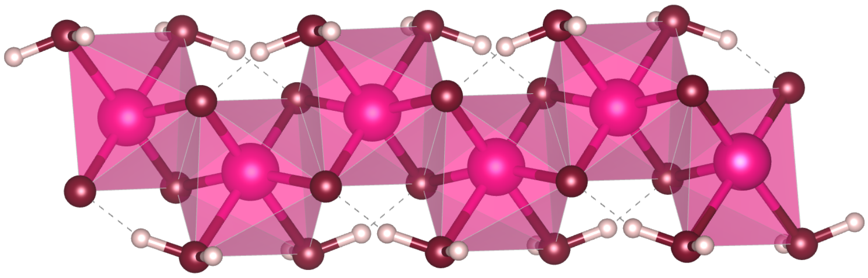

FIGURE S4.2: Optimized crystal structure of β-TcO_2-chain. Tc is shown in pink, O in red and H in pale pink. Atomic sizes are adapted for visualization.

TABLE S4.4: Intramolecular distance in Å between Tc and surrounding atoms of the β-TcO_2-chain in comparison with previously reported theoretical data[30]. Reported are the distances to the next coordination shells of nearest oxygen (μ-O) connecting to other TcO_6 octahedra, to nearest oxygen part of an OH_2-group as well as to the next Tc cations. The respective coordination numbers align with the reported[30]. A dispersion correction was applied using the DFT-D3 term by Grimme et al.[86,87]. Additionally, valence triple-zeta polarization (TZVP) basis sets for O and H were tested.

	Tc - (μ-O)	Tc - OH_2	Tc - Tc_1	Tc - Tc_2	Tc - Tc_3
Oliveira et al.[30]	1.980	2.230	2.530	4.600	6.980
CP2K DZVP	1.968	2.152	2.532	4.602	6.982
CP2K DZVP DFT-D3	1.968	2.155	2.533	4.601	6.982
CP2K TZVP DFT-D3	1.968	2.152	2.532	4.601	6.981

4.5.2 Tc substitution for octahedrally coordinated Fe

Substitution mechanisms in the surface slab

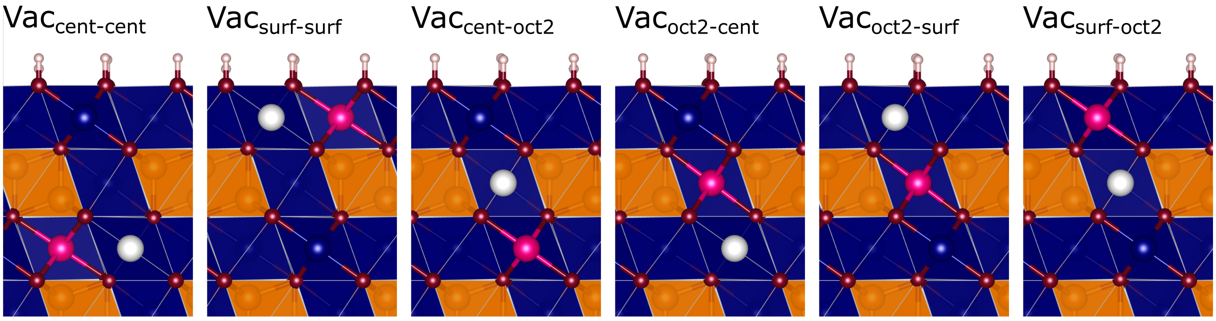

$\mathrm{Vac_{cent\text{-}cent}}$ $\mathrm{Vac_{surf\text{-}surf}}$ $\mathrm{Vac_{cent\text{-}oct2}}$ $\mathrm{Vac_{oct2\text{-}cent}}$ $\mathrm{Vac_{oct2\text{-}surf}}$ $\mathrm{Vac_{surf\text{-}oct2}}$

FIGURE S4.3: Schematic visualization of substitution mechanisms in the surface slab, in which two edge-connected octahedrally coordinated Fe (blue) are replaced by on Tc (pink) and one vacancy (white). Tetrahedrally coordinated Fe are depicted in orange, O in red and surface-H in pale pink.

TABLE S4.5: Coordination numbers (CN) and distances (r) of the first coordination shells around Tc substituting an octahedrally coordinated Fe in the magnetite (111) surface slab, without (Iso mechanisms) or with vacancy (Vac mechanisms).

	O		$\mathrm{Fe_{oct}}$		$\mathrm{Fe_{tet}}$	
mechanism	CN	r [Å]	CN	r [Å]	CN	r [Å]
$\mathrm{Iso_{cent}}$	6	2.040	6	2.938	6	3.496
$\mathrm{Iso_{oct2}}$	6	2.066	6	2.864	6	3.560
$\mathrm{Iso_{surf}}$	6	2.055	5	2.933	3	3.487
$\mathrm{Vac_{cent\text{-}cent}}$	6	2.017	5	2.971	6	3.474
$\mathrm{Vac_{surf\text{-}surf}}$	6	2.032	4	2.954	3	3.384
$\mathrm{Vac_{cent\text{-}oct2}}$	6	2.017	5	2.977	6	3.468
$\mathrm{Vac_{oct2\text{-}cent}}$	6	2.019	5	2.968	6	3.491
$\mathrm{Vac_{oct2\text{-}surf}}$	6	2.021	5	2.974	6	3.487
$\mathrm{Vac_{surf\text{-}oct2}}$	6	2.033	4	2.952	3	3.435

Electronic analysis

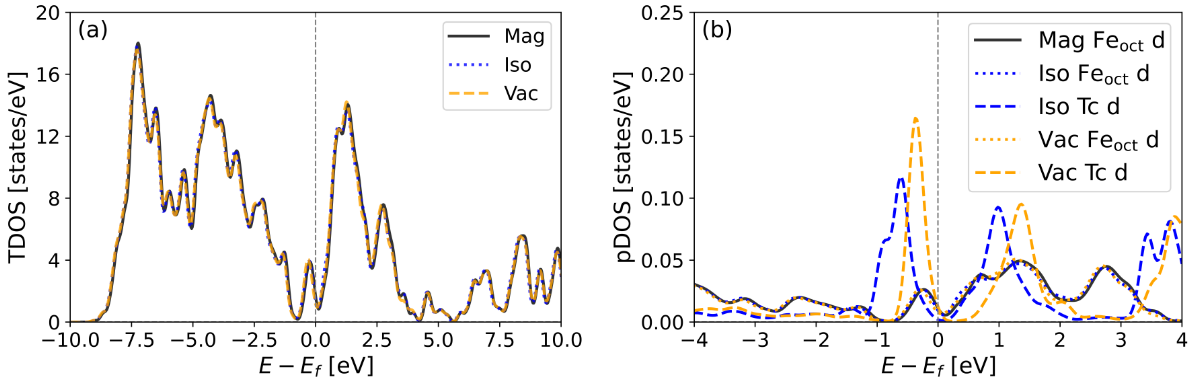

FIGURE S4.4: (a) Total density of states (TDOS) of possible Tc substitutions for octahedrally coordinated Fe (Fe_{oct}) in a $2 \times 2 \times 2$ supercell, substitution of one Fe by one Tc (Iso, blue) and of two Fe by one Tc and one vacancy (Vac, orange). For comparison, the TDOS of the optimized pristine magnetite (Mag) is plotted (black). (b) Projected density of states (pDOS) of Tc and Fe_{oct} d-states in the substitution systems and pristine Mag normalized to the number of respective atoms. For all data sets, the PDOS script by Tiziano Müller was used applying a convolution with Gaussian functions, standard deviation $\sigma = 0.004$ eV.

TABLE S4.6: Electronic band gaps (E_g) of the different systems based on a $2 \times 2 \times 2$ magnetite supercell and in comparison to pristine magnetite. The mean and median of the minority spin state occupation of octahedrally coordinated Fe in each system (Figure S4.5) are presented, too.

System	$E_g(\alpha)$ [eV]	$E_g(\beta)$ [eV]	mean min. spin	median min. spin
Mag	1.553	0.160	0.502	0.499
Iso	1.250	0.205	0.505	0.498
Iso (charge 1)	1.239	0.134	0.498	0.492
Vac	0.944	0.125	0.497	0.499

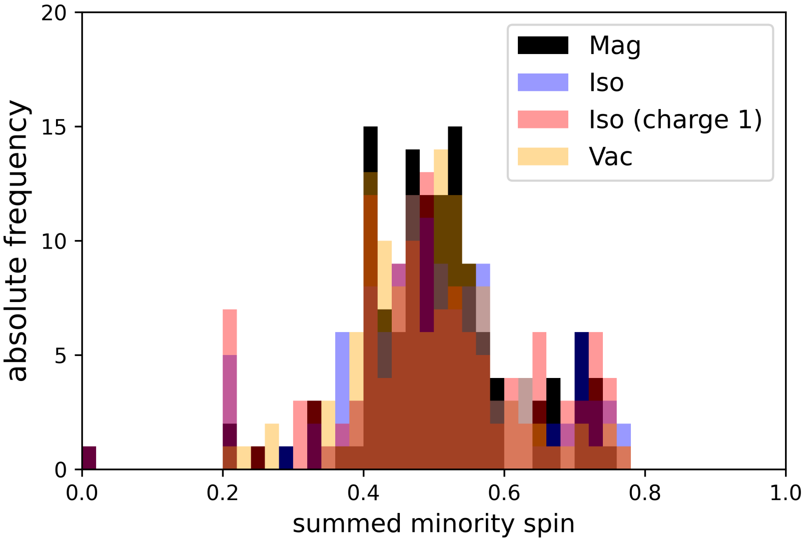

FIGURE S4.5: Histogram of the frequency of partial atomic charges, i.e., minority spin, obtained from the Mulliken population analysis of octahedrally coordinated Fe (spin down only, bin width = 0.02) in magnetite with possible Tc substitution (supercell with 2 × 2 × 2 unit cells). The charges of all *d*-orbitals of each Fe (d-2, d-1, d0, d+1, d+2) were summed (threshold per orbital: 0.2). As the distribution is unimodal and almost continuous, a clear distinction between Fe^{2+} and Fe^{3+} appears to be difficult (see Table S4.6, too).

TABLE S4.7: Occupation for 4d-orbitals of Tc substituting Fe_{oct} in magnetite summed for all five 4d-Orbitals based on Mulliken charge analysis (threshold per orbital: 0.2).

		spin up	spin down		spin up	spin down
Mag bulk	Iso	3.464	1.414	Vac	3.289	1.530
	Iso (charge 1)	3.465	1.419			
Mag surf.	Iso_{cent}	3.396	1.646	$Vac_{cent\text{-}cent}$	3.411	1.367
	Iso_{oct2}	3.195	2.019	$Vac_{surf\text{-}surf}$	3.538	1.180
	Iso_{surf}	3.440	1.624	$Vac_{cent\text{-}oct2}$	3.377	1.462
				$Vac_{oct2\text{-}cent}$	3.262	1.677
				$Vac_{oct2\text{-}surf}$	3.365	1.543
				$Vac_{surf\text{-}oct2}$	3.459	1.363

Thermodynamic considerations

To calculate the formation energy (Figure 4.4 in the main text of the manuscript), the approach proposed by Bianchetti et al.[29] was applied. The simplified reaction equation can be written as described in Equation S4.1. n signifies the number of created vacancies, i.e. 0 or 1 in the investigated systems. The formation energy E_{form} can then be calculated according to Equation S4.2. The chemical potentials of Fe and Tc, μ_{Fe} and μ_{Tc}, respectively, can be expressed as function of the chemical potential of oxygen, μ_{O} (Equation S4.3, Equation S4.4). To investigate the dependency of the formation energy on the amount of oxygen, the chemical potential of oxygen depends on the variable μ'_{O} (Equation S4.5) ranging from $-1\,\text{eV}$ to $0\,\text{eV}$[29]. All used energies E_{SCF} and chemical potentials of Fe_3O_4, TcO_2, O_2 and H_2 were obtained from *ab initio* simulations and are listed in Table S4.8.

$$\text{Mag system} + \text{Tc} \rightarrow \text{Mag-Tc system} + (1+n)\text{Fe} \tag{S4.1}$$

$$E_{\text{form}} = E_{\text{Mag-Tc system}} + (1+n)\mu_{\text{Fe}} - E_{\text{Mag system}} - \mu_{\text{Tc}} \tag{S4.2}$$

$$\mu_{\text{Fe}} = \frac{1}{3}(\mu_{\text{Fe}_3\text{O}_4} - 4\mu_{\text{O}}) \tag{S4.3}$$

$$\mu_{\text{Tc}} = \mu_{\text{TcO}_2} - 2\mu_{\text{O}} \tag{S4.4}$$

$$\mu_{\text{O}} = \frac{1}{2}\mu_{\text{O}_2} + \mu'_{\text{O}} \tag{S4.5}$$

TABLE S4.8: SCF energies of investigated systems. For the compounds in the first column, values are reported per formula unit.

	E_{SCF} [Ha]		E_{SCF} [Ha]		E_{SCF} [Ha]
Fe_3O_4	−434.1502	Iso	−27 742.8847	Vac	−27 619.4914
(β-)TcO_2	−112.6917	Iso_{cent}	−35 791.3538	$\text{Vac}_{\text{cent-cent}}$	−35 667.9489
O_2	−31.9284	Iso_{oct2}	−35 791.3378	$\text{Vac}_{\text{surf-surf}}$	−35 667.9739
H_2	−1.1619	Iso_{surf}	−35 791.3413	$\text{Vac}_{\text{cent-oct2}}$	−35 667.9493
				$\text{Vac}_{\text{oct2-cent}}$	−35 667.9482
				$\text{Vac}_{\text{oct2-surf}}$	−35 667.9747
				$\text{Vac}_{\text{surf-oct2}}$	−35 667.9429

4.6 References

[1] Papagiannopoulou, D. Technetium-99m Radiochemistry for Pharmaceutical Applications. *J. Labelled Compd. Radiopharm.* **2017**, *60*, 502–520.

[2] Warwick, P.; Aldridge, S.; Evans, N.; Vines, S. The Solubility of Technetium(IV) at High pH. *Radiochim. Acta* **2007**, *95*, 709–716.

[3] Churakov, S. V.; Hummel, W.; Fernandes, M. M. Fundamental Research on Radiochemistry of Geological Nuclear Waste Disposal. *Chimia* **2020**, *74*, 1000–1009.

[4] Yalçıntaş, E.; Gaona, X.; Scheinost, A. C.; Kobayashi, T.; Altmaier, M.; Geckeis, H. Redox Chemistry of Tc(VII)/Tc(IV) in Dilute to Concentrated NaCl and $MgCl_2$ Solutions. *Radiochim. Acta* **2015**, *103*, 57–72.

[5] Yalçıntaş, E.; Gaona, X.; Altmaier, M.; Dardenne, K.; Polly, R.; Geckeis, H. Thermodynamic Description of Tc(IV) Solubility and Hydrolysis in Dilute to Concentrated NaCl, $MgCl_2$ and $CaCl_2$ Solutions. *Dalton Trans.* **2016**, *45*, 8916–8936.

[6] Wersin, P.; Johnson, L.; Schwyn, B.; Berner, U.; Curti, E. *Redox Conditions in the Near Field of a Repository for SF/HLW and ILW in Opalinus Clay*; NAGRA tech. report 02-13, 2003.

[7] Jaisi, D. P.; Dong, H.; Plymale, A. E.; Fredrickson, J. K.; Zachara, J. M.; Heald, S.; Liu, C. Reduction and Long-term Immobilization of Technetium by Fe(II) Associated with Clay Mineral Nontronite. *Chem. Geol.* **2009**, *264*, 127–138.

[8] Chen, P.; Churakov, S. V.; Glaus, M.; Van Loon, L. R. Impact of Fe(II) on ^{99}Tc Diffusion Behavior in Illite. *Appl. Geochem.* **2023**, *156*, 105759.

[9] Chen, P.; Van Loon, L. R.; Koch, S.; Alt-Epping, P.; Reich, T.; Churakov, S. V. Reactive Transport Modeling of Diffusive Mobility and Retention of TcO_4^- in Opalinus Clay. *Appl. Clay Sci.* **2024**, *251*, 107327.

[10] Cui, D.; Eriksen, T. E. Reduction of Pertechnetate by Ferrous Iron in Solution: Influence of Sorbed and Precipitated Fe(II). *Environ. Sci. Technol.* **1996**, *30*, 2259–2262.

[11] Yalçıntaş, E.; Scheinost, A. C.; Gaona, X.; Altmaier, M. Systematic XAS Study on the Reduction and Uptake of Tc by Magnetite and Mackinawite. *Dalton Trans.* **2016**, *45*, 17874–17885.

[12] Schmeide, K.; Rossberg, A.; Bok, F.; Azzam, S. S. A.; Weiss, S.; Scheinost, A. C. Technetium Immobilization by Chukanovite and Its Oxidative Transformation Products: Neural Network Analysis of EXAFS Spectra. *Sci. Total Environ.* **2021**, *770*, 145334.

[13] Liu, J.; Pearce, C.; Qafoku, O.; Arenholz, E.; Heald, S.; Rosso, K. Tc(VII) Reduction Kinetics by Titanomagnetite ($Fe_{3-x}Ti_xO_4$) Nanoparticles. *Geochim. Cosmochim. Acta* **2012**, *92*, 67–81.

[14] Maes, A.; Geraedts, K.; Bruggeman, C.; Vancluysen, J.; Rossberg, A.; Hennig, C. Evidence for the Interaction of Technetium Colloids with Humic Substances by X-ray Absorption Spectroscopy. *Environ. Sci. Technol.* **2004**, *38*, 2044–2051.

[15] Skomurski, F. N.; Rosso, K. M.; Krupka, K. M.; McGrail, B. P. Technetium Incorporation into Hematite (Fe_2O_3). *Environ. Sci. Technol.* **2010**, *44*, 5855–5861.

[16] Smith, F. N.; Taylor, C. D.; Um, W.; Kruger, A. A. Technetium Incorporation into Goethite (α-FeOOH): An Atomic-scale Investigation. *Environ. Sci. Technol.* **2015**, *49*, 13699–13707.

[17] Rodríguez, D. M.; Mayordomo, N.; Scheinost, A. C.; Schild, D.; Brendler, V.; Müller, K.; Stumpf, T. New Insights into Tc(VII) Removal by Pyrite: A Spectroscopic Approach. *Environ. Sci. Technol.* **2020**, *54*, 2678–2687.

[18] Boglaienko, D.; Soltis, J. A.; Kukkadapu, R. K.; Du, Y.; Sweet, L. E.; Holfeltz, V. E.; Hall, G. B.; Buck, E. C.; Segre, C. U.; Emerson, H. P.; Katsenovich, Y.; Levitskaia, T. G. Spontaneous Redox Continuum Reveals Sequestered Technetium Clusters and Retarded Mineral Transformation of Iron. *Commun. Chem.* **2020**, *3*.

[19] Grambow, B.; Smailos, E.; Geckeis, H.; Müller, R.; Hentschel, H. Sorption and Reduction of Uranium(VI) on Iron Corrosion Products under Reducing Saline Conditions. *Radiochim. Acta* **1996**, *74*, 149–154.

[20] Johnson, L.; Schneider, J.; Zuidema, P.; Gribi, P.; Mayer, G.; Smith, P.; Kunz, B.; Frei, C. *Project Opalinus Clay - Demonstration of Disposal for Spent Fuel, Vitrified High-level Wast and Long-lived Intermediate-level Waste*; NAGRA tech. report 02-05, 2002.

[21] King, F. *Corrosion of Carbon Steel under Anaerobic Conditions in a Repository for SF and HLW in Opalinus Clay*; NAGRA tech. report 08-12, 2008.

[22] Schlegel, M. L.; Bataillon, C.; Blanc, C.; Prêt, D.; Foy, E. Anodic Activation of Iron Corrosion in Clay Media under Water-saturated Conditions at 90 °C: Characterization of the Corrosion Interface. *Environ. Sci. Technol.* **2010**, *44*, 1503–1508.

[23] El Hajj, H.; Abdelouas, A.; El Mendili, Y.; Karakurt, G.; Grambow, B.; Martin, C. Corrosion of Carbon Steel under Sequential Aerobic-Anaerobic Environmental Conditions. *Corros. Sci.* **2013**, *76*, 432–440.

[24] Wersin, P.; Jenni, A.; Mäder, U. K. Interaction of Corroding Iron with Bentonite in the ABM1 Experiment at Äspö, Sweden: A Microscopic Approach. *Clays Clay Miner.* **2015**, *63*, 51–68.

[25] Heald, S. M.; Krupka, K. M.; Brown, C. F. Incorporation of Pertechnetate and Perrhenate into Corroded Steel Surfaces Studied by X-ray Absorption Fine Structure Spectroscopy. *Radiochim. Acta* **2011**, *100*, 243–253.

[26] Kobayashi, T.; Scheinost, A. C.; Fellhauer, D.; Gaona, X.; Altmaier, M. Redox Behavior of Tc(VII)/Tc(IV) under Various Reducing Conditions in 0.1 M NaCl Solutions. *Radiochim. Acta* **2013**, *101*, 323–332.

[27] Lee, M.-S.; Um, W.; Wang, G.; Kruger, A. A.; Lukens, W. W.; Rousseau, R.; Glezakou, V.-A. Impeding ^{99}Tc(IV) Mobility in Novel Waste Forms. *Nat. Commun.* **2016**, *7*.

[28] Bauters, S.; Scheinost, A. C.; Schmeide, K.; Weiss, S.; Dardenne, K.; Rothe, J.; Mayordomo, N.; Steudtner, R.; Stumpf, T.; Abram, U.; Butorin, S. M.; Kvashnina, K. O. Signatures of Technetium Oxidation States: A New Approach. *Chem. Commun.* **2020**, *56*, 9608–9611.

[29] Bianchetti, E.; Oliveira, A. F.; Scheinost, A. C.; Valentin, C. D.; Seifert, G. Chemistry of the Interaction and Retention of Tc(VII) and Tc(IV) Species at the Fe_3O_4 (001) Surface. *J. Phys. Chem. C* **2023**, *127*, 7674–7682.

[30] Oliveira, A. F.; Kuc, A.; Heine, T.; Abram, U.; Scheinost, A. C. Shedding Light on the Enigmatic $TcO_2 \cdot x\ H_2O$ Structure with Density Functional Theory and EXAFS Spectroscopy. *Chem. Eur. J.* **2022**, *28*.

[31] Um, W.; Chang, H.-S.; Icenhower, J. P.; Lukens, W. W.; Serne, R. J.; Qafoku, N. P.; Westsik, J. H.; Buck, E. C.; Smith, S. C. Immobilization of 99-Technetium (VII) by Fe(II)-Goethite and Limited Reoxidation. *Environ. Sci. Technol.* **2011**, *45*, 4904–4913.

[32] Smith, F. N.; Um, W.; Taylor, C. D.; Kim, D.-S.; Schweiger, M. J.; Kruger, A. A. Computational Investigation of Technetium(IV) Incorporation into Inverse Spinels: Magnetite (Fe_3O_4) and Trevorite ($NiFe_2O_4$). *Environ. Sci. Technol.* **2016**, *50*, 5216–5224.

[33] Lukens, W. W.; Saslow, S. A. Facile Incorporation of Technetium into Magnetite, Magnesioferrite, and Hematite by Formation of Ferrous Nitrate in Situ: Precursors to Iron Oxide Nuclear Waste Forms. *Dalton Trans.* **2018**, *47*, 10229–10239.

[34] Saslow, S. A.; Pearce, C. I.; Bowden, M. E.; Lukens, W. W.; Kim, D.-S.; Kruger, A. A.; Um, W. Kinetics of Co-mingled ^{99}Tc and Cr Removal during Mineral Transformation of Ferrous Hydroxide. *ACS Earth Space Chem.* **2019**, *4*, 218–228.

[35] Wang, G.; Saslow, S. A.; Eaton, W. C.; Kruger, A. A.; Asmussen, R. M. Removal of Technetium from Waste Stream by Iron Spinel and Stability against Leaching. *ACS Earth Space Chem.* **2023**, *7*, 1770–1780.

[36] McBeth, J. M.; Lloyd, J. R.; Law, G. T. W.; Livens, F. R.; Burke, I. T.; Morris, K. Redox Interactions of Technetium with Iron-bearing Minerals. *Mineral. Mag.* **2011**, *75*, 2419–2430.

[37] Marshall, T. A.; Morris, K.; Law, G. T. W.; Mosselmans, J. F. W.; Bots, P.; Parry, S. A.; Shaw, S. Incorporation and Retention of 99-Tc(IV) in Magnetite under High pH Conditions. *Environ. Sci. Technol.* **2014**, *48*, 11853–11862.

[38] Shannon, R. D. Revised Effective Ionic Radii and Systematic Studies of Interatomic Distances in Halides and Chalcogenides. *Acta Cryst. A* **1976**, *32*, 751–767.

[39] Katheras, A. S.; Karalis, K.; Krack, M.; Scheinost, A. C.; Churakov, S. V. Stability and Speciation of Hydrated Magnetite {111} Surfaces from *Ab Initio* Simulations with Relevance for Geochemical Redox Processes. *Environ. Sci. Technol.* **2024**, *58*, 935–946.

[40] Katheras, A. S.; Karalis, K.; Krack, M.; Scheinost, A. C.; Churakov, S. V. Computational Study on the Octahedral Surfaces of Magnetite Nanoparticles and Their Solvent Interaction. *Environ. Sci. Technol.* **2024**, *58*, 21068–21076.

[41] VandeVondele, J.; Krack, M.; Mohamed, F.; Parrinello, M.; Chassaing, T.; Hutter, J. QUICKSTEP: Fast and Accurate Density Functional Calculations Using a Mixed Gaussian and Plane Waves Approach. *Comput. Phys. Commun.* **2005**, *167*, 103–128.

[42] Kühne, T. D. et al. CP2K: An Electronic Structure and Molecular Dynamics Software Package - Quickstep: Efficient and Accurate Electronic Structure Calculations. *J. Chem. Phys.* **2020**, *152*, 194103.

[43] Goedecker, S.; Teter, M.; Hutter, J. Separable Dual-Space Gaussian Pseudopotentials. *Phys. Rev. B* **1996**, *54*, 1703–1710.

[44] Krack, M. Pseudopotentials for H to Kr Optimized for Gradient-corrected Exchange-Correlation Functionals. *Theor. Chem. Acc.* **2005**, *114*, 145–152.

[45] Bosoni, E. et al. How to Verify the Precision of Density-functional-theory Implementations Via Reproducible and Universal Workflows. *Nat. Rev. Phys.* **2023**, *6*, 45–58.

[46] VandeVondele, J.; Hutter, J. Gaussian Basis Sets for Accurate Calculations on Molecular Systems in Gas and Condensed Phases. *J. Chem. Phys.* **2007**, *127*, 114105.

[47] VandeVondele, J.; Hutter, J. An Efficient Orbital Transformation Method for Electronic Structure Calculations. *J. Chem. Phys.* **2003**, *118*, 4365–4369.

[48] Hubbard, J. Electron Correlations in Narrow Energy Bands. *Proc. Roy. Soc. Lond. Math. Phys. Sci.* **1963**, *276*, 238–257.

[49] Dudarev, S. L.; Botton, G. A.; Savrasov, S. Y.; Humphreys, C. J.; Sutton, A. P. Electron-Energy-Loss Spectra and the Structural Stability of Nickel Oxide: An LSDA+U Study. *Phys. Rev. B* **1998**, *57*, 1505–1509.

[50] Mravlje, J.; Aichhorn, M.; Georges, A. Origin of the High Néel Temperature in $SrTcO_3$. *Phys. Rev. Lett.* **2012**, *108*, 197202.

[51] Zhang, W.; Tong, P. Structural, Elastic, Magnetic and Electronic Properties of 4d Perovskite $CaTcO_3$: A DFT+U Investigation. *J. Phys.: Condens. Matter* **2012**, *24*, 185401.

[52] Horvat, A.; Pourovskii, L.; Aichhorn, M.; Mravlje, J. Theoretical Prediction of Antiferromagnetism in Layered Perovskite Sr_2TcO_4. *Phys. Rev. B* **2017**, *95*, 205115.

[53] Dickson, J. O.; Harsh, J. B.; Lukens, W. W.; Pierce, E. M. Perrhenate Incorporation into Binary Mixed Sodalites: The Role of Anion Size and Implications for Technetium-99 Sequestration. *Chem. Geol.* **2015**, *395*, 138–143.

[54] Coutelot, F.; Thomas, R. J.; Seaman, J. C. Using Porous Iron Composite (PIC) Material to Immobilize Rhenium as an Analogue for Technetium. *Environ. Int.* **2019**, *128*, 379–389.

[55] Rodriguez, E. E.; Poineau, F.; Llobet, A.; Sattelberger, A. P.; Bhattacharjee, J.; Waghmare, U. V.; Hartmann, T.; Cheetham, A. K. Structural Studies of TcO_2 by Neutron Powder Diffraction and First-principles Calculations. *J. Am. Chem. Soc.* **2007**, *129*, 10244–10248.

[56] Kresse, G.; Hafner, J. *Ab Initio* Molecular Dynamics for Liquid Metals. *Phys. Rev. B* **1993**, *47*, 558–561.

[57] Kresse, G.; Hafner, J. *Ab Initio* Molecular-Dynamics Simulation of the Liquid-Metal–Amorphous-Semiconductor Transition in Germanium. *Phys. Rev. B* **1994**, *49*, 14251–14269.

[58] Kresse, G.; Furthmüller, J. Efficient Iterative Schemes for *Ab Initio* Total-Energy Calculations Using a Plane-Wave Basis Set. *Phys. Rev. B* **1996**, *54*, 11169–11186.

[59] Kresse, G.; Furthmüller, J. Efficiency of $Ab - Initio$ Total Energy Calculations for Metals and Semiconductors Using a Plane-Wave Basis Set. *Comput. Mater. Sci.* **1996**, *6*, 15–50.

[60] Sasaki, S. Radial Distribution of Electron Density in Magnetite, Fe_3O_4. *Acta Cryst. B* **1997**, *53*, 762–766.

[61] Scheinost, A. C. et al. ROBL-II at ESRF: A Synchrotron Toolbox for Actinide Research. *J. Synchrotron Rad.* **2021**, *28*, 333–349.

[62] Rehr, J. J.; Albers, R. C. Theoretical Approaches to X-ray Absorption Fine Structure. *Rev. Mod. Phys.* **2000**, *72*, 621–654.

[63] Ankudinov, A. L.; Ravel, B.; Rehr, J. J.; Conradson, S. D. Real-Space Multiple-Scattering Calculation and Interpretation of X-ray-Absorption Near-Edge Structure. *Phys. Rev. B* **1998**, *58*, 7565–7576.

[64] Rehr, J. J.; Kas, J. J.; Prange, M. P.; Sorini, A. P.; Takimoto, Y.; Vila, F. *Ab Initio* Theory and Calculations of X-ray Spectra. *Comptes Rendus. Physique* **2008**, *10*, 548–559, Theoretical spectroscopy.

[65] Taylor, C. D. Oxidation of Technetium Metal As Simulated by First Principles. *J. Phys. Chem. C* **2014**, *118*, 10017–10023.

[66] Xiao, X.-B.; Liu, B.-G. Field-induced Half-metallic Phase in Epitaxial TcO_2 Bilayer on Rutile TiO_2 Surface. *J. Magn. Magn. Mater.* **2021**, *540*, 168478.

[67] Wang, G.; Olszta, M. J.; Saslow, S. A.; Kim, D.-S.; Bowden, M. E.; Um, W.; Wang, J.; Kruger, A. A. A Focused Ion Beam-scanning Transmission Electron Microscopy with Energy-dispersive X-ray Spectroscopy Study on Technetium Incorporation within Iron Oxides through $Fe(OH)_2(s)$ Mineral Transformation. *ACS Earth Space Chem.* **2021**, *5*, 525–534.

[68] Li, Z.; Chanéac, C.; Berger, G.; Delaunay, S.; Graff, A.; Lefèvre, G. Mechanism and Kinetics of Magnetite Oxidation under Hydrothermal Conditions. *RSC Adv.* **2019**, *9*, 33633–33642.

[69] Yanase, A.; Hamada, N. Electronic Structure in High Temperature Phase of Fe_3O_4. *J. Phys. Soc. Jpn.* **1999**, *68*, 1607–1613.

[70] Mulliken, R. S. Electronic Population Analysis on LCAO–MO Molecular Wave Functions. I. *J. Chem. Phys.* **1955**, *23*, 1833–1840.

[71] Pegg, I. L. Behavior of Technetium in Nuclear Waste Vitrification Processes. *J. Radioanal. Nucl. Chem.* **2015**, *305*, 287–292.

[72] Schwaminger, S. P.; Bauer, D.; Fraga-García, P.; Wagner, F. E.; Berensmeier, S. Oxidation of Magnetite Nanoparticles: Impact on Surface and Crystal Properties. *Cryst. Eng. Comm.* **2017**, *19*, 246–255.

[73] Yamazaki, T.; Solheid, P. Maghemite-to-Magnetite Reduction across the Fe-redox Boundary in a Sediment Core from the Ontong-Java Plateau: Influence on Relative Palaeointensity Estimation and Environmental Magnetic Application. *Geophys. J. Int.* **2011**, *185*, 1243–1254.

[74] Auffan, M.; Rose, J.; Proux, O.; Borschneck, D.; Masion, A.; Chaurand, P.; Hazemann, J.-L.; Chaneac, C.; Jolivet, J.-P.; Wiesner, M. R.; Van Geen, A.; Bottero, J.-Y. Enhanced Adsorption of Arsenic onto Maghemites Nanoparticles: As(III) as a Probe of the Surface Structure and Heterogeneity. *Langmuir* **2008**, *24*, 3215–3222.

[75] Yuan, K.; Lee, S. S.; Cha, W.; Ulvestad, A.; Kim, H.; Abdilla, B.; Sturchio, N. C.; Fenter, P. Oxidation Induced Strain and Defects in Magnetite Crystals. *Nat. Commun.* **2019**, *10*.

[76] Lininger, C. N.; Cama, C. A.; Takeuchi, K. J.; Marschilok, A. C.; Takeuchi, E. S.; West, A. C.; Hybertsen, M. S. Energetics of Lithium Insertion into Magnetite, Defective Magnetite, and Maghemite. *Chem. Mater.* **2018**, *30*, 7922–7937.

[77] Jordan, N.; Ritter, A.; Foerstendorf, H.; Scheinost, A.; Weiß, S.; Heim, K.; Grenzer, J.; Mücklich, A.; Reuther, H. Adsorption Mechanism of Selenium(VI) onto Maghemite. *Geochim. Cosmochim. Acta* **2013**, *103*, 63–75.

[78] Mejia-Santillan, M.; Pariona, N.; Bravo-C., J.; Herrera-Trejo, M.; Montejo-Alvaro, F.; Zarate, A.; Perry, D.; Mtz-Enriquez, A. Physical and Arsenic Adsorption Properties of Maghemite and Magnetite Sub-microparticles. *J. Magn. Magn. Mater.* **2018**, *451*, 594–601.

[79] Wechsler, B. A.; Lindsley, D. H.; Prewitt, C. T. Crystal Structure and Cation Distribution in Titanomagnetites ($Fe_{3-x}Ti_xO_4$). *Am. Mineral.* **1984**, *69*, 754–770.

[80] Zhou, W.; Peacor, D. R.; der Voo, R. V.; Mansfield, J. F. Determination of Lattice Parameter, Oxidation State, and Composition of Individual Titanomagnetite/Titanomaghemite Grains by Transmission Electron Microscopy. *J. Geophys. Res. Solid Earth* **1999**, *104*, 17689–17702.

[81] Pearce, C.; Qafoku, O.; Liu, J.; Arenholz, E.; Heald, S.; Kukkadapu, R.; Gorski, C.; Henderson, C.; Rosso, K. Synthesis and Properties of Titanomagnetite ($Fe_{3-x}Ti_xO_4$) Nanoparticles: A Tunable Solid-state Fe(II/III) Redox System. *J. Colloid Interface Sci.* **2012**, *387*, 24–38.

[82] Ferreira, F. F.; Corrêa, H. P. S.; Orlando, M. T. D.; Passamai, J. L.; Orlando, C. G. P.; Cavalcante, I. P.; Garcia, F.; Tamura, E.; Martinez, L. G.; Rossi, J. L.; de Melo, F. C. L. Pressure Study of Monoclinic ReO_2 up to 1.2 GPa Using X-ray Absorption Spectroscopy and X-ray Diffraction. *J. Synchrotron Radiat.* **2008**, *16*, 48–56.

[83] Huber, S.; Bercx, M.; Hörmann, N.; Uhrin, M.; Pizzi, G.; Marzari, N. Materials Cloud Three-dimensional Crystals Database (MC3D). 2022.

[84] Magnéli, A.; Siitonen, S.; Skrifvars, B.; Schliack, J.; Reio, L. Studies on Rhenium Oxides. *Acta Chem. Scand.* **1957**, *11*, 28–33.

[85] Ivanovskii, A.; Chupakhina, T.; Zubkov, V.; Tyutyunnik, A.; Krasilnikov, V.; Bazuev, G.; Okatov, S.; Lichtenstein, A. Structure and Electronic Properties of New Rutile-like Rhenium(IV) Dioxide $\mathrm{Reo_2}$. *Phys. Lett. A* **2005**, *348*, 66–70.

[86] Grimme, S.; Antony, J.; Ehrlich, S.; Krieg, H. A Consistent and Accurate *Ab Initio* Parametrization of Density Functional Dispersion Correction (DFT-D) for the 94 Elements H-Pu. *J. Chem. Phys.* **2010**, *132*, 154104.

[87] Grimme, S.; Ehrlich, S.; Goerigk, L. Effect of the Damping Function in Dispersion Corrected Density Functional Theory. *J. Comput. Chem.* **2011**, *32*, 1456–1465.

Chapter 5: Sorption of Pu(III) at the magnetite (111) surface

Sorption complex of Pu(III) at the magnetite {111} surface: Description by *ab initio* simulations and comparison with EXAFS data

This chapter is currently in preparation for submission. The manuscript is written in cooperation with Matthias Krack, Thomas Zimmermann, Andreas C. Scheinost, and Sergey V. Churakov.

Abstract

Pu is an important radionuclide in the nuclear power generation. After the energy generation and alongside other radioactive waste, it is foreseen for deep underground storage for several hundred thousand years. Over time, the Pu may be dissolved from the waste matrix and be mobilized. Surrounding minerals in the repository such as magnetite have been shown to interact with Pu and contribute to its retention. In this study, the previously experimentally proposed Pu(III) sorption complex on the common magnetite (111) surface has been investigated computationally. In comparison to experimental data, the location of the sorption complex was confirmed. Moreover, the performed *ab initio* molecular dynamics simulations were shown to provide a powerful tool in the atomistic investigation of chemical complexes.

5.1 Introduction

Plutonium is a heavy radioactive element with applications in various fields. In civil usage, Pu is part of MOX, mixed oxide fuel, present as pellets in fuel rods in which Pu and U oxides are combined. From the chain reaction of their nuclear fission with dominating α- and β^--decay[1], electricity can be generated in nuclear power plants. After the use, the spent nuclear fuel (SNF) and other high-level waste (HLW) from reprocessing need to be stored long-term protecting the living environment from the still present harmful radiation. The reprocessing needs to be performed carefully, historically, e.g., the Hanford site (Washington, USA)[2] and the Mayak reprocessing plant (Chelyabinsk, Russia)[3] still suffer from extended contamination with Pu.

In many countries, e.g., France, and Switzerland, the long-term disposal of radioactive waste is foreseen in deep geological repositories taking advantage of a system of geological and technical barriers[4]. SNF and HLW will be encapsulated in carbon steel canisters before placing them in underground tunnels. The tunnel cavities will be filled up with bentonite, a clay with self-sealing properties against incoming water. However, it is expected that the contact of porewater with the steel canisters cannot be avoided over the required disposal time leading to corrosion of the steel canisters. Subsequently, a deterioration of the canisters and their possible breaching is expected allowing for a dissolution of the radioactive material.

Pu is expected to cause the main radiotoxicity of the nuclear waste up to approximately 100 ka[5]. For this redox-sensitive element, the surrounding conditions play an important role regarding its oxidation state and solubility involved. Common redox states range from Pu(VI) to Pu(III). Especially Pu(IV) and Pu(III) are relevant under repository conditions[6]. Pu(IV) has a lower solubility due to the observed formation of PuO_2 from Pu(VI)[6,7] and can be further reduced to $Pu(OH)_3$[8,9]. In fact, PuO_2 has been found to be the highest oxidized stable Pu oxide[10]. Moreover, these oxidation states are much more likely to be potentially immobilized by co-precipitation of Fe(II) bearing compounds. In this way, e.g., an almost perfect removal of Pu_{aq} from Fukushima seawater could be achieved by co-precipitation with $Fe(OH)_2$[11]. The sorption at minerals is another effective immobilization strategy. E.g., sorption at (Na)-montmorillonite has been experimentally proven including a surface-mediated reduction mechanism[12,13]. In fact, Fe bearing minerals were found to sorb Pu more efficiently compared to minerals that do not contain Fe[13].

Magnetite (Fe_3O_4) as mixed Fe(II)/Fe(III) oxide as common subsurface Fe mineral can act as reducing agent for Pu and provide a surface for sorption[14]. Furthermore, in the repository context, the anoxic corrosion of the steel canisters leads to a formation of prevalently magnetite at the canister surface[5,15]. Due to the expected long-term reducing conditions in the repository[16], Pu(III) can be stabilized[8,9]. Furthermore, over a wide pH range, a stable sorption of Pu(III) on the magnetite surface could be shown, even in presence of competing trivalent ions[17].

To investigate experimentally the oxidation state and the coordination environment of Pu, the powerful tool of X-ray absorption spectroscopy (XAS) can be used[7]. Kirsch et al.[6] conducted batch-sorption experiments on Fe(II) containing minerals, namely magnetite, mackinawite (FeS) and chukanovite ($Fe_2(CO_3)(OH)_2$) under anoxic conditions and analyzed with XAS. They observed a rapid uptake of the dissolved Pu. With magnetite, a reduction to Pu(III) was confirmed; with the other minerals as well as dissolved Fe(II), the higher oxidized Pu(IV)O_2 occurred signifying weaker reductive capabilities of these Fe compounds. In fact, a surface-mediated reduction was proposed to be more effective at the oxygen-terminated surfaces. In a previous study[18], we confirmed a stable existence of such a surface under expected repository conditions[16]. With the technique of extended X-ray absorption spectroscopy (EXAFS), a tridentate sorption complex at three edge-sharing FeO_6 octahedra was proposed. In coprecipitation experiments conducted by Dumas et al.[19], the reduced Pu(III) was taken up by magnetite, too. Half of it was immobilized by formation of a tridentate sorption complex at the magnetite (111) surface and half was structurally incorporated. However, the large size of the Pu(III) compared to Fe ions[20] leads to a structural incompatibility. Hence, in an experimental long-term simulation, the structurally incorporated Pu is pushed out of the crystal structure and the ratio of sorbed to incorporated species shifts to 2:1[19].

The experimental efforts can be supported by computational approaches such as density functional theory (DFT) as used in the present study. The first challenge was to confirm a suitable description using the DFT+U approach[21] for the strongly correlated 5f electrons in Pu[22–25] as these possess the highest energy[26]. Hence, they are responsible for electronic interactions and can contribute to chemical bonding. After thoroughly validating the modeling setup focusing on the repository relevant Pu(III) and Pu(IV) coordinated by oxygen, we simulated the proposed tridentate sorption complex using *ab initio* molecular dynamics (AIMD) simulations for 10 ps. Based on the time-averaged crystal structure of the sorption complex, the experimentally suggested sorption complex could be confirmed. Moreover, a more detailed structure of the surrounding hydration shell was obtained.

5.2 Materials and Methods

Ab initio and AIMD simulations

Atomistic simulations were performed following the methodology developed and validated in our previous studies[18,27,28]. In brief, spin-polarized crystal structure calculations based on Density Functional Theory (DFT) were performed using the PBE functional with PBEsol parametrization. The Gaussian Plane Wave (GPW) method implemented in the QUICKSTEP module of CP2K[29] (version 2023.1) was used and 3D periodic boundary conditions were applied. GTH-type[30–32] norm-conserving scalar-relativistic pseudo-potentials were applied in combination with MOLOPT basis sets (DZVP)[33]. For Pu, the combination of norm-conserving pseudo-potential and GTH-type basis set was used which was recently developed by Lu et al.[34] testing a range of plutonium chlorides up to the highest oxidation state of Pu (heptavalent). For the simulations in the present study, an auxiliary basis set of plane waves with an electronic density cutoff of 600 Ry was employed to expand the electronic density. The target accuracy of the geometry optimizations in a self-consistent field (SCF) approach was 3.0×10^{-7} Ha per molecular orbital. In systems with solvent water, a dispersion correction was applied using the DFT-D3 term by Grimme et al.[35,36].

To improve the description of the 3d-electronic states of iron in magnetite, the DFT+U method[21,37] was employed with an effective Hubbard U parameter of 1.9 eV as validated in a previous study on the magnetite crystal structure[18]. If not stated otherwise, in all simulations the valence electron count in the system fulfilled the electro-neutrality condition.

Furthermore, spin polarization was applied to the initialization of wave functions in the magnetite systems. For ferrous iron, it was $(2S + 1)_{Fe^{2+}} = 5$ and $(2S + 1)_{Fe^{3+}} = 6$ for ferric iron, respectively. Ferric and ferrous irons are assumed to alternate in the octahedral positions of the magnetite structure resulting in $(2S + 1)_{Fe_{oct}} = 5.5$ with all spins aligned up. The ferric tetrahedral sites in magnetite were considered as spin down. Based on Pu(0) with a simplified electronic configuration $7s^2\ 5f^6$, Pu(III) and Pu(IV) were initialized as $7s^0 5f^5$ and $7s^0 5f^4$ with initial high-spin multiplicity of $(2S + 1)_{Pu^{3+}} = 6$ and $(2S + 1)_{Pu^{4+}} = 5$, respectively.

After the geometry optimization of initial Pu complexes, AIMD simulations were performed in the NVT ensemble at 300 K. The temperature was controlled by the Canonical Sampling Velocity Rescaling (CSVR) thermostat[38]. An adaptive barostat with a time constant of 1 ps at 1 bar was applied. The equations of motion of the atoms were integrated with a 0.5 fs time-step. After a pre-equilibration time of 2 ps, simulations were run for 15 ps for the Pu aquo complex and 8 ps for the sorption complex. For the latter, the accuracy of SCF cycles was slightly increased to 5.0×10^{-7} Ha per molecular orbital for faster convergence.

5.2.1 Benchmarking of Hubbard U parameter for Pu(III) and Pu(IV)

In line with our previous studies[18,27,28], we applied the DFT+U approach[21,37] to improve the description of the d-electronic states of Fe. Accordingly, to provide accurate description of the Pu 5f-orbitals[22,39], the U parameter for Pu needs to be calibrated. The plutonium species relevant in the context of deep geological repository are Pu(III)[8,9] and Pu(IV)[7] oxides.

The cubic polymorphs of these plutonium oxides were simulated to reveal the optimal value of the U parameter. For both oxides, ferro- (FM) and antiferromagnetic (AFM) setups were tested. Pu(III) was investigated in the α-Pu_2O_3 polymorph with a lattice parameter $a = 11.04\,\text{Å}$[40] in a $2 \times 2 \times 2$ supercell. Pu(IV) was simulated using a $3 \times 3 \times 3$ supercell based on the cubic unit cell of PuO_2 with lattice parameter $a = 5.396\,\text{Å}$[40]. Several values for the U parameter were tested in a range of 0 eV to 4 eV to provide the best agreement with of structural properties and electronic band gap with experimental data.

5.2.2 Pu(III) complexes in solvent

With the validated Hubbard U parameter, two Pu(III) complexes were investigated: (i) the aquo complex and (ii) the proposed sorption complex at the magnetite (111) surface.

Pu(III) aquo complex in aqueous solution

The stable coordination number of Pu(III) in aqueous solution remains unclear. Pu(III) aquo complexes were reported to be coordinated by eight[41], or possibly by nine[42] water molecules in pure water solvent. For comparison, stabilized in a crystallized solid form by triflic acid, a nine-fold water-coordination was reported based on single-crystal X-ray diffraction[43]. Experimental EXAFS in combination with the magnetite surface suggest a nine-fold coordination of the Pu(III) cation[6,19], too.

Hence, to investigate the coordination number in aqueous solution, a nine-fold coordinated Pu(III) complex with a random orientation of the water molecules was setup. The initial Pu-O distance was 2.3 Å similar to the distances in plutonium oxides[44]. The complex was placed in a cubic simulation box ($a = 20\,\text{Å}$) with 259 other water molecules representing a density of water of $\rho = 1\,\text{g}\,\text{cm}^{-3}$. The initial position of the atoms in the simulation box was obtained using the Packmol software[45] by randomly distributing the water molecules around the Pu(III) aquo complex. The total system charge of the system with the Pu(III) aquo ion was set to +3.

Pu(III) sorption complex at the magnetite (111) surface

The magnetite (111) surface structure was investigated in a previous study[18], the main features are summarized in the following. Magnetite (Fe_3O_4) has an inverse spinel structure with octahedrally (Fe_{oct}) and tetrahedrally (Fe_{tet}) coordinated iron ions. For the magnetite (111) surface, different surface terminations are possible. However, expecting environmental conditions and present water, terminations with fully coordinated Fe cations and a surface protonation appear to be feasible. Under repository conditions[16], the expected surface termination has been found to be octahedrally coordinated Fe ions[18] occupying three quarters of a complete monolayer. This leads to the occurrence of cavities as investigated in a previous study[27]. Disregarding possible surface protonation, two three-fold rotation axes can be imagined perpendicular to the surface, one between three edge-sharing Fe octahedra, one in the center of a cavity. Below each cavity, a Fe_{tet} ion is located being part of a sandwiched arrangement of Fe_{tet} - Fe_{oct} - Fe_{tet}.

According to previous spectroscopic studies[6,19], Pu(III) is expected to form a tridentate surface complex above the three edge-sharing Fe octahedra. In addition to three surface oxygen anions, the plutonium coordination shell may contain six water molecules. For the present study, an according system setup was prepared. The basis was formed by an adapted magnetite surface slab corresponding to oct1_out2.5 for comparison. The dimensions of the slab were 11.84 Å × 20.52 Å × 14.04 Å, half the size of previous studies[18,28] saving computational resources.

One Pu(III) complex was set symmetrically on either side of the surface slab to cancel the dipole moment across the slab. In this way, polarization effects could be avoided and statistics improved. The separation of Pu ions are at least 15 Å, which is sufficient to screen ion-ion interaction. Accounting for the bonds of Pu to surface-O forming the sorption complex, one surface-H was removed from the corresponding surface-O.

The initial water configuration of the simulation setup was achieved using the Packmol software[45] by adding 128 water molecules to each side of the slab. Like for the Pu(III) aquo complex, this corresponds to a water density of $\rho = 1\,\mathrm{g\,cm^{-3}}$.

5.3 Results and Discussion

5.3.1 Hubbard *U* parameter for relevant oxygen coordinated Pu species

To obtain the value of the Hubbard U parameter for relevant Pu species, a comparison of structural and electronic properties was conducted. The investigated plutonium oxides represent relevant Pu phases in a nuclear waste matrix[7,46]. Their crystal structure – base-centered cubic and fluorite-structure type –, reflects a wide range of plutonium-oxygen coordination environments ranging from six to eight and approximating the proposed nine-fold coordination of the Pu(III) sorption complex on the magnetite (111) surface[6,19].

The anti-ferromagnetic (AFM) phases were studied for the sake of comparison as these have been shown to provide the best agreement with the experimental data and yield a lower energy than the FM phases[23,24,47–49]. The obtained averaged parameters for the AFM phases are listed in Table 5.1. The closer agreement of the AFM phases to both structural and electronic properties compared to the FM phases is confirmed. More details can be found in SI (Table S5.1, Table S5.2).

Additionally, Figure 5.1 shows the electronic band gap of the investigated cubic plutonium oxides. The band gap can be reproduced for Pu_2O_3 with the value of $U = 3.5\,\mathrm{eV}$. For PuO_2, a higher value of at least $U = 3.8\,\mathrm{eV}$ provides the best agreement. A similar trend, namely the larger U value for higher oxidation states of plutonium was reported by other studies[50], too.

For both investigated plutonium oxides, the obtained orbital occupation based on Mulliken charge analysis reflects the expected electronic configuration in the 5f orbitals, i.e., for Pu(III)

$5f^5$ and for Pu(IV) $5f^4$. These results can be used to compare the occupation in more complex systems and track the oxidation state of plutonium.

TABLE 5.1: Averaged lattice parameter a and electronic band gap E_g of the investigated plutonium oxides in anti-ferromagnetic ordering. The deviations (dev.) to literature data regarding a[40] and E_g[51,52] are reported, too.

	Pu_2O_3				PuO_2			
U [eV]	a [Å]	dev. [%]	E_g [eV]	dev. [%]	a [Å]	dev. [%]	E_g [eV]	dev. [%]
0.0	10.979	−0.549	0.250	−81.865	5.390	−0.111	0.712	−60.471
1.5	11.036	−0.033	0.394	−71.469	5.395	−0.021	0.973	−45.925
2.0	11.047	0.059	0.617	−55.295	5.394	−0.029	1.134	−36.976
2.5	11.054	0.125	0.890	−35.522	5.393	−0.049	1.326	−26.323
3.0	11.059	0.168	1.156	−16.211	5.392	−0.074	1.399	−22.294
3.1	11.059	0.172	1.187	−13.989	5.392	−0.080	1.507	−16.295
3.2	11.059	0.176	1.242	−10.028	5.391	−0.087	1.545	−14.190
3.3	11.060	0.182	1.291	−6.428	5.391	−0.094	1.582	−12.087
3.4	11.061	0.186	1.334	−3.313	5.391	−0.101	1.614	−10.316
3.5	11.061	0.189	1.377	−0.214	5.390	−0.107	1.664	−7.583
3.6	11.061	0.190	1.433	3.857	5.390	−0.114	1.620	−10.017
3.7	11.061	0.192	1.473	6.735	5.389	−0.121	1.658	−7.910
3.8	11.044	0.035	1.518	10.005	5.389	−0.129	1.784	−0.886
3.9	11.061	0.192	1.562	13.196	5.389	−0.136	1.674	−6.991
4.0	11.061	0.191	1.606	16.369	5.388	−0.144	1.783	−0.927

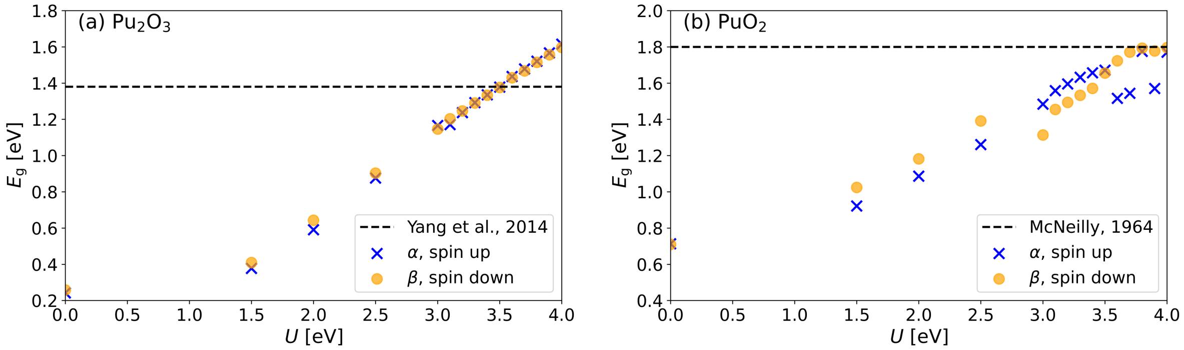

FIGURE 5.1: Electronic band gaps of cubic plutonium oxides in anti-ferromagnetic ordering, (a) Pu_2O_3 and (b) PuO_2. Both spin up (α, blue) and spin down (β, orange) are shown. For comparison, literature values are provided (dashed black).

Combining the analyses above, the preferential value of the *U* parameter can be concluded. For Pu(III), it is chosen as 3.5 eV and further used in the present study simulating Pu(III) complexes.

5.3.2 Simulated Pu(III) complexes

Pu complex in pure water

A snapshot of the AIMD simulation depicting the Pu(III) complex in aqueous solution is shown in Figure 5.2 (left). In agreement with Table S5.3 in SI, the first coordination shell is formed by eight oxygen anions (Figure 5.2 (right)) and water molecules, respectively. In comparison with the results from the previously modeled Pu_2O_3, the orbital occupation agrees and confirms the trivalent Pu oxidation state.

Although experimental studies reported a spectrum of Pu-water coordination numbers ranging between 8 and 9, the preference of an eight-fold coordination for the Pu(III) aquo complex observed in this work is in line with previous studies using various computational techniques[41,42,53]. Moreover, the averaged distance of around 2.50 Å for the first coordination shell by O_{H_2O} agrees well with the reported range of 2.49 Å to 2.51 Å from experimental studies[54,55]. Hence, we assume to capture the Pu-water interaction well with our simulation setup.

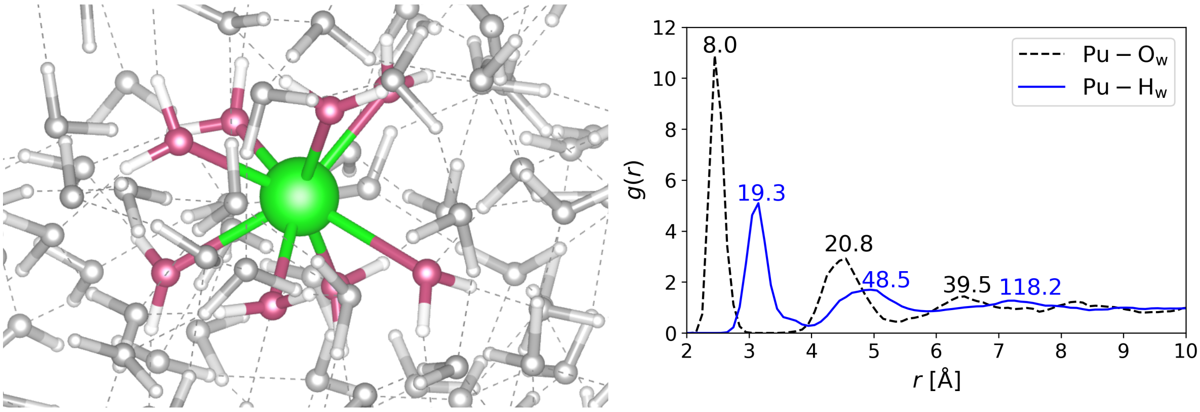

Figure 5.2: Left: Snapshot of the Pu(III) aquo complex in aqueous solution obtained from AIMD. Pu is shown in green, O and H of the first coordination shell in smaller spheres of pink and white, respectively. The other surrounding water molecules are shown in light gray. Atomic sizes were adapted for visualization. Right: Radial distribution function (RDF, *g(r)*) of Pu surrounded by water-O and water-H with corresponding coordination numbers.

Tridentate Pu complex at the magnetite (111) surface

TABLE 5.2: Averaged coordination number (CN) and distance (r) of Pu in the proposed tridentate sorption complex at the magnetite (111) surface[6] obtained by averaging the 8 ps AIMD trajectory. The first column lists the range of considered boundaries for the evaluation as obtained from the radial pair distribution function (RDF). The subscripts "s" and "w" in the coordinating neighbor column (coord.) signify H and O belonging to the initial surface and water portion of the system, respectively.

range [Å]	coord.	r [Å]	CN	exp. r [Å]	exp. CN
0.00-3.05	O_s	2.427 ± 0.139	3.00 ± 0.00	2.45[19], 2.49[6]	9[6,19]
0.00-3.15	O_w	2.477 ± 0.128	4.02 ± 0.12		
0.00-4.15	H_w	3.262 ± 0.319	13.06 ± 0.67		
0.00-3.75	H_s	3.280 ± 0.215	2.85 ± 0.49		
0.00-4.35	Fe_{oct}	3.494 ± 0.154	3.00 ± 0.00	3.54[6,19]	3[6,19]
3.05-3.95	O_s	3.686 ± 0.160	1.80 ± 0.41		
3.95-4.65	O_s	4.311 ± 0.183	4.00 ± 0.89		
3.15-5.05	O_w	4.376 ± 0.386	7.39 ± 1.20		
3.75-5.35	H_s	4.616 ± 0.383	6.33 ± 0.71		
4.65-5.75	O_s	5.087 ± 0.208	10.24 ± 0.75		
4.15-6.25	H_w	5.323 ± 0.527	28.42 ± 1.88		
4.35-6.05	Fe_{oct}	5.418 ± 0.300	6.11 ± 0.34		
0.00-7.05	Fe_{tet}	5.902 ± 0.193	4.00 ± 0.00	4.20[19]	3[19]

Table 5.2 lists the averaged distances and coordination shells around the sorbed Pu at the magnetite (111) surface up to 5.5 Å as commonly considered range for EXAFS spectra analysis[19]. In comparison with experimental data, the distance of the first oxygen coordination shell can be reproduced well. Complimenting experimental EXAFS, the simulations can differentiate in the first coordination shell between bonds by surface-oxygen (Pu-O_s) and water-oxygen (Pu-O_w). The latter are longer by 0.05 Å. Moreover, the distance of 2.46 Å would result from a weighted average perfectly aligning with experimental results[6,19]. However, a striking difference is noted as both surface- and water-oxygen in this first coordination shell only add up to seven coordinating oxygen ions compared to the proposed nine-fold coordination.

In line with our previous observations[18,27], it is possible that the experimentally present oxidation state of the surface-Fe resembles more Fe^{3+}. However, for the sake of computational comparability with a bulk-like magnetite, the simulations assumed $Fe^{2.5+}$. With a more positive surface charge, water could be drawn closer to the Fe-surface and, in turn, to the adsorbed Pu. In this way, at least one water molecule more might be part of this first coordination shell. Moreover, EXAFS is known to possibly differ in the fitting of the coordination shell of plus/minus one tenth of the assumed number[56] and a reduced coordination number is possible.

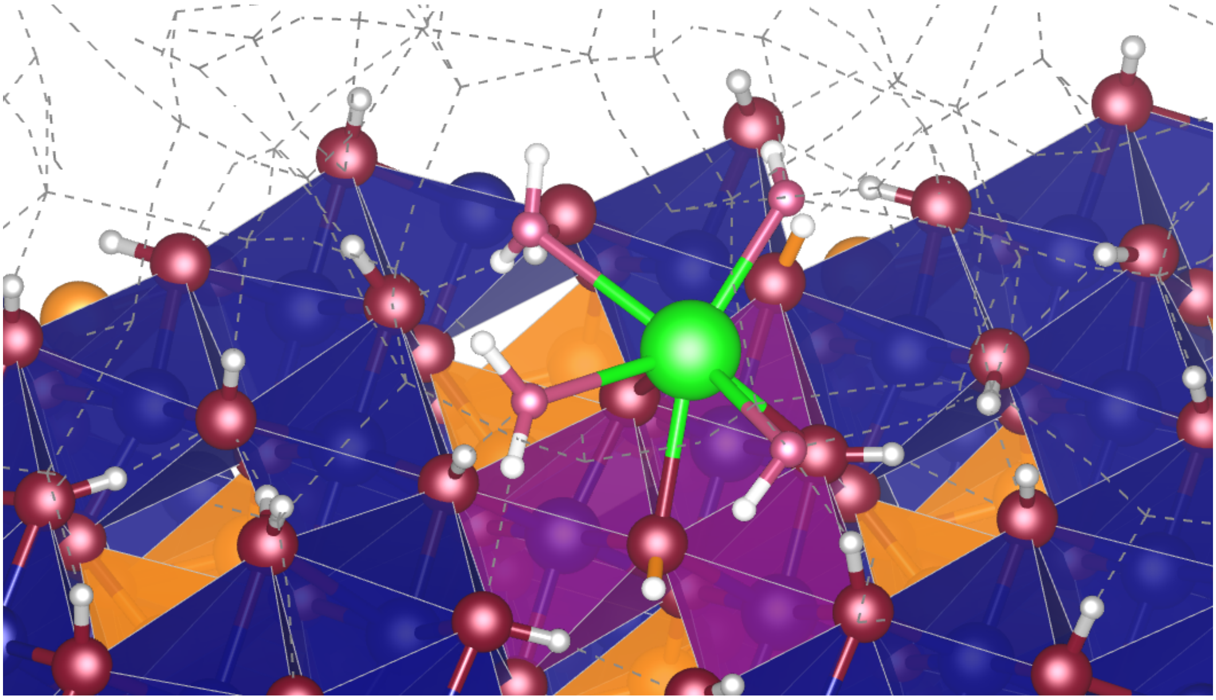

FIGURE 5.3: Perspective view of the tridentate Pu(III) sorption complex at the magnetite (111) surface obtained from a snap shot of the AIMD simulation. Pu is shown in green, tetrahedrally coordinated Fe in orange, octahedrally coordinated Fe in blue. The corresponding Fe polyhedra are shown in the respective color. However, for highlighting purposes, the edge-connected Fe octahedra that serve as sorption basis for the Pu(III) complex were shown in purple. O and H from the magnetite slab are shown in medium sized red and gray spheres, those in the water solvent forming the first coordination shell in smaller spheres of pink and white, respectively. The remaining water molecules as well as hydrogen bridges are depicted as dashed lines, and atomic sizes were adapted for visualization.

The first Fe coordination shell (Fe_{oct}) is in perfect alignment with experimental data and refers to the three edge-sharing FeO_6 octahedra at the octahedrally terminated magnetite (111) surface (purple octahedra in Figure 5.3). This high accordance is, however, to be expected as the input structure for the simulation was prepared in this way. The first water coordination shell is visualized in Figure 5.3. As can be seen, two of these water molecules tend to become OH-groups, and the remaining hydrogen cation lead to an increased protonation of the magnetite surface (orange cylinders in Figure 5.3). An increased hydrophilic behavior of the surface-O compared to the water-O can be deduced, for surface-O three-fold connected to Fe_{oct} (surface-O at upper orange cylinder), too.

Furthermore, Dumas et al.[19] fitted another Fe-coordination shell with three Fe ions at a distance of 4.20 Å attributing them to the tetrahedrally coordinated Fe cations. They expected them to be those from inside the surface cavities as shown in a previous study[27]. Contrasting, our results show that these would be at a distance of around 5.90 Å from the Pu(III) cation, a striking deviation of 1.70 Å. Moreover, there would be a fourth Fe_{tet} in the same x,y-position as the Pu, yet underneath in the magnetite surface. Additional analysis is needed to understand these differences.

5.3.3 Findings in context

Our findings on Pu(III) complexes are well in line with experimental observations. More specifically, the presented atomistic simulations not only allow for a precise identification of the atomic structure, also potentially harmful experiments with, e.g., radioactive substances may be reduced to a minimum. Moreover, the AIMD simulations can be used to investigate possible geometries and changes to the hydration shell under the influence of changing solvents.

The magnetite (111) surface has been shown to provide the sorption matrix for various trivalent and tridentate inner sphere complexes. Apart from the here discussed Pu(III) complex, sorption complexes of Am(III)/Eu(III)[57] have been proposed in the same position as the Pu(III) complex. On the other hand, As(III)[58–60] and Sb(III)[61] complexes are expected to be positioned above the triangular cavities in the magnetite (111) surface with octahedral termination. AIMD simulations to obtain averaged structures in combination with experimental EXAFS once more can be beneficial to identify the prevalent structures.

5.4 Acknowledgment

The authors acknowledge the funding from the German Federal Ministry of Education and Research (BMBF, KRIMI project - 02NUK056C), access to Swiss National Supercomputing Centre (CSCS, project number s1179) and access to the HPC cluster (UBELIX) at the University of Bern. Further, the authors thank Eva Doloszeski for her support in simulating the investigated plutonium oxides.

5.5 Supporting Information

5.5.1 Benchmarking of U parameter at plutonium oxides

TABLE S5.1: Additional information regarding the lattice parameters a, b and c of the AFM and FM phases of Pu_2O_3. The electronic band gaps E_g are separated in spin up (α) and spin down (β).

	AFM			FM				
U [eV]	a [Å]	b [Å]	c [Å]	a [Å]	b [Å]	c [Å]	$E_{g,\alpha}$ [eV]	$E_{g,\beta}$ [eV]
0.0	10.987	10.978	10.973	10.939	10.942	10.945	0.039	3.719
1.5	10.963	11.105	11.041	10.923	11.122	11.025	0.030	3.635
2.0	11.014	11.122	11.005	10.979	11.165	10.973	0.136	3.541
2.5	11.037	11.123	11.001	11.008	11.164	10.975	0.389	3.498
3.0	11.043	11.110	11.024	11.012	11.158	10.995	0.626	3.473
3.1	11.043	11.115	11.019	11.024	11.154	10.990	0.679	3.469
3.2	11.043	11.111	11.024	11.025	11.154	10.991	0.724	3.466
3.3	11.042	11.108	11.030	11.026	11.152	10.993	0.771	3.463
3.4	11.042	11.107	11.033	11.029	11.150	10.994	0.814	3.461
3.5	11.044	11.103	11.036	11.031	11.146	10.997	0.860	3.461
3.6	11.044	11.101	11.038	11.032	11.147	10.996	0.898	3.458
3.7	11.044	11.097	11.043	11.035	11.146	10.996	0.940	3.456
3.8	11.047	11.042	11.042	11.038	11.143	10.996	0.983	3.453
3.9	11.048	11.095	11.040	11.038	11.140	11.000	1.026	3.452
4.0	11.044	11.089	11.050	11.041	11.135	11.002	1.069	3.449

TABLE S5.2: Additional information regarding the lattice parameters a, b and c of the AFM and FM phases of PuO_2. The electronic band gaps E_g are separated in spin up (α) and spin down (β).

	AFM			FM				
U [eV]	a [Å]	b [Å]	c [Å]	a [Å]	b [Å]	c [Å]	$E_{g,\alpha}$ [eV]	$E_{g,\beta}$ [eV]
0.0	5.383	5.384	5.403	5.386	5.388	5.387	0.192	0.034
1.5	5.424	5.400	5.361	5.410	5.409	5.364	0.536	5.066
2.0	5.422	5.400	5.361	5.406	5.405	5.367	0.762	5.109
2.5	5.418	5.396	5.367	5.398	5.400	5.378	1.000	5.154
3.0	5.411	5.395	5.370	5.398	5.394	5.381	1.075	5.199
3.1	5.407	5.398	5.370	5.405	5.418	5.352	1.108	5.202
3.2	5.407	5.398	5.369	5.405	5.417	5.351	1.146	5.208
3.3	5.406	5.398	5.369	5.403	5.414	5.356	1.209	5.234
3.4	5.405	5.397	5.369	5.403	5.414	5.355	1.245	5.240
3.5	5.404	5.394	5.372	5.391	5.390	5.386	1.258	5.249
3.6	5.405	5.394	5.371	5.400	5.414	5.357	1.168	5.235
3.7	5.403	5.393	5.372	5.403	5.410	5.357	1.209	5.243
3.8	5.402	5.393	5.372	5.401	5.411	5.356	1.404	5.274
3.9	5.403	5.392	5.371	5.399	5.409	5.359	1.445	5.283
4.0	5.402	5.391	5.371	5.403	5.405	5.358	1.453	5.292

5.5.2 Pu(III) aquo complex in aqueous solution

TABLE S5.3: Averaged coordination number (CN) and Pu-O and Pu-H distances (r) for Pu aquo-complex obtained by averaging 15 ps long AIMD trajectory. The first column lists the applied boundaries as obtained from the radial pair distribution function (RDF).

Shell [Å]	Neighbor	r [Å]	CN
0.00-3.30	O	2.503 ± 0.113	8.00 ± 0.00
0.00-4.00	H	3.224 ± 0.248	19.28 ± 0.83
3.30-5.50	O	4.625 ± 0.352	20.80 ± 1.08
4.00-6.00	H	5.109 ± 0.487	48.47 ± 2.30
5.50-7.60	O	6.687 ± 0.544	39.52 ± 2.13
6.00-8.50	H	7.390 ± 0.677	118.23 ± 3.91

5.6 References

[1] Live Chart of Nuclides. `https://www-nds.iaea.org/relnsd/vcharthtml/VChartHTML.html`, International Atomic Energy Agency (IAEA).

[2] Batuk, O. N. et al. Multiscale Speciation of U and Pu at Chernobyl, Hanford, Los Alamos, Mcguire Afb, Mayak, and Rocky Flats. *Environ. Sci. Technol.* **2015**, *49*, 6474–6484.

[3] Skipperud, L.; Salbu, B.; Oughton, D. H.; Drozcho, E.; Mokrov, Y.; Strand, P. Plutonium Contamination in Soils and Sediments at Mayak PA, Russia. *Health Phys.* **2005**, *89*, 255–266.

[4] Churakov, S. V.; Hummel, W.; Fernandes, M. M. Fundamental Research on Radiochemistry of Geological Nuclear Waste Disposal. *Chimia* **2020**, *74*, 1000–1009.

[5] Johnson, L.; Schneider, J.; Zuidema, P.; Gribi, P.; Mayer, G.; Smith, P.; Kunz, B.; Frei, C. *Project Opalinus Clay - Demonstration of Disposal for Spent Fuel, Vitrified High-level Wast and Long-lived Intermediate-level Waste*; NAGRA tech. report 02-05, 2002.

[6] Kirsch, R.; Fellhauer, D.; Altmaier, M.; Neck, V.; Rossberg, A.; Fanghänel, T.; Charlet, L.; Scheinost, A. C. Oxidation State and Local Structure of Plutonium Reacted with Magnetite, Mackinawite, and Chukanovite. *Environ. Sci. Technol.* **2011**, *45*, 7267–7274.

[7] Kvashnina, K. O.; Romanchuk, A. Y.; Pidchenko, I.; Amidani, L.; Gerber, E.; Trigub, A.; Rossberg, A.; Weiss, S.; Popa, K.; Walter, O.; Caciuffo, R.; Scheinost, A. C.; Butorin, S. M.; Kalmykov, S. N. A Novel Metastable Pentavalent Plutonium Solid Phase on the Pathway from Aqueous Plutonium(VI) to PuO_2 Nanoparticles. *Angew. Chem. - Int. Ed.* **2019**, *58*, 17558–17562.

[8] Cho, H.-R.; Youn, Y.-S.; Jung, E. C.; Cha, W. Hydrolysis of Trivalent Plutonium and Solubility of $Pu(OH)_3$ (am) under Electrolytic Reducing Conditions. *Dalton Trans.* **2016**, *45*, 19449–19457.

[9] Cho, S.; Kim, H.-K.; Kim, T.-H.; Cha, W.; Cho, H.-R. Thermodynamic Studies on the Hydrolysis of Trivalent Plutonium and Solubility of $Pu(OH)_3$(am). *Inorg. Chem.* **2022**, *61*, 12643–12651.

[10] Gouder, T.; Seibert, A.; Havela, L.; Rebizant, J. Search for Higher Oxides of Pu: A Photoemission Study. *Surf. Sci.* **2007**, *601*, L77–L80.

[11] Men, W.; Zheng, J.; Wang, H.; Ni, Y.; Aono, T.; Maxwell, S. L.; Tagami, K.; Uchida, S.; Yamada, M. Establishing Rapid Analysis of Pu Isotopes in Seawater to Study the Impact of Fukushima Nuclear Accident in the Northwest Pacific. *Sci. Rep.* **2018**, *8*.

[12] Zavarin, M.; Powell, B. A.; Bourbin, M.; Zhao, P.; Kersting, A. B. Np(V) and Pu(V) Ion Exchange and Surface-mediated Reduction Mechanisms on Montmorillonite. *Environ. Sci. Technol.* **2012**, *46*, 2692–2698.

[13] Begg, J. D.; Zavarin, M.; Zhao, P.; Tumey, S. J.; Powell, B.; Kersting, A. B. Pu(V) and Pu(IV) Sorption to Montmorillonite. *Environ. Sci. Technol.* **2013**, *47*, 5146–5153.

[14] Powell, B. A.; Fjeld, R. A.; Kaplan, D. I.; Coates, J. T.; Serkiz, S. M. $Pu(V)O_2^+$ Adsorption and Reduction by Synthetic Magnetite (Fe_3O_4). *Environ. Sci. Technol.* **2004**, *38*, 6016–6024.

[15] King, F. *Corrosion of Carbon Steel under Anaerobic Conditions in a Repository for SF and HLW in Opalinus Clay*; NAGRA tech. report 08-12, 2008.

[16] Wersin, P.; Johnson, L.; Schwyn, B.; Berner, U.; Curti, E. *Redox Conditions in the Near Field of a Repository for SF/HLW and ILW in Opalinus Clay*; NAGRA tech. report 02-13, 2003.

[17] Felmy, A. R.; Moore, D. A.; Pearce, C. I.; Conradson, S. D.; Qafoku, O.; Buck, E. C.; Rosso, K. M.; Ilton, E. S. Controls on Soluble Pu Concentrations in PuO_2/Magnetite Suspensions. *Environ. Sci. Technol.* **2012**, *46*, 11610–11617.

[18] Katheras, A. S.; Karalis, K.; Krack, M.; Scheinost, A. C.; Churakov, S. V. Stability and Speciation of Hydrated Magnetite {111} Surfaces from *Ab Initio* Simulations with Relevance for Geochemical Redox Processes. *Environ. Sci. Technol.* **2024**, *58*, 935–946.

[19] Dumas, T.; Fellhauer, D.; Schild, D.; Gaona, X.; Altmaier, M.; Scheinost, A. C. Plutonium Retention Mechanisms by Magnetite under Anoxic Conditions: Entrapment Versus Sorption. *ACS Earth Space Chem.* **2019**, *3*, 2197–2206.

[20] Shannon, R. D. Revised Effective Ionic Radii and Systematic Studies of Interatomic Distances in Halides and Chalcogenides. *Acta Cryst. A* **1976**, *32*, 751–767.

[21] Hubbard, J. Electron Correlations in Narrow Energy Bands. *Proc. Roy. Soc. Lond. Math. Phys. Sci.* **1963**, *276*, 238–257.

[22] Ai, J.; Liu, T.; Gao, T.; Ao, B. First-Principles Study of Electronic Structure and Metal-Insulator Transition of Plutonium Dihydride and Trihydride. *Comput. Mater. Sci.* **2012**, *51*, 127–134.

[23] Lu, Y.; Yang, Y.; Zheng, F.; Zhang, P. Electronic and Thermodynamic Properties of α-Pu_2O_3. *Phys. Lett. A* **2014**, *378*, 3060–3065.

[24] Chen, J.-L.; Kaltsoyannis, N. DFT+U Study of Uranium Dioxide and Plutonium Dioxide with Occupation Matrix Control. *J. Phys. Chem. C* **2022**, *126*, 11426–11435.

[25] Chen, J.-L.; Blaha, P.; Kaltsoyannis, N. DFT+U Simulation of the X-ray Absorption Near-edge Structure of Bulk UO_2 and PuO_2. *J. Phys. Chem. C* **2023**, *127*, 17994–18000.

[26] Teterin, Y. A.; Maslakov, K. I.; Teterin, A. Y.; Ivanov, K. E.; Ryzhkov, M. V.; Petrov, V. G.; Enina, D. A.; Kalmykov, S. N. Electronic Structure and Chemical Bonding in PuO_2. *Phys. Rev. B* **2013**, *87*, 245108.

[27] Katheras, A. S.; Karalis, K.; Krack, M.; Scheinost, A. C.; Churakov, S. V. Computational Study on the Octahedral Surfaces of Magnetite Nanoparticles and Their Solvent Interaction. *Environ. Sci. Technol.* **2024**, *58*, 21068–21076.

[28] Katheras, A. S.; Krack, M.; Zimmermann, T.; Scheinost, A. C.; Churakov, S. V. Incorporation Mechanism of Tc(IV) in Magnetite Revealed by EXAFS Measurements and *Ab Initio* Simulations. (submitted to *Environmental Science & Technology* on December 27, 2024).

[29] Kühne, T. D. et al. CP2K: An Electronic Structure and Molecular Dynamics Software Package - Quickstep: Efficient and Accurate Electronic Structure Calculations. *J. Chem. Phys.* **2020**, *152*, 194103.

[30] Goedecker, S.; Teter, M.; Hutter, J. Separable Dual-Space Gaussian Pseudopotentials. *Phys. Rev. B* **1996**, *54*, 1703–1710.

[31] Krack, M. Pseudopotentials for H to Kr Optimized for Gradient-corrected Exchange-Correlation Functionals. *Theor. Chem. Acc.* **2005**, *114*, 145–152.

[32] Bosoni, E. et al. How to Verify the Precision of Density-functional-theory Implementations Via Reproducible and Universal Workflows. *Nat. Rev. Phys.* **2023**, *6*, 45–58.

[33] VandeVondele, J.; Hutter, J. Gaussian Basis Sets for Accurate Calculations on Molecular Systems in Gas and Condensed Phases. *J. Chem. Phys.* **2007**, *127*, 114105.

[34] Lu, J.-B.; Cantu, D. C.; Xu, C.-Q.; Nguyen, M.-T.; Hu, H.-S.; Glezakou, V.-A.; Rousseau, R.; Li, J. Norm-conserving Pseudopotentials and Basis Sets to Explore Actinide Chemistry in Complex Environments. *J. Chem. Theory Comput.* **2021**, *17*, 3360–3371.

[35] Grimme, S.; Antony, J.; Ehrlich, S.; Krieg, H. A Consistent and Accurate *Ab Initio* Parametrization of Density Functional Dispersion Correction (DFT-D) for the 94 Elements H-Pu. *J. Chem. Phys.* **2010**, *132*, 154104.

[36] Grimme, S.; Ehrlich, S.; Goerigk, L. Effect of the Damping Function in Dispersion Corrected Density Functional Theory. *J. Comput. Chem.* **2011**, *32*, 1456–1465.

[37] Dudarev, S. L.; Botton, G. A.; Savrasov, S. Y.; Humphreys, C. J.; Sutton, A. P. Electron-Energy-Loss Spectra and the Structural Stability of Nickel Oxide: An LSDA+U Study. *Phys. Rev. B* **1998**, *57*, 1505–1509.

[38] Bussi, G.; Donadio, D.; Parrinello, M. Canonical Sampling through Velocity Rescaling. *J. Chem. Phys.* **2007**, *126*, 014101.

[39] Zheng, J.-J.; Wang, B.-T.; Marco, I. D.; Li, W.-D. Electronic Structure and Phase Stability of Plutonium Hydrides: Role of Coulomb Repulsion and Spin-Orbital Coupling. *Int. J. Hydrog. Energy* **2014**, *39*, 13255–13265.

[40] Holley, C. J.; Mulford, R.; Huber, E. J.; Head, E.; Ellinger, F.; Bjorklund, C. *Second United Nations International Conference on the Peaceful Uses of Atomic Energy*; 1958.

[41] Ryzhkov, M. V.; Enyashin, A. N.; Delley, B. Plutonium Complexes in Water: New Approach to *Ab Initio* Modeling. *Radiochim. Acta* **2021**, *109*, 327–342.

[42] Blaudeau, J.-P.; Zygmunt, S. A.; Curtiss, L. A.; Reed, D. T.; Bursten, B. E. Relativistic Density Functional Investigation of $Pu(H_2O)_n{}^{3+}$ Clusters. *Chem. Phys. Lett.* **1999**, *310*, 347–354.

[43] Matonic, J. H.; Scott, B. L.; Neu, M. P. High-yield Synthesis and Single-crystal X-ray Structure of a Plutonium(III) Aquo Complex: $[Pu(H_2O)_9][CF_3SO_3]_3$. *Inorg. Chem.* **2001**, *40*, 2638–2639.

[44] Gerber, E. et al. The Missing Pieces of the PuO_2 Nanoparticle Puzzle. *Nanoscale* **2020**, *12*, 18039–18048.

[45] Martínez, L.; Andrade, R.; Birgin, E. G.; Martínez, J. M. Packmol: A Package for Building Initial Configurations for Molecular Dynamics Simulations. *J. Comput. Chem.* **2009**, *30*, 2157–2164.

[46] Haschke, J. M.; Dinh, L. N.; McLean, W. The Plutonium-Oxygen Phase Diagram in the 25-900 °C Range: Non-existence of the $PuO_{1.515}$ Phase. *J. Nucl. Mater.* **2015**, *458*, 275–280.

[47] Shi, H.; Zhang, P. First-Principles Study of α-Pu_2O_3. *J. Nucl. Mater.* **2012**, *420*, 159–163.

[48] Njifon, I. C.; Bertolus, M.; Hayn, R.; Freyss, M. Electronic Structure Investigation of the Bulk Properties of Uranium–plutonium Mixed Oxides (U, Pu)O_2. *Inorg. Chem.* **2018**, *57*, 10974–10983.

[49] Pegg, J. T.; Shields, A. E.; Storr, M. T.; Wills, A. S.; Scanlon, D. O.; de Leeuw, N. H. Hidden Magnetic Order in Plutonium Dioxide Nuclear Fuel. *Phys. Chem. Chem. Phys.* **2018**, *20*, 20943–20951.

[50] Kowalski, P. M.; Beridze, G.; Li, Y.; Ji, Y.; Friedrich, C.; Şaşioğlu, E.; Blügel, S. Feasible and Reliable *AB initio* Approach to Computation of Materials Relevant for Nuclear Waste

Management. *Additive Manufacturing and Strategic Technologies in Advanced Ceramics* **2016**, 205–217.

[51] Yang, Y.; Lu, Y.; Zhang, P. Optical Properties of PuO_2 and α-Pu_2O_3 by GGA+U+QA Studies. *J. Nucl. Mater.* **2014**, *452*, 414–418.

[52] McNeilly, C. The Electrical Properties of Plutonium Oxides. *J. Nucl. Mater.* **1964**, *11*, 53–58.

[53] Odoh, S. O.; Bylaska, E. J.; de Jong, W. A. Coordination and Hydrolysis of Plutonium Ions in Aqueous Solution Using Car–Parrinello Molecular Dynamics Free Energy Simulations. *J. Phys. Chem. A* **2013**, *117*, 12256–12267.

[54] Allen, P. G.; Bucher, J. J.; Shuh, D. K.; Edelstein, N. M.; Reich, T. Investigation of Aquo and Chloro Complexes of ${UO_2}^{2+}$, NpO^{2+}, Np^{4+}, and Pu^{3+} by X-ray Absorption Fine Structure Spectroscopy. *Inorg. Chem.* **1997**, *36*, 4676–4683.

[55] Brendebach, B.; Banik, N. L.; Marquardt, C. M.; Rothe, J.; Denecke, M.; Geckeis, H. X-ray Absorption Spectroscopic Study of Trivalent and Tetravalent Actinides in Solution at Varying pH Values. *Radiochim. Acta* **2009**, *97*, 701–708.

[56] Newville, M. Fundamentals of XAFS. *Rev. Mineral. Geochem.* **2014**, *78*, 33–74.

[57] Morelová, N.; Finck, N.; Lützenkirchen, J.; Schild, D.; Dardenne, K.; Geckeis, H. Sorption of Americium / Europium onto Magnetite under Saline Conditions: Batch Experiments, Surface Complexation Modelling and X-ray Absorption Spectroscopy Study. *J. Colloid Interface Sci.* **2020**, *561*, 708–718.

[58] Auffan, M.; Rose, J.; Proux, O.; Borschneck, D.; Masion, A.; Chaurand, P.; Hazemann, J.-L.; Chaneac, C.; Jolivet, J.-P.; Wiesner, M. R.; Van Geen, A.; Bottero, J.-Y. Enhanced Adsorption of Arsenic onto Maghemites Nanoparticles: As(III) as a Probe of the Surface Structure and Heterogeneity. *Langmuir* **2008**, *24*, 3215–3222.

[59] Wang, Y.; Morin, G.; Ona-Nguema, G.; Menguy, N.; Juillot, F.; Aubry, E.; Guyot, F.; Calas, G.; Brown, G. E. Arsenite Sorption at the Magnetite–Water Interface during Aqueous Precipitation of Magnetite: EXAFS Evidence for a New Arsenite Surface Complex. *Geochim. Cosmochim. Acta* **2008**, *72*, 2573–2586.

[60] Morin, G.; Wang, Y.; Ona-Nguema, G.; Juillot, F.; Calas, G.; Menguy, N.; Aubry, E.; Bargar, J. R.; Brown, G. E. EXAFS and HRTEM Evidence for As(III)-containing Surface Precipitates on Nanocrystalline Magnetite: Implications for As Sequestration. *Langmuir* **2009**, *25*, 9119–9128.

[61] Kirsch, R.; Scheinost, A. C.; Rossberg, A.; Banerjee, D.; Charlet, L. Reduction of Antimony by Nano-particulate Magnetite and Mackinawite. *Mineral. Mag.* **2008**, *72*, 185–189.

Chapter 6: Conclusions and Outlook

6.1 Conclusions

Considering the importance of magnetite in natural environment, the present thesis addresses the thermodynamic stability of the prevalent bulk magnetite surface as well as of magnetite nanoparticles, and selected mechanism of Tc and Pu uptake. The inherent ensemble of Fe(II) and Fe(III) cations enables magnetite to take part in redox reactions, e.g., reducing contaminants in the subsurface. Moreover, magnetite is an important mineral in the long-term disposal of radioactive waste, where steel canisters isolating the nuclear waste in the underground are expected to develop a magnetite corrosion layer at their surface. Under such conditions, magnetite may contribute to the retention of contaminants or radionuclides present in formation water. Thereby, the uptake occurs as sorption at the surface or incorporation into the crystal structure.

In the magnetite crystal structure, Fe cations are present in two coordination environments as tetrahedrally and octahedrally coordinated Fe. Especially the latter are of great importance as they host an equal ratio of Fe(II) and Fe(III) in the idealized bulk structure and can buffer redox conditions. However, to investigate possible interactions with contaminants, a detailed knowledge on the surface speciation is required. In the present thesis, the most commonly observed magnetite (111) surface was studied in depth. While previous studies focused on its speciation in vacuum, protonated oxygen-terminated surfaces were studied here reflecting expected idealized terminations of macroscopic crystals. A detailed surface stability analysis was conducted taking into account factors of temperature, pH, and E_h, to determine the surface termination with lowest energy that is expected to represent a long-term stable surface. Between the two likely resulting terminations of an octahedral and mixed tetrahedral termination, the surface with fully coordinated octahedral Fe cations was identified as the dominant one. Specifically the consideration of water as solvent and the corresponding interaction energy were shown to be essential in developing a meaningful scientific model and led to a perfect agreement with experimental results.

The performed atomistic simulations allowed for a detailed investigation of the relevant protonation pattern. For both the assumed infinite magnetite surface as well as derived octahedrally shaped nanoparticles this pattern corresponded to the concept of bond valence sum. Moreover, the degree of surface saturation with hydrogen had a direct impact on the oxidation state of the Fe cations, especially close to the surface. The coherent surface stability analysis suggests that the dominant octahedral surface shows an elevated Fe charge resembling Fe(III) close to the crystal surface taking into account water interaction, too. These results not only contrast the expected mixed valence state in the bulk magnetite structure, they are relevant over a wide range of environmental circumstances such as the expected long-term repository conditions with slightly reducing E_h of $-0.3\,\mathrm{V}$ to $-0.1\,\mathrm{V}$ and circum-neutral pH of 6.9 to 7.9[1]. Moreover, the nanoparticles show a much stronger degree of interaction with the water solvent. This can be attributed to the non-flat geometry compared to the infinite (111) surface, as nanoparticles possess edges and vertices influencing possible interactions with dissolved ions, too. The here simulated magnetite nanoparticles of 2 nm size are, to the best of our knowledge, the largest particles simulated by density functional theory (DFT). The obtained results highlight the importance of a molecular consideration of the non-flat and possibly non-ideal surface and contribute immensely to the understanding of the surface structure in more realistic scenarios.

In the context of radioactive waste disposal, interactions of magnetite with two important radionuclides, Tc and Pu, were studied. The uptake of contaminants from the aqueous phase commonly occurs as sorption at the mineral surface and/or incorporation into the magnetite crystal structure. For each mechanism, corresponding crystal structures for one radionuclide were studied.

The incorporation of Tc(IV) into the magnetite structure was investigated following the mechanism previously discussed in literature in which Tc substitutes for octahedrally coordinated Fe. However, this aliovalent cation substitution hypothesis left the question of charge compensation. Based on the findings obtained in this thesis, this question could be answered revealing the dominant substitution mechanism to include the formation of a vacancy. Moreover, for the first time the incorporation in the magnetite (111) surface was studied and the favorable position of the vacancy close to the crystal surface was revealed. These findings agree well with spectroscopic results obtained from X-ray absorption spectroscopy (XAS). Especially the XAS derived method of extended X-ray absorption fine structure (EXAFS) provided valuable information on the coordination environment.

According to previous EXAFS experiments, Pu(III) forms strong tridentate surface complexes at the octahedrally terminated magnetite (111) surface. In corresponding simulations performed for this thesis, this complex could be confirmed to be sorbed to three edge-sharing FeO_6 octahedra. The averaged Pu-O distance of 2.50 Å shows a high agreement to experimental results. Furthermore, the presented study allows for detailed insight into the coordination numbers that are more difficult to obtain correctly with experimental methods. E.g., the coordination number in water was shown to be eight instead of the proposed nine-fold coordination in a Pu(III) aquo complex.

In the present thesis, the *ab initio* method of DFT was applied to investigate the atomic structure of magnetite and its derived systems with Tc and Pu. The application of the additional Hubbard U parameter (DFT+U) provided an immense improvement on the accuracy of simulations regarding the Fe 3d- and Pu 5f-electrons. Within the presented studies, reasonable values for the relevant oxidation states and coordination environments were validated. The following *ab initio* simulations of the crystal interface provided a meaningful foundation to conduct thermodynamic calculations. Important factors were the system energy as entropic term as well as vibrations of the lattice – especially the surface groups – as main entropic contributions. Moreover, variability of the solution chemistry including background electrolyte, changes in pH etc., were successfully accounted for. The applied methodology will be useful for further scientific endeavors.

6.2 Open questions and direction for further research

6.2.1 Magnetite-maghemite transformation

The investigation of Tc and Pu uptake by magnetite conducted in this thesis uses the pristine magnetite structure as reference material to study ion adsorption and incorporation mechanisms. The presented characterization of the magnetite surface in a wide range of relevant environmental conditions reveals that magnetite surfaces have the tendency to become oxidized even under reducing conditions. Moreover, the here identified energetically favorable Tc(IV) incorporation mechanism suggests a competitive oxidation and the formation of vacancies in the crystal structure as reaction to the charge imbalance.

The combination of both phenomena is characteristic for the maghemitization of magnetite, i.e., the transformation to maghemite. Maghemite is a cubic ferric iron oxide whose structure can be derived from the magnetite one considering that one sixth of the occupied octahedral sites in magnetite are vacant in maghemite. The stepwise oxidation of magnetite to maghemite involves thereby the partial conversion of Fe(II) to Fe(III)[2] and leaching of excess iron ions. Thus, the system setup used in this study closely resembles the onset of the surface induced magnetite-maghemite transformation. To better understand the advanced steps of oxidative ion uptake by magnetite, the mechanism of the magnetite maghemitization should be explored in future computational studies at the molecular scale.

The transition from magnetite to maghemite and the co-existence of both minerals is a common phenomenon in environmental systems. The analysis of these minerals in ocean-floor basalts[3] and marine sediments[4] allows tracing the redox conditions during their formation and their evolution in course of marine diagenesis. The transition from magnetite to maghemite is also known in the context of deep geological repositories, where it is expected that a passivating maghemite layer forms on top of the steel corrosion product magnetite[5]:

$$\mathrm{Fe^{2+}Fe_2^{3+}O_4 + 2\,H^+ \rightarrow Fe_2^{3+}O_3 + Fe^{2+} + H_2O} \tag{6.1}$$

The maghemite film has a low porosity and influences the amount of dissolved $\mathrm{Fe^{2+}}$ in the surrounding water by diminishing its diffusion through the film[5]. In turn, maghemite and dissolved $\mathrm{Fe^{2+}}$ have been observed experimentally as important reaction partners for the magnetite-water equilibrium in the environmentally relevant pH range of 6.5 to 8.5[6]. The corresponding nanoparticles have been found to be bio-compatible[7], too. Under more extreme conditions both acidic[8] and at high pH[9], the transition of magnetite to maghemite has been observed to a smaller extend[10].

The oxidation of magnetite is observed to occur first at the outer regions of the nanoparticles. Over time, this leads to the formation of distinct core-shell particles with a core of magnetite and a surrounding maghemite shell. These structures have been observed from the redox cycling for Fe(II,III) in magnetite by Fe-metabolizing bacteria[11]. Complementary, a bioreduction of the maghemite particles to iron compounds including magnetite is possible[12] showing the high environmental relevance of this topic.

In fact, the dissolved Fe(II) in equilibrium with magnetite and the maghemite shell can to some extend re-charge the maghemite and lead to a transition back to magnetite[13]. However, other substances present in the solution may lead to the formation of Fe(II) complexes and reduce this re-charging[14]. If the same amount of Fe stays in the particle, due to the introduction of vacancies, a slight increase of the particle size is observed[15]. Moreover, upon heating, maghemite transforms to the more stable polymorph hematite and the shell is detached from the magnetite core[11]. These transitions represent interesting phenomena that need to be understood in more detail.

The interaction of maghemite with contaminants is another fascinating field. For the core-shell particle with maghemite shell, a decreased amount of dissolved Fe(II) was shown to slow down the reduction of, e.g., Se[10] as important step of its immobilization. However, the immobilization via sorption is only slightly affected, as the stable (111) surfaces are almost identical[16]. Interestingly, even an increased removal of As has been observed with higher amount of maghemite as it presents a more ordered surface with active sorption sites[17]. For several toxic ions, the availability of surface-Fe octahedra is required to form stable sorption complexes. Their structure can depend on the pH conditions[18] and should be validated by numerical simulations. The sorption reduces the surface energy and if all available sorption sites are saturated, maghemite crystals have been proven to grow[19].

6.2.2 Stability of nanoparticles and crystal growth

The formation and stability of nano-crystalline magnetite precursors and further growth to macroscopic crystals remains to be yet another fascinating topic with open research questions and industrial applications. E.g., the growth of a crystalline magnetite thin film as passivating hydrothermal corrosion product on mild steel has been observed with its black color[20]. Commonly, magnetite is grown on noble metals such as Pt and achieves a high crystal quality with few surface defects[21].

The DFT+U setup developed in this thesis can be used as a basis for molecular scale computational studies on the magnetite and maghemite growth mechanisms. It has been shown to provide more accurate and reliable results compared to standard DFT in the investigation of thin transition metal oxide film growth on both metallic and oxidic substrates[22]. DFT+U was successfully shown to investigate the growth of Tc oxide on the Tc surface simulating the intermediate transition steps[23], too. Moreover, the method of nudged elastic band can be combined with DFT (NEB-DFT) to characterize mechanisms of the elementary reaction steps. A successful application of such methods was recently demonstrated by Rudin et al.[24,25], who investigated the kink site formation on the barite (001) surface and possible incorporation of the radionuclide Ra following a sorption mechanism.

The sorption mechanisms of contaminants as well as dissolved monomers of the mineral are greatly influenced by the surface stability and speciation as well as the surface-solvent interaction at the interface[26]. Currently, methods based on classical force fields are used to simulate these phenomena. *Ab initio* simulations based on DFT would be necessary for validation and the consideration of electronic effects. Moreover, incorporation structures can be studied in detail as presented in this thesis.

The incorporation of high-valent and large-size radionuclides such as U(VI) into the magnetite structure has been observed mainly in co-precipitation experiments. I.e., the uptake occurs alongside the magnetite crystal growth and results in a co-existence of U(IV) and U(VI) in the crystal structure that catalyzes further uptake[27]. Alongside the reduction, Fe(II) is released into the solution[28,29] and can interact with other dissolved species. These processes can be subject to further investigation, too.

Crystal growth is always a non-equilibrium process[30] and requires the understanding of the reaction pathway and kinetics of elementary reaction steps going beyond this thesis. Ketteler et al.[31] observed the substrate-dependent co-growth of iron oxides by cycled deposition and oxidation of iron on Ru. They identified the reaction driving force to result from the electrostatic and thermodynamic energy gain that the growth provides. Contrasting in wet-chemical precipitation experiments, magnetite nucleation from solution is followed by rapid growth of the crystals. Moreover, a rapid agglomeration of nanometer-sized primary particles without an intermediate amorphous bulk precursor phase was observed[32]. The final shape of the nanoparticles can be controlled by the growth reaction time[26].

As shown before, the combination of experiment and simulation can be used to study the different stages of the crystal development. It allows for an investigation from the microscopic to the macroscopic scale and unites the various advantages of different approaches. In this way, valuable knowledge on these environmentally significant systems can be gained.

6.3 References

[1] Wersin, P.; Johnson, L.; Schwyn, B.; Berner, U.; Curti, E. *Redox Conditions in the Near Field of a Repository for SF/HLW and ILW in Opalinus Clay*; NAGRA tech. report 02-13, 2003.

[2] Winsett, J.; Moilanen, A.; Paudel, K.; Kamali, S.; Ding, K.; Cribb, W.; Seifu, D.; Neupane, S. Quantitative Determination of Magnetite and Maghemite in Iron Oxide Nanoparticles Using Mössbauer Spectroscopy. *SN Appl. Sci.* **2019**, *1*, 1636.

[3] Zhou, W.; Peacor, D. R.; der Voo, R. V.; Mansfield, J. F. Determination of Lattice Parameter, Oxidation State, and Composition of Individual Titanomagnetite/Titanomaghemite Grains by Transmission Electron Microscopy. *J. Geophys. Res. Solid Earth* **1999**, *104*, 17689–17702.

[4] Yamazaki, T.; Solheid, P. Maghemite-to-Magnetite Reduction across the Fe-redox Boundary in a Sediment Core from the Ontong-Java Plateau: Influence on Relative Palaeointensity Estimation and Environmental Magnetic Application. *Geophys. J. Int.* **2011**, *185*, 1243–1254.

[5] Johnson, L. H.; Smith, P. A. *The Interaction of Radiolysis Products and Canister Corrosion Products and the Implications for Spent Fuel Dissolution and Radionuclide Transport in a Repository for Spent Fuel*; NAGRA tech. report 00-04, 2000.

[6] Robinson, T. C.; Latta, D. E.; Leddy, J.; Scherer, M. M. Redox Potentials of Magnetite Suspensions under Reducing Conditions. *Environ. Sci. Technol.* **2022**, *56*, 17454–17461.

[7] González-Alonso, D.; González, J.; Gavilán, H.; Fock, J.; Zeng, L.; Witte, K.; Bender, P.; Barquín, L. F.; Johansson, C. Revealing a Masked Verwey Transition in Nanoparticles of Coexisting Fe-Oxide Phases. *RSC Adv.* **2021**, *11*, 390–396.

[8] Sun, Y.-k.; Ma, M.; Zhang, Y.; Gu, N. Synthesis of Nanometer-size Maghemite Particles from Magnetite. *Colloids Surf., A* **2004**, *245*, 15–19.

[9] Um, W.; Wang, G.; Jung, H. B.; Peterson, R. A. *Technetium Removal Using Tc-Goethite Coprecipitation*; resreport PNNL-22967.

[10] Poulain, A.; Fernandez-Martinez, A.; Greneche, J.-M.; Prieur, D.; Scheinost, A. C.; Menguy, N.; Bureau, S.; Magnin, V.; Findling, N.; Drnec, J.; Martens, I.; Mirolo, M.; Charlet, L. Selenium Nanowire Formation by Reacting Selenate with Magnetite. *Environ. Sci. Technol.* **2022**, *56*, 14817–14827.

[11] Byrne, J. M.; Klueglein, N.; Pearce, C.; Rosso, K. M.; Appel, E.; Kappler, A. Redox Cycling of Fe(II) and Fe(III) in Magnetite by Fe-metabolizing Bacteria. *Science* **2015**, *347*, 1473–1476.

[12] O'Loughlin, E. J.; Boyanov, M. I.; Flynn, T. M.; Gorski, C. A.; Hofmann, S. M.; McCormick, M. L.; Scherer, M. M.; Kemner, K. M. Effects of Bound Phosphate on the Bioreduction of Lepidocrocite (γ-FeOOH) and Maghemite (γ-Fe_2O_3) and Formation of Secondary Minerals. *Environ. Sci. Technol.* **2013**, *47*, 9157–9166.

[13] Jungcharoen, P.; Pédrot, M.; Choueikani, F.; Pasturel, M.; Hanna, K.; Heberling, F.; Tesfa, M.; Marsac, R. Probing the Effects of Redox Conditions and Dissolved Fe^{2+} on Nanomagnetite Stoichiometry by Wet Chemistry, XRD, XAS and XMCD. *Environ. Sci.: Nano* **2021**, *8*, 2098–2107.

[14] Jungcharoen, P.; Pédrot, M.; Heberling, F.; Hanna, K.; Choueikani, F.; Catrouillet, C.; Dia, A.; Marsac, R. Prediction of Nanomagnetite Stoichiometry (Fe(II)/Fe(III)) under Contrasting pH and Redox Conditions. *Environ. Sci.: Nano* **2022**, *9*, 2363–2371.

[15] Schwaminger, S. P.; Bauer, D.; Fraga-García, P.; Wagner, F. E.; Berensmeier, S. Oxidation of Magnetite Nanoparticles: Impact on Surface and Crystal Properties. *Cryst. Eng. Comm.* **2017**, *19*, 246–255.

[16] Börsig, N.; Scheinost, A. C.; Schild, D.; Neumann, T. Mechanisms of Selenium Removal by Partially Oxidized Magnetite Nanoparticles for Wastewater Remediation. *Appl. Geochem.* **2021**, *132*, 105062.

[17] Mejia-Santillan, M.; Pariona, N.; Bravo-C., J.; Herrera-Trejo, M.; Montejo-Alvaro, F.; Zarate, A.; Perry, D.; Mtz-Enriquez, A. Physical and Arsenic Adsorption Properties of Maghemite and Magnetite Sub-microparticles. *J. Magn. Magn. Mater.* **2018**, *451*, 594–601.

[18] Jordan, N.; Ritter, A.; Foerstendorf, H.; Scheinost, A.; Weiß, S.; Heim, K.; Grenzer, J.; Mücklich, A.; Reuther, H. Adsorption Mechanism of Selenium(VI) onto Maghemite. *Geochim. Cosmochim. Acta* **2013**, *103*, 63–75.

[19] Auffan, M.; Rose, J.; Proux, O.; Borschneck, D.; Masion, A.; Chaurand, P.; Hazemann, J.-L.; Chaneac, C.; Jolivet, J.-P.; Wiesner, M. R.; Van Geen, A.; Bottero, J.-Y. Enhanced Adsorption of Arsenic onto Maghemites Nanoparticles: As(III) as a Probe of the Surface Structure and Heterogeneity. *Langmuir* **2008**, *24*, 3215–3222.

[20] Machmudah, S.; Zulhijah, R.; Wahyudiono; Setyawan, H.; Kanda, H.; Goto, M. Magnetite Thin Film on Mild Steel Formed by Hydrothermal Electrolysis for Corrosion Prevention. *Chem. Eng. J.* **2015**, *268*, 76–85.

[21] Ritter, M.; Weiss, W. Fe_3O_4(111) Surface Structure Determined by LEED Crystallography. *Surf. Sci.* **1999**, *432*, 81–94.

[22] Barcaro, G.; Thomas, I. O.; Fortunelli, A. Validation of Density-Functional Versus Density-Functional+U Approaches for Oxide Ultrathin Films. *J. Chem. Phys.* **2010**, *132*, 124703.

[23] Taylor, C. D. Oxidation of Technetium Metal As Simulated by First Principles. *J. Phys. Chem. C* **2014**, *118*, 10017–10023.

[24] Rudin, S.; Kowalski, P. M.; Klinkenberg, M.; Bornhake, T.; Bosbach, D.; Brandt, F. Simulation of Crystal Growth by an Innovative Hybrid Density Functional Theory Continuum Solvation Approach: Kink Site Formation on Barite (001). *Cryst. Growth Des.* **2023**, *24*, 159–170.

[25] Rudin, S.; Kowalski, P. M.; Klinkenberg, M.; Bosbach, D.; Brandt, F. Anisotropy of Barite during Crystal Growth and the Uptake of Radium. *Cryst. Growth Des.* **2024**,

[26] Zhang, L.; He, R.; Gu, H.-C. Synthesis and Kinetic Shape and Size Evolution of Magnetite Nanoparticles. *Mater. Res. Bull.* **2006**, *41*, 260–267.

[27] Fu, D.-m.; Li, M.; Hua, Y.-l.; Gao, F.-y.; Wu, X.-y.; Zhang, X.-w.; Fang, Q.; Bi, L.; Cai, T. Evidence for In-situ Electric-Induced Uranium Incorporation into Magnetite Crystal in Acidic Wastewater. *Sep. Purif. Technol.* **2022**, *291*, 120957.

[28] White, A. F.; Peterson, M. L. Reduction of Aqueous Transition Metal Species on the Surfaces of Fe(II)-Containing Oxides. *Geochim. Cosmochim. Acta* **1996**, *60*, 3799–3814.

[29] Singer, D. M.; Chatman, S. M.; Ilton, E. S.; Rosso, K. M.; Banfield, J. F.; Waychunas, G. A. U(VI) Sorption and Reduction Kinetics on the Magnetite (111) Surface. *Environ. Sci. Technol.* **2012**, *46*, 3821–3830.

[30] Sun, W.; Kitchaev, D. A.; Kramer, D.; Ceder, G. Non-equilibrium Crystallization Pathways of Manganese Oxides in Aqueous Solution. *Nat. Commun.* **2019**, *10*.

[31] Ketteler, G.; Ranke, W. Heteroepitaxial Growth and Nucleation of Iron Oxide Films on Ru(0001). *J. Phys. Chem. B* **2003**, *107*, 4320–4333.

[32] Baumgartner, J.; Dey, A.; Bomans, P. H. H.; Le Coadou, C.; Fratzl, P.; Sommerdijk, N. A. J. M.; Faivre, D. Nucleation and Growth of Magnetite from Solution. *Nat. Mater.* **2013**, *12*, 310–314.

Declaration of Originality

Declaration of consent

on the basis of Article 18 of the PromR Phil.-nat. 19

Name/First Name: Katheras, Anita Sonja

Registration Number: 20-143-996

Study program: Earth Sciences

Bachelor ☐ Master ☐ Dissertation ☒

Title of the thesis: Atomic scale characterization of Tc and Pu uptake by magnetite based on atomistic simulations and X-ray absorption spectroscopy

Supervisor: Prof. Dr. Sergey V. Churakov

I declare herewith that this thesis is my own work and that I have not used any sources other than those stated. I have indicated the adoption of quotations as well as thoughts taken from other authors as such in the thesis. I am aware that the Senate pursuant to Article 36 paragraph 1 litera r of the University Act of September 5th, 1996 and Article 69 of the University Statute of June 7th, 2011 is authorized to revoke the doctoral degree awarded on the basis of this thesis.

For the purposes of evaluation and verification of compliance with the declaration of originality and the regulations governing plagiarism, I hereby grant the University of Bern the right to process my personal data and to perform the acts of use this requires, in particular, to reproduce the written thesis and to store it permanently in a database, and to use said database, or to make said database available, to enable comparison with theses submitted by others.

Bern, January 13, 2025
Place/Date

Anita Sonja Katheras
Signature